MULTIHADRON PRODUCTION IN HIGH-ENERGY COLLISIONS AND FORWARD RAPIDITY MEASUREMENT OF INCLUSIVE PHOTONS IN Pb+Pb COLLISIONS AT $\sqrt{s_{\mathrm{NN}}} = 2.76$ TeV IN ALICE EXPERIMENT AT LHC

A THESIS

Submitted in partial fulfilment of the

requirements for the award of the degree

of

DOCTOR OF PHILOSOPHY

By

ADITYA NATH MISHRA

DISCIPLINE OF PHYSICS

INDIAN INSTITUTE OF TECHNOLOGY INDORE

May 2016

Dedicated

to

My **Family**

Acknowledgements

First and foremost I would like to thank the God, who gave me patience, strength and courage to pursue my dreams and complete this thesis work.

I am greatly indebted to my thesis supervisor Prof. Raghunath Sahoo, who has profoundly and continuously encouraged me throughout the Ph. D. period. I acquired the ability to learn, to think, and to question myself, to talk and to communicate with people in a professional and concise way, to be strict and cautious in research but respectful to people's work at the same time, and last but not least, the attitude that "one should either do nothing or give his best". His sense of humour, strictness to his students and constant support at the same time, all make an invaluable mix from which I, as his student, benefited a lot. I am very thankful for his patience which he dealt with me during my hard time, his critical remarks and valuable suggestions.

I would like to thank my PSPC committee members Prof. Ankhi Roy and Prof. Swadesh Shaoo for their encouragement and insightful comments. I would also like to thank all the faculty members and staff members of the IIT Indore for their help and support. I am very thankful to the Physics Discipline of IIT Indore for providing me all required facilities. I would like to thanks to all the members of the Experimental High-Energy Physics (EHEP) lab: Arvind, Dhananjaya, Pooja, Pragati, Prateek, Sushanta and Sunil. The most useful discussions and forming of new problems have taken place during the tea time. I also thank Dr. Swatantra Tiwari and Dr Trambak Bhattacharya for the wonderful company in EHEP lab.

I would also like to thank Dr. Prakhar Garg for his constant support and encouragement like a best friend and philosopher.

I would like to express my thanks to Dr. Satyajit Jena, who helped me a lot during PMD data analysis. Whenever I got stuck with computational or physics related issues, his suggestions helped me to overcome.

I would like to thank ALICE software team and Prof. Latchezar Betev for helping me in computation and providing the necessary resources.

I would like to take this opportunity to thank our Indian Photon Multiplicity Detector (PMD) collaborators. Our colleagues at Variable Energy Cyclotron Centre, Kolkata, were always helpful for a new-comer in the group. I would like to convey my sincere gratitude to Prof. D. K. Srivastava and Prof. Y.P. Viyogi for their valuable advice, inspiration and encouragement during these years. I am really grateful and indebted to Prof. Tapan Nayak, VECC, for his constant encouragement, valuable discussions and suggestions. I express my sincere thank to Mr. T. Samanta and Mr. Vikas Singhal for their constant help in matters related to grid computing at VECC. I would also like to thank VECC grid peer for proving me enormous support for my huge computational work.

It was a great time that I spent at IIT Indore and learned many things with my friends Ajay, Shailendra, Mahesh, Bijay, Sudip, Nitesh, Nishant, Rakesh and Maruthi. I am thankful to Ankita who was with me in all the circumstances to motivate and cheer me up during my Ph.D Her constant believe in me made me confident to work harder for my thesis.

I can not forget my school days friends Amit, Rajendra, Neeraj, Ritu, Ravi and Sunil to keep the friendship live till today. Without their consistent support to me and my family in all manners, this journey could not have ended successfully.

Because of Mrs. Gayatri Sahu's caring nature, I feel very homely during my stay at IIT Indore. I still remember the taste of green tea she used to prepare for me and Prof. Sahoo when I used to work late hours with him. Specially, her two kids Mamun and Papun, I can not forget who used to play with me in my leisure time.

I thank Prof. Basanta K. Nandi and Dr. Nirbhay K. Behera for their

valuable discussions while writing review on "Charged Particle, Photon Multiplicity, and Transverse Energy Production in High-Energy Heavy-Ion Collisions" which helped for my better understanding.

I had the pleasure to work with Prof. Edward K. G. Sarkisyan and Prof. Alexander S. Sakharov from CERN, Geneva, who devoted their valuable time and effort in making me understand the phenomenology of multiparticle mechanism under the Participant Dissipating Energy Approach analysis. I am thankful to your mentorship which made my journey of Ph.D comfortable.

I would also like to thank Prof. Sudhir Raniwala and Dr. Rashmi Raniwala, University of Rajasthan, Jaipur, to introduce me with the physics of heavy-ion collisions, which became helpful for my Ph.D, program.

I am also thankful to the organizers of different schools/ conferences/ symposium/ workshops, that I have attended during my research period, for providing me an opportunity to interact with experts of my field and present my research ideas in front of national and international physics community.

The thesis is the beginning of the journey amid ups and downs of the road and I would not have come this far without the love and support of my wonderful parents, sisters and brothers. I profoundly thank my parents, my sisters, my brothers and all my relatives and friends for their constant love, support, encouragement and most of all, having faith in me.

(Aditya Nath Mishra)

ABSTRACT

Quantum Chromodynamics (QCD), the theory of strong interaction, predicts a phase transition from ordinary nuclear or hadronic matter to a deconfined state of quarks and gluons, called Quark-Gluon Plasma (QGP). Such a phase transition occurs at very high temperatures and/or net baryon densities. It is possible to create these extreme conditions of high temperature and/or net baryon density in the laboratory by colliding heavy-ions at relativistic velocities.

Over the last three decades, a large number of dedicated experimental programs have been taken place all over the world to explore the QCD phase diagram. Systems of various temperatures and densities are expected to be formed in the laboratory by colliding heavy nuclei. Around 1980's, Lawrence Berkeley National Laboratory (LBNL) started heavy-ion program with a beam of heavy-ions up to 1 GeV/nucleon energy, colliding with a fixed target. After that Relativistic Heavy-Ion Collider (RHIC) took forward these studies by colliding Au+Au ions in a wide range of centre of mass energies per nucleon ($\sqrt{s_{\rm NN}}$) from 5.5 to 200 GeV. Now-a-days, the Large Hadron Collider (LHC) is continuing with the collisions of Pb+Pb ions at $\sqrt{s_{\rm NN}} = 2.76$ and 5.02 TeV at the European Organization for Nuclear Research (CERN). The properties of this new phase of partonic matter, QGP, has been discovered first at RHIC and possibly at the SPS energies, but it needs to be studied in details for better understanding of the new state of deconfined matter. For further studies of QGP, A Large Ion Collider Experiment (ALICE), one of the largest experiments in the world at the LHC at CERN, has been designed to study the physics of QGP in heavy-ion collisions.

The ALICE experiment is made up of several sub-detectors. These sub-detectors can be divided in two parts: central barrel detectors and the forward detectors. The central detectors have pseudorapidity coverage of $|\eta| < 1$ and mainly devoted for tracking and particle identification in the very high-multiplicity environment. A few specialized small detector

systems are installed in the forward region of ALICE ($|\eta| > 1$). Photon Multiplicity detector (PMD) is one of the forward detectors in ALICE with full azimuthal coverage in the pseudorapidity region $2.3 < \eta < 3.8$. The PMD is designed to measure the multiplicity and the spatial distribution of photons in the forward rapidity region.

Most of the photons are the decay product of π^0, produced in heavy-ion collisions. Therefore the photon measurements provide complimentary information of the charged particles. In addition, the study of global observables of multiparticle production and their universality in different type of high-energy collisions is of crucial importance to understand the underlying dynamics of strong interaction.

In the present thesis a very first ALICE measurement of photon multiplicity distributions at forward rapidities ($2.3 < \eta < 3.8$) is presented using a highly granular preshower Photon Multiplicity Detector (PMD) in Pb+Pb collisions at $\sqrt{s_{\rm NN}} = 2.76$ TeV. This study is done for various collision centrality classes and are compared with corresponding results for charged particles. Also, we present charged particle and transverse energy production as a function of collision centrality and collision energy, in the framework of nucleon and quark participants. These participants are estimated using a Monte Carlo-based nuclear overlap model.

Further, we analyze the midrapidity pseudorapidity density of charged particles and transverse energy, measured in nucleus-nucleus collisions in the whole available range of $\sqrt{s_{\rm NN}}$ from a few GeV at GSI up to a few TeV at LHC. The dependency of these key variables on $\sqrt{s_{\rm NN}}$ and on the number of participants have been revealed within the participant dissipating energy (PDE) approach.

To find a solution to the RHIC "puzzle" of the difference between the centrality independence of the mean multiplicity vs. the monotonic decrease of the midrapidity pseudorapidity density with the increase of centrality. We study the centrality and $\sqrt{s_{\rm NN}}$ dependance of charged particle mean multiplicity within the PDE approach. In the last we make predictions for the observables namely mean multiplicity, midrapidity pseudorapidity density of charged particles and midrapidity transverse energy density for the upcoming LHC collision energies.

In brief the thesis is organized as follows:

Chapter 1 gives an introduction of the relativistic heavy-ion and proton-proton collisions, the concept of Quark Gluon Plasma (QGP), and the proposed signatures of QGP in heavy-ion collisions.

In **chapter 2**, we introduce the world's largest and most powerful particle accelerator LHC and the experiment dedicated to study heavy-ion collisions, ALICE with its all sub-detectors.

Chapter 3 describes the step by step analysis procedure for measurement of multiplicity and pseudorapidity distributions of photons at forward rapidity using PMD in the ALICE experiment for Pb+Pb collisions at $\sqrt{s_{\rm NN}} = 2.76$.

In **chapter 4**, we study the charged particle and transverse energy production mechanism from AGS, SPS, Relativistic Heavy-Ion Collider (RHIC) to Large Hadron Collider (LHC) energies in the framework of nucleon and quark participants.

In **chapter 5**, we analyze the mean multiplicity ($N_{\rm ch}$), midrapidity pseudorapidity density of charged particles ($dN_{\rm ch}/d\eta$) and of the transverse energy ($E_{\rm T}/d\eta$) measured in nucleus-nucleus collisions in the whole available range of the collision c.m. energy per nucleon within the approach of the dissipation of the effective energy pumped in by the participants of the collisions, which forms the effective-energy budget in the multiparticle production process.

Chapter 6 provides the summary and conclusions drawn from this thesis work and some future insights are also provided in the area of relativistic heavy-ion collisions.

.

PUBLICATIONS

List of Publications:

(Publications with [*] are included in this thesis.)

1. [*] **"Centrality dependence of midrapidity density from GeV to TeV heavy-ion collisions in the effective-energy universality picture of hadroproduction"**
   E. K. G. Sarkisyan, A. N. Mishra, R. Sahoo and A. S. Sakharov, arXiv:1603.09040 [hep-ph], Phys. Rev. D Rapid Comms. (In Press).

2. [*] **"Multihadron production dynamics exploring the energy balance in hadronic and nuclear collisions"**
   E. K. G. Sarkisyan, A. N. Mishra, R. Sahoo and A. S. Sakharov, Phys. Rev. D **93**, 054046 (2016).

3. [*] **"Effective-energy budget in multiparticle production in nuclear collisions"**
   A. N. Mishra, R. Sahoo, E. K. G. Sarkisyan and A. S. Sakharov, Eur. Phys. J. C **74**, 3147 (2014).

4. [*] **"Transverse energy and charged particle production in heavy-ion collisions: From RHIC to LHC"**
   R. Sahoo and A. N. Mishra, Int. J. Mod. Phys. E **23**, 1450024 (2014).

5. **"Energy and Centrality dependence of $dN_{\mathrm{ch}}/d\eta$ and $dE_{\mathrm{T}}/d\eta$ in Heavy-Ion Collisions from $\sqrt{s_{\mathrm{NN}}}$ =7.7 GeV to 5.02 TeV"**
   A. N. Mishra, R. Sahoo, P. Sahoo, P. Pareek, N. K. Behera and B. K. Nandi, arXiv:1505.00700 [hep-ph]

6. **"Charged Particle, Photon Multiplicity, and Transverse Energy Production in High-Energy Heavy-Ion Collisions"**
   R. Sahoo, A. N. Mishra, N. K. Behera and B. K. Nandi, Adv. High Energy Phys. **2015**, 612390 (2015).

7. **“Higher harmonic flow coefficients of identified hadrons in Pb-Pb collisions at $\sqrt{s_{\mathrm{NN}}} = 2.76$ TeV”**
J. Adam, ..., A. N. Mishra *et al.* (ALICE Collaboration), arXiv:1606.06057 [nucl-ex].

8. **“Elliptic flow of electrons from heavy-flavour hadron decays at mid-rapidity in Pb-Pb collisions at $\sqrt{s_{\mathrm{NN}}} = 2.76$ TeV”**
J. Adam, ..., A. N. Mishra *et al.* (ALICE Collaboration), arXiv:1606.00321 [nucl-ex].

9. **“D-meson production in p-Pb collisions at $\sqrt{s_{\mathrm{NN}}} = 5.02$ TeV and in pp collisions at $\sqrt{s} = 7$ TeV”**
J. Adam, ..., A. N. Mishra *et al.* (ALICE Collaboration), arXiv:1605.07569 [nucl-ex].

10. **“Measurement of azimuthal correlations of D mesons and charged particles in pp collisions at $\sqrt{s} = 7$ TeV and p-Pb collisions at $\sqrt{s_{\mathrm{NN}}} = 5.02$ TeV”**
J. Adam, ..., A. N. Mishra *et al.* (ALICE Collaboration), arXiv:1605.06963 [nucl-ex].

11. **“Pseudorapidity dependence of the anisotropic flow of charged particles in Pb+Pb collisions at $\sqrt{s_{\mathrm{NN}}} = 2.76$ TeV”**
J. Adam, ..., A. N. Mishra *et al.* (ALICE Collaboration), arXiv:1605.02035 [nucl-ex]

12. **“Correlated event-by-event fluctuations of flow harmonics in Pb+Pb collisions at $\sqrt{s_{\mathrm{NN}}} = 2.76$ TeV”**
J. Adam, ..., A. N. Mishra *et al.* (ALICE Collaboration), arXiv:1604.07663 [nucl-ex]

13. **“Measurement of transverse energy at midrapidity in Pb+Pb collisions at $\sqrt{s_{\mathrm{NN}}} = 2.76$ TeV”**
J. Adam, ..., A. N. Mishra *et al.* (ALICE Collaboration), arXiv:1603.04775 [nucl-ex]

14. **“Centrality dependence of charged jet production in p+Pb collisions at $\sqrt{s_{\rm NN}}$ = 5.02 TeV”**
J. Adam, ..., A. N. Mishra *et al.* (ALICE Collaboration), arXiv:1603.03402 [nucl-ex]

15. **“Centrality dependence of ψ(2S) suppression in p+Pb collisions at $\sqrt{s_{\rm NN}}$ = 5.02 TeV”**
J. Adam, ..., A. N. Mishra *et al.* (ALICE Collaboration), arXiv:1603.02816 [nucl-ex]

16. **“Measurement of D-meson production versus multiplicity in p+Pb collisions at $\sqrt{s_{\rm NN}} = 5.02$ TeV”**
J. Adam, ..., A. N. Mishra *et al.* (ALICE Collaboration), arXiv:1602.07240 [nucl-ex]

17. **“Particle identification in ALICE: a Bayesian approach”**
J. Adam, ..., A. N. Mishra *et al.* (ALICE Collaboration), arXiv:1602.01392 [physics.data-an]

18. **“Anisotropic flow of charged particles in Pb+Pb collisions at $\sqrt{s_{\rm NN}} = 5.02$ TeV”**
J. Adam, ..., A. N. Mishra *et al.* (ALICE Collaboration), Phys. Rev. Lett. **116**, 132302 (2016).

19. **“Production of $K^*(892)^0$ and ϕ(1020) in p+Pb collisions at $\sqrt{s_{\rm NN}}$ = 5.02 TeV”**
J. Adam, ..., A. N. Mishra *et al.* (ALICE Collaboration), Eur. Phys. J. C **76**, 245 (2016).

20. **“Multiplicity dependence of charged pion, kaon, and (anti)proton production at large transverse momentum in p+Pb collisions at $\sqrt{s_{\rm NN}}$ = 5.02 TeV”**
J. Adam, ..., A. N. Mishra *et al.* (ALICE Collaboration), arXiv:1601.03658 [nucl-ex]

21. **“Multipion Bose-Einstein correlations in $p+p$, p+Pb, and Pb+Pb collisions at the LHC”**
J. Adam, ..., A. N. Mishra *et al.* (ALICE Collaboration), arXiv:1512.08902 [nucl-ex]

22. **“Multi-strange baryon production in p+Pb collisions at $\sqrt{s_{\rm NN}} = 5.02$ TeV”**
J. Adam, ..., A. N. Mishra *et al.* (ALICE Collaboration), arXiv:1512.07227 [nucl-ex]

23. **“Centrality dependence of the charged-particle multiplicity density at mid-rapidity in Pb+Pb collisions at $\sqrt{s_{\rm NN}} = 5.02$ TeV”**
J. Adam, ..., A. N. Mishra *et al.* (ALICE Collaboration), arXiv:1512.06104 [nucl-ex]

24. **“Charge-dependent flow and the search for the chiral magnetic wave in Pb+Pb collisions at $\sqrt{s_{\rm NN}} = 2.76$ TeV”**
J. Adam, ..., A. N. Mishra *et al.* (ALICE Collaboration), Phys. Rev. C **93**, 044903 (2016).

25. **“Measurement of an excess in the yield of J/ψ at very low $p_{\rm T}$ in Pb+Pb collisions at $\sqrt{s_{\rm NN}} = 2.76$ TeV”**
J. Adam, ..., A. N. Mishra *et al.* (ALICE Collaboration), arXiv:1509.08802 [nucl-ex]

26. **“Pseudorapidity and transverse-momentum distributions of charged particles in proton-proton collisions at $\sqrt{s} = 13$ TeV”**
J. Adam, ..., A. N. Mishra *et al.* (ALICE Collaboration), Phys. Lett. B **753**, 319 (2016).

27. **“Inclusive quarkonium production at forward rapidity in pp collisions at $\sqrt{s} = 8$ TeV”**
J. Adam, ..., A. N. Mishra *et al.* (ALICE Collaboration), Eur. Phys. J. C **76**, 184 (2016).

28. **"Charged-particle multiplicities in proton-proton collisions at $\sqrt{s} = 0.9$ to 8 TeV"**

    J. Adam, ..., A. N. Mishra *et al.* (ALICE Collaboration), arXiv:1509.07541 [nucl-ex]

29. **"Measurement of electrons from heavy-flavour hadron decays in p+Pb collisions at $\sqrt{s_{\rm NN}} = 5.02$ TeV"**

    J. Adam, ..., A. N. Mishra *et al.* (ALICE Collaboration), Phys. Lett. B **754**, 81 (2016).

30. **"Azimuthal anisotropy of charged jet production in $\sqrt{s_{\rm NN}} =$ 2.76 TeV Pb+Pb collisions"**

    J. Adam, ..., A. N. Mishra *et al.* (ALICE Collaboration), Phys. Lett. B **753**, 511 (2016).

31. **"Direct photon production in Pb+Pb collisions at $\sqrt{s_{\rm NN}} =$ 2.76 TeV"**

    J. Adam, ..., A. N. Mishra *et al.* (ALICE Collaboration), Phys. Lett. B **754**, 235 (2016).

32. **"Centrality evolution of the charged-particle pseudorapidity density over a broad pseudorapidity range in Pb+Pb collisions at $\sqrt{s_{\rm NN}} =$ 2.76 TeV"**

    J. Adam, ..., A. N. Mishra *et al.* (ALICE Collaboration), Phys. Lett. B **754**, 373 (2016).

33. **"Measurement of D_s^+ production and nuclear modification factor in Pb+Pb collisions at $\sqrt{s_{\rm NN}} =$ 2.76 TeV"**

    J. Adam, ..., A. N. Mishra *et al.* (ALICE Collaboration), J. High Energy Phys. **1603**, 082 (2016).

34. **"Multiplicity and transverse momentum evolution of charge-dependent correlations in $p+p$, p+Pb, and Pb+Pb collisions at the LHC"**

    J. Adam, ..., A. N. Mishra *et al.* (ALICE Collaboration), Eur. Phys. J. C **76**, 86 (2016).

35. **“Transverse momentum dependence of D-meson production in Pb+Pb collisions at $\sqrt{s_{\mathrm{NN}}}$ = 2.76 TeV”**
J. Adam, ..., A. N. Mishra *et al.* (ALICE Collaboration), J. High Energy Phys. **1603**, 081 (2016).

36. **“Coherent ψ(2S) photo-production in ultra-peripheral Pb+Pb collisions at $\sqrt{s_{\mathrm{NN}}}$ = 2.76 TeV”**
J. Adam, ..., A. N. Mishra *et al.* (ALICE Collaboration), Phys. Lett. B **751**, 358 (2015).

37. **“Precision measurement of the mass difference between light nuclei and anti-nuclei”**
J. Adam, ..., A. N. Mishra *et al.* (ALICE Collaboration), Nature Phys. **11**, 811 (2015).

38. **“Study of cosmic ray events with high muon multiplicity using the ALICE detector at the CERN Large Hadron Collider”**
J. Adam, ..., A. N. Mishra *et al.* (ALICE Collaboration), JCAP **1601**, 032 (2016).

39. **“Centrality dependence of pion freeze-out radii in Pb+Pb collisions at $\sqrt{s_{\mathrm{NN}}}$ = 2.76 TeV”**
J. Adam, ..., A. N. Mishra *et al.* (ALICE Collaboration), Phys. Rev. C **93**, 024905 (2016).

40. **“Event shape engineering for inclusive spectra and elliptic flow in Pb+Pb collisions at $\sqrt{s_{\mathrm{NN}}} = 2.76$ TeV”**
J. Adam, ..., A. N. Mishra *et al.* (ALICE Collaboration), Phys. Rev. C **93**, 034916 (2016).

41. **“Elliptic flow of muons from heavy-flavour hadron decays at forward rapidity in Pb+Pb collisions at $\sqrt{s_{\mathrm{NN}}} = 2.76$ TeV”**
J. Adam, ..., A. N. Mishra *et al.* (ALICE Collaboration), Phys. Lett. B **753**, 41 (2016).

42. **“Production of light nuclei and anti-nuclei in $p + p$ and Pb+Pb collisions at energies available at the CERN Large Hadron Collider”**

J. Adam, ..., A. N. Mishra *et al.* (ALICE Collaboration), Phys. Rev. C **93**, 024917 (2016).

43. **“ϕ-meson production at forward rapidity in p+Pb collisions at $\sqrt{s_{\rm NN}}$ = 5.02 TeV and in pp collisions at $\sqrt{s}$ = 2.76 TeV”**

J. Adam, ..., A. N. Mishra *et al.* (ALICE Collaboration), arXiv:1506.09206 [nucl-ex]

44. **“$^{3}_{\Lambda}$H and $^{3}_{\Lambda}\overline{\rm H}$ production in Pb+Pb collisions at $\sqrt{s_{\rm NN}}$ = 2.76 TeV”**

J. Adam, ..., A. N. Mishra *et al.* (ALICE Collaboration), Phys. Lett. B **754**, 360 (2016).

45. **“Centrality dependence of inclusive J/ψ production in p+Pb collisions at $\sqrt{s_{\rm NN}} = 5.02$ TeV”**

J. Adam, ..., A. N. Mishra *et al.* (ALICE Collaboration), J. High Energy Phys. **1511**, 127 (2015).

46. **“Differential studies of inclusive J/ψ and ψ(2S) production at forward rapidity in Pb+Pb collisions at $\sqrt{s_{\rm NN}}$ = 2.76 TeV”**

J. Adam, ..., A. N. Mishra *et al.* (ALICE Collaboration), arXiv:1506.08804 [nucl-ex]

47. **“Forward-central two-particle correlations in p+Pb collisions at $\sqrt{s_{\rm NN}}$ = 5.02 TeV”**

J. Adam, ..., A. N. Mishra *et al.* (ALICE Collaboration), Phys. Lett. B **753**, 126 (2016).

48. **“One-dimensional pion, kaon, and proton femtoscopy in Pb+Pb collisions at $\sqrt{s_{\rm NN}}$ =2.76 TeV”**

J. Adam, ..., A. N. Mishra *et al.* (ALICE Collaboration), Phys. Rev. C **92**, 054908 (2015).

49. **"Search for weakly decaying $\bar{\Lambda}$n and $\Lambda\Lambda$ exotic bound states in central Pb+Pb collisions at $\sqrt{s_{\mathrm{NN}}}$ = 2.76 TeV"**
J. Adam, ..., A. N. Mishra *et al.* (ALICE Collaboration), Phys. Lett. B **752**, 267 (2016).

50. **"Centrality dependence of the nuclear modification factor of charged pions, kaons, and protons in Pb+Pb collisions at $\sqrt{s_{\mathrm{NN}}} = 2.76$ TeV"**
J. Adam, ..., A. N. Mishra *et al.* (ALICE Collaboration), Phys. Rev. C **93**, 034913 (2016).

51. **"Centrality dependence of high-p$_T$ D meson suppression in Pb+Pb collisions at $\sqrt{s_{\mathrm{NN}}} = 2.76$ TeV"**
J. Adam, ..., A. N. Mishra *et al.* (ALICE Collaboration), J. High Energy Phys. **1511**, 205 (2015).

52. **"Measurement of jet quenching with semi-inclusive hadron-jet distributions in central Pb+Pb collisions at $\sqrt{s_{\mathrm{NN}}} = 2.76$ TeV"**
J. Adam, ..., A. N. Mishra *et al.* (ALICE Collaboration), J. High Energy Phys. **1509**, 170 (2015).

53. **"Measurement of charm and beauty production at central rapidity versus charged-particle multiplicity in proton-proton collisions at $\sqrt{s} = 7$ TeV"**
J. Adam, ..., A. N. Mishra *et al.* (ALICE Collaboration), J. High Energy Phys. **1509**, 148 (2015).

54. **"Inclusive, prompt and non-prompt J/ψ production at mid-rapidity in Pb+Pb collisions at $\sqrt{s_{\mathrm{NN}}}$ = 2.76 TeV"**
J. Adam, ..., A. N. Mishra *et al.* (ALICE Collaboration), J. High Energy Phys. **1507**, 051 (2015).

55. **“Measurement of pion, kaon and proton production in $p + p$ collisions at $\sqrt{s} = 7$ TeV”**
J. Adam, ..., A. N. Mishra *et al.* (ALICE Collaboration), Eur. Phys. J. C **75**, 226 (2015).

56. **“Coherent ρ^0 photoproduction in ultra-peripheral Pb+Pb collisions at $\sqrt{s_{\rm NN}} = 2.76$ TeV”**
J. Adam, ..., A. N. Mishra *et al.* (ALICE Collaboration), J. High Energy Phys. **1509**, 095 (2015).

57. **“Rapidity and transverse-momentum dependence of the inclusive J/ψ nuclear modification factor in p+Pb collisions at $\sqrt{s_{\rm NN}}$ = 5.02 TeV”**
J. Adam, ..., A. N. Mishra *et al.* (ALICE Collaboration), J. High Energy Phys. **1506**, 055 (2015).

58. **“Measurement of dijet k_T in p+Pb collisions at $\sqrt{s_{\rm NN}}$=5.02 TeV”**
J. Adam, ..., A. N. Mishra *et al.* (ALICE Collaboration), Phys. Lett. B **746**, 385 (2015).

59. **“Measurement of charged jet production cross sections and nuclear modification in p+Pb collisions at $\sqrt{s_{\rm NN}} = 5.02$ TeV”**
J. Adam, ..., A. N. Mishra *et al.* (ALICE Collaboration), Phys. Lett. B **749**, 68 (2015).

60. **“Measurement of jet suppression in central Pb+Pb collisions at $\sqrt{s_{\rm NN}}$ = 2.76 TeV”**
J. Adam, ..., A. N. Mishra *et al.* (ALICE Collaboration), Phys. Lett. B **746**, 1 (2015).

61. **“Two-pion femtoscopy in p+Pb collisions at $\sqrt{s_{\rm NN}} = 5.02$ TeV”**
J. Adam, ..., A. N. Mishra *et al.* (ALICE Collaboration), Phys. Rev. C **91**, 034906 (2015).

62. **"Forward-backward multiplicity correlations in $p+p$ collisions at $\sqrt{s}$ = 0.9, 2.76 and 7 TeV"**
J. Adam, ..., A. N. Mishra *et al.* (ALICE Collaboration), J. High Energy Phys. **1505**, 097 (2015).

63. **"Centrality dependence of particle production in p+Pb collisions at $\sqrt{s_{\rm NN}}$= 5.02 TeV"**
J. Adam, ..., A. N. Mishra *et al.* (ALICE Collaboration), Phys. Rev. C **91**, 064905 (2015).

64. **"Inclusive photon production at forward rapidities in $p+p$ collisions at $\sqrt{s}$ = 0.9, 2.76 and 7 TeV"**
B. B. Abelev, ..., A. N. Mishra *et al.* (ALICE Collaboration), Eur. Phys. J. C **75**, 46 (2015).

65. **"Charged jet cross sections and properties in $p+p$ collisions at $\sqrt{s}=7$ TeV"**
B. B. Abelev, ..., A. N. Mishra *et al.* (ALICE Collaboration), Phys. Rev. D **91**, 112012 (2015).

66. **"Production of inclusive Υ(1S) and Υ(2S) in p+Pb collisions at $\sqrt{s_{\rm NN}}=5.02$ TeV"**
B. B. Abelev, ..., A. N. Mishra *et al.* (ALICE Collaboration), Phys. Lett. B **740**, 105 (2015).

67. **"Event-by-event mean $p_{\rm T}$ fluctuations in $p+p$ and Pb+Pb collisions at the LHC"**
B. B. Abelev, ..., A. N. Mishra *et al.* (ALICE Collaboration), Eur. Phys. J. C **74**, 3077 (2014).

68. **"Exclusive J/ψ photoproduction off protons in ultra-peripheral p+Pb collisions at $\sqrt{s_{\rm NN}}=5.02$ TeV"**
B. B. Abelev, ..., A. N. Mishra *et al.* (ALICE Collaboration), Phys. Rev. Lett. **113**, 232504 (2014).

69. **"Multiplicity dependence of jet-like two-particle correlation structures in p+Pb collisions at $\sqrt{s_{\rm NN}}$ =5.02 TeV"**

B. B. Abelev, ..., A. N. Mishra *et al.* (ALICE Collaboration), Phys. Lett. B **741**, 38 (2015).

70. **"Production of $\Sigma(1385)^{\pm}$ and $\Xi(1530)^{0}$ in proton-proton collisions at $\sqrt{s} = 7$ TeV"**
B. B. Abelev, ..., A. N. Mishra *et al.* (ALICE Collaboration), Eur. Phys. J. C **75**, 1 (2015).

71. **"Multiparticle azimuthal correlations in p+Pb and Pb+Pb collisions at the CERN Large Hadron Collider"**
B. B. Abelev, ..., A. N. Mishra *et al.* (ALICE Collaboration), Phys. Rev. C **90**, 054901 (2014).

72. **"Elliptic flow of identified hadrons in Pb+Pb collisions at $\sqrt{s_{\rm NN}} = 2.76$ TeV"**
B. B. Abelev, ..., A. N. Mishra *et al.* (ALICE Collaboration), J. High Energy Phys. **1506**, 190 (2015).

73. **"Suppression of $\Upsilon(1S)$ at forward rapidity in Pb+Pb collisions at $\sqrt{s_{\rm NN}} = 2.76$ TeV"**
B. B. Abelev, ..., A. N. Mishra *et al.* (ALICE Collaboration), Phys. Lett. B **738**, 361 (2014).

74. **"Beauty production in $p + p$ collisions at $\sqrt{s} = 2.76$ TeV measured via semi-electronic decays"**
B. B. Abelev, ..., A. N. Mishra *et al.* (ALICE Collaboration), Phys. Lett. B **738**, 97 (2014).

75. **"Measurement of electrons from semileptonic heavy-flavour hadron decays in pp collisions at $\sqrt{s} = 2.76$ TeV"**
B. B. Abelev, ..., A. N. Mishra *et al.* (ALICE Collaboration), Phys. Rev. D **91**, 012001 (2015).

76. **"Suppression of ψ(2S) production in p+Pb collisions at $\sqrt{s_{\rm NN}}$ = 5.02 TeV"**
B. B. Abelev, ..., A. N. Mishra *et al.* (ALICE Collaboration), JHEP **1412**, 073 (2014).

77. **“Neutral pion production at midrapidity in p+p and Pb+Pb collisions at** $\sqrt{s_{\rm NN}} = 2.76\,\rm TeV$**”**
B. B. Abelev, ..., A. N. Mishra *et al.* (ALICE Collaboration), Eur. Phys. J. C **74**, 3108 (2014).

78. **“Measurement of prompt D-meson production in p+Pb collisions at $\sqrt{s_{\rm NN}} = 5.02$ TeV”**
B. B. Abelev, ..., A. N. Mishra *et al.* (ALICE Collaboration), Phys. Rev. Lett. **113**, 232301 (2014).

79. **“Transverse momentum dependence of inclusive primary charged-particle production in p+Pb collisions at** $\sqrt{s_{\rm NN}} =$ 5.02 **TeV”**
B. B. Abelev, ..., A. N. Mishra *et al.* (ALICE Collaboration), Eur. Phys. J. C **74**, 3054 (2014).

80. **“Azimuthal anisotropy of D meson production in Pb+Pb collisions at** $\sqrt{s_{\rm NN}} = 2.76$ **TeV”**
B. B. Abelev, ..., A. N. Mishra *et al.* (ALICE Collaboration), Phys. Rev. C **90**, 034904 (2014).

81. **“Measurement of visible cross sections in proton-lead collisions at $\sqrt{s_{\rm NN}} = 5.02$ TeV in van der Meer scans with the ALICE detector”**
B. B. Abelev, ..., A. N. Mishra *et al.* (ALICE Collaboration), JINST **9**, P11003 (2014).

82. **“Freeze-out radii extracted from three-pion cumulants in p+p , p+Pb and Pb+Pb collisions at the LHC”**
B. B. Abelev, ..., A. N. Mishra *et al.* (ALICE Collaboration), Phys. Lett. B **739**, 139 (2014).

83. **“**$K^{*}(892)^{0}$ **and** $\phi(1020)$ **production in Pb+Pb collisions at $\sqrt{s_{\rm NN}} = 2.76$ TeV”**
B. B. Abelev, ..., A. N. Mishra *et al.* (ALICE Collaboration), Phys. Rev. C **91**, 024609 (2015).

84. **“Measurement of quarkonium production at forward rapidity in $p+p$ collisions at $\sqrt{s} = 7$ TeV”**
B. B. Abelev, ..., A. N. Mishra *et al.* (ALICE Collaboration), Eur. Phys. J. C **74**, 2974 (2014).

85. **“Performance of the ALICE Experiment at the CERN LHC”**
B. B. Abelev, ..., A. N. Mishra *et al.* (ALICE Collaboration), Int. J. Mod. Phys. A **29**, 1430044 (2014).

86. **“Production of charged pions, kaons and protons at large transverse momenta in $p+p$ and Pb+Pb collisions at $\sqrt{s_{\mathrm{NN}}}$ =2.76 TeV”**
B. B. Abelev, ..., A. N. Mishra *et al.* (ALICE Collaboration), Phys. Lett. B **736**, 196 (2014).

87. **“Centrality, rapidity and transverse momentum dependence of J/ψ suppression in Pb+Pb collisions at $\sqrt{s_{\mathrm{NN}}}$=2.76 TeV”**
B. B. Abelev, ..., A. N. Mishra *et al.* (ALICE Collaboration), Phys. Lett. B **734**, 314 (2014).

88. **“Two- and three-pion quantum statistics correlations in Pb+Pb collisions at $\sqrt{s_{\mathrm{NN}}} =$ 2.76 TeV at the CERN Large Hadron Collider”**
B. B. Abelev, ..., A. N. Mishra *et al.* (ALICE Collaboration), Phys. Rev. C **89**, 024911 (2014).

89. **“J/ψ production and nuclear effects in p+Pb collisions at $\sqrt{s_{\mathrm{NN}}} =$ 5.02 TeV”**
B. B. Abelev, ..., A. N. Mishra *et al.* (ALICE Collaboration), JHEP **1402**, 073 (2014).

90. **“Multiplicity Dependence of Pion, Kaon, Proton and Lambda Production in p+Pb Collisions at $\sqrt{s_{\mathrm{NN}}} =$ 5.02 TeV”**
B. B. Abelev, ..., A. N. Mishra *et al.* (ALICE Collaboration), Phys. Lett. B **728**, 25 (2014).

91. **"Multi-strange baryon production at mid-rapidity in Pb+Pb collisions at $\sqrt{s_{\mathrm{NN}}}$ = 2.76 TeV"**
B. B. Abelev, ..., A. N. Mishra *et al.* (ALICE Collaboration), Phys. Lett. B **728**, 216 (2014)., Erratum: [Phys. Lett. B **734**, 409 (2014).]

92. **"K_S^0 and Λ production in Pb+Pb collisions at $\sqrt{s_{NN}}$ = 2.76 TeV"**
B. B. Abelev, ..., A. N. Mishra *et al.* (ALICE Collaboration), Phys. Rev. Lett. **111**, 222301 (2013).

93. **"Long-range angular correlations of π, K and p in p+Pb collisions at $\sqrt{s_{\mathrm{NN}}}$ = 5.02 TeV"**
B. B. Abelev, ..., A. N. Mishra *et al.* (ALICE Collaboration), Phys. Lett. B **726**, 164 (2013).

94. **"Multiplicity dependence of two-particle azimuthal correlations in $p+p$ collisions at the LHC"**
B. Abelev, ..., A. N. Mishra *et al.* (ALICE Collaboration), JHEP **1309**, 049 (2013).

95. **"Multiplicity dependence of the average transverse momentum in $p+p$,p+Pb, and Pb+Pb collisions at the LHC"**
B. B. Abelev, ..., A. N. Mishra *et al.* (ALICE Collaboration), Phys. Lett. B **727**, 371 (2013).

96. **"Energy Dependence of the Transverse Momentum Distributions of Charged Particles in $p+p$ Collisions Measured by ALICE"**
B. B. Abelev, ..., A. N. Mishra *et al.* (ALICE Collaboration), Eur. Phys. J. C **73**,12, 2662 (2013).

97. **"Directed Flow of Charged Particles at Midrapidity Relative to the Spectator Plane in Pb+Pb Collisions at $\sqrt{s_{\mathrm{NN}}}$=2.76 TeV"**
B. Abelev, ..., A. N. Mishra *et al.* (ALICE Collaboration), Phys. Rev. Lett. **111**, 232302 (2013).

98. **"Centrality dependence of the pseudorapidity density distribution for charged particles in Pb+Pb collisions at $\sqrt{s_{\rm NN}}$ = 2.76 TeV"**
E. Abbas, ..., A. N. Mishra *et al.* (ALICE Collaboration), Phys. Lett. B **726**, 610 (2013).

99. **"J/Psi Elliptic Flow in Pb+Pb Collisions at $\sqrt{s_{\rm NN}}$ = 2.76 TeV"**
E. Abbas, ..., A. N. Mishra *et al.* (ALICE Collaboration), Phys. Rev. Lett. **111**, 162301 (2013).

100. **"Centrality dependence of π, K, p production in Pb+Pb collisions at $\sqrt{s_{\rm NN}}$ = 2.76 TeV"**
B. Abelev, ..., A. N. Mishra *et al.* (ALICE Collaboration), Phys. Rev. C **88**, 044910 (2013).

101. **"Centrality determination of Pb+Pb collisions at $\sqrt{s_{\rm NN}}$ = 2.76 TeV with ALICE"**
B. Abelev, ..., A. N. Mishra *et al.* (ALICE Collaboration), Phys. Rev. C **88**, 044909 (2013).

102. **"Charge correlations using the balance function in Pb+Pb collisions at $\sqrt{s_{\rm NN}}$ = 2.76 TeV"**
B. Abelev, ..., A. N. Mishra *et al.* (ALICE Collaboration), Phys. Lett. B **723**, 267 (2013).

103. **"Long-range angular correlations on the near and away side in p+Pb collisions at $\sqrt{s_{\rm NN}} = 5.02$ TeV"**
B. Abelev, ..., A. N. Mishra *et al.* (ALICE Collaboration), Phys. Lett. B **719**, 29 (2013).

104. **"Transverse momentum distribution and nuclear modification factor of charged particles in p+Pb collisions at $\sqrt{s_{\rm NN}} =$ 5.02 TeV"**
B. Abelev, ..., A. N. Mishra *et al.* (ALICE Collaboration), Phys. Rev. Lett. **110**, 082302 (2013).

105. **“Pseudorapidity density of charged particles in p+Pb collisions at $\sqrt{s_{\mathrm{NN}}} = 5.02$ TeV”**
B. Abelev, ..., A. N. Mishra *et al.* (ALICE Collaboration), Phys. Rev. Lett. **110**, 032301 (2013).

Conference proceedings:

International:

1. **A. N. Mishra**, R. Sahoo, E. K. G. Sarkisyan, DAE Symp. Nucl. Phys. **58**, 754 (2013).

2. **A. N. Mishra**, R. Mazumder, and R. Sahoo, AIP Conference Proceedings, 1536, 1348 (2013).

3. **A. N. Mishra**, R. Sahoo, E. K. G. Sarkisyan and A.S. Sakharov., Eur. Phys. J. Web of Conf. **90**, 01001 (2015), arXiv: 1411.7792 (*Invited Talk*).

4. **A. N. Mishra**, E. K. G. Sarkisyan, R. Sahoo, and A. S. Sakharov, [To be published in SLAC Spires e-conf. volume (2015)] (*Invited Talk*).

5. **A. N. Mishra**, Raghunath Sahoo, E. K. G. Sarkisyan and A. S. Sakharov. [To be published in Proceedings of Science (2015)].

6. P. Pareek, **A. N. Mishra**, P. Sahoo, and R. Sahoo, [To be published in Proceedings of Science (2015)].

7. **A. N. Mishra**, E. K. G. Sarkisyan, R. Sahoo, and A. S. Sakharov, [To be published in Eur. Phys. J. Web of Conf (2016)] (*Invited Talk*).

8. E. K. G. Sarkisyan, **A. N. Mishra**, R. Sahoo, and A. S. Sakharov, [To be published in Acta Physica Pol. B: Proceedings Supplement (2016)] (*Invited Talk*).

National:

1. **A. N. Mishra**, R. Mazumder, R. Sahoo and B. K. Nandi, DAE Symp. Nucl. Phys. **57**, 772 (2012).

2. **A. N. Mishra**, R. Sahoo,E. K. G. Sarkisyan, A. S. Sakharov, DAE Symp. Nucl. Phys. **59**, 740 (2014).

3. P. Pareek, **A. N. Mishra**, P. Sahoo, R. Sahoo, DAE Symp. Nucl. Phys. **59**, 738 (2014).

4. **A. N. Mishra**, R. Sahoo, E. K. G. Sarkisyan and A. S. Sakharov, DAE Symp. Nucl. Phys. **60**, 750 (2015).

5. D. Thakur, P. Garg, S. Tripathy, A. Khuntia, **A. N. Mishra** and R. Sahoo, DAE Symp. Nucl. Phys. **60**, 738 (2015).

Contents

Figures

Tables

Chapter 1

Introduction

The theories and discoveries made by thousands of physicists since the 1930's have resulted in a remarkable insight into the fundamental structure of matter: everything in the universe is found to be made from a few basic building blocks called fundamental particles, governed by four fundamental forces. Our best understanding of how these particles and three of the forces are related to each other is encapsulated in the Standard Model of particle physics. Developed in the early 1970's, it has successfully explained many experimental results and precisely predicted a wide variety of phenomena. Over time and through many experiments, the Standard Model has proved to be a well-tested theory.

1.1 The Standard Model

There are four conventionally accepted fundamental interactions in nature: Strong, Electromagnetic, Weak and Gravitational. Each one is understood as the dynamics of a field. There have been various attempts to unite all the four interactions to have one unified model. But so far only three fundamental interactions, *i.e.* Strong, Electromagnetic and Weak, are incorporated in a model, known as the Standard Model (SM) [1, 2]. The SM describes the universe in terms of elementary building blocks of matter (quarks and leptons) and interactions between them via force carriers (bosons). The SM categorizes all the elementary particles into groups such as quarks, leptons, gauge bosons and the recently discovered Higgs boson. Further, the leptons and the quarks can be sub-divided into 3 generations. The lightest and most stable particles belong to the first generation, whereas the second and third generations are made up of heavier and less stable particles. There are six quarks paired in 3 generations: the up (u) and down quarks (d) are from first generation, followed by the charm (c) and strange (s) quarks from second generation and then the top (t) and bottom (b) or beauty quarks from third generation. The quarks are fractional charged particles. The up, charm and top quarks (u, c, t) have $+2/3$ unit of electronic charge whereas down, strange and beauty quarks (d, s, b) have $-1/3$ unit of electronic charge. Quarks participate in all three types of interactions. The strong interaction is mediated by gluons, the electromagnetic interaction is mediated by photons and the $W^{\pm}$ and Z^0 bosons are the mediating particles in the weak interactions. The photon and gluons are massless, whereas $W^{\pm}$ and Z^0 are massive particles. Similarly, the six leptons are divided in three generations: the electron (e) and the electron neutrino (ν_e); and the muon (μ) and muon neutrino (ν_μ); and the tau (τ) and tau neutrino (ν_τ). The e, μ and τ all have an electric charge and a sizeable mass, whereas the neutrinos are electrically neutral with a very little mass. Leptons participate both in Electromagnetic and Weak interactions with an exception that only neutrinos are weakly interacting particles.

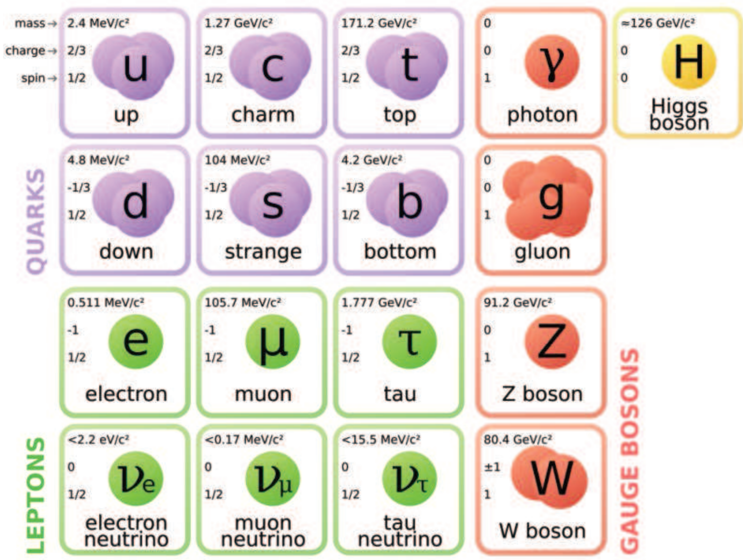

Figure 1.1. The schematic representation of Standard model of elementary particles.

The SM also incorporates another fundamental property of the nature named as symmetry. Symmetry of all these three fundamental interactions is studied by gauge theory and the field is known as gauge field. The quanta of gauge field is known as the gauge bosons, which are the force carriers. The SM is a relativistic quantum field theory that incorporates the basic principles of quantum mechanics and special theory of relativity. lt is a gauge theory with the non-abelian gauge group $SU(3)_c \otimes SU(2)_L \times U(1)_Y$ instead of a simple abelian gauge group, $U(1)_{em}$, of Quantum Electrodynamics (QED). In SM, non-abelian gauge group is made up of twelve gauge bosons: one massless photon, three massive weak bosons and eight massless gluons. The symmetry of these groups implies that the gauge bosons should be massless. But in 1973, $W^{\pm}$ and Z^0-bosons are discovered with a finite mass (around 80 GeV/c^2), which led to adopt the Higgs mechanism [3, 4], which proposes explanation of the generation of masses for the fundamental particles of the universe through electroweak symmetry breaking.

In July 2012, A Toroidal LHC ApparatuS (ATLAS) and the Compact Muon Solenoid (CMS) at Large Hadron Collider (LHC) at CERN announced the experimental evidence of a new particle in the mass region around 126 GeV [5, 6], which is consistent with the Higgs boson predicted by the Standard Model. Two theoretical physicists François Englert and Peter W. Higgs were jointly awarded with the Nobel prize in Physics 2013 for their contribution to the theory of Higgs mechanism.

1.2 Quantum Chromodynamics (QCD)

Quantum Chromodynamics (QCD) [1] is the theory of the strong interactions, which describes the interactions between quarks and gluons, via exchange of massless gluons. QCD calculations indicate that the potential between two quarks can be given as:

$$V(r) = -\frac{4}{3}\frac{\alpha_s(r)}{r} + kr, \tag{1.1}$$

where α_s is the coupling strength, k the string constant and r is the distance between quarks.

For small values of r, the first term of the Eq. 1.1 dominates and the system behaves similarly to the electrodynamic case. At larger values of r, the potential energy between two quarks increases with separation until enough energy is available to form a new quark-antiquark pair, which occurs only if the quarks are separated. This leads to the fact that all quarks are confined within hadrons, and one can not observe a free or isolated quark in nature. Quarks are always found as part of a 3 quark state, called baryons or a quark-antiquark state, known as a mesons. This property is known as “confinement”. Recently, Large Hadron Collider beauty (LHCb) experiment at Large Hadron Collider (LHC) has reported the discovery of a confined state of four quarks and antiquark, named as *pentaquark* [7].

On the other hand “Asymptotic freedom” implies that at very short distances or large momentum transfers the coupling strength becomes asymptotically weaker [8]. The coupling strength, α_s is not a constant. It depends on the momentum transfer in the interaction according to the following relation:

$$\alpha_s \approx \frac{2\pi}{(11 - \frac{2}{3}n_f)\ln(Q^2/\Lambda_{QCD})}. \tag{1.2}$$

Here n_f is the number of active quarks, Q^2 is the momentum transfer and Λ_{QCD} shows the characteristic energy scale of QCD.

For large values of Q^2, perturbative QCD (pQCD) calculations are used to understand the processes occurring at short distances, this is the reason α_s is called as *running coupling constant* of QCD. However for small Q^2, one can only use numerical methods and Lattice QCD is such a well-established non-perturbative approach. Fig. 1.2 shows α_s measured in several experiments at different energies as a function of momentum transfer (Q). At low Q^2, coupling constant is large and perturbative treatment is not applicable. In this region coupling constant is so large that quarks become confined in a hadron. The processes with small momentum transfer is called soft processes and can be explained by the well established non-perturbative approach, Lattice QCD.

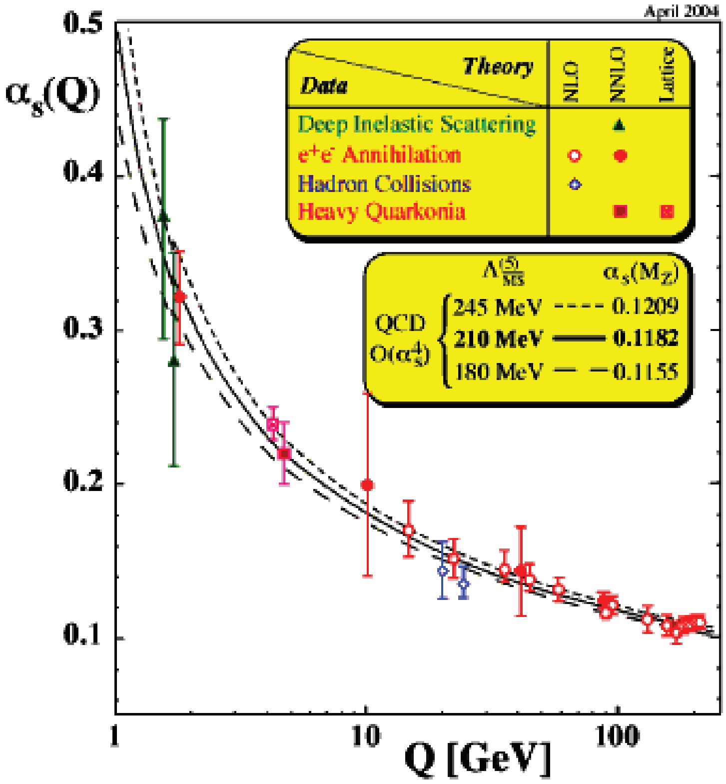

Figure 1.2. QCD coupling constant (α_s) as a function of momentum transfer [9].

1.3 Lattice QCD and Phase Diagram

According to Lattice QCD calculations, at sufficiently large temperatures and energy densities, one expects a transition from normal nuclear matter to a deconfined state of quarks and gluons. This is illustrated in Fig. 1.3, which shows Lattice QCD calculations for the temperature T dependence of the energy density ϵ scaled by T^4. ϵ/T^4 is proportional to number of degree of freedom for the system. It is observed that at the temperature around critical temperature, *i.e.* $T = T_c$ (T_c ~154 MeV), ϵ/T^4 has a sharp increase, which slowly saturates at higher temperatures below the value of the Stefan-Boltzmann value [10, 11], shown by arrows for different flavors in Fig. 1.3. One of the most important observation is that at T_c, sudden

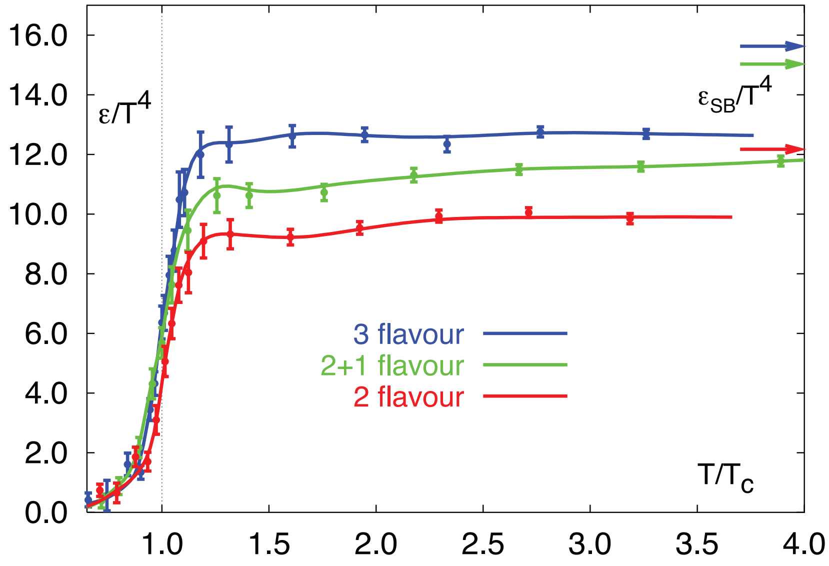

Figure 1.3. The energy density in QCD from lattice calculations. When the temperature T reaches the critical temperature T_c, the number of degrees of freedom rapidly rises indicating that quarks and gluons become relevant degrees of freedom. The arrows on top represents the Stefan-Boltzmann values for a perfect Bose gas at asymptotically high temperature. The figure is taken from [11]

increase in the degrees of freedom indicates a possible phase transition from hadronic phase to deconfined state of quarks and gluons, called Quark-Gluon Plasma (QGP). Although the T_c varies with the quark flavors, but the observation of the sudden increase of the degrees of freedom at T_c remains valid for all quark flavors.

The conjectured QCD phase diagram is shown in Fig. 1.4, which maps out the different phases of QCD matter as a function of baryon chemical potential (μ_B) and temperature (T) [12]. If μ_B increases beyond a critical value keeping the temperature low, there is a possibility of formation of baryon rich QGP, which is produced in Neutron Stars. At a very high temperature and $\mu_B \sim 0$, Lattice QCD predicts a rapid cross-over from hadronic to QGP phase. This scenario is similar to the early Universe scenario. Lattice QCD predicts a boundary in the QCD phase diagram, which separates the region of matter dominated by hadronic degrees of freedom from that dominated by partonic degrees of freedom. This boundary is called the "first order phase transition" line or the "QCD phase boundary". The point on this QCD phase boundary, where first order phase transition ends and cross-over starts, is called "critical point". One of the main objectives of the high-energy heavy-ion collision experiments is to map the QCD phase diagram, to locate the position of critical point, and to determine the QCD phase boundary.

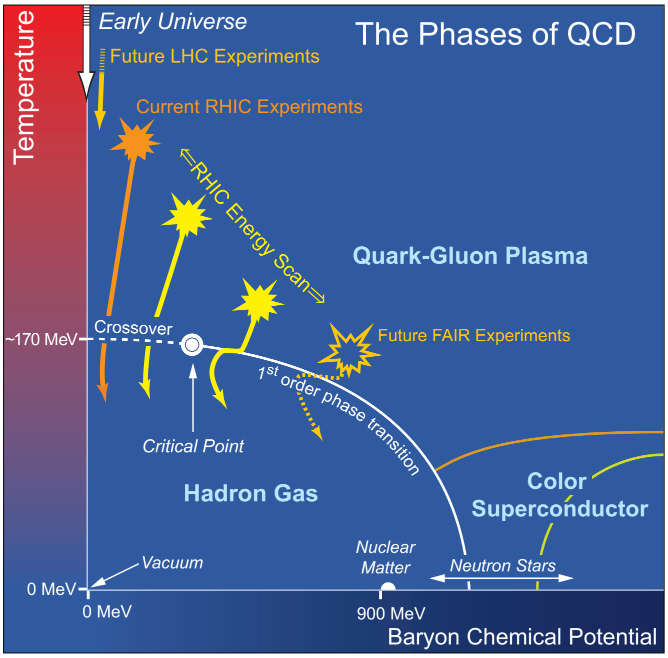

Figure 1.4. Phase diagram of QCD in the temperature and baryon chemical potential plane. The figure is adopted from Ref. [12].

1.4 Relativistic Heavy-ion Collisions

Relativistic heavy-ion collisions provide a unique opportunity to study a new state of matter, Quark Gluon Plasma in the laboratory. In the high-energy heavy-ion collision experiments, two nuclei are accelerated to ultra-relativistic velocities, as a result these nuclei, which are spherical in shape are Lorentz contracted along the direction of motion (beam direction or z-axis by convention) and look like disks. Then these Lorentz contracted disks are made to collide with each other. The overlap region of the disks depend upon the impact parameter. The nucleons which are in the overlap region are called *participants* and those which do not participate are called *spectators* [13]. A schematic diagram of different stages of the heavy-ion collision are shown in Fig. 1.5.

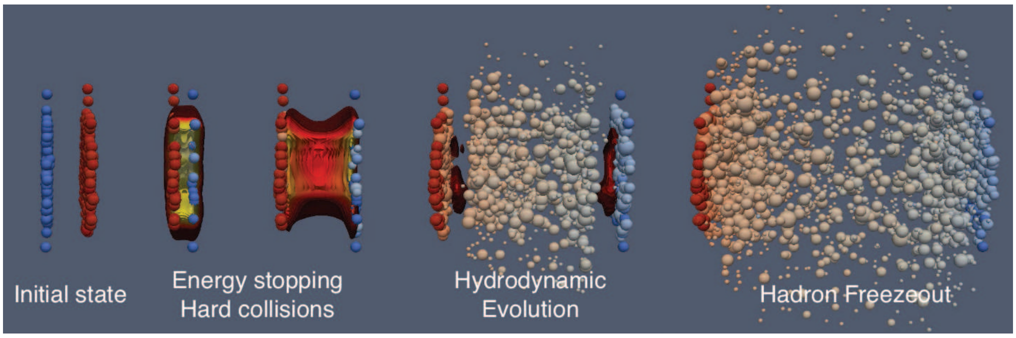

Figure 1.5. A schematic picture of the time evolution of heavy-ion collision. The figure is adopted from Ref. [13].

Fig. 1.6 shows the longitudinal space-time evolution of a relativistic nucleus-nucleus collision, from the moment of nuclear overlap, via pre-equilibrium to the formation of final state hadrons. Consider a heavy-ion collision at $z = 0, t = 0$. Depending on the energy of the colliding nuclei, the nucleons are either opaque or transparent to each other. If the energy is sufficiently high, the nucleons pass through each other leaving behind a trail of energy into a small volume, called firewall. If the energy density is sufficiently high inside the firewall, it can form a strongly interacting matter consisting of deconfined quarks and gluons, QGP. Lattice QCD calculation show that beyond a critical energy density of $\sim$1 GeV/fm^3 (or temperature $\sim$ 200 MeV) matter exists in a QGP phase [11]. Initially the QGP may not be in thermal equilibrium, but subsequent equilibration may bring it to a local equilibrium at some proper time τ_0. Now as the firewall expands it's temperature drops down and at a later proper time the hadronization takes place. At the same time particle production continues. After a certain time, the inelastic processes cease, leading to the *Chemical freeze-out*. The corresponding temperature is called chemical freeze-out temperature ($T_{\rm ch}$). At this stage the chemical composition of the produced particles get fixed (the particle ratios are frozen) but the constituents can interact among themselves via elastic scattering which may further change the

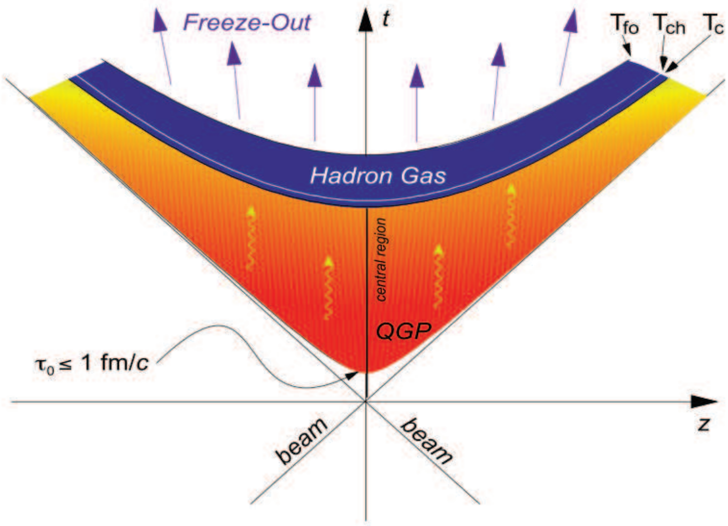

Figure 1.6. A schematic depicting the longitudinal space-time evolution of relativistic nucleus-nucleus collision.

shape of their transverse momentum spectra. When the mean free path of the particles exceeds the dynamical size of the firewall, the elastic interaction among the hadrons also ceases. This is called kinetic freeze out and the corresponding temperature is known as kinetic freeze out temperature ($T_{\rm fo}$). At this point of time, particles come out of the fireball and detected by the surrounding detectors.

1.5 Proposed Signatures of the QGP

The secondary particle production in heavy-ion collisions carry the information related to the possible formation of QGP.

The QGP can not be detected directly in the heavy-ion collision experiments, only the produced particles are detected by the surrounding detectors. These particles may carry out the information about the initial state collisions, which may be used to find the QGP signature. According to the theory there are some proposed QGP signatures which can be measured in the experiments. Some of the QGP signature are discussed below in brief.

- In heavy-ion and proton-proton collisions the net strangeness before the collision is zero. Strangeness production is a signature and a diagnostic tool of QGP formation and understanding its properties. It has been observed that strange particle yield get enhanced in heavy-ion collisions in comparison with the $p + p(\bar{p})$ collisions. *Strangeness enhancement* has been clearly observed in various experiments [14, 15].

- *Jet quenching* is another strong evidence of the QGP in heavy-ion collisions. In case of dijet production in heavy-ion collisions the away side jet traverse through the hot and dense medium and loses most of its energy or may even completely absorbed by the medium [16]. This effect is known as "jet quenching". So the dijet asymmetry in heavy-ion collisions may provide the signature of the QGP.

- *Nuclear modification factor* ($\mathrm{R_{AA}}$) is defined as the ratio of yield in heavy-ion collisions and in $p + p(\bar{p})$ collisions, normalized to the number of binary collisions. It is observed that in $p+\mathrm{Pb}$ collisions $\mathrm{R_{pPb}}$ is consistent with unity after $p_{\mathrm{T}} \simeq 2$ GeV/c while in most central Pb+Pb collisions, $\mathrm{R_{PbPb}}$ is much less than one. The strong suppression observed in central Pb+Pb collisions is an important signature of QGP [17]. This has been observed for light and heavy-flavour as well.

- J/ψ particle is the bound state of a charm quark (c) and a charm antiquark ($\bar{c}$). If QGP is formed in heavy-ion collisions, the J/ψ production will be inhibited due to the Debye screening. Hence, the $c\bar{c}$ pair could not be able to form a J/ψ. This phenomenon is known as *J/ψ suppression* and has been observed in various experiment [18, 19]. However, at the LHC enegies, the energy is sufficient enough to contribute substantially to J/ψ yield through the process called recombination or coalescence mechanism.

- The photons, produced through gluonic channels: $q\bar{q} \rightarrow \gamma g$, $gq \rightarrow \gamma q$ and $g\bar{q} \rightarrow \gamma\bar{q}$, are called *direct photon* [20–22]. Photons interact with particles in the collision region only through electromagnetic interactions. Consequently, their mean-free path is expected to be too large and they may not suffer a collision after they are produced. As a result, these high-energy photons, produced in the interior of the plasma, usually pass through the surrounding matter without interacting, carrying information directly from wherever they were formed to the detector.

- The fluctuations of conserved quantities in a finite phase space window, like *net charge flucutaion* [23–25], are predicted to be one of the most sensitive signals of the QGP formation and phaTse transition and may provide a complementary understanding of strong interactions. To study net charge fluctuations the ratio of positive to negative charge particles, *i.e.* $R = N_+/N-$, is used to avoid volume fluctuations. The observable D, which is a measure of charge fluctuations per unit entropy can be defined as:

$$D = \langle N_{ch} \rangle \langle \delta R^2 \rangle = 4 \frac{\langle \delta Q^2 \rangle}{N_{ch}} \tag{1.3}$$

  It has been shown that $D = 4$ for an uncorrelated pion gas, and after taking resonance yields into account, the value decreases to $D \simeq 3$. Lattice calculations which include the quark - quark interactions give a quantitatively different estimate for a QGP phase, *i.e.* $D \simeq 1.0 - 1.5$, which is significant lower than hadron gas. where the uncertainty arises from the uncertainty of relating the entropy to the number of charged particles in the final state [5]. Thus, a measurement of D can be effectively used as a probe for distinguishing the two phases, the hadron gas and the QGP [26].

1.6 Multiparticle Production in High-energy Collisions

Multiparticle production is one of the most intriguing topics in high-energy collisions. The observables measured "first-day" in high-energy collisions, namely charged particle multiplicity ($N_{\rm ch}$) and densities in pseudorapidity ($dN_{\rm ch}/d\eta$ and $dE_{\rm T}/d\eta$), are immediate characteristics of the process and bring important information on the underlying dynamics of strong interactions [27]. From fixed target to collider experiments, multiparticle production has been studied over a wide range of collision energies starting from few GeV to few TeV at LHC. These observables can also throw more light in providing insight into the partonic structure of the colliding nuclei. The evolution of these observables with energy, measured in experiments, is discussed in the following sections.

1.6.1 Shapes of Charged Particle Pseudorapidity Density Distributions

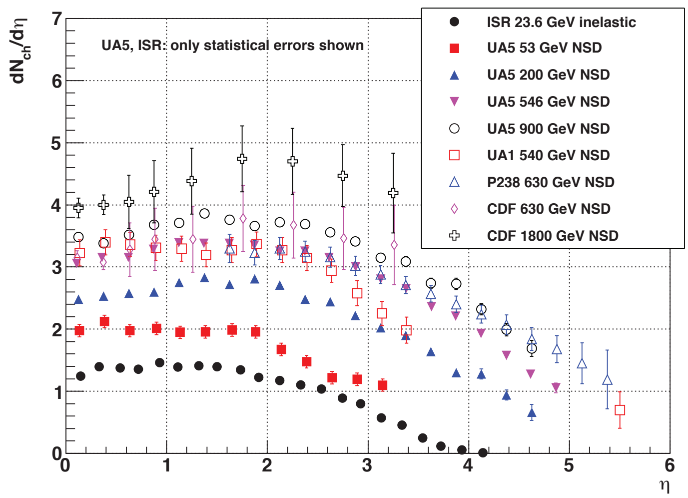

Figure 1.7. The $dN_{\rm ch}/d\eta$ in NSD $p + p(\bar{p})$ collisions measured in various experiments. The figure is taken from Fig. [28].

The $dN_{\rm ch}/d\eta$ has been measured in a variety of experiments for different colliding species in the energy range spanning a few GeV to a few TeV per nucleon. Some of the distributions for $p + p(\bar{p})$ and Pb+Pb collisions are presented in Fig. 1.7 to 1.9. It is clear that $dN_{\rm ch}/d\eta$ (or $dN_{\rm ch}/dy$) distributions in $p + p(\bar{p})$ and A+A collisions have similar properties in shape parameters [28]. The width and the amplitude of the $dN_{\rm ch}/d\eta$ increases with increase in collision energy [29]. Also it has been observed that width of the central plateau region increases with energy. Moreover, the plateau region converts into a dip at higher energies as shown in Figs. 1.7 and 1.9. This dip in the pseudorapidity distribution depends on the mass of the particles. Kaons have more dip than pions and protons have more dip than pions and kaons at midrapidity [30]. This dip is not observed in rapidity distributions, which can be understood by looking into the transformation from rapidity to pseudorapidity variable [31, 32]. The transformation is given by the following relation.

$$\frac{dN}{d\eta} = J(\eta, p_T)\frac{dN}{dy}, \tag{1.4}$$

where $\mathrm{J}(\eta, \mathrm{p_T})$ is Jacobian and can be given by

$$J(\eta, p_T) = \frac{p_T \cosh\eta}{\sqrt{m_0^2 + p_T^2\cosh^2\eta}} \tag{1.5}$$

Hence, for a fixed collision energy, higher is the mass of the particle lower is the value of the Jacobian, which leads to higher degree of dip in the pseudorapidity distribution. Landau hydrodynamical and Fermi models predict that the pseudorapidity distributions of the produced particles follow a Gaussian distribution [33]. However, later rapidity was used to characterize the particle production using Landau hydrodynamics by Carruthers and Duong-van [30]. Fitting a double Gaussian function to the pseudorapidity spectra is motivated by the trend of the data starting from SPS [34] to LHC [35] at CERN. The width-parameters extracted from fitting function are used to study the dynamics of the system.

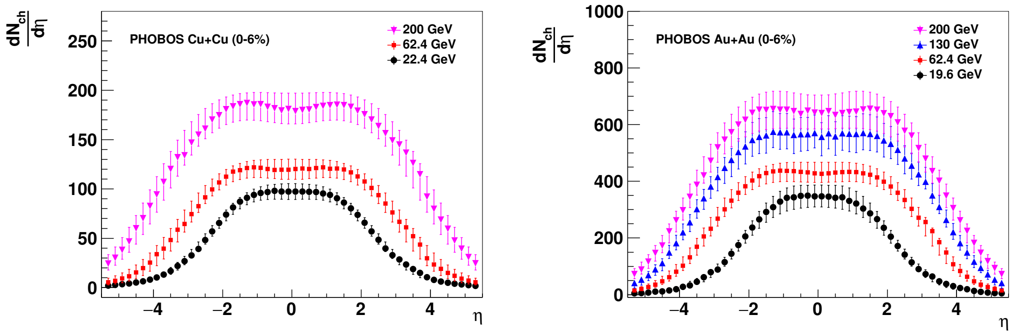

a) b)

Figure 1.8. The $dN_{\rm ch}/d\eta$ as a function of η (a) Cu+Cu collisions at $\sqrt{s_{\rm NN}}$ = 22.4, 62.4 and 200 GeV. (b) Au+Au collisions at $\sqrt{s_{\rm NN}} = 19.6$, 62.4 and 200 GeV by PHOBOS experiments. The figures are taken from Ref. [29].

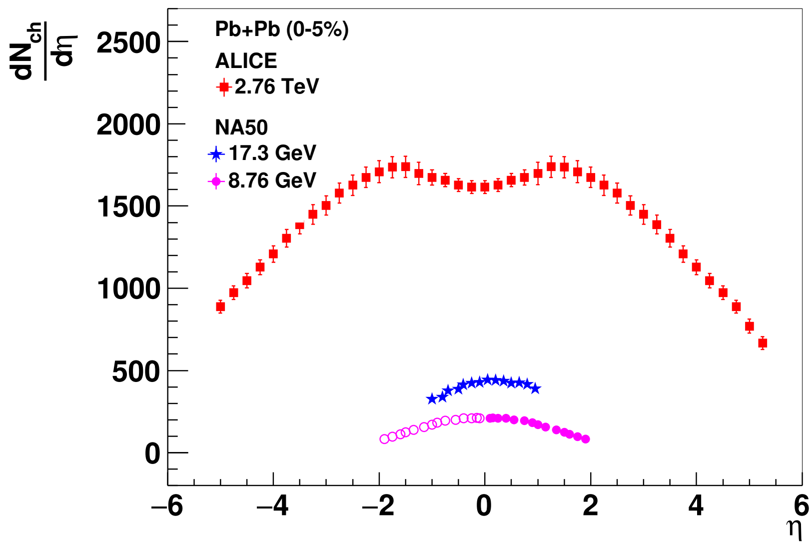

Figure 1.9. $dN_{\rm ch}/d\eta$ distributions of Pb+Pb collision systems for the most central events at different collision energies. The figure is adopted from Ref. [29].

1.6.2 System Size Dependence of Multiplicity Density

The study of the system size dependence of $dN_{\rm ch}/d\eta$ may give some additional information about evolution of the collisions system. Fig. 1.10 shows the $N_{\rm part}$-normalized $dN_{\rm ch}/d\eta$ at midrapidity for Pb+Pb collisions at $\sqrt{s_{\rm NN}} = 2.76$ TeV for LHC and for Au+Au collisions at $\sqrt{s_{\rm NN}} = 200$GeV

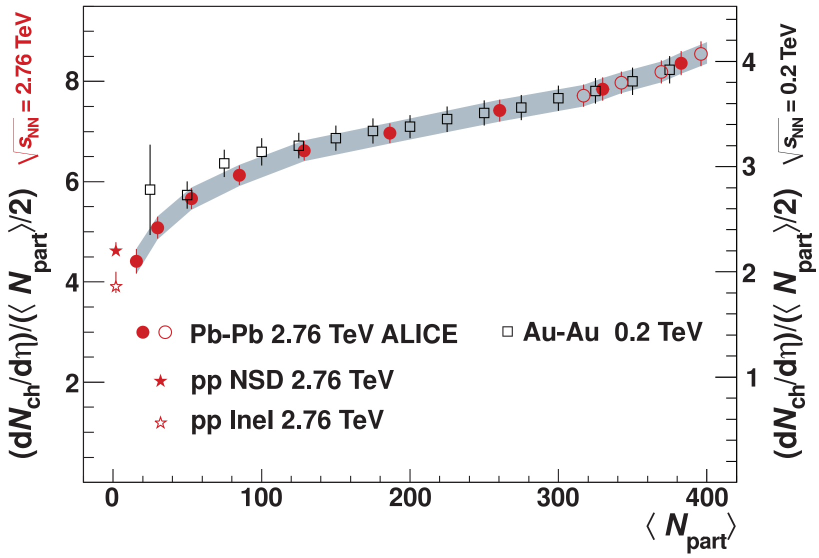

Figure 1.10. $(dN_{\text{ch}}/d\eta)/(N_{\text{part}}/2)$ as a function of N_{part} measured by ALICE and RHIC. The RHIC data are scaled by a factor of 2.1 (axis for the RHIC data shown on the right). Furthermore the plot includes ALICE $p+p$ data at $\sqrt{s}$ = 2.36 and 7 TeV. The figure is adopted from Ref. [36].

for RHIC, as a function of collision centralities (or N_{part}). A scaling factor of 2.15 has been multiplied with the RHIC data to make a direct comparison with that of LHC data. If the different centrality classes have same properties, then the distribution of $(dN_{\text{ch}}/d\eta)/(N_{\text{part}}/2)$ should be flat and approximately at the level of $p+p(\bar{p})$ collisions [36]. It is clear from Fig. 1.10 that $(dN_{\text{ch}}/d\eta)/(N_{\text{part}}/2)$ grows with N_{part} at both RHIC and LHC and at lower N_{part} values, it approaches the level of $p+p(\bar{p})$ collisions.

The processes, which lead to the production of small transverse momentum particles ($p_{\text{T}} \sim 0.4$ GeV/c) are called soft processes. On the other hand, the processes which produce the particles with large transverse momenta ($p_{\text{T}} > 1-2\ GeV/c$) are called hard processes. In the framework of "wounded nucleon model" [37], it is observed that the $dN_{\text{ch}}/d\eta$ scales with some power of N_{part} up to the SPS energy. That is called power-law fit and is given by

$$\frac{dN}{d\eta} = N_{part}^{\alpha}, \tag{1.6}$$

where α is found to be ∼1 for SPS energies. This linear relation with

N_{part} is interpreted as that the particle production up to SPS energies is mainly from the soft processes. However, the particle multiplicity at RHIC and LHC energies could not be explained by the above relationship. Therefore, a two-component model was adopted which incorporates both the contributions of soft and hard processes by considering the N_{part} and N_{coll} to describe the final state hadron multiplicity [38, 39].

1.6.3 Collision Energy Dependence of Multiplicity Density

Several experiments have studied $dN_{\text{ch}}/d\eta$ distribution at various c.m. energies for $p + p(\bar{p})$ and heavy-ion collisions. The results for A+A central collisions and $p + p(\bar{p})$ Non-Single Diffractive (NSD) and INELastic (INEL) collisions are summarized in Fig. 1.11. To explain N_{part}-normalized $dN_{\text{ch}}/d\eta$ at midrapidity, different phenomenological functions are fitted to data. Logarithmic function explains data upto top RHIC energy. However, it underestimates LHC data by 26%. On the other hand, a power-law fit seems to overestimate the low energy data for nucleus-nucleus collisions while explaining the high-energy data up to LHC energies [40]. The data sets seem to fit to a power-law behaviour with the power decreasing while going from A+A to $p + p(\bar{p})$ collisions. These observations are found to go inline with constituent quark picture [41–47].

1.6.4 System Size Dependance of Charged Particle Multiplicty

The N_{part}-normalized charged particle multiplicities, $N_{\text{ch}}/(N_{\text{part}}/2)$, measured by PHOBOS for Cu+Cu and Au+Au, and ALICE experiments for Pb+Pb collisions are shown in Fig. 1.12, 1.13, 1.14, respectively. It is observed from Fig. 1.12 and 1.13 that the $N_{\text{ch}}/(N_{\text{part}}/2)$ scales perfectly with N_{part} within the statistical uncertainties and show almost centrality independent behaviour. However, similar effect is not observed for Pb+Pb

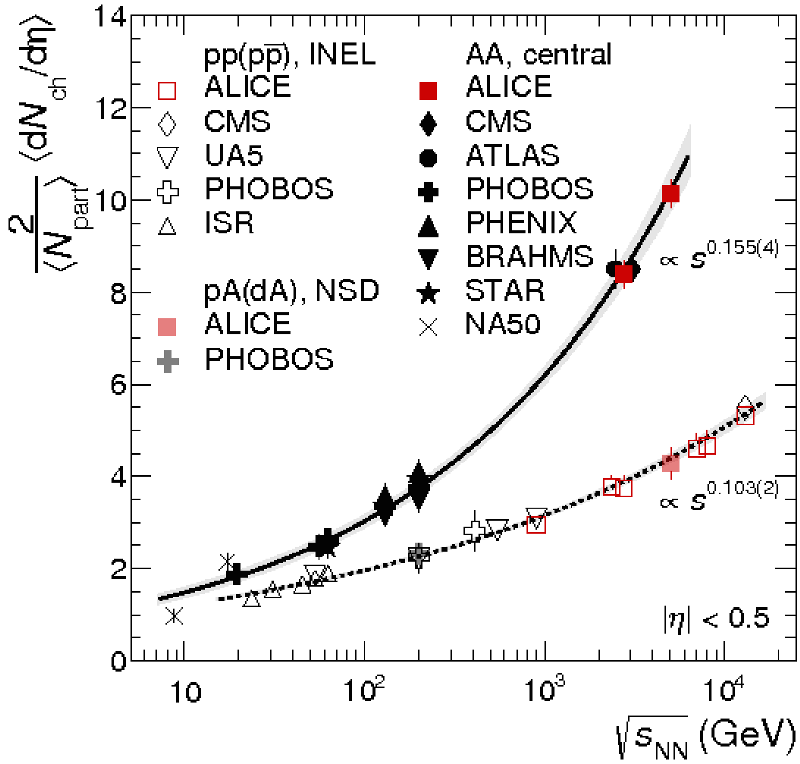

Figure 1.11. $(dN_{\rm ch}/d\eta)/(N_{\rm part}/2)$ for central Pb+Pb and Au+Au collisions as a function of $\sqrt{s_{\rm NN}}$. Measurements for INEL $p + p(\bar{p})$ collisions as a function of $\sqrt{s}$ are also shown. The figure is taken from [40]

collisions at $\sqrt{s_{\rm NN}} = 2.76$ TeV, as shown in Fig. 1.14. The monotonic increase of $N_{\rm ch}/(N_{\rm part}/2)$ with centrality can be explained by the increased gluonic contributions in the midrapidity region [48, 49] and hence a participant scaling is violated. This needs further theoretical understanding along with the availability of higher energy data. We propose explaining in Chapter 5.8.

1.6.5 Universality in Multiparticle Production

In order to understand the available experimental data, various theoretical and phenomenological models have been proposed. Most of these models are based on the phenomenological approaches such as geometrical, hydrodynamical, and statistical approaches etc [27]. However, the diverse nature of the experimental data poses a major challenge before physics community to find out any scaling relationship in multiparticle production among all

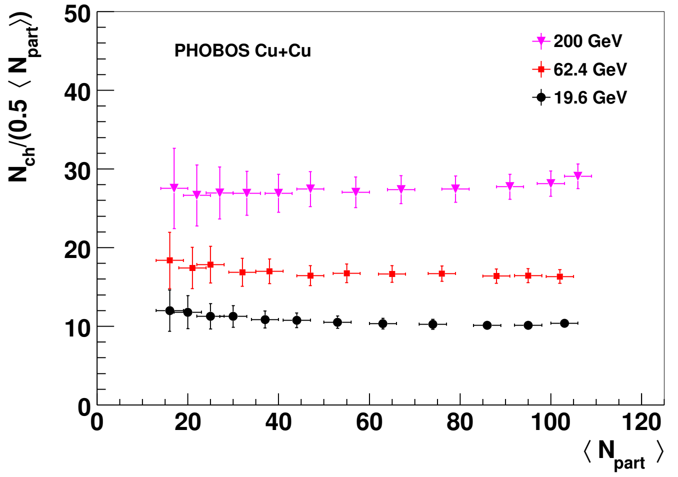

Figure 1.12. $N_{\rm ch}/(N_{\rm part}/2)$ as a function of $N_{\rm part}$ for Cu+Cu collisions at different collision energies. The figure is taken from Ref. [29].

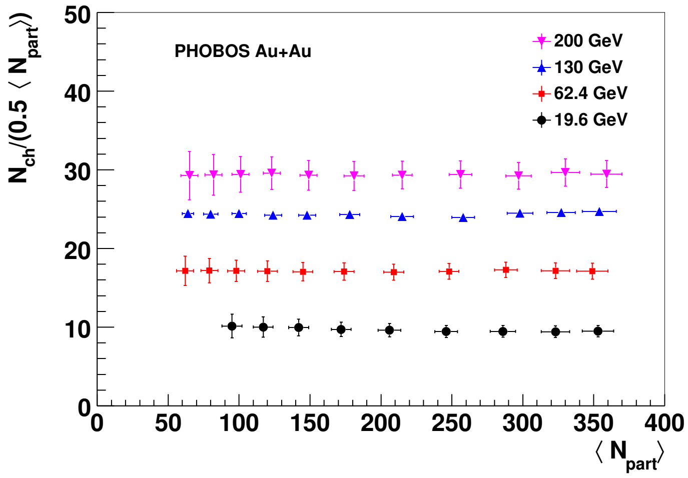

Figure 1.13. $N_{\rm ch}/(N_{\rm part}/2)$ as a function of $N_{\rm part}$ for Au+Au collisions at different collision energies. The figure is taken from Ref. [29].

types of collisions.

In Fig. 1.15(a), $(dN_{\rm ch}/d\eta)/(N_{\rm part}/2)$ of charged particles produced in central Au+Au collisions at $\sqrt{s_{\rm NN}}$ = 19.6 and 200 GeV are compared with e^+e^- and $p+\bar{p}$ systems. It is observed that the $(dN_{\rm ch}/d\eta)/(N_{\rm part}/2)$ for $p+\bar{p}$ system is quite different from e^+e^- and heavy-ion systems.

The PHOBOS experiment has measured the $N_{\rm ch}/(N_{\rm part}/2)$ in Au+Au collisions as a function of the $N_{\rm part}$ for three different energies (Fig.1.15(b)).

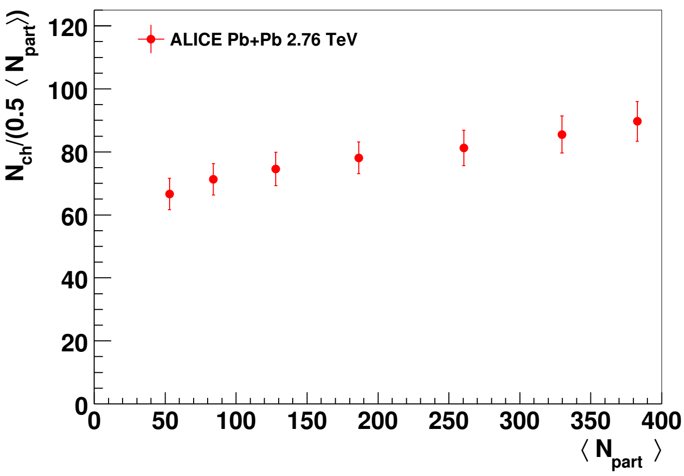

Figure 1.14. $N_{\rm ch}/(N_{\rm part}/2)$ as a function of $N_{\rm part}$ for Pb+Pb collisions at $\sqrt{s_{\rm NN}}$ = 2.76 TeV. The figure is adopted from Ref. [29].

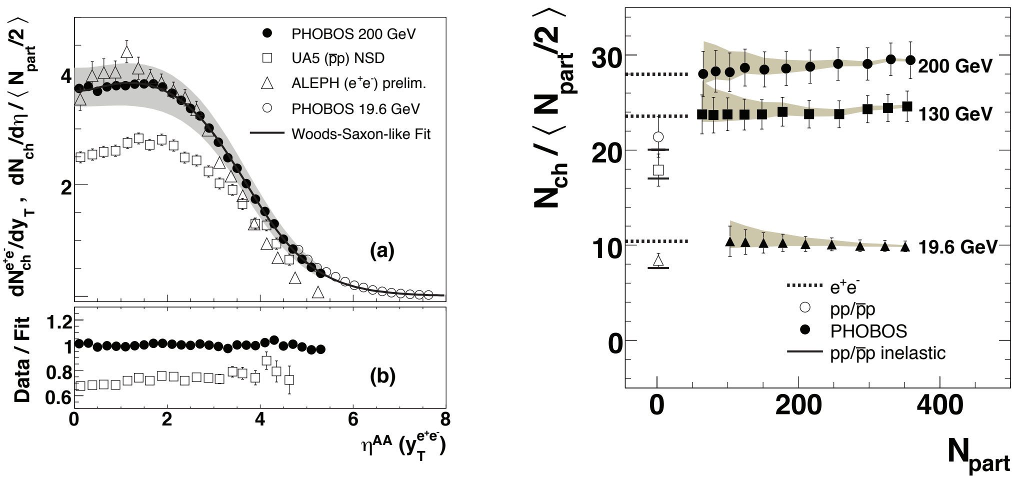

a)

b)

Figure 1.15. (a) $(dN_{\rm ch}/d\eta)/(N_{\rm part}/2)$ of charged particles produced in central Au+Au collisions at $\sqrt{s_{\rm NN}}$ = 19.6 and 200 GeV, compared with elementary systems. (b) $N_{\rm ch}/(N_{\rm part}/2)$ vs. $N_{\rm part}$ is shown for $\sqrt{s_{\rm NN}}$ =19.6, 130, and 200 GeV as closed symbols. The open symbols show UA5 data at 200 GeV and results from an interpolation of NSD data at other energies. The dotted lines show the values from the e^+e^- fit [50].

A very weak centrality dependence is observed, reminiscent of "wounded nucleon" scaling, but with a proportionality factor that is different than that seen in $p+p(\bar{p})$ collisions. It is evident from Fig. 1.16 that above SPS energies, $N_{\rm ch}/(N_{\rm part}/2)$ in central events evolves with $\sqrt{s}$ in the same

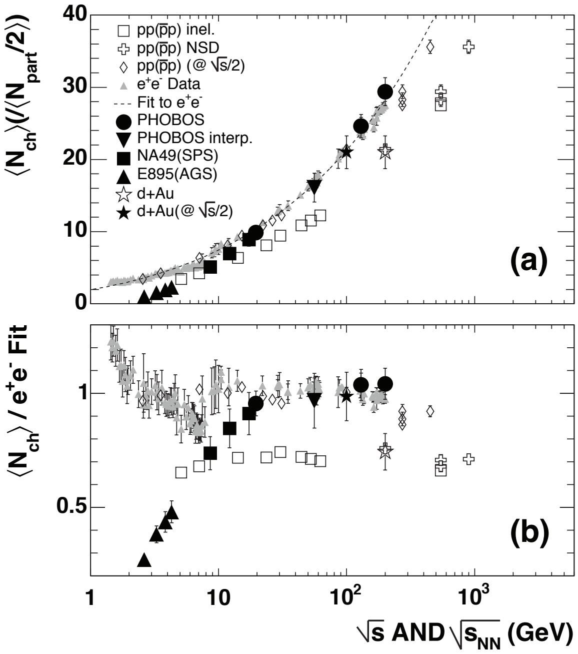

Figure 1.16. (a) The total charged multiplicity for different collision systems. The diamonds are the $p + p(\bar{p})$ data with $E_{\rm eff} = \sqrt{s}/2$. (b) The data in (a) divided by the e^+e^- fit, to allow direct comparison of different data at the same $\sqrt{s}$ [50].

way and is very close to the e^+e^- data. This is somewhat suggestive of a common mechanism of particle production in strongly-interacting systems, controlled mainly by the amount of energy available for particle production [50]. This may be related to the multiple collisions suffered by each participant nucleon, which could substantially reduce the leading particle effect seen in $p + p(\bar{p})$ collisions and suggests that after the first few collisions per participant, the $N_{\rm ch}/(N_{\rm part}/2)$ saturates near the value measured in e^+e^- reactions.

Ultimately, the existence of simple scaling behavior with $E_{\rm eff} = \sqrt{s}/2$ and $N_{\rm part}$ constraints on particle production than previously considered based on the idea of leading particle. Without some overall constraint, it is difficult to understand how the various physics effects contribute independently to the bulk particle production in A+A collisions.

On the other hand the effective energy and the corresponding inelasticity are related to the 3-quark structure of the nucleon [51, 52]. In this simple picture the interaction of one of the three valence quarks in each nucleon would correspond to an average inelasticity $\langle K \rangle = 1/3$.

This inelasticity coefficient has been estimated by fitting following function to the $p + p(\bar{p})$ data.

$$f_{pp}(\sqrt{s}) = f_{ee}(K\sqrt{s}) + n_0. \tag{1.7}$$

Here, n_0 corresponds to the contribution from the leading protons to the total multiplicity and is expected to be close to $n_0 = 2$. While fitting Eq.1.7 to $p + p(\bar{p})$ data one obtains $K = 0.35 \pm 0.01$ and $n_0 = 2.2 \pm 0.19$.

This discussion leads to the conclusion that e^+e^- and $p + p(\bar{p})$ multiplicities will show a universal behaviour if $p + p(\bar{p})$ data is scaled by 1/3 [53]; which is in contrast with the earlier predictions made by PHOBOS experiment to scale by 1/2 [50].

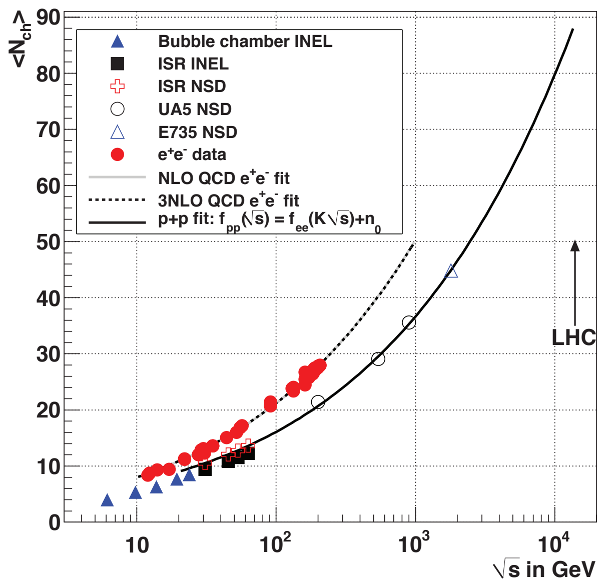

Figure 1.17. $N_{\rm ch}$ as a function of c.m. collision energy for e^+e^- and $p + p(\bar{p})$. The figures is adopted from Ref. [53].

Therefore, the non-availability of consistent universal scaling in charged particle multiplicities and no available scaling for charged particle density, motivates us to further explore the universal scaling for both the observables in all type of collision systems. This aspect is discussed in

Chapters 4 & 5 in details, while exploring a universal multiparticle production mechanism in hadronic and nuclear collisions.

Chapter 2

Experimental Setup

"It doesn't matter how beautiful your theory is, it doesn't matter how smart you are. If it doesn't agree with experiment, it's wrong."

— Richard Feynman

In this Chapter we give a brief introduction of the Large Hadron Collider (LHC) and the A Large Ion Collider Experiment (ALICE). A short overview and physics goals of all the sub-detectors of ALICE are discussed.

2.1 Large Harron Collider (LHC)

The Large Hadron Collider (LHC) at CERN is the world's largest and most powerful particle accelerator [54]. It first started up on 10^{th} September 2008, and remains the latest addition to CERN's accelerator complex. The LHC tunnel of circumference 27 km is situated 100 to 175 meter underground of French-Swiss border near the city of Geneva. Inside the tunnel, there are two separate beam pipes surrounded by superconducting dipole magnets with a number of accelerating structures to boost the energy of the particles along the way. The schematic view of LHC ring and CERN facilities for beam production to beam injection is shown in Fig. 2.1. Injection procedures for proton beam and Pb ion beam to the main LHC ring involve multi-stage process [55], which are discussed herewith.

Proton beams are produced by stripping hydrogen atoms using an electric field. These produced protons are accelerated by Linear Accelerator (LINAC2) up to 50 GeV and then injected to Proton Synchrotron Booster

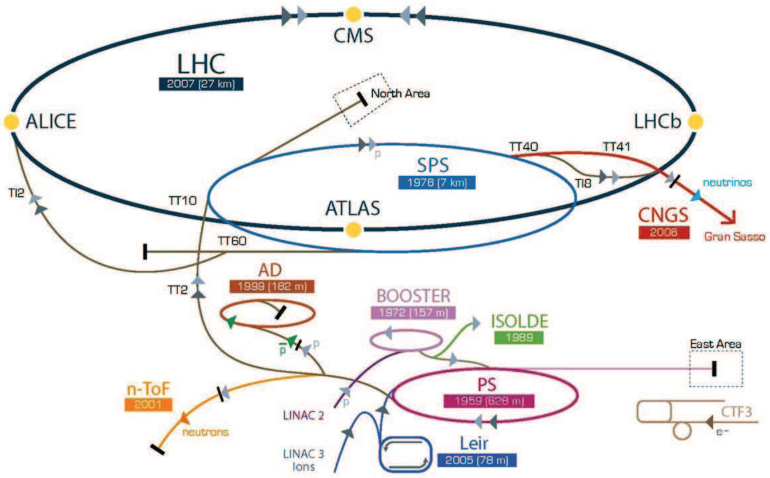

Figure 2.1. CERN accelerator complex at the LHC.

(PSB) , which accelerates the protons to 1.4 GeV. Then the PSB injects the beam to Proton Synchrotron (PS), where proton beam is accelerated to 25 GeV. Further the proton beams are sent to Super Proton Synchrotron (SPS) and accelerated to 450 GeV. Finally, the proton beams are injected to the LHC ring.

Lead ion (Pb^{82+}) production is a more complex than proton beam. A pure Lead sample is heated upto $550°C$ to get pure vaporised lead sample. The lead vapour is initially ionized by passing electrical current and then these Pb ions are accelerated by LINAC3. Pb ion beams are then passed through carbon foil for further stripping of electrons to make Pb^{54+}. Before injecting to PS, Pb^{54+} are accelerated to 72 MeV per nucleon in Low Energy Ion Ring (LEIR). The final stripping of the rest of the electrons of Pb^{54+} are done in PS and Pb^{82+} are generated. PS accelerates the ion beam to 5.9 GeV and then sends to SPS, where ion beam is accelerated to 177 GeV per nucleon.

After that the ion beams are injected to the two beam pipes of the LHC ring. The beam in one pipe circulates clockwise while the beam in the other pipe circulates anticlockwise. The circulating beams are made to collide at four different collisions points where four major detector facilities are established to record the collision data. Fig. 2.2 shows the LHC layout with all four major experiments.

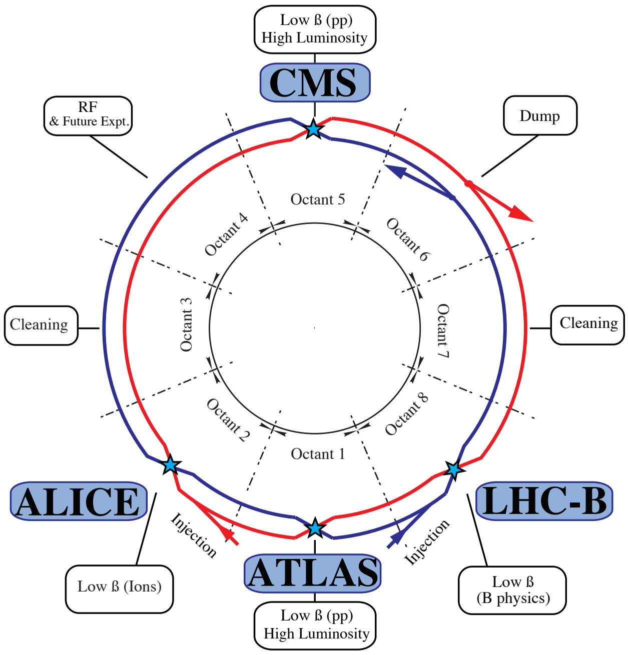

Figure 2.2. Schematic view of the LHC.

A Toroidal LHC ApparatuS (ATLAS) and Compact Muon Solenoid (CMS) are two high luminosity general purpose experiments situated opposite to each other in LHC ring at Point 1 and Point 5, respectively. The main physics goal to design ATLAS and CMS is to address the Standard Model (SM) prediction: the Higgs Boson [3, 4]. Recently, discovery of *Higgs Boson* is announced by these two experiments in the mass region around 126 GeV [5, 6]. In addition to Higgs Boson search, physics beyond SM like SUper-SYmmetry (SUSY) particles and extra dimensions can also be studied by these two experiments. Large Hadron Collider beauty (LHCb) experiment is a small dedicated experiment to deal with matter anti-matter puzzle in the Universe. It is installed at Point 8 of the LHC ring. The ALICE is a custom built detector for the heavy-ion collisions to study the matter created at high temperature and/or energy density for the possible formation of Quark Gluon Plasma (QGP), a deconfined state of quarks and gluons (collectively called as partons). The ALICE is located at point 2 and takes data for $p + p$, $p +$ Pb and Pb+Pb collisions. The proton data will be used as a reference data to the heavy-ion-collisions. The important parameters of LHC accelerator are summarized in Table 2.1.

Table 2.1. Some LHC nominal proton and lead beam parameters (3^{rd} and 4^{th} columns). The last column are the actual values used in proton beams in 2012.

	Units	Proton	Lead	June 2012
Number of magnets		9593		
Number of dipoles		1232		
Number of quadrupoles		392		
Beam energy	TeV	7	2.76/n	4
Bunches per beam		2808	592	1380
Protons/ions per bunch		1.15x10^{11}	7x10^{7}	1.48x10^{11}
Bunch separation	ns	25	100	50
Luminosity	$cm^{-2}s^{-1}$	10^{34}	10^{27}	6.8x10^{33}
Beam size at IP	μm	16.7	15.9	19
Beam current	A	0.582	6.12x10^{-3}	0.369

2.2 A Large Ion Collider Experiment (ALICE)

ALICE focuses on the physics of strongly interacting matter at extreme temperatures and/or energy densities. The existence of the QGP and its properties are key issues in QCD for understanding *color confinement* and *chiral symmetry restoration*. ALICE is the only experiment at LHC, which is specially designed for the heavy-ion program. It has excellent tracking and Particle IDentification (PID) capabilities over a wide range of momenta starting from 100MeV/c to 100 GeV/c, which allows to study soft physics (intermediate p_T) and high p_T jets ($p_T > 10$GeV/c). The ALICE is made up of various sub-detectors. These sub-detectors (shown in Fig. 2.3) can be categorized in three major parts as followings:

- *Central barrel detectors* having pseudorapidity $|\eta| \leq 0.9$ contained within the L_3 magnet of maximum magnetic field strength of 0.5 T. The central barrel detectors are optimized for tracking and PID of produced charged particles.

- *Muon spectrometer* is installed in forward pseudorapidity ($2.4 \leq \eta \leq 4.0$) to study quarkonia ($J/\psi, \psi', \Upsilon, \Upsilon', \Upsilon''$) production via their decay in dimuon channels.

- *Forward detectors* are some specialized small detector systems installed in the forward pseudorapidity region ($\eta \geq 1.0$) with different physics goals.

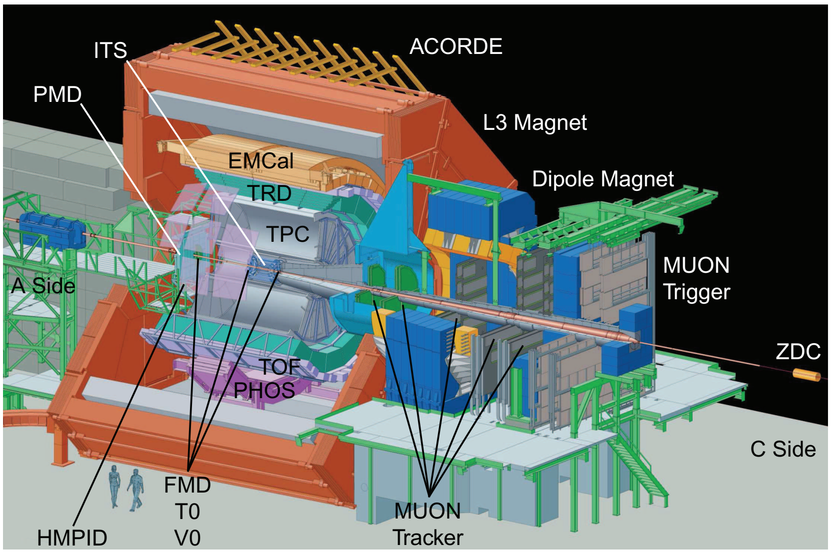

Figure 2.3. A schematic diagram of the ALICE with all sub-detectors [28].

Fig. 2.4 shows the pseudorapidity acceptance (η) of the ALICE sub-detectors with charged particle pseudorapidity density ($dN_{\rm ch}/d\eta$) prediction for p+p collisions by event generator Pythia [56]. The sub-detectors have full azimuth coverage (ϕ) except for the ones marked with an asterisk. A summary of all the sub-detectors is given in Table 4.1. The mechanical design and physics goals of ALICE sub-detectors are described in the following sections.

2.3 Central Barrel Detectors

The Central barrel detectors, covering midrapidity region $|\eta| < 0.9$ over the full azimuthal coverage are installed symmetrically around the intersection point and placed inside a large solenoidal magnet L3 with nominal magnetic field of 0.5T. These detectors are mainly used for tracking and PID of charged particles using various techniques. The central barrel consists of Inner Tracking System (ITS), Time Projection Chamber (TPC),

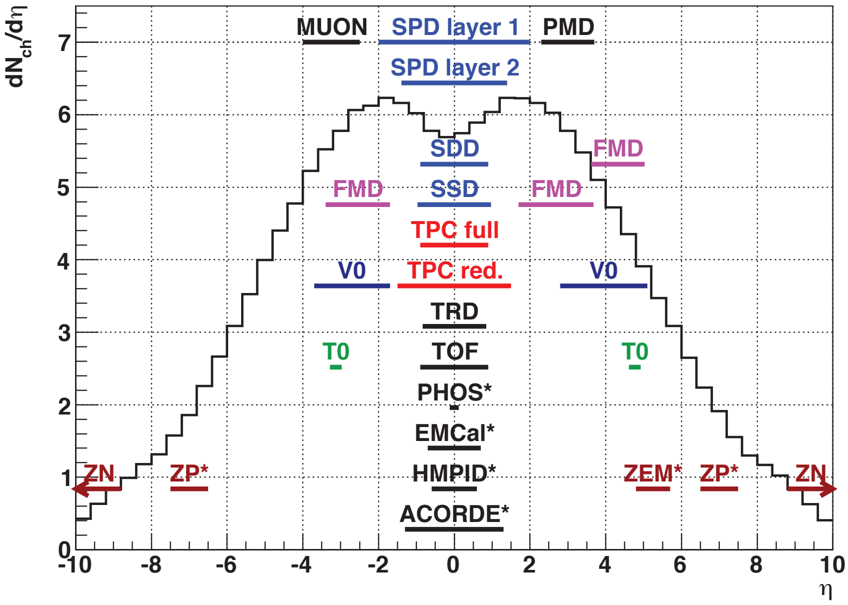

Figure 2.4. The pseudorapidity acceptance of the ALICE sub-detectors at LHC [28].

Transition Radiation Detector (TRD), Time-Of-Flight (TOF) , High Momentum Particle Identification (HMPID), PHOton Spectrometer (PHOS), Electro Magnetic Calorimeter (EMCAL) and ALICE Cosmic Ray Detector (ACORDE). All the detectors except HMPID, PHOS, EMCAL and ACORDE have full azimuthal coverage around the beam pipe. Detector components and their performance are briefly discussed here.

2.3.1 Inner Tracking System (ITS)

The Inner Tracking System (ITS) [57] is the inner most detector of ALICE, which consists of three subsystems (Silicon Pixel Detector, Silicon Drift Detector and Silicon Strip Detector) each with two concentric silicon layers around the beam pipe. In order to achieve the required impact parameter resolution in the high multiplicity environment produced in Pb+Pb collisions in ALICE, SPD layers have been chosen for the innermost two layers followed by two layers of SDD. The two outer layers, where the track density is smaller, are equipped with double-sided SSD. The locations of SPD, SDD and SSD are suitably chosen to optimize the individual detector

Table 2.2. A summary of sub-detectors of ALICE [54]

Detectors	Position (cm)	Acceptance (η)	Acceptance (ϕ)	technology	purpose
SPD (layer1, 2)	3.9, 7.6	$\pm$2, $\pm$1.4	full	Si Pixel	tracking, vertex
SDD (layer 3, 4)	15.0, 23.9	$\pm$0.9, $\pm$0.9	full	Si drift	tracking, PID
SSD (layer 5, 6)	38, 43	$\pm$0.97, $\pm$0.1	full	Si strip	tracking, PID
TPC (IORC, OROC)	85, 247	$\pm$0.9	full	Ne drift, MWPC	tracking, PID
TRD	290, 368	$\pm$0.8	full	TR, Xe drift, MWPC	tracking, $e^{\pm}$ id
TOF	370, 399	$\pm$0.9	full	MRPC	PID
PHOS	460, 478	$\pm$0.12	220, 320	$PbWO_4$	photons
EMCAL	430, 455	$\pm$0.7	80, 187	Pb, scint	photons, jets
HMPID	490	$\pm$0.6	1, 59	$C_6F14, RICH, MWPC$	PID
ACORDE	850	$\pm$1.3	30, 150	scint.	cosmics
FMD	320	3.6 $< \eta <$ 5.0	full	Si strip	charged particle
	80	1.7 $< \eta <$ 3.7	full	Si strip	
	-70	-3.4 $< \eta <$ -1.7	full	Si strip	
PMD	367	2.3 $< \eta <$ 3.9	full	Pb+PC	photons
ZDC	$\pm$113 m	$\eta >$ 8.8	full	W+quartz	forward neutrons
	$\pm$113 m	6.5 $< \eta <$ 7.5	ϕ <10	brass, quartz	forward protons
	7.3 m	4.8 $< \eta <$ 5.7	ϕ <32	Pb, quartz	photons
V0	340	2.8 $< \eta <$ 5.1	full	scint.	time, vettex
	-90	-3.7 $< \eta <$ -1.7	full	scint.	
T0	370	4.6 $< \eta <$ 4.9	full	quartz	time, vetex
	-70	-3.3 $< \eta <$ -3.0	full	quartz	
MCH	-14.2, -5.4 m	-4.0 $< \eta <$ -2.5	full	MWPC	muon tracking
MTR	-17.1, 16.1 m	-4.0 $< \eta <$ -2.5	full	RPC	muon trigger

performance in the high multiplicity environment. These subsystems are located at radii between 3.9 cm and 43.9 cm and cover the pseudorapidity range $|\eta| < 0.9$ for vertices located within 6.0 cm with respect to the nominal interaction point. The four outer layers have analog readout and therefore can be used for particle identification via dE/dx measurement in the non-relativistic $(1/\beta^2)$ region. The analog readout has a dynamic range large enough to provide the dE/dx measurement for low-momentum, highly ionising particles down to the lowest momentum at which tracks can still be reconstructed.

The main aims of the ITS are to determine primary as well as secondary (decays of D and B mesons, and hyperons) vertices with resolution better than 100 μm and to provide high-resolution tracking of charged particles for low momentum particles (below 100 MeV/c). It also improves the momentum and angle resolution of particles tracked by the Time Projection Chamber (TPC) by expanding the acceptance to the dead regions of the TPC. A schematic layout of ITS is shown in Fig. 2.5

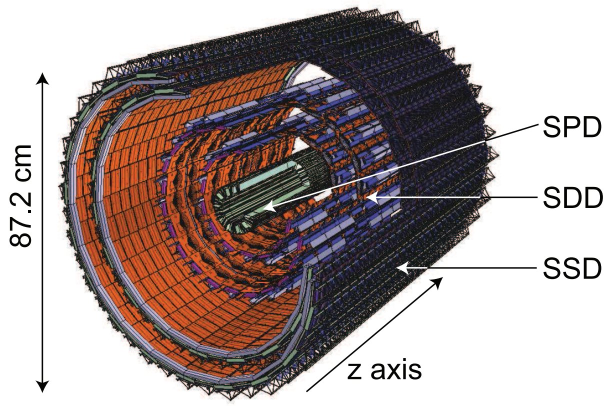

Figure 2.5. Layout of Inner Tracking System.

- **Silicon Pixel Detector (SPD):** Two inner most layers (1st and 2nd) of the ITS, with radii 3.9 cm and 7.6 cm from the interaction point, constitute the SPD and each layer of SPD is made up of hybrid silicon pixels which consist of silicon detector diodes with a thickness of 200 μm. It plays an important role in reconstructing the primary vertex and measurement of impact parameter of secondary tracks coming from weakly decaying particles, like strange baryons and D-mesons. The information from the SPD alone is sufficient to form so-called tracklets and thus to measure the charged particle multiplicity. Its wider pseudorapidity coverage ($|\eta| < 1.75$) provides extended rapidity coverage for the multiplicity measurement.
- **Silicon Drift Detector (SDD):** The next two layers (3rd and 4th) of the ITS are called Silicon Drift Detector (SDD) and are located at average radii of 14.9 and 23.8 cm, respectively. It is composed of homogeneous high-resistivity silicon layers with thickness of 300 μm. SDD gives position information with spatial precision of 35 μm. It also provides two out of four energy-loss (dE/dx) samples needed for the particle identification (PID).

- **Silicon Strip Detector (SSD):** The two outermost layers (5th and 6th) of ITS are called SSD and are located at average radii of 38.0 and 43.9 cm from the interaction point, respectively. These layers are made up of 300 μm thick double-sided silicon micro-strip sensor. The SSD layers are crucial for the track matching from the TPC to the ITS. They provide a two dimensional measurement of the track position and dE/dx information to assist particle identification, in particular for low-momentum particles.

2.3.2 Time Projection Chamber (TPC)

The TPC is the main detector in the ALICE central barrel and also known as the heart of the ALICE detector system [58]. TPC is designed to provide, in combination with the other central barrel detectors, charged-particle momentum measurements with good two-track separation (efficiency larger than 90%), particle identification (dE/dx resolution better than 10%), and vertex determination. TPC has full azimuthal coverage of 360° with pseudorapidity coverage of $|\eta| < 0.9$ [59].

The TPC is made of a large cylindrical field cage, surrounding the ITS with a active volume of 90 m^3, which makes it the largest TPC of the world. A Schematic view of the TPC detector is shown in Fig. 2.6. The active volume has an inner and outer radii of 85 cm and 250 cm respectively, with an overall length of 500 cm in the beam direction (z-direction). It is filled with a gas mixture of Ne and CO_2 in proportions of 90:10. Most recently it was proposed to add 5% N_2 gas to the mixture to provide higher gain stability. A high voltage (HV) electrode (30 μm thick) is located at its axial centre, aligned to the interaction point, divides the gas volume in two symmetric drift regions of 250 cm in length and creates the highly uniform electrostatic field through out the gas volume of the TPC. The readout chambers are installed at the two end plates of the cylinder ($z = \pm 2.5$ m), based on the Multi-Wire Proportional Chamber (MWPC) technique. Each end-plate is segmented into 18 trapezoidal sectors with cathode pad readout covering an overall active area of 32.5 m^2. The Readout chambers are specially designed to adapt the high track density expected in Pb+Pb at LHC.

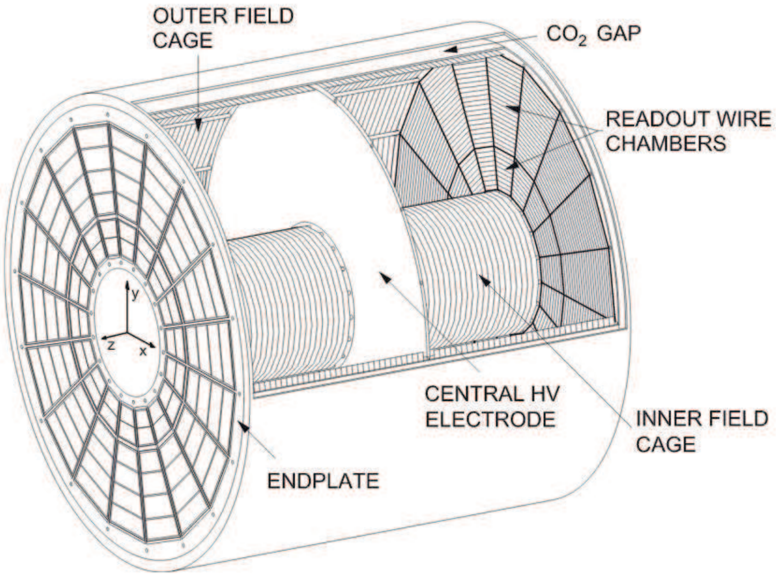

Figure 2.6. A Schematic view of the ALICE TPC.

Particle Identification Method

When a charged particle traverses through the TPC active volume, it ionises the gas along their path. The electrons produced in ionization, drifts parallel to the electric and magnetic field, towards one of the end plates. The charge collected at the end plate is proportional to the energy loss of particles in the gas mixture. The image of the ionizing track is broadened by the transverse diffusion of electrons during the drifting. The magnetic field reduces this effect by forcing the electrons to go in helical paths around the magnetic field. The magnetic field also bends the paths of the ionizing particles, making it possible to measure their momentum from the curvature of the track. At the end plates, which are divided in 18 sectors, Multi-Wire Proportional Chamber (MWPC) creates an avalanche of electrons in the strong field around the anode wires. The released electrons induce a signal on the cathode plane, which is divided into pads of size 4 - 6 mm (ϕ-direction) and 7.5 -15 mm (r-direction). The signals on the pads are amplified and digitized by the Front End electronics and passed further to the DAQ The location of the signal on the pad plane gives the $r\phi$-position of the track. The position along the beam axis (z-axis) is determined by measuring the time taken by the charged particles to reach at the end plates. This conversion from time to distance is what gives the TPC its name-“Time Projection Chamber”.

The total energy loss of the traveling charged particle, *i.e.*the integral over all energies lost to the individual gas atoms inside TPC, is given by the Bethe-Bloch formula,

$$-\frac{dE}{dx} = 2\pi N_a r_e^2 m_e c^2 \rho \frac{Z}{A}\frac{z^2}{\beta^2}\left[\ln\left(\frac{2m_e\gamma^2 v^2 W_{max}}{I^2}\right) - 2\beta^2 - \delta - 2\frac{C}{Z}\right] \quad (2.1)$$

where

N_a: Avogadro’s number

m_e: mass of electron

$r_e(= e^2/m_e)$: classical electron radius

Z: atomic number of the absorbing material

A: atomic weight of the absorbing material

$\gamma = 1/\sqrt{1-\beta^2}$

I: mean excitation potential

W_{max}: maximum energy transfer in a single collision

δ: density correction

C: shell correction

c: speed of light

Fig. 2.7 shows the measured dE/dx versus particle momentum (p) in the TPC detector, demonstrating the clear separation between the different charged particle species [60]. The continuous curves are the Bethe-Bloch parameterization used in the analysis for different particle hypotheses [61].

TPC can identify charged particles in a broad range of transverse momentum from 0.1 GeV/c to 100 GeV/c with momentum resolution of 6% (below 10 GeV/c) and the dE/dx resolution better than 5% (for isolated tracks) [62]. In conjunction with the ALICE TRD and ITS, TPC can also be used to study vector meson resonances, charm and beauty by measuring

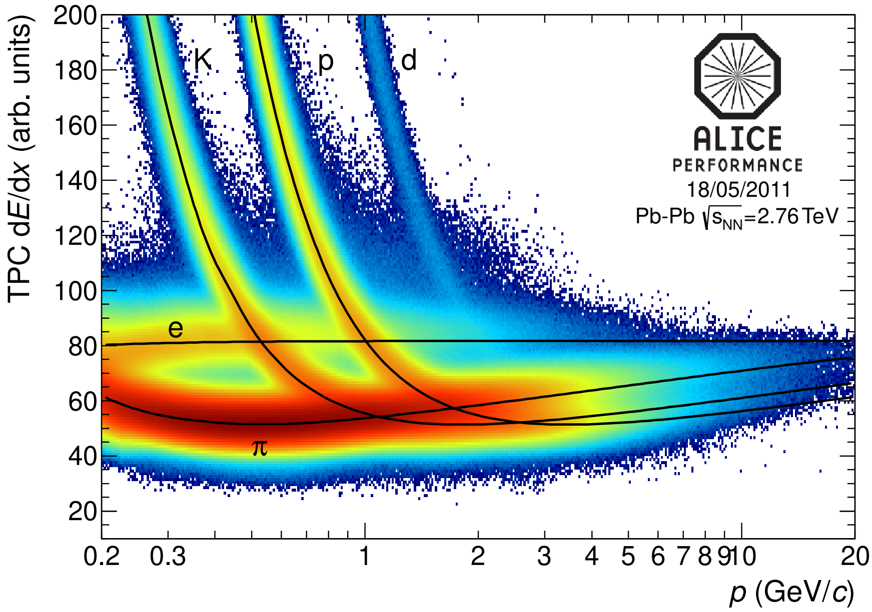

Figure 2.7. Specific energy loss (dE/dx) in the TPC vs. particle momentum in Pb+Pb at $\sqrt{s_{NN}} = 2.76$ TeV. The continuous line shows the parameterizations of the expected mean energy loss using Bethe-Bloch formula. Figure is taken from Ref. [60].

leptonic observables.

2.3.3 Transition Radiation Detector (TRD)

The main purpose of the Transition Radiation Detector (TRD) [63] in ALICE is to provide identification of the electron passing through central barrel region, especially at higher momenta above 1 GeV/c. Layout of ALICE TRD is shown in Fig. 2.8. Electrons with the momenta below 1 GeV/c can be identified in the TPC via specific energy loss measurement. TRD is placed in between TPC and TOF at a radial position of 290 cm to 368 cm from the beam pipe. It has a coverage of $|\eta| \leq 0.84$ in pseudorapidity and 360° azimuth. TRD consists of 18 supermodules, where each supermodule contains 30 modules arranged in five stacks along z-direction and six layers in radius. Each individual layer is made up of a radiator, a drift chamber and Multi Wire Proportional Counter (MWPC) with readout electronics. The drift chamber is filled with a gas mixture of Ar and CO_2 in the ratio of 85:15 and total active area subtended by the pads is 716 m^2 [63].

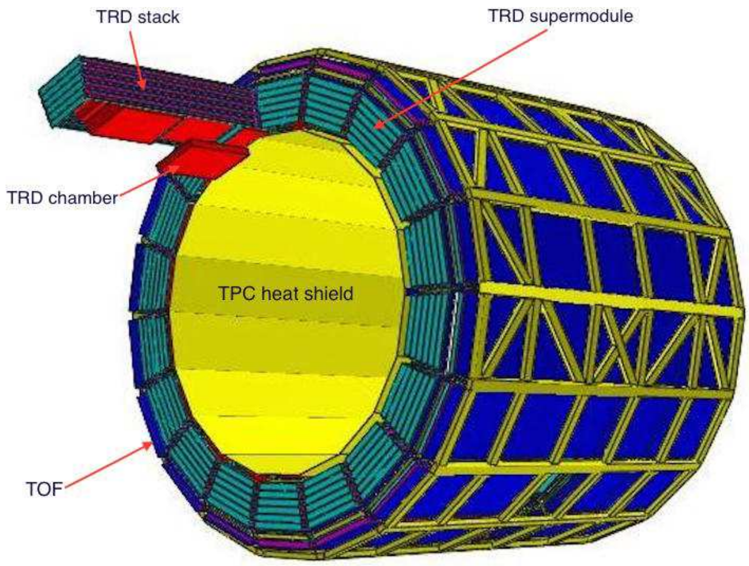

Figure 2.8. A schematic layout of TRD in the ALICE space frame.

The working principle of TRD is shown schematically in Fig. 2.9. When a relativistic charged particle ($\gamma \geq 1000$) traverses through the boundaries between media having different dielectric constants (refraction indices), radiates photons in the soft X-rays range, called Transition Radiation (TR). The working principle of TRD is based on the phenomena of Transition Radiation. The high-energy electrons with $\gamma \geq 1000$ produces about 1.45 X-ray photons (TR) in the energy range of 1 to 30 keV and these photons are detected by the gaseous detector. The pion can not emit TR below a momentum about 100 GeV/c, which helps TRD to achieve a 100% pion rejection capability for momenta above 1 GeV/c in central Pb-Pb collisions, this allows for the better measurement of J/ψ production through di-electron channel using ALICE detector at LHC. It also provides a fast trigger (L1) for charged particles with high momentum in ALICE.

2.3.4 Time-Of-Flight (TOF)

The Time-Of-Flight (TOF) detector [64, 65] is a gas based Multigap Resistive Plate Chamber (MRPC), where a high and uniform electric field is applied over the full sensitive gaseous volume of the detector. TOF is located around the TRD with 270 cm inner and 399 cm outer radius

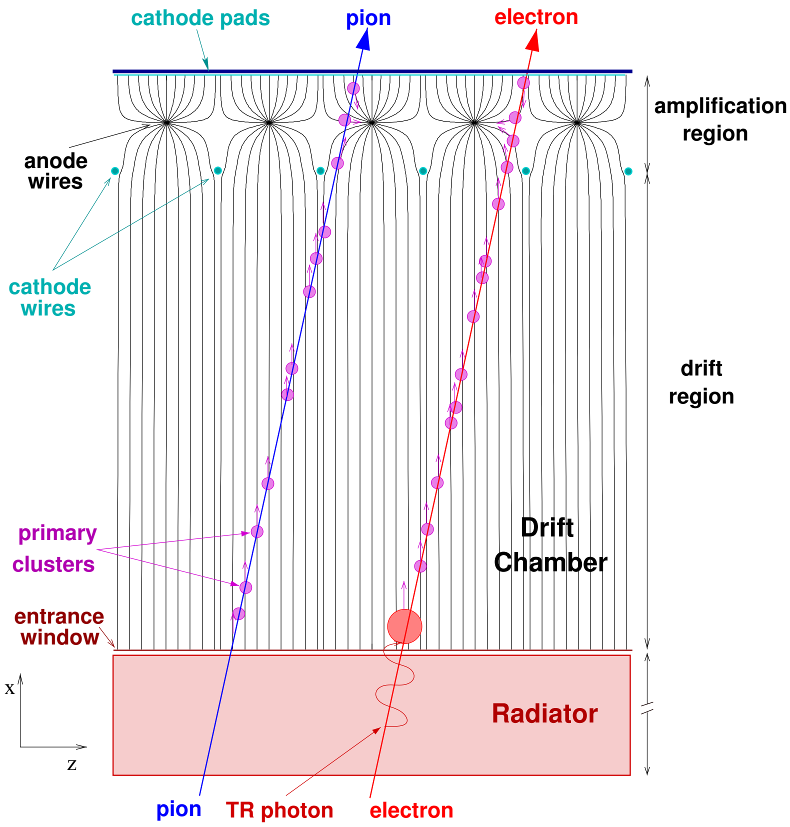

Figure 2.9. Working principle of TRD [63].

from the beam pipe. It has a coverage of $|\eta| \leq 0.9$ in pseudorapidity and $45° \leq \phi \leq 135°$ in azimuth. The main goal of TOF detector in ALICE is to identify charged particles in the intermediate momentum range: below 2.5 GeV/c for pions and kaons, up to 4 GeV/c for protons, with a p/K and K/p separation better than 3σ [66, 67]. The TOF, coupled with the tracking systems ITS and TPC, provides better track and vertex reconstruction and event-by-event identification of large samples of pions, kaons and protons. In addition, these identified kaons help in invariant mass studies, in particular the detection of open-heavy flavour states and vector-meson resonances.

MRPC provides an intrinsic time resolution better than 50 ps with an efficiency close to 100% and a large operational plateau. The TOF is made up of 1593 MRPCs arranged in 90 gas-tight modules. The whole structure is divided into 18 sectors in ϕ with 5 segment in z-direction. Each sector contains a supermodule more than 9 m long: five modules are grouped

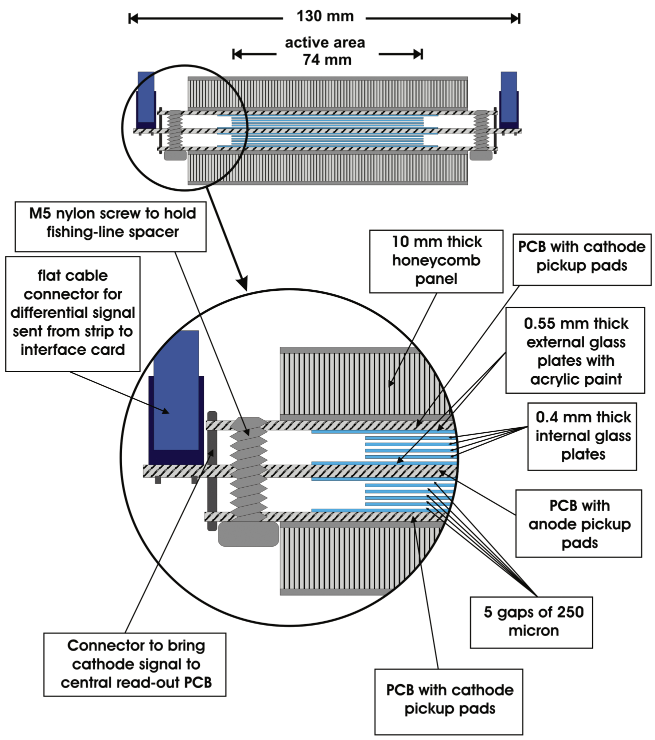

Figure 2.10. A Schematic diagram of cross-sectional view of the double-stack 10-gap TOF MRPC strip [68].

in a line to form one supermodule [68]. The basic building block of the TOF is a 10-gap double-stack MRPC strip (see Fig. 2.10), with an active area of $120 \times 7.4\ cm^2$ and subdivided into two rows of 48 pads with the dimension of $3.5 \times 2.5\ cm^2$. The strips are placed inside gas-tight modules, act as Faraday cages, with a gas mixture of $C_2H_2F_4(90\%), i\text{-}C_4H_{10}(5\%)$ and $SF_6(5\%)$ at atmospheric pressure and are positioned transversely to the beam direction in a tilted manner to minimize the dead area.

A Schematic diagram and principle of operation of a MRPC is shown in Fig. 2.11. When a charged particle passes through the gaseous volume it ionises the gas and the high electric field amplifies this ionization by an electron avalanche. The resistive plates stop the avalanche development in each gap and the total signal is the sum of the signals from all gaps whereas the time jitter of the signal depends on the width of the individual gap. These signals are then collected by the readouts with almost zero drift time. The Time-Of-Flight (TOF) technique is based on the measurement of the particle time-of-flight between collision point and the arrival of the

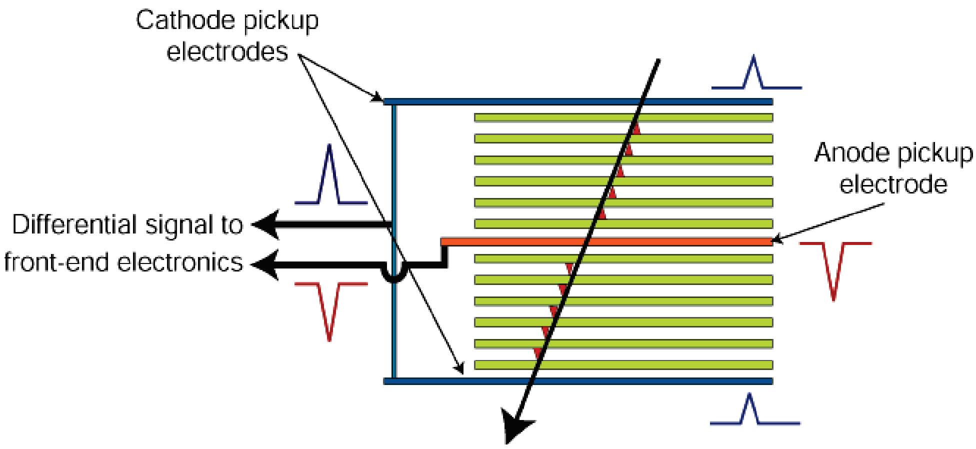

Figure 2.11. A Schematic diagram and principle of operation of a MRPC

particles in the TOF. If t is the time of flight and L is trajectory length of the particle in TOF then mass of the particle can be calculated as,

$$m^2 = \frac{p^2}{c^2}\left(\frac{c^2t^2}{L^2} - 1\right) \tag{2.2}$$

Then, the time-of-flight difference for two particles having unequal mass m_1 and m_2 with same momentum p and the same trajectory length L can be given by (in the limit $m^2c^2/p^2 < 1$)

$$t_1 - t_2 = \frac{L}{2c}\left(\frac{m_1c^2 - m_2c^2}{p^2}\right) \tag{2.3}$$

The TOF detector identifies particles with the number of standard deviations in the time-of-flight difference of two particles

$$n_\sigma = \frac{t_1 - t_2}{\delta t} \tag{2.4}$$

where δt is the time resolution of the TOF detector. The TOF also provides a pre-trigger (before *L0*) "wake-up" signal to the TRD in around 200 ns.

2.3.5 High Momentum Particle Identification (HMPID)

High-Momentum Particle Identification Detector (HMPID) is a proximity focusing Ring-Imaging Cherenkov (RICH) detector for high-momentum particle identification [69]. It is the largest detector of this kind, using CsI photosensitive elements, ever used in High-Energy Physics experiments and the only "CsI-RICH" at LHC. HMPID is made up of 7 modules of $1.5 \times 1.5\ m^2$, placed at 500 cm from the beam line at the 2 o'clock position to minimize the density of arriving particles. It has a coverage of $|\eta| \leq 0.6$ in pseudorapidity and $1.2° \leq \phi \leq 58.8°$ azimuth. The HMPID detector is designed to extend the momentum range for the measurement of ratio of π/K up to 3 GeV/c and K/p up to 5 GeV/c, on a track-by-track basis. It enhances the particle identification capability of the ALICE detector beyond the momentum range allowed by the energy loss in detectors like ITS, TPC and Time of Flight (TOF). The geometry of HMPID is optimized with respect to particle yields at high-p_T in hadronic and nuclear collisions, and with respect to the large opening angle needed for the two-particle correlation measurements at the LHC energies. In addition, HMPID can also be used to identify light nuclei and anti-nuclei (d, t, ^{3}He, α) at high-p_T in midrapidity region [70].

2.3.6 PHOton Spectrometer (PHOS)

ALICE PHOton Spectrometer (PHOS) is a high resolution electromagnetic calorimeter. It is designed to detect and identify photons and measure their high resolution 4-momenta in order to perform the ALICE physics programme which exploits direct photons and light neutral mesons (π^0 and η mesons mainly) as probes [59, 71]. PHOS detects photons with a broad dynamical range in transverse momentum of 5 MeV to 100 GeV, which allows to access key information about the hard and soft processes occurring in $p + p$, p+A and A+A collisions at LHC energies. It is placed inside the solenoidal magnet and on the bottom of ALICE set-up at a distance of 460 cm from the interaction point with coverage of 100° in azimuth and $|\eta| < 0.12$ in pseudorapidity.

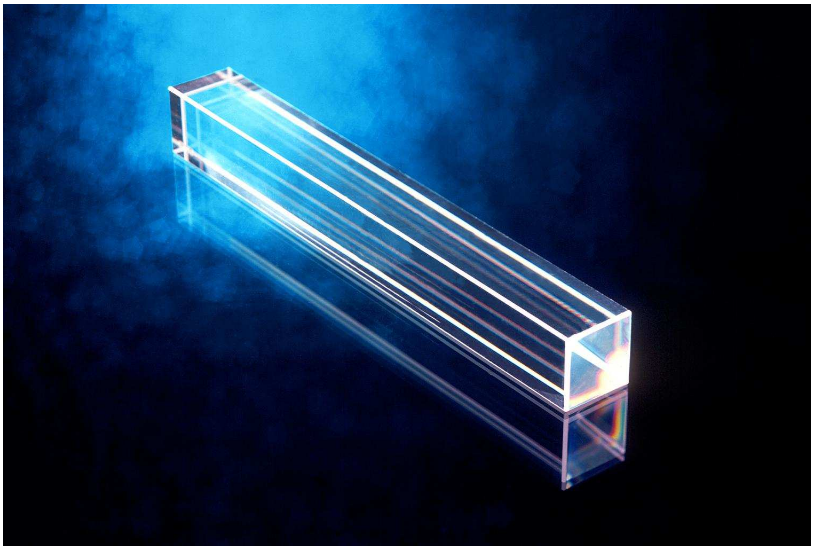

Figure 2.12. $PbWO_4$ PHOS crystal in ALICE

PHOS detector is made up of an electromagnetic calorimeter (EMC), and a Charged Particle Veto (CPV) detector. The EMC is divided into 5 modules, consisting of 64×56 lead-tungstate scintillator crystals, PbWO4 (or PWO), shown in Fig. 2.12. Each crystal is a 18 cm long parallelopiped, which is equivalent to 20 radiation length units ($X_0[PbWO_4] = 0.89$ cm). Their cross section is 22×22 mm^2 which corresponds to the 90 % of the Moliere radius ($r_M[PbWO_4] = 20$ mm). The scintillation light is in the visible near UV wavelength range and is detected by 5×5 mm^2 Avalanche Photo-Diodes (APD) coupled to low-noise pre-amplifiers. The CPV detector consists of MWPC with cathode pad as a read-out. Each ECM module is covered by a CPV module with an active area of $144.6 \times 6.6 \times 1.4$ m^3 and filled with a gas mixture of Ar and CO_2 in the ratio of 80:20 at a pressure slightly above atmospheric pressure. CPV is used to provide discrimination against charged particles.

2.3.7 Electro Magnetic Calorimeter (EMCAL)

The ElectroMagnetic CALorimeter (EMCAL) is a Pb-scintillator sampling calorimeter with cylindrical geometry. It is placed inside the L3 magnet coil and at a radius of about 450 cm from the beam pipe. It covers the pseudorapidity region $|\eta| < 0.7$ and $\phi = 107°$ and is positioned opposite to the PHOS in the azimuthal direction and adjacent to HMPID. EMCAL is designed to measure π^0 and η by measuring decay photons like PHOS detector. EMCAL is larger than PHOS in size with an acceptance of about 23% of phase space of the central pseudorapidity region, but provides lower granularity and energy resolution. It is made up of 10 full size and 2 one-third size supermodules in the full detector acceptance. The full size module covers $\Delta\eta = 0.7$ and $\phi = 20°$, whereas the one-third module covers $\Delta\eta = 0.7$ and $\phi = 7°$. It provides fast and efficient triggers (L_0, L_1) for hard jets, photons and electrons. It also measures the neutral components of jets, which allow the full reconstruction of jets in all type of collisions at LHC. Together with the TPC, EMCAL provides a good energy resolution for jet reconstruction and high sensitivity to jet-quenching effects expected at LHC [72, 73].

2.3.8 ALICE Cosmic Ray Detector (ACORDE)

ALICE Cosmic Ray DEtector (ACORDE) is an array of plastic scintillators located at a radial distance of 850 cm on the top of the L3 magnet coil to trigger cosmic rays. It is made up of two scintillator counters, each of them with effective area of 190×20 cm^2, placed on top of each other and read out in coincidence. ACORDE covers the pseudorapidity region $|\eta| < 0.13$ and $-60° < \phi < 60°$ azimuth and provides a fast L_0 trigger to ALICE Central Trigger Process when atmospheric muons pass through the ALICE detectors. ACORDE is mainly used for calibration, alignment and performance of tracking detectors like ITS, TPC, TOF and HMPID. ACORDE can measure atmospheric muons which allow to analyze the muon momentum spectra with very high precision in a large range of energy (100 GeV to 2 TeV) [74].

2.4 Forward Detectors

ALICE experiment is equipped with some specialized small detector systems installed in the forward pseudorapidity region on the both sides of the interaction points, such as Forward Multiplicity Detector (FMD), Photon Multiplicity Detector (PMD), Zero Degree Calorimeter (ZDC) and detectors for trigger and timing (VZERO (V0) and TZERO (T0)). In this section, we give a brief description of these detectors.

2.4.1 Forward Multiplicity Detector (FMD)

Forward Multiplicity Detector (FMD) [75] is specially designed to measure the charged particles produced in the collisions, which are emitted at very small angles relative to the beam direction (z-axis). It is made up of 5 discs of silicon pad detectors (FMD1i, FMD2i, FMD2o, FMD3i, FMD3o), 2 of them are located on the muon spectrometer side and rest 3 are on the opposite side (Fig. 2.13). The FMD is the primary detector, which measures the charged particles multiplicity distribution over a pseudorapidity coverages of $-3.4 < \eta < -0.17$ and $1.7 < \eta < 5.0$ corresponding to an angular coverage $0.75^\circ < \phi < 21^\circ$ [74]. In addition to charged particle multiplicity measurements, FMD is also capable to study elliptic flow and multiplicity fluctuations. These observables are essential to understand the properties of the Quark Gluon Plasma, and the phase transition from normal matter to QGP.

2.4.2 VZERO (V0)

ALICE VZERO (V0) [75] is a small angle detector consisting of two arrays of 32 plastic scintillating counters, named as V0A and V0C, which are installed on both sides of the interaction point. The V0A is placed 330 cm

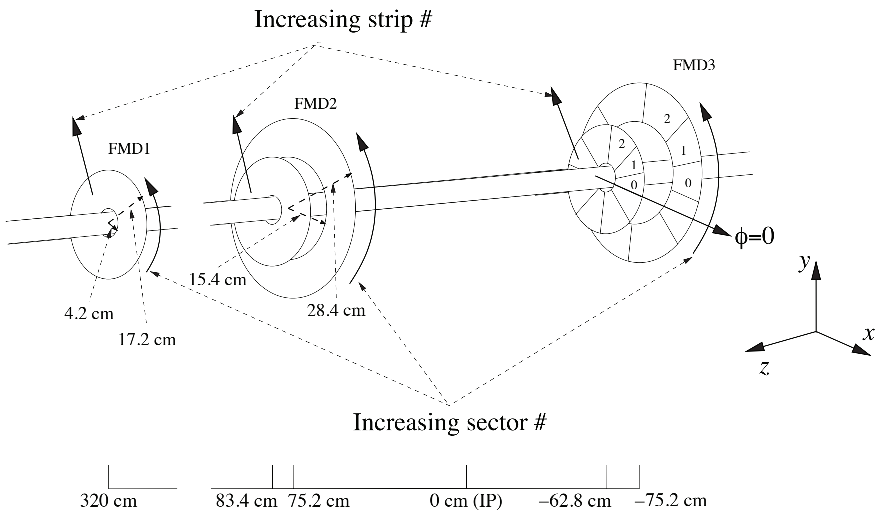

Figure 2.13. Layout of the FMD rings in the ALICE experiment. FMD2 and FMD3 are placed on both sides of the ITS detector while FMD1 is much further away from the interaction point (IP).

away from the interaction point on the side opposite to the muon spectrometer. The V0C is fixed at the front face of the hadronic absorber, 90 cm away from the vertex. It provides Minimum-Bias triggers and Centrality Triggers for the central barrel detectors in p+p and Pb+Pb collisions. Fig. 2.13 shows both the scintillating counters V0A and V0C covering the pseudorapidity ranges, $2.8 < \eta < 5.1$ and $-3.7 < \eta < -1.7$, respectively.

The V0 detector is used to measure beam luminosity, multiplicity and azimuthal distributions of charged particles. The control of the luminosity allows the determination of the absolute cross-section value of reaction processes. The knowledge of the charged particle multiplicity is essential for the evaluation of the centrality in nucleus-nucleus collisions. Furthermore, it is also used to estimate the centrality of the collision by adding up the energy deposited by the charged particles in the two disks V0A and V0C. This observable scales with the number of primary particles generated in the collision and therefore to the centrality.

2.4.3 TZERO (T0)

ALICE TZERO (T0) [75] is the fast timing and trigger detector consisting of two arrays of Cherenkov counters, called T0A and T0C. The T0A is placed at a distance of 375 cm from the interaction point, opposite to the Muon spectrometer with the pseudorapidity coverage of $4.61 < \eta < 5.92$, whereas the other component T0C is placed at a distance of 727 cm from the interaction point on the opposite side of T0A with the pseudorapidity coverage of $-3.28 < \eta < -2.97$. Each array of T0 detector is made up of 12 cylindrical counters equipped with a quartz radiator and a photomultiplier tube. The T0 detector is also used for online luminosity monitoring providing fast feedback to the accelerator team.

2.4.4 Zero Degree Calorimeter (ZDC)

Zero Degree Calorimeters (ZDC) [76] is located on both sides of the nominal interaction point at a distance of 116 m, exactly along the beam line. The ZDCs are used to detect the energy of the spectator nucleons in order to determine the overlap region of the colliding nuclei in heavy-ion collisions. It also provides an estimation of the reaction plane in the nuclear collisions at LHC. Each ZDC is constructed by two distinct detectors: one for spectator neutrons (ZN) placed at $0°$ with respect to the beam axis and is used to detect neutral particles at pseudorapidities $|\eta| > 8.7$ and the other for spectator protons (ZP) located externally to the outgoing beam pipe on the side where positive particles are deflected. Note that the position of ZP take care of the deflection of the spectator protons due to the magnetic field.

The ZDCs are *quartz-fibre spaghetti calorimeters*, with silica optical fibres as active material embedded in a dense absorber. The principle of operation is based on the detection of the Cherenkov light produced in the fibres by charged particles of the shower, induced by the spectator nucleons.

There are also two small electromagnetic calorimeters (ZEM) used to compliment ZDC placed at about 7.35 m from the interaction point, on both sides of the LHC beam pipe, opposite to the muon arm to detect the energy of particles emitted in the pseudorapidity coverage $4.8 < \eta < 5.7$. A combination of signals coming from these two calorimeters (ZDC and ZEM) provides three L1 triggers meant for event classification (central, semi-central and minimum bias events) [74].

2.4.5 Photon Multiplicity Detector (PMD)

The Photon Multiplicity Detector (PMD) [77, 78] is a preshower detector with an array of gaseous proportional counters. It is designed to provide the measurements of multiplicity and the pseudorapidity distributions of photons in the forward rapidities ($2.3 < \eta < 3.9$) with full azimuthal coverage ($0° < \phi < 360°$).

PMD is made up of two identical planes of honeycomb chambers with a lead converter plate of thickness of 3 radiation length ($3X_0$) sandwiched in between them. The plane towards the interaction point (IP) is known as the Charged Particle Veto (CPV) plane while, the plane behind the lead plates is known as the Preshower plane (PRE). CPV is used for improving the photon hadron discrimination. When a photon passes through lead convertor plate, it produces a shower of electrons and positrons by the combined effect of pair production and bremsstrahlung emission. These shower particles produce signals in preshower plane, which are read by PMD's Front End Electronics (FEE). PMD detector is discussed in more details in Chapter 4.

2.5 Muon Spectrometer

The ALICE forward muon spectrometer [79] is optimized to measure the quarkonia ($J/\psi, \psi', \Upsilon, \Upsilon', \Upsilon''$) and the low-mass vector meson (ρ, ω and ϕ) production via their decay in the $\mu^+\mu^-$ (dimuon) channel. In addition, muon spectrometer can also investigate heavy flavours (D^+, D^-, B^+ and

B^-) through their semi-muonic disintegration. Heavy quarkonium states (charmonium and bottomonium), provide an essential tool to study the early and hot stage of heavy-ion collisions.

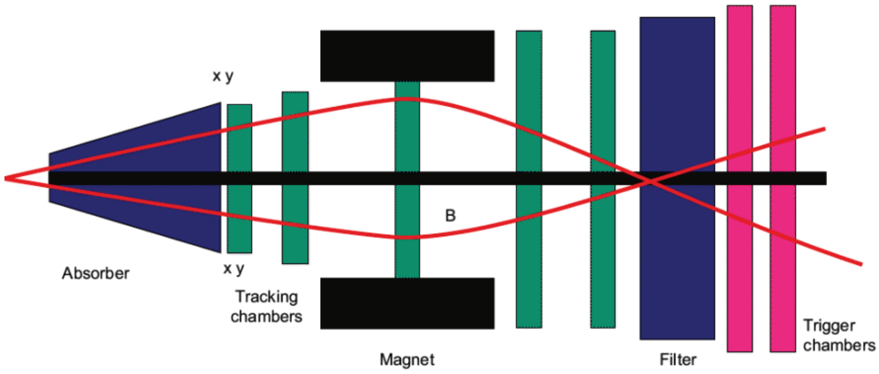

Figure 2.14. The main components of the ALICE muon spectrometer: an absorber to filter the background, a set of tracking chambers before, inside and after the magnet and a set of trigger chambers.

The main components of the ALICE muon spectrometer is shown in Fig. 2.14. The muon spectrometer is located on the C side of the ALICE experiment and consists of a front absorber placed 90 cm from the interaction point, 10 high-granularity tracking chambers, a large dipole magnet with 3 Tm integrated field, a 15 m long small angle absorber, four large area trigger chambers and a muon filter made up of a 1.2 m thick iron wall [79–82]. The muon spectrometer covers the polar angular range $171^\circ < \theta < 178^\circ$ ($-4.0 < \eta - 2.5$) over the full azimuthal coverage for muons with transverse momentum $p_T > 4$ GeV/c.

An important specification of the muon spectrometer is its mass resolution (100 MeV/c^2 at 10 GeV/c^2), which allows the separation of the $\Upsilon(1S), \Upsilon(2S), \Upsilon(3S)$ substates in the large background environment of central Pb-Pb collisions [74].

2.6 ALICE Online System

The ALICE online systems are the Central Trigger Processor (CTP), the High Level Trigger system (HLT), the Data Acquisition system (DAQ) and the Detector Control System (DCS). The co-ordination and synchronization of the mentioned online systems is controlled by Experiment Control System (ECS).

2.6.1 Central Trigger Processor (CTP)

The ALICE Central Trigger Processor (CTP) [83, 84] is a low-level hardware trigger consists of 24 Local Trigger Units (LTU) for each detector system. CTP is responsible for the correct selection of physically interesting events that are not commonly produced in collisions at LHC. The CTP receives and process trigger signal from trigger detectors and provides three levels of hardware triggers: The first level trigger is known as the *L0*, which is delivered after 1.2 μs, the second level is *L1* and is delivered after 6.5 μs and the final trigger is *L2* and is delivered after 100 μs. The output from the ALICE CTP go to the LTUs of each detector and then Front-End Electronics (FEE) of the detector via Low Voltage Differential Signalling (LVDS) cables and optical fibres. A block diagram of the ALICE CTP is shown in Fig. 2.15.

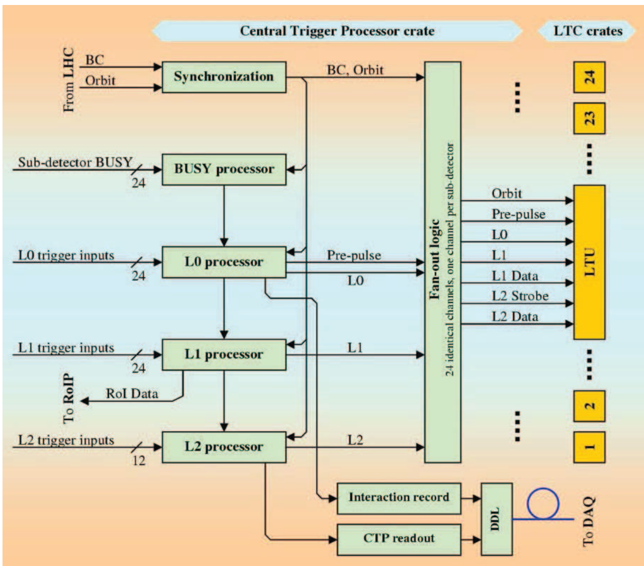

Figure 2.15. A block diagram of the ALICE CTP

Finally, another important feature of the CTP is the past-future protection, which ensures that events are not superimposed by too many pile-up collisions. The busy times of the different detectors vary significantly, therefore the window in which pile-up is recognized depends not only on the current partition of the detectors but also on the collision system.

2.6.2 High Level Trigger (HLT)

The ALICE High Level Trigger (HLT) [83] is a software trigger which consists of a farm of multiprocessor computers, designed to analyse Large Hadron Collider (LHC) events online. The HLT can reduce the size of the stored events by selecting the regions of interest and by applying compression algorithms on the accepted and selected data.

The HLT receives a copy of the raw data via 454 Detector Data Links (DDL), then performs reconstruction of data for each detector individually. In the same step a region of interest can be selected. In the last optional step, if the trigger decision is positive, the data is compressed. Then trigger decision, partial readout information, compressed data, and the reconstruction outputs are sent to LDCs and subsequently processed by the DAQ.

2.6.3 Data Acquisition System (DAQ)

The main role of ALICE Data Acquisition system (DAQ) [83] is to collect the collision data from different sub-detectors and save it to permanent storage (tape). A first layer of computers, called Local Data Concentrators (LDCs), reads out the event fragments from the optical Detector Data Links (DDLs) with the higher data rate (above 13GB/s). The DDLs are point-to-point links running at maximum 6 GB/s and up to 12 of them can be connected to the same LDC unit. The event fragments is assembled into sub-events and then shipped to a second layer of computers, Global Data Collectors (GDCs), which assembles them in a full event. Then these events are recorded to a Transient Data Storage (TDS) before being migrated to the Permanent Data Storage (PDS) and published via the ALICE Grid.

2.6.4 Experiment Control System (ECS)

The ALICE Experiment Control System (ECS) [83] is a part of the ALICE control system, which is responsible for the co-ordination and synchronization of the online systems (CTP, HLT, DAQ and DCS). The interface of ECS with other online system in shown in Fig. 2.16. The ALICE ECS also provides a unified view of the experiment and a central point, where all the operations to manage the different aspects of the experiment are initiated and controlled. The major software components of the ALICE ECS are: Partition Control Agent (PCA), the Detector Control Agent (DCA), the ECS database, and the Human Interfaces (HI).

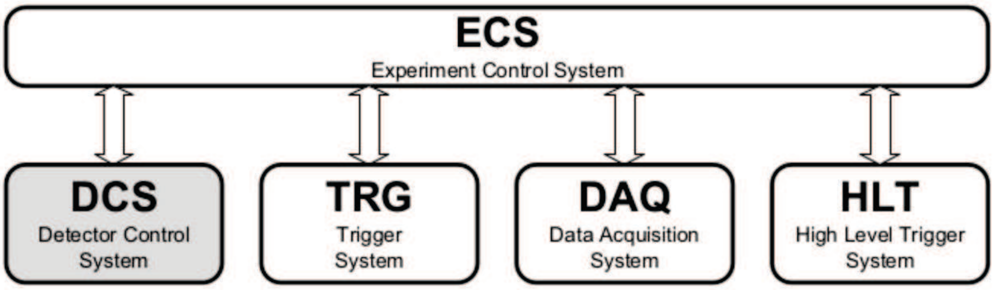

Figure 2.16. The interface of ECS with other online system in the ALICE experiment.

The *Detector Control Agent (DCA)* controls standalone data-acquisition runs for the detector working alone. There is one DCA for every detector. *Partition Control Agent (PCA)* controls the running of a partition of the detectors taking data during physics of technical runs. There is one PCA per partition. Both the DCA and the PCA are based on Finite-State Machines (FSM). Several operators can concurrently use Human Interfaces to the same PCA or the same DCA, but only the master operator can send commands to it.

The *ECS database* describes the partitions in terms of ALICE detectors. Each partition includes a list of detectors assigned to it. The database includes information on whether each detector is presently active or not. Additional information on the status (running/not running) of the PCA controlling the partition and on the Human Interface process having mastership over the PCA is also given. For every detector the ECS database contains the status of its DCA (running/not running), the partition name when the detector is active in a partition, information on the Human Interface process having mastership over the DCA when the detector is operated in standalone mode.

Three different *Human Interface* programs give access to a DCA (DCAHI), to a PCA (PCAHI), and to the ECS database (ECSHI) to access the DCA, PCA and ECS database, respectively.

2.7 ALICE Offline System

The objective of the ALICE Offline Project [85] is the development and operation of the framework for data processing. This project includes tasks such as simulation, calibration, reconstruction, alignment, visualization and data analysis. These are the final steps of the experimental activity, aimed at interpreting the data collected by the experiment and at extracting the physics content. The required computing resources to process the ALICE data exceed the computing power of a single institute and even centres like CERN. Therefore, data processing is distributed onto several computing centres located worldwide. ALICE uses the ALICE Environment (AliEn) system as a user interface to connect to the Grid composed of ALICE-specific services that are part of the AliEn framework and basic services of Grid middleware installed at different sites.

The simulation and reconstruction of ALICE events are done by a dedicated frame work called AliRoot. The AliEn and AliRoot framework are discussed in the subsequent sections.

2.7.1 Data Processing

The data processing strategy varies according to the type of collisions. In p+p collisions, the data recorded by the sub-detectors are written by the

DAQ on a disk buffer at the Tier-0 computing centre at CERN. In parallel to this, the following activities proceed on the raw data:

- RAW data are copied to the CASTOR [86] tapes.
- then exported to the Tier-1 centres to have a second distributed copy for the successive reconstruction passes.
- First pass is processing at the Tier-0 centre, which includes reconstruction, production of calibration and alignment constants and scheduled analysis.
- Fast processing of selected data sets on the CERN Analysis Facility (CAF).

In case of heavy-ion collisions processing of raw data occurs in the following steps:

- Registration of the RAW data in CASTOR.
- then partial export to the Tier-1 centres to allow remote users to examine the data locally.
- to provide rapid feedback on the offline chains, partial first pass processing at the Tier-0.
- Fast processing, mainly calibration, alignment, reconstruction and analysis on the CAF.

2.7.2 ALICE Framework

To process the huge amount of ALICE data, a concept of Grid is developed through a distributed computing resources all around the world. The implementation of the Grid concept is done by a software called Grid middleware and ALICE has developed a Grid middleware called AliEn [87], as a user interface to connect to the Grid. The AliEn Web Services play the central role in enabling AliEn as a distributed computing environment.

The user interacts with them by exchanging Simple Object Access Protocol (SOAP) messages and they constantly exchange messages between themselves behaving like a true Web of collaborating services. AliEn has been extensively used to produce a large amount of simulated data as well as the data recorded and reconstructed in the p+p, Pb+Pb and p+Pb collisions. The simulation data used in this analysis has been produced at these sites.

2.7.3 AliRoot Framework

The AliRoot offine framework [87] is based on the Object Oriented programming for simulation, alignment, calibration, reconstruction, visualization, quality assurance, and analysis of experimental and simulated data. AliRoot is based on the ROOT framework [88]. Most of the codes are written in C++ computer language with some parts in Fortran computer language that are wrapped inside C++ codes. The schematic picture of simulation framework is shown in Fig. 2.17 and briefly described below:

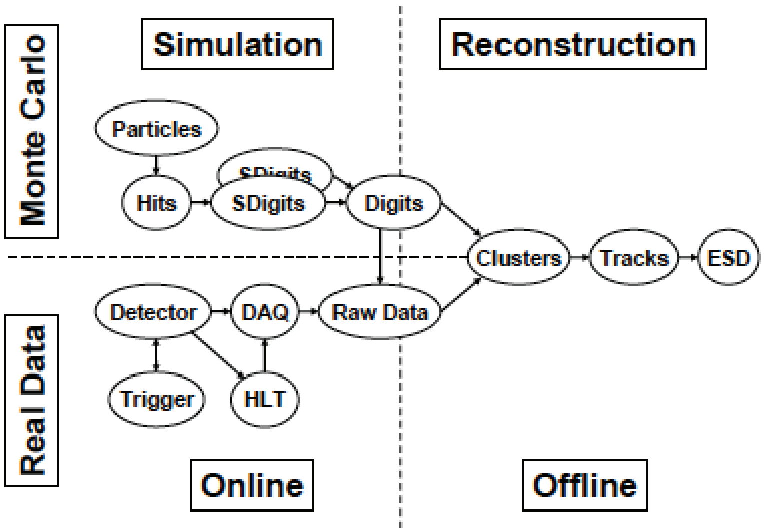

Figure 2.17. A schematic picture of the AliRoot Framework. This figure is taken from the Ref. [54].

Event Generation

The AliRoot framework provides interfaces to the several event generators such as PYTHIA [89, 90], PHOJET [91, 92], HIJING [93], DPMJET [94], AMPT [95] etc. The data produced by the event generators contain full information about the generated particles *e.g.*, PID, momentum, charge, mass and mother-daughter relationship.

Detector response simulation

The generated particles are transported through the detector geometry. The detector response is simulated for each crossing of the particles through detector using a monte-carlo transport package. Within the AliRoot framework, available transport packages are GEANT3 [54], GEANT4 [96] and FLUKA [97]. The transport packages contain detailed information of the ALICE detector, including services and support structures, absorbers, shielding, beam pipe, flanges, and pumps. When the generated particles pass through the transport package, they undergo all possible interactions, which they would undergo during the real experiment. The information of hits (energy deposition information with space and time coordinates) are stored for each detector. The information are complemented by the so-called track references corresponding to the location where the particles are crossing user defined reference planes. Then the hits are converted into digits taking into account the detector and associated electronics response function. Finally, the digits are stored in the specific hardware format of each detector as raw data.

Alignment and calibration framework

The AliRoot framework also takes care of the misalignment in positioning the different part of detectors from their ideal position. When the simulation program is started, the ideal geometry is generated by the compiled code or read from the OCDB, where it was saved in a previous run. Several objects are marked as alignable, that is the geometrical modeller is ready to accept modifications to their position, even if they were obtained by replication. The framework then reads the alignment objects which contain the adjustments in the position of the alignable objects. The particle transport is then performed in the modified geometry. During the reconstruction of the real data, the best alignment objects are loaded from the OCDB.

During first pass reconstruction, the alignment objects are taken from the survey data. For subsequent reconstruction passes, the alignment objects are produced by the alignment algorithms optimizing the reconstruction quality during processing of raw data.

The calibration framework is similar to the alignment one. The initial calibration constants come either from the detector properties as measured during construction, or from algorithms running online during data-taking aimed at providing a partial calibration sufficient for the first-pass data reconstruction. During the reconstruction itself, better calibration constants can be calculated and stored in the OCDB.

Reconstruction framework

As described earlier both the physics data and simulated data are stored in the same raw data format. These raw data are then reconstructed using the same algorithms. The output of the reconstruction is the ESD (Event Summary Data), which contains only high-level information such as the position of the event vertex, parameters of reconstructed charged particles together with their PID information, positions of secondary-vertex candidates, parameters of particles reconstructed in the calorimeters, and integrated signals of some sub-detectors.

Analysis

The analysis framework is developed to analyse the reconstructed or simulated data. As the first step, the analysis framework extracts a subset of the Datasets from the File Catalogue using meta-data selection. Then the framework negotiates with dedicated Grid services balancing between local data access and data replication. Once the distribution is decided, the analysis framework creates sub-jobs. The framework collects and merges available results from all terminated sub-jobs on request. An analysis object associated with the analysis task remains persistent in the Grid environment so the user can go offline and reload an analysis task at a later date, check the status, merge current results, or resubmit the same task with a modified analysis code.

Chapter 3

Inclusive Photon Production in Pb+Pb collisions at $\sqrt{s_{\text{NN}}} = 2.76$ TeV

The Photon Multiplicity Detector (PMD) is designed to measure the photon multiplicity and its pseudorapidity distributions in the forward rapidity region. In 1991, first attempt was made to use a PMD at the CERN SPS in the WA93 experiment [98] and after that PMD was subsequently used in the WA98 experiment [99] at CERN SPS, the STAR experiment [100] at RHIC and in the ALICE experiment [74] at the LHC. With the same physics goals, the PMD has gone through a technological evolution from a plastic scintillator pads in WA98 experiment to a hybrid gas proportional counter in STAR and ALICE experiments.

3.1 Design Evolution of the Photon Multiplicity Detector

The fixed target experiments WA93 and WA98 were using PMD, which consisted of plastic scintillator pads. The outcoming light from the scintillator pads transported to read out devices through Wavelength Shifting Fibres (WLS) and converted into electrical signals. The image intensifier and Charge-Coupled Device (CCD) camera were used as a readout system in PMD. In WA93, PMD was made up of four quadrants of light-tight box, each quadrant having 1875 pads with the uniform pad size of 2 cm × 2 cm through out the detector. A picture of WA98 PMD is shown in Fig. 3.1. It was installed at a distance of 10.09 m from the interaction point with the pseudorapidity coverage of $2.8 < \eta < 5.2$. However, to improve light collection and to reduce distortion of CCD images a modified fabrication technology was used in WA98 experiment. Four different pad sizes were used to keep the pad occupancy and the multiple hit probability low. The readout system was made up of image intensifier and CCD camera similar to WA93 experiment. The WA98 PMD was installed at 21.5 m from the target with a pseudorapidity coverage of $2.5 < \eta < 4.2$.

Figure 3.1. Picture of the PMD as installed in the WA98 experiment at the CERN-SPS.

The PMD in STAR experiment at RHIC, shown in Fig. 3.2, was consisted of two identical planes: The Preshower (PRE) plane and the Charge Particle Veto (CPV) plane. These planes consist of array of cellular hexagonal proportional counters (cross section 1.0 cm^2 and depth 0.8 cm) with a gas mixture of Ar (70%) and CO_2 (30%) as the sensitive medium. Each plane of PMD contains twelve super-modules, each of them being a gas tight chamber consisting of 4-9 unit modules of 576 cells each arranged in a rhombus matrix. The CPV plane was introduced to improve the photon-hadron discrimination. In total, each plane of STAR-PMD has 82,944 proportional counters. The FEE for signal processing is based on the use of GASSIPLEX chips developed at CERN [9]. The entire PMD has been divided into 48 chains. The detector was installed at a distance of

5.4 m from the IP. It covers a pseudorapidity region of $2.3 < \eta < 3.8$ with full azimuthal coverage. A picture of STAR-PMD is shown in Fig. 3.2. The ALICE-PMD uses the same photon detection principle, which was used for STAR-PMD.

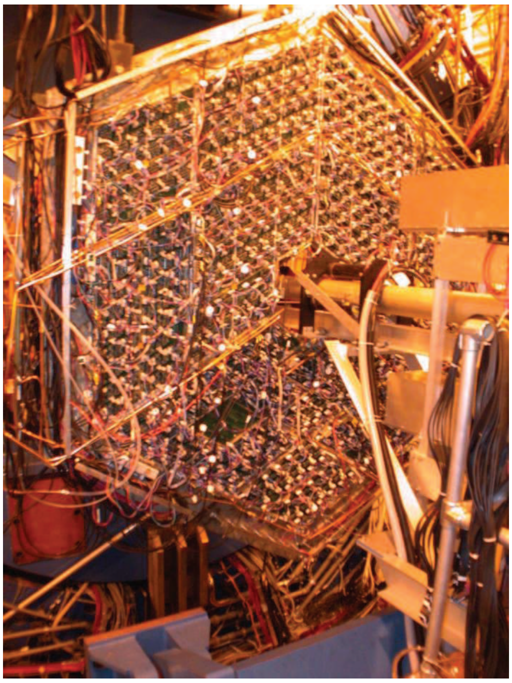

Figure 3.2. Picture of the PMD as installed in the STAR experiment at the RHIC.

3.2 Photon Multiplicity Detector in ALICE

The Photon multiplicity detector (PMD) in ALICE is designed to measure the multiplicity and the spatial distribution of inclusive photons at TeV energies. It consists of two identical planes of proportional counters and a lead converter sandwiched between them. PMD is installed at 367.2 cm away from the IP and covers pseudorapidity range of $2.3 < \eta < 3.9$ with full azimuthal coverage. The mechanical design, assembly and the readout architecture of PMD are discussed in details in later sections in this chapter.

3.2.1 Mechanical Design and Construction

The PMD consists of the following mechanical parts:

- two identical planes, the PRE and the CPV;
- lead converter plate;
- support structure;

Each plane of the PMD consists of 24 modules and each of the modules consist of 4608 numbers of honeycomb structured cells. A schematic of the PMD honeycomb cell is shown in Fig. 3.3. Each module is rectangular in shape and has an independent gas-tight unit. Modules can be handled *i.e.* fabricated, tested and installed individually. There are two types of modules in PMD: the short type and the long type. The short type module contains 48 rows and 96 columns while the long type contains 96 rows and 46 columns (shown in Fig. 3.4). The basic building block of PMD is hexagonal cells having 0.23 cm^2 cross section area and 0.5 cm depth. To handle high multiplicity environment at LHC compared to STAR-PMD at RHIC, the ALICE-PMD has cells of smaller dimension, *i.e.* it has higher granularity.

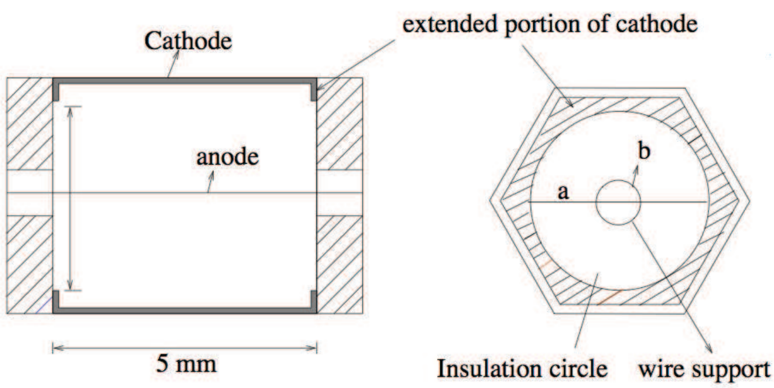

Figure 3.3. A Schematic layout of ALICE-PMD unit cell. Figure is adopted from [77].

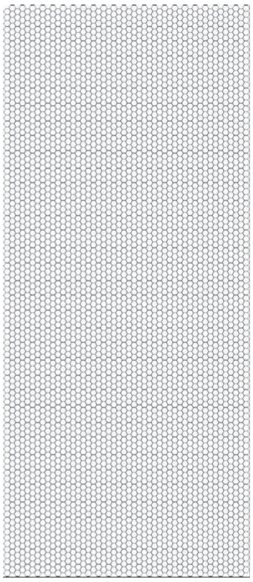

a)

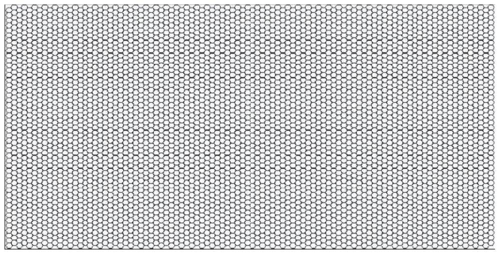

b)

Figure 3.4. (a) Long type module with 96 rows and 48 columns. (b) Short type module with 48 rows and 96 columns. Figure is adopted from [77].

An array of 48×96 or 96×48 such cells is made using a thin copper sheet (0.2 mm thick) and is known as honeycomb chambers. The honeycomb chamber is placed between two gold plated Printed Circuit Boards (PCB). Gold plated tungsten wires of diameter 20 μm are inserted through the centre of each cell and a proper tension is applied in the wire during soldering. The gold plated tungsten wires are used as anodes. The signal from the anode wires of 32 cells (in 4 rows and 8 columns) are grouped into one connector fixed on the top PCB. There are 72 connectors in a module and each connector extracts the signal from the 32 cells. The bottom PCB has only soldering islands without signal tracks, serving as anchor points. The inner part of both the PCBs are gold plated, with circular islands near the anode wire. Together with the honeycomb wall they form part of an extended cathode going very close to the anode wire. Assembly of a unit module is shown in Fig. 3.5. Each module is kept inside air-tight containers, made up of 2 mm thick stainless steel (SS) material. There are two nozzles for inflow and outflow of gas. A mixture of Ar and CO_2 is used as an active medium with a ratio of 70:30. The gas mixture flows continuously through all the modules of PMD.

The PMD contains a rectangular Pb convertor plate sandwiched be-

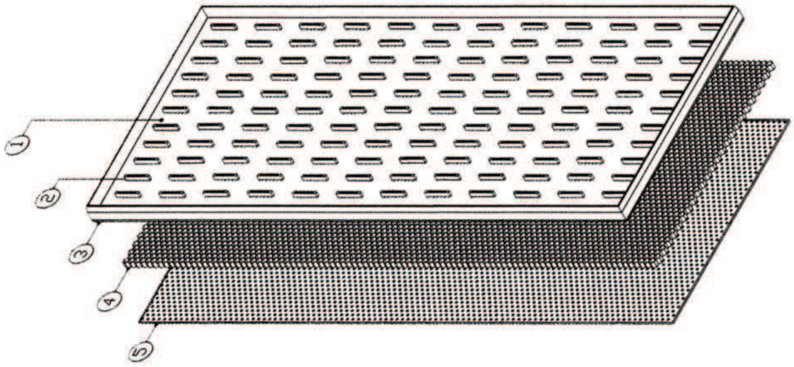

Figure 3.5. A Schematic layout showing components of unit module of PMD: (1) Top PCB, (2) 32-pin ETEC connectors, (3) edge frame, (4) honeycomb of 48×96 cells, (5) bottom PCB. Figure is adopted from [77].

tween CPV and PRE plane. There are two types of Pb plates depending on unit module size. The long type Pb plate has a dimension of 49.05 cm$\times$21.7 cm and the short one has 42.5 cm$\times$25.15 cm. The thickness of the plate is 1.5 cm which corresponds to three radiation length ($3X_0$). There is a 5 mm SS plate to support the lead converter plate and the module. Each SS plate contains 10 modules of the PMD. Fig. 3.6 shows two halves of the PMD (looking towards the IP), situated on the both side of the beam pipe. Each half has independent gas supply, electronic accessories and cooling systems. The PMD is supported by a SS girder, which helps to move both halves of the PMD to bring them together for data taking and to separate for maintenance and service.

3.2.2 Front End Electronics (FEE) and Readout

The PMD is a gaseous detector with gold plated anode wire readout. The FEE boards, based on a 16-channel Multiplexed ANAlog Signal (MANAS) processor chips, collect signals from detector through flexible kapton cables. Then these signals are processed and digitized in Multi Chip Module (MCM) and send to the Translator Board (TB) via back plane. After that the signals are transferred to the Cluster ReadOut Concentrator (CRO-

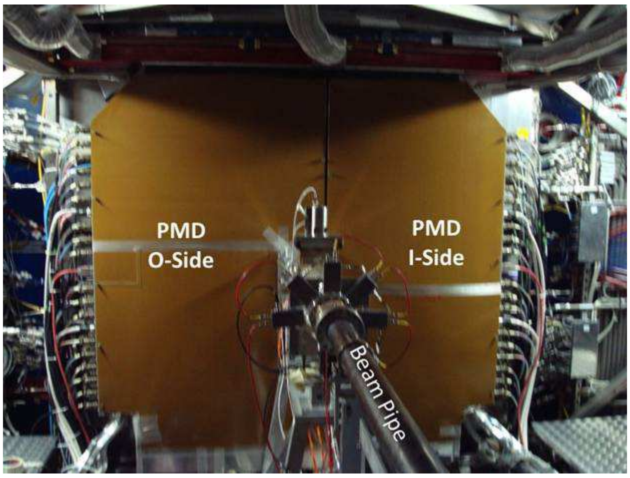

Figure 3.6. Picture of the PMD (looking towards the IP) as installed in the ALICE experiment at the CERN-LHC.

CUS) system via Patch Bus (PB) cables. Further, from the CROCUS signals are transferred to the PMD DAQ via DDL. The PMD DAQ is then connected to the main DAQ of the ALICE detector.

Some of the important electronic components of the PMD readout are discussed in details below:

FEE Board: The FEE board of PMD consists of four MANAS chips, two serial 12 bit Analog to Digital Convertors (AD7476), two inverting buffer amplifiers and a custom built ASIC called Muon Arm Readout Chip (MARC). A schematic circuit diagram of the PMD FEE is shown in Fig. 3.7.

The design of the MANAS chip is based on the GLASSIPLEX with useful modifications like high-voltage isolation and a calibration capacitor on each channel. Fig. 3.8 shows all the components of the MANAS chip. It is designed and fabricated by the Indian team of the ALICE experiment. It has sixteen input channels and one output channel. The main components of the MANAS chip are Charge Sensitive Amplifier (CSA), Deconvolution Filter (DF), Semi Gaussian Shaper (SGS), Track/Hold and the analog multiplexers. The CSA collects the charge from the anode wire and integrate using its feedback capacitor. The DF removes this long tail in the signal produced due to slow motion of the charge and ensure the

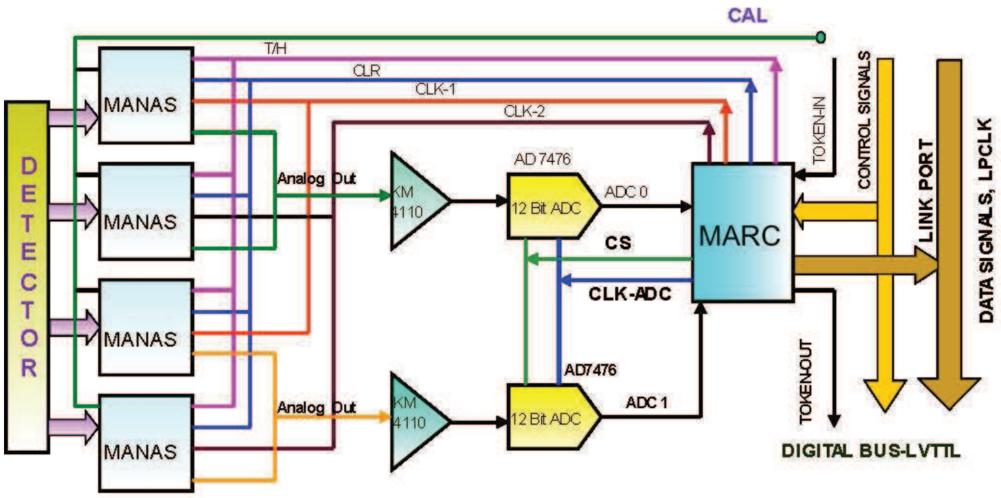

Figure 3.7. A schematic diagram showing the circuit of the PMD-FEE board.

base line restoration. The SGS shapes the pulses to Semi Gaussian shape which is essential to avoid pile up. It improves the signal-to-noise ratio and ensures faster base line restoration. To ensure the maximum charge collection, the time constant of the SGS is kept large. A properly timed Track/Hold pulse opens the switch at the instant when the peak of the input signal arrives. The analog multiplexer has 16 switches and the outputs from all these switches are connected together to form a single output from the chip. The switches are controlled by clock (CLK) signals.

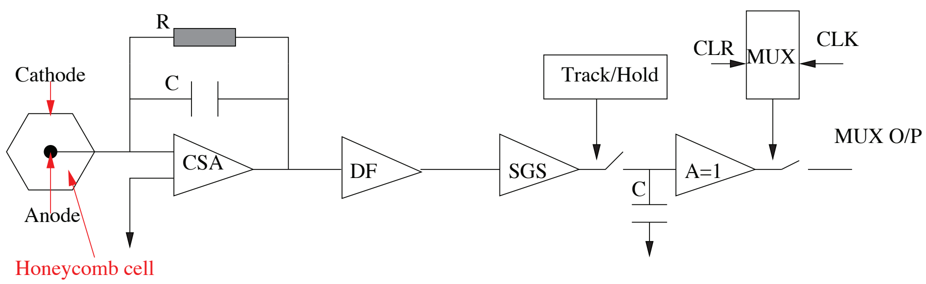

Figure 3.8. A circuit diagram of MANAS chip with its all components

Since ADCs accept only positive signals, so two buffer amplifiers are used in FEE board to invert signals (collected from the detector) from negative to positive. Then output analog signal from MANAS chip is converted to digital signal using ADCs. The ADCs are 12-bit serial ADCs with analog input range of 2.5 V and digitizing the signal at the speed of 1 Million Sample per second. Then the digitized output signal is sent to the MARC. The MARC is a custom-built ASIC, which controls four MANAS chips, 2 two serial 12-bit ADCs and performs zero suppression on data.

Translator Board (TB): The TB receives signal from FEE board which are Low Voltage Transistor Transistor Logic (LVTTL) type signals . It converts all the LVTTL type signals to Low Voltage Differential Signals (LVDS) before sending to the CROCUS and also translates all the LVDS signals from CROCUS to LVTTL.

Patch Bus Cables: A flexible flat and twisted pair cables, known as PATCH BUS cables, are used to transfer the LVDS signals from TB to CROCUS and vies-versa. It is a halogen free forty core cable with 1.27 mm pitch 40-pin female type SAMTEC connectors at both ends. To minimize the electromagnetic disturbances, the cable is covered with aluminium tapes. The PMD uses 200 patch bus cables with the length of 8.5 m for the readout.

CROCUS: The Cluster Read Out Concentrator Unit System (CROCUS) is one of the important readout electronic components of the PMD. It gathers and concentrates the signals from the FEE board through patch bus cable and transfers to the DAQ. It receives and distributes the trigger signal to the detector and allows the calibration. It also detects the breakdown in the data acquisition chain. There are total four CROCUSs to control all the chains in the PMD. Two of them are connected to two halves of the Preshower plane and the rest two are connected to two halves of the CPV plane. The CROCUS consists of one Concentrator Board (CRT) and five Frontal Boards (FRTs). The FRTs has two DSPs to mange the FEEs via patch bus cable. These concentrate Level-I data, which is coming from FEEs and transfer the data to Level-II data concentration crocus system. The FRTs also send the calibration signal to the detectors. The main objectives of the CRT are the data acquisition from the FRTs and distribution of the trigger signal to them.

Multi Chip Module (MCM): The MCM is composed of four MANAS chip, an ADC and a complete custom designed digital processor chip called Muon Arm Readout Chip (MARC). The function of the MCM is to collect signals from 64 cells, ADC conversion through charge amplifiers/shapers, convert the data into digital values, pedestal subtraction, and transmission to the Digital Signal Processor (DSP) through digital local buses. The bus is of single-master multi-slave configuration. These buses communicate bi-directionally between the DSP and the MCM. In one direction it allows the downloading of parameters such as threshold and individual pedestal values for each channel into the MCMs and in the other direction, the MCMs communicate the zero-suppressed readout data and status information to the DSPs. A maximum 24 MCMs can be connected to a bus.

Digital Signal Processor (DSP): Several buses run through each chamber, making the data available to the DSP boards, which are located on the edge of the detector. Each DSP board is connected to a DDL card for onward transmission of the data to the ALICE DAQ system.

The details of the hardware implementation and protocol can be found in Ref. [101].

3.2.3 Working Principle

The ALICE-PMD consists of two identical planes, the Charged Particle Veto (CPV) and preshower (PRE) plane with a three radiation length thickness ($3X_0$) Pb converter plate sandwiched between them. The schematic of working principle of PMD is depicted in Fig. 3.9.

When a photon is incident on PMD, it passes through the Pb convertor plate and produces an electromagnetic shower of photons, electrons and positrons by the combined effect of pair production and the bremsstrahlung emission [61]. Further, these shower particles hit the PRE plane and produce signals in several cells of the sensitive volume (Ar/CO_2) of the detector. On the other hand, most of the the charged hadrons affect only single

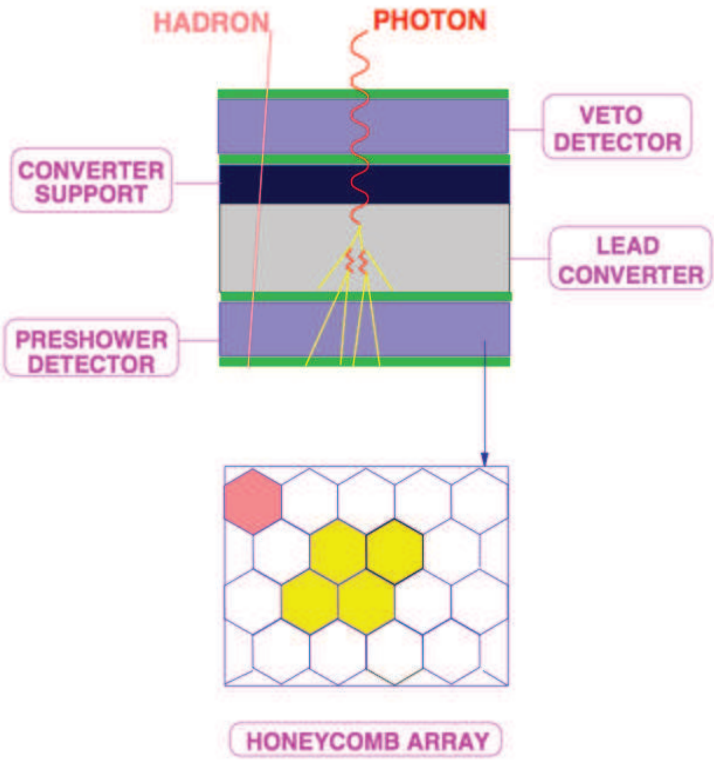

Figure 3.9. A Schematic showing the working principle of PMD [102].

cell and produce a signal representing Minimum-Ionizing Particles (MIP). The thickness of the Pb converter plate is kept $3X_0$, which is optimized to keep the conversion probability of photons high and the transverse shower spread small to minimize the shower overlap in the high-energy heavy-ion collisions [102]. The CPV plane, placed towards the IP acts as a veto for the charged particles in order to improve photon hadron discrimination. The schematic layout of ALICE-PMD is shown in Fig. 3.10.

3.2.4 The Physics Goals

The important physics goals of PMD are the following:

- The collision energy and centrality or nucleon participants dependence of average photon multiplicity in forward rapidity region and limiting fragmentation behavior of photons.
- The photons, measured using PMD in forward rapidity can be used to

determine the reaction plane for the study of the azimuthal anisotropy and flow of the charged particles in midrapidity, which can be used to probe the thermalization of the medium formed in heavy-ion collisions.

- The photon measurement helps to study critical phenomena near the phase boundary which leads to fluctuations in global observables like multiplicity, mean transverse momentum and pseudorapidity distributions.

- Signals of chiral-symmetry restoration (e.g. disoriented chiral condensates) can be studied through the measurement of $N_\gamma/N_{\rm ch}$ in a common part of phase space.

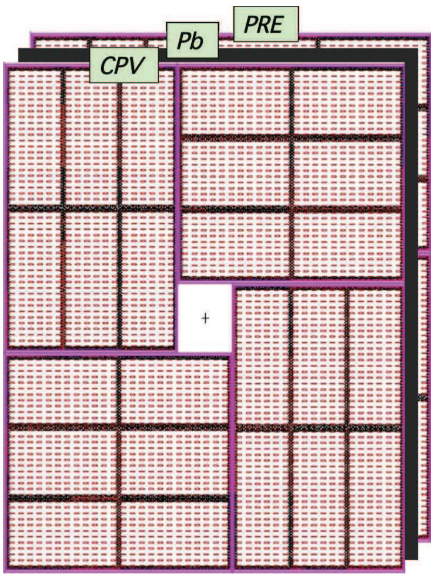

Figure 3.10. A Schematic layout of ALICE-PMD looking from IP.

3.3 The Analysis Details

In this section, we discuss step by step data analysis procedure for obtaining the multiplicity and the pseudorapidity distributions of photons in forward pseudorapidity region using the PMD in ALICE at the CERN for the Pb+Pb collisions at $\sqrt{s_{\rm NN}}$ = 2.76 TeV. The flowchart showing simulation framework and data flow of the PMD is shown in Fig. 3.11.

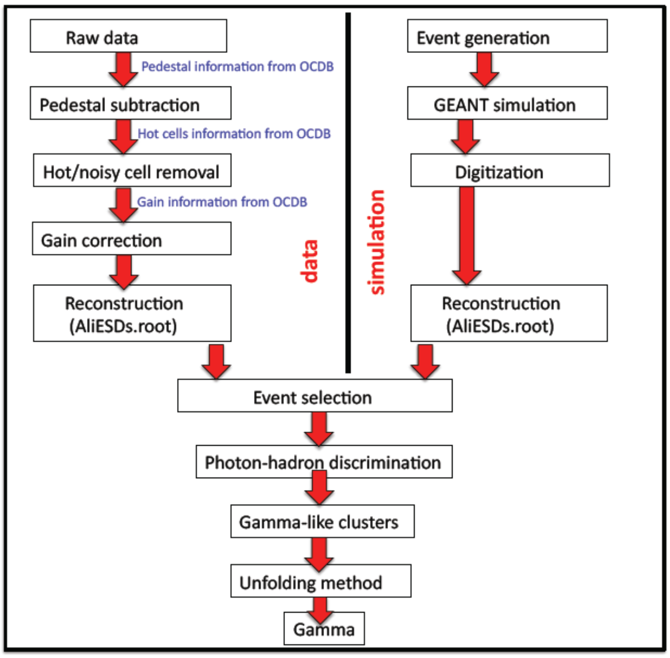

Figure 3.11. The flow chart showing all the steps involved in the data analysis.

3.3.1 Datasets and Event Selection

In this data analysis, we use the data taken by the PMD in 2010 for Pb+Pb collisions at $\sqrt{s_{\rm NN}} = 2.76$ TeV. The data set is chosen such a way that the acceptance of the PMD is same for all the runs. The simulation data having same acceptance as the corresponding experimental data sets are called anchor runs. But for this analysis we use simulation data with full PMD geometry. The details of the data sets used in the analysis are given in Table 3.1.

Table 3.1. Details of the data set used in the analysis

Collision system	Pb+Pb
Collision energy	$\sqrt{s_{\rm NN}} = 2.76$ TeV
Data sets	LHC10h
Vertex cut	$-10 < V_z(\rm cm) < 10$
Simulation data set	LHC11a10a_bis (using HIJING event generator)

3.3.2 Zero Suppression

After the collision, if a valid trigger condition is generated, the analog signals from the detector are digitized and temporarily stored in a shift register available with the FEE. Then these signals are compared with the threshold value stored earlier. The recording is performed for the data having values above the threshold value. This process is known as *zero suppression*. The main purpose of recording zero suppression data is to reduce the data volume by rejecting the noise and baseline data. We record zero suppression data for the PMD for further processing.

3.3.3 Pedestal Subtraction

The output in terms of ADC for each channel number is obtained from the FEE boards without any signals at the MANAS inputs, are termed as pedestal and corresponding run is called *pedestal run*. While recording the raw data from PMD we do not subtract the pedestal, therefore, before doing any analysis on raw data, the pedestal must be subtracted from raw data. A dedicated pedestal run is taken in absence of beams and data is stored in the Offline Conditioned Data Base (OCDB). The pedestal values are fetched from OCDB and subtracted from the real signals during the first pass reconstruction of the data. It helps to remove electronic noise from the real data. It is found that the pedestal of each channel is reasonably stable ($\sim$250 ADC) with a very small fluctuation (rms = $\sim$ 1). In the present analysis a value "mean + 5 $\times$ rms" is used for pedestal subtraction.

3.3.4 Data Cleanup (Noisy/Hot Cell Removal)

The cells having very high hit frequency and low ADC value as compared to other nearby cells are known as *hot or noisy cell*. To get clean data for physics analysis, these cells have to be removed before the reconstruction pass. The hit frequency of each cell of a module (*e.g.* module 22) before the hot cell cleanup is shown in Fig. 3.12(a). One can see that there are few cells which show quite high number of hits as compared to the other normal cells. Due to these hot cells some spikes are found in the lower ADC values of the ADC distribution (shown in Fig. 3.13(a)).

A method, based on the fact that the particle density is uniform over full-ϕ for a small η-ring is used to identify and reject hot cells. The steps are as following:

- Read raw data.
- Divide the full η-coverage (2.3 - 3.9) of PMD into small slices.
- Plot a hit distributions of cells for each of the η rings.
- Fit a Gaussian function to each of the distribution.
- Obtain mean and root-mean-square (rms) of the Gaussian function
- Determine a cut-off value on number of hits for the given η-ring. In the present work we use "mean + constant $\times$ rms", where value of *constant* is optimized to get threshold.
- Declare the cells as "*hot cells*", which have the number of hits above the threshold value.
- Store row and column information of these hot cells in the OCDB.
- Repeat the exercise for each η-ring and reject all hot cells.

The hit frequency and ADC distribution after the hot/noisy cells removal are shown in Fig. 3.12(b) and Fig. 3.13(b) respectively. It can be seen clearly that the ADC distribution looks reasonable once these hot cells are removed.

3.3.5 Gain Correction

PMD is a highly granular detector with a large number of cells with 0.23 cm^2 cross section and 0.5 cm depth. Ideally all the cells in PMD

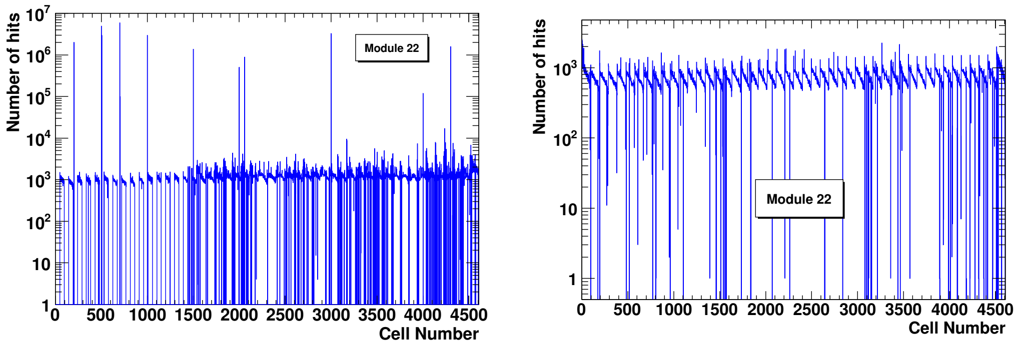

(a) (b)

Figure 3.12. ADC distribution of the same module (module 22): (a) Number of hits of all the cells for a particular module before hot/noisy cells removal. Spikes indicate the hot cells. (b) Number of hits of all the cells for a particular module after hot/noisy cells removal.

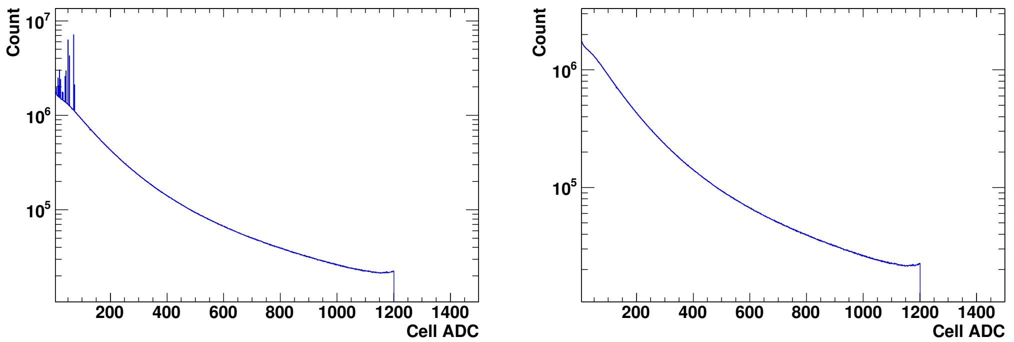

(a) (b)

Figure 3.13. ADC distribution of the same module (module 22): (a) before the hot cells removal (b) after the hot cells removal.

are kept uniform *i.e.* similar geometry and similar size. Therefore, One would expect to get a similar response from all the cells, when a particular set of particles of a given energy are allowed to pass through them. However, in the real situation, cells are not exactly same in geometry and size. At microscopic level they may differ from ideal situation and also gas distribution may also be non-uniform for all the cells. It is also observed that the gain of each cell in their associated electronics is not same. Therefore, these factors as a whole, make the detector response non-uniform or in other words we call it non-uniform gain. The gain of four different modules are shown in Fig. 3.14. One can see that cell-to-cell gain variation in a module is more than 20%. Therefore, gain normalization is needed to make detector response uniform in order to compare with the simulation

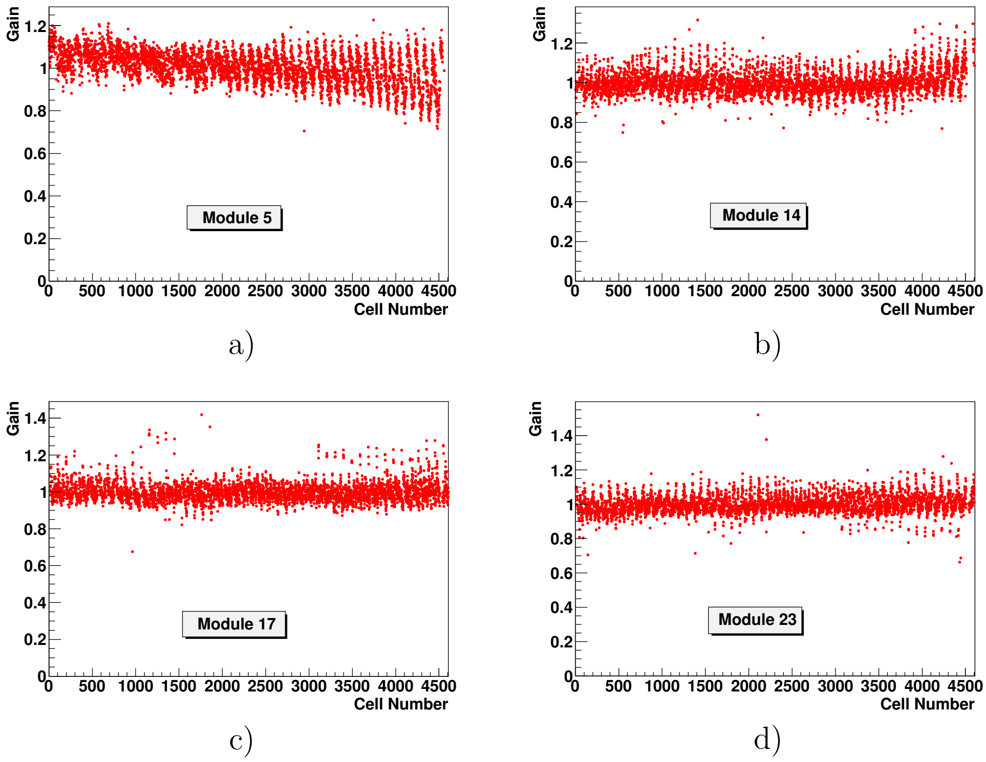

Figure 3.14. Gain of PMD modules without correction.

results.

A method for the gain normalization, being well tested and already used in STAR at RHIC, has been adopted in ALICE. The method is based on the observation and the fact that the MIPs mostly affect only one cell and deposit a minimum amount of energy while passing through honeycomb proportional counters of the PMD. The ADC distribution of the each *isolated cell* is well explained by the Landau-distribution (see Fig. 3.15). The isolated cell is defined as a cell which records hits but none of its six neighbors records any hit. These cells are assumed to be from MIPs. An isolated cell is shown pictorially in Fig. 3.16.

Ideally, the parameters of the Landau distribution are expected to be uniform for all cells. In this method, one tries to normalize these parameters. The various steps for implementation of the adopted procedure is as following:

- Read the raw data and find out the isolated cells.

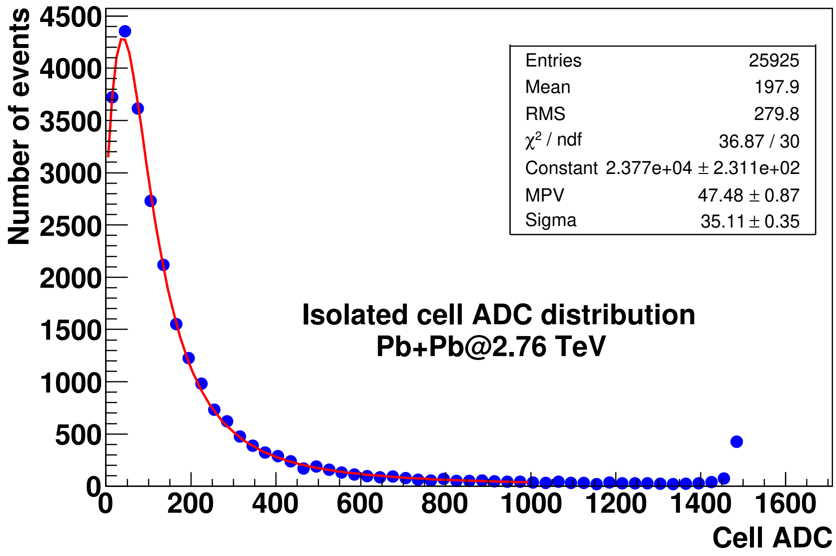

Figure 3.15. The isolated cell ADC distribution for one of the cells in module 10 of PMD preshower plane in Pb+Pb collisions at $\sqrt{s_{\mathrm{NN}}}$ =2.76 TeV. The distribution is fitted with Landau function.

- Plot ADC distribution of one of the isolated cells of a module and fit it by Landau distribution.
- Plot ADC distribution of a module taking into account all the isolated cells in that module and fit it by Landau distribution.
- Determine the mean ADC for each isolated cell.
- Determine the mean ADC for that particular module.
- Calculate the correction factor by the following formula

$$\text{Gain factor} = \frac{\text{mean ADC for the isolated cell}}{\text{Mean ADC of the module with all isolated cells}}$$

- Export the gain factors to the OCDB for later use during the reconstruction.

An estimate has been made from simulation data, that around 2.5k events are needed in Pb+Pb collisions at $\sqrt{s_{\mathrm{NN}}} = 2.76$ TeV, so that each cell will have reasonable statistics as an isolated cell and the statistically significant gain factors can be obtained.

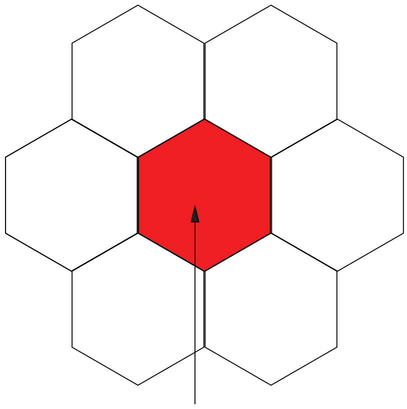

Figure 3.16. A pictorial representation of an isolated cell.

3.3.6 Photon Reconstruction

After pedestal subtraction, removal of hot/noisy cells and gain normalization, the raw data are processed to perform further reconstruction. The photon reconstruction proceeds in two steps: first clustering of all the hits in PMD and then photon-hadron discrimination.

Clustering Algorithm

A number of continuous cells with non-zero ADC are termed as clusters. This type of clusters are known as superclusters and are separated by the cells having zero ADC. During the reconstruction of raw data, the clustering of cells are done via a clustering algorithm [103]. This clustering algorithm is used in $p + p$ collision, where low occupancy is observed and named as a *crude clustering*. These superclusters themselves can be identified as the particles (charged particles or photons) falling on the PMD. However, in the high multiplicity environment such as Pb+Pb collisions particle density is very high. Therefore, there is a finite probability of merging of cluster resulting into bigger superclusters consisting of a large number of cells. Therefore, to identify the particles, superclusters need to be divided into smaller clusters which are called *refined clusters* and the method is called refine clustering.

The cluster contains various information such as the ADC of the cluster summing over all the cells of the cluster, number of cells contained in the cluster, the position of the clusters (x, y, z) in the global coordinate system with respect to the nominal interaction point etc. Both photon and charged particle make cluster, therefore an algorithm is used to discriminate the photons from the hadrons, discussed in the next section.

Photon-Hadron Discrimination

For an incident photon, the cluster size (total number of cells in the cluster) is larger and the cluster ADC is higher as compared to the cluster size and cluster ADC corresponding to an incident hadron. Using these two cluster properties, we put a suitable threshold on cluster size and cluster ADC to reject hadrons from the data sample. so that most of the hadrons can be rejected from the data sample.

There is another method that one can use for photon-hadron discrimination. This method is based on the use of the hit information from the CPV plane of the PMD. As we discussed earlier, CPV records one hit for hadrons while no hit for photons. A combination of CPV and preshower plane shows that for a hadron track, there is back-to-back hits in CPV plane and preshower plane along z-direction, whereas for a photon track, corresponding to cluster of many cells on the preshower plane there is no hit on the CPV plane. Using these properties photons and hadrons are identified. The performance of the method is studied using the simulated data and can be found in Ref. [104]. However, due to a very limited coverage of CPV in the data sets used in the present analysis, this method is not applied rather we adopted the method discussed earlier.

After the photon-hadron discrimination, the clusters in the photon rich sample are known as gamma like clusters (γ_{like}). However, this sample contains some hadrons as well and some of the incident photon clusters are missing. Therefore, even after applying the threshold, there is a possible contamination from the non-photon clusters and there is a loss of photon clusters. The corresponding factors are obtained using simulated data for correcting the final photon multiplicity in data from such kind of effects.

3.3.7 Event Selection and Data Quality Checks

The next important step is to select good events for analysing data. It is observed that the reconstructed position of the Z-vertex is not exactly at the nominal IP. Fig. 3.17 shows the distribution of the Z-position of the reconstructed vertex in Pb+Pb collisions at $\sqrt{s_{\rm NN}} = 2.76$ TeV, which corresponds to the observed longitudinal size of the interaction regions along the beam axis. The Z-position of the vertex is important because the change in vertex Z-position will change the pseudorapidity coverage of the detectors. For the present analysis we have selected all the events having Z-vertex position within ± 10 from the IP.

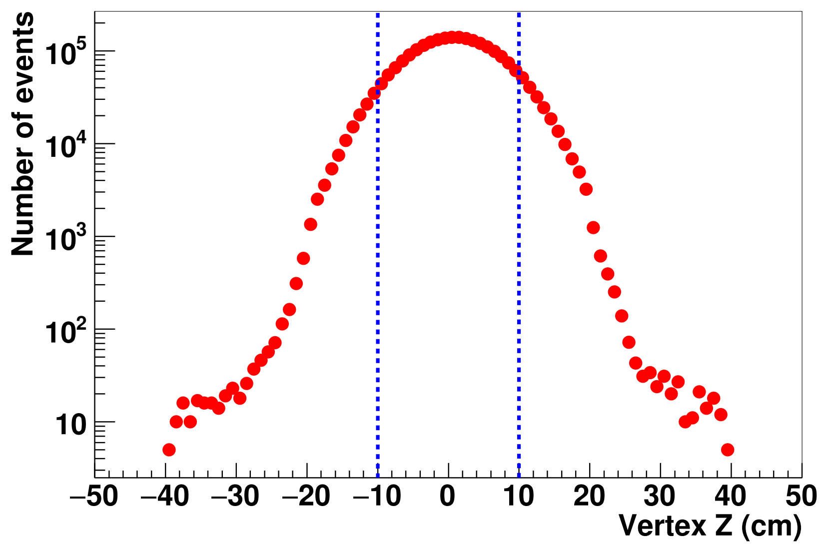

Figure 3.17. Z-vertex distribution in Pb+Pb collisions at $\sqrt{s_{\rm NN}} = 2.76$ TeV. The dotted lines indicate the selection of the Z-vertex used in the analysis.

Fig. 3.18 shows the position of the hits on the PMD preshower plane. The numbers shown in the figure correspond to the module number. Each coloured ring resembles to a η bin of bin width $\Delta\eta = 0.2$. Smaller ring corresponds to higher η bin, *i.e.* first bin corresponds to $2.3 < \eta < 2.5$. The areas showing no hits correspond to the non-functional and uninstalled part of the PMD. The acceptance correction in pseudorapidity distributions of photons is performed for non-functional part of the PMD.

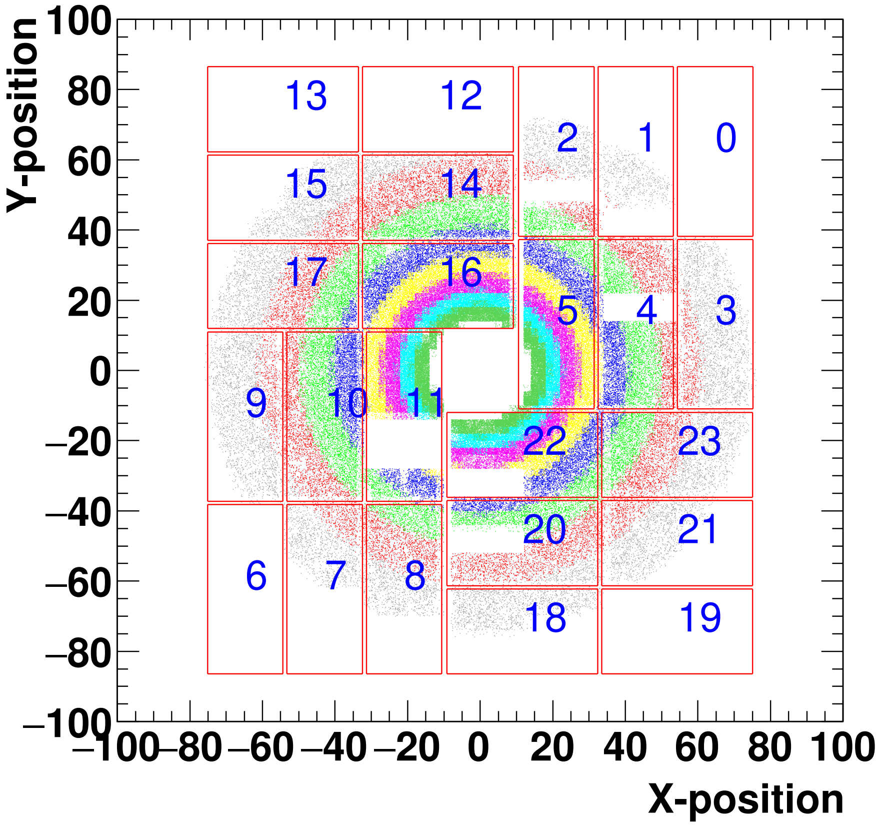

Figure 3.18. X-Y display of hits of the preshower plane of PMD for the experimental data for Pb+Pb collisions at $\sqrt{s_{\rm NN}} = 2.76$ TeV. Different boxes represent different modules and numbers shown in the boxes are the module numbers. The colored angular rings correspond to different resign in η.

We also study the correlation between the $\gamma_{\rm like}$ multiplicity measured in PMD ($N_{\gamma\rm like}^{\rm PMD}$) and raw multiplicity of charged particles measured in V0A ($2.8 < \eta < 5.1$) denoted by $N_{\rm ch}^{\rm V0}$ and FMD ($1.7 < \eta < 5.0$) named as $N_{\rm ch}^{\rm FMD}$ in Pb+Pb collisions at $\sqrt{s_{\rm NN}} = 2.76$ for eight different centralities. Different colors correspond to different centralities starting from 0-5% to 70-80%. For this study we use the common pseudorapidity coverage, $2.3 < \eta < 3.9$, of these detectors. Fig. 3.19 and Fig. 3.20 show the correlation of $N_{\gamma\rm like}^{\rm PMD}$ with $N_{\rm ch}^{\rm V0}$ and $N_{\rm ch}^{\rm FMD}$, respectively. The V0A and FMD detectors are positioned in front of PMD. Although these multiplicities are at raw level without any corrections, nevertheless a reasonable correlation is seen. Here different color corresponds to different centralities as mention in the legend.

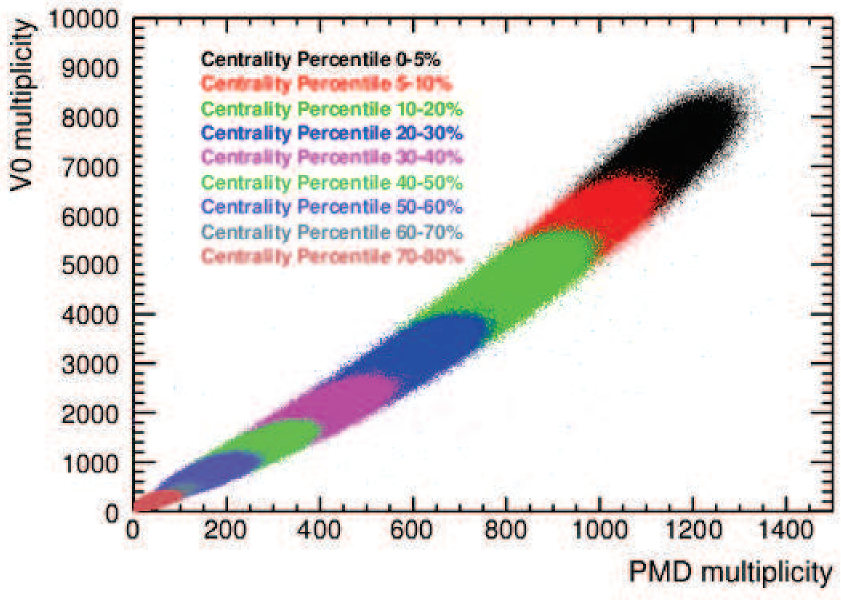

Figure 3.19. PMD raw multiplicity vs. V0 raw multiplicity.

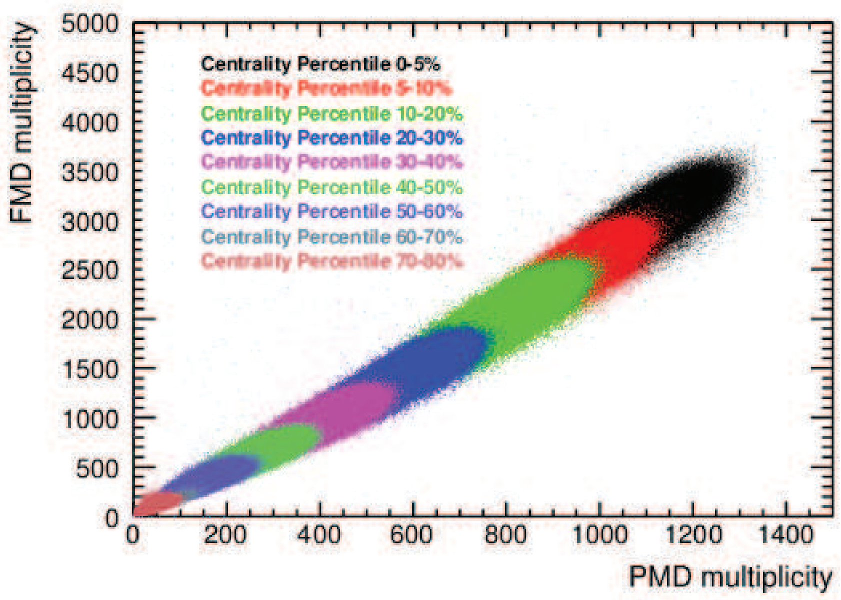

Figure 3.20. PMD raw multiplicity vs. FMD raw multiplicity.

3.4 Efficiency and Purity Correction

The efficiency (ϵ_γ) of the photon detection using PMD detector is defined as the ratio of the number of photons detected above the discrimination threshold ($N^{\rm th}_{\gamma {\rm like}}$) within a given coverage to the number of incident photons ($N^{\rm inc}_{\gamma}$) within the same coverage:

$$\epsilon_\gamma = \frac{N^{th}_{\gamma like}}{N^{inc}_\gamma}, \tag{3.1}$$

The purity ($\mathrm{f_p}$) is defined as the ratio of the number of photons detected above the discrimination threshold (N^{th}_γ) to the $N^{\mathrm{th}}_{\gamma\mathrm{like}}$ within the same coverage:

$$f_p = \frac{N^{th}_\gamma}{N^{th}_{\gamma like}}, \tag{3.2}$$

where N^{th}_γ is the number of the photon detected in PMD above photon-hadron discrimination threshold. Using the estimated values of $\mathrm{f_p}$ in simulation, we obtain the number of photons incident on the detector (N_γ) by the following relation:

$$N_\gamma = N^{th}_{\gamma like} \times \frac{f_p}{\epsilon_\gamma}, \tag{3.3}$$

A Monte Carlo simulation is performed using HIJING event generator for Pb+Pb collisions at $\sqrt{s_{\mathrm{NN}}} = 2.76$ TeV. Then the produced particles are passed through the detector framework package GEANT3 to incorporate full ALICE detector framework. The correction parameters, ϵ_γ and $\mathrm{f_p}$ are estimated for eight different centralities in Pb+Pb collisions at $\sqrt{s_{\mathrm{NN}}} = 2.76$ TeV. Fig. 3.21 and Fig. 3.22 show the pseudorapidity dependance of ϵ_γ and f_{p} for eight different centralities. The values of ϵ_γ and f_{p} depend on the selected discrimination threshold. The effect of the change of discrimination threshold on the pseudorapidity and multiplicity distributions of photons can be taken as systematic uncertainties. The present study is done for various discrimination thresholds but not all of the plots are shown here. The study for two different discrimination threshold (cluster ADC > 432 and cluster ncell > 2 and cluster ADC > 648 and cluster ncell > 2) are shown in here.

As mentioned earlier, ϵ_γ and f_{p} varies with discrimination threshold.

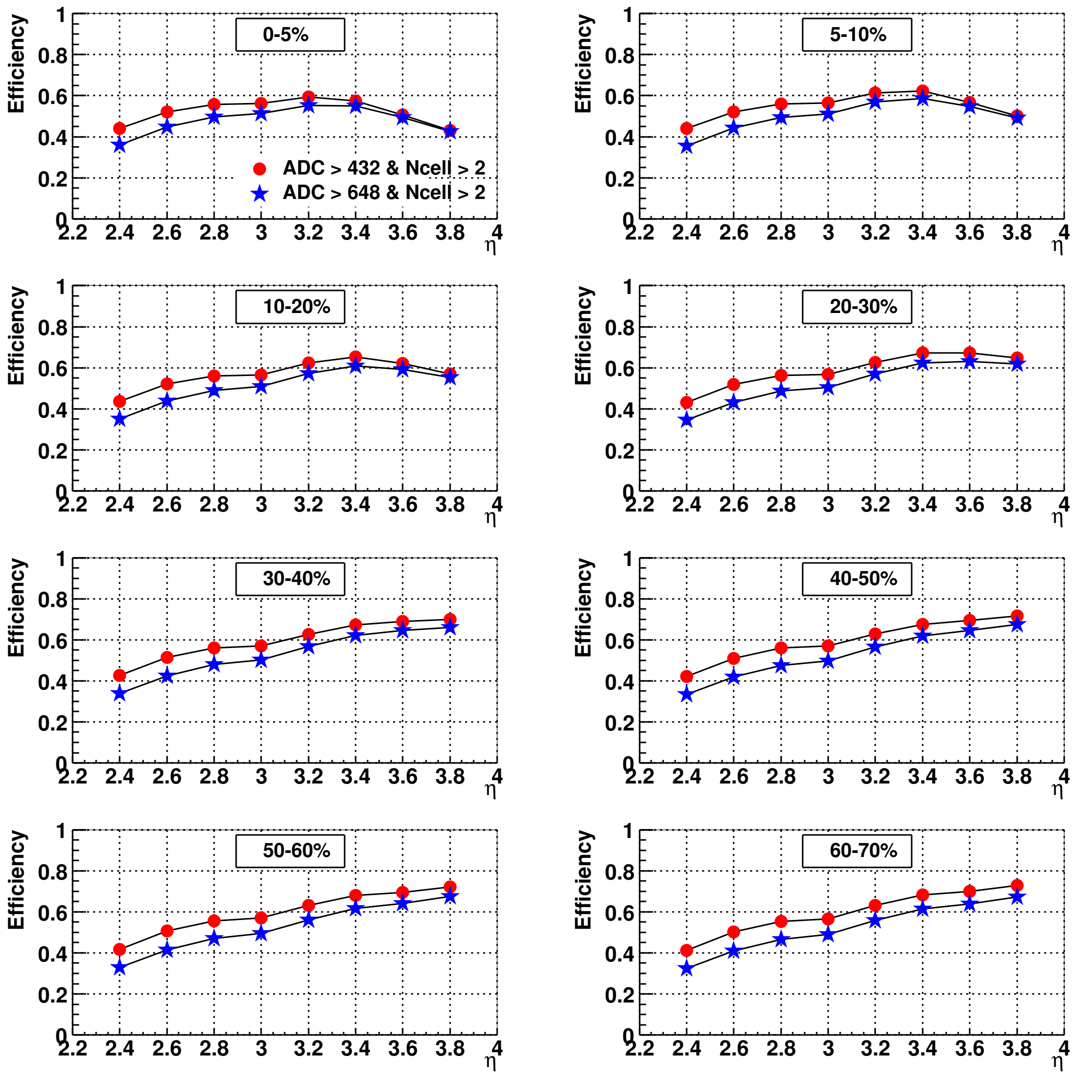

Figure 3.21. The PMD efficiency for eight different centralities with two different photon-hadron discrimination thresholds.

It is found that as we move towards tight discrimination threshold the efficiency decreases and the purity increases at all values of η. Therefore, the discrimination threshold needs to be optimized such that one gets a reasonably pure sample but at the same time the efficiency should not be very low. Results for two discrimination threshold are shown in Fig. 3.21 and 3.22.

For the further study, we use above mentioned discrimination thresholds: ADC $>$ 432 and cluster ncell $>$ 2; and ADC $>$ 648 and cluster ncell $>$ 2. The corresponding results on pseudorapidity and multiplicity distributions are shown in the following sections.

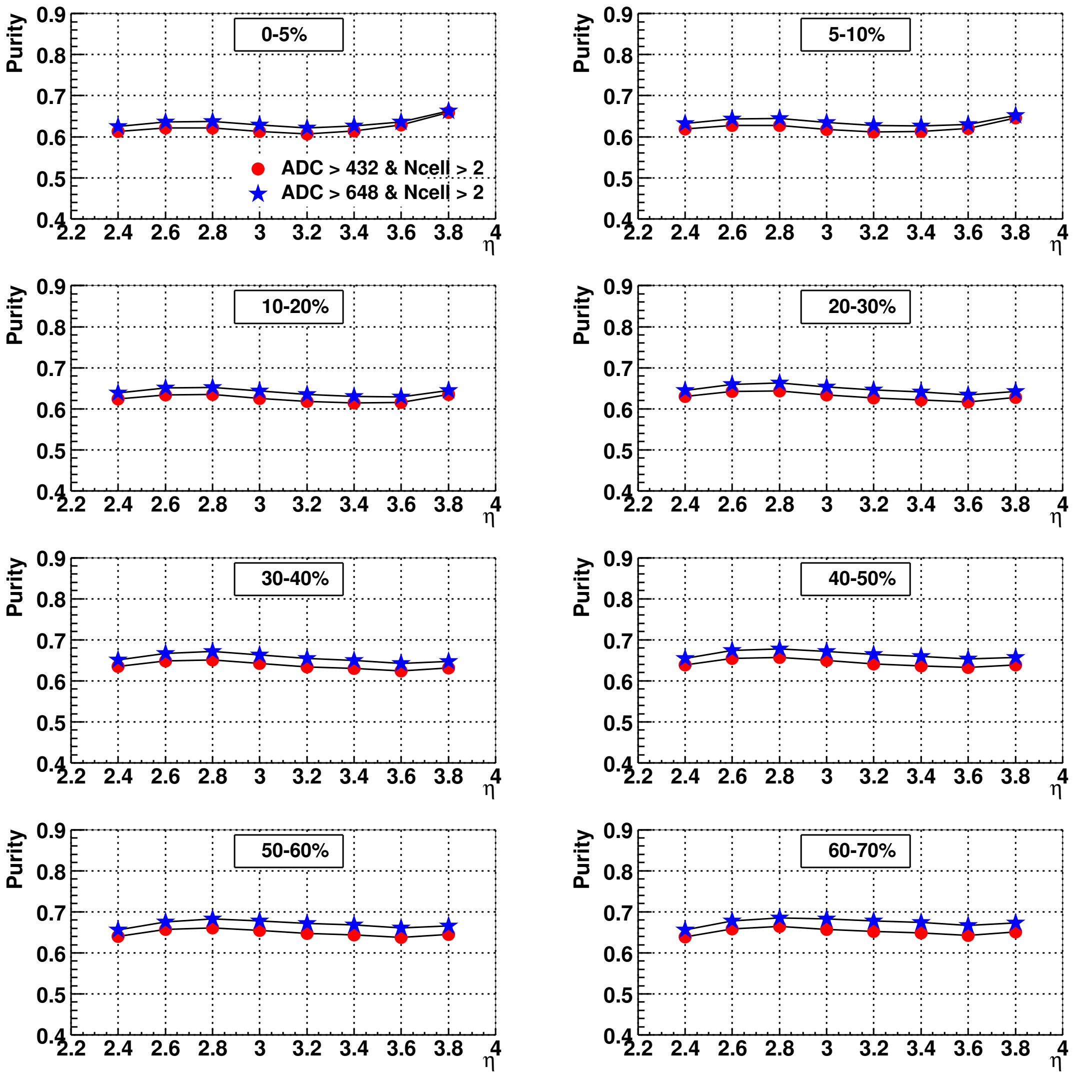

Figure 3.22. Purity of photon sample for eight different centralities with two different photon-hadron discrimination thresholds.

3.5 Results on Pseudorapidity Distribution of Photons in Pb+Pb Collisions at $\sqrt{s_{\rm NN}} = 2.76$ TeV

In this section we study the variation in particle density with η for eight different centralities. Fig. 3.23 and Fig. 3.24 show the uncorrected and corrected $dN_\gamma/d\eta$ distributions in Pb+Pb collisions at $\sqrt{s_{\rm NN}} = 2.76$ TeV, respectively. It is observed that the photon yield increases with decrease in η, *i.e.* more photons are produced at lower emission angle. We also observe

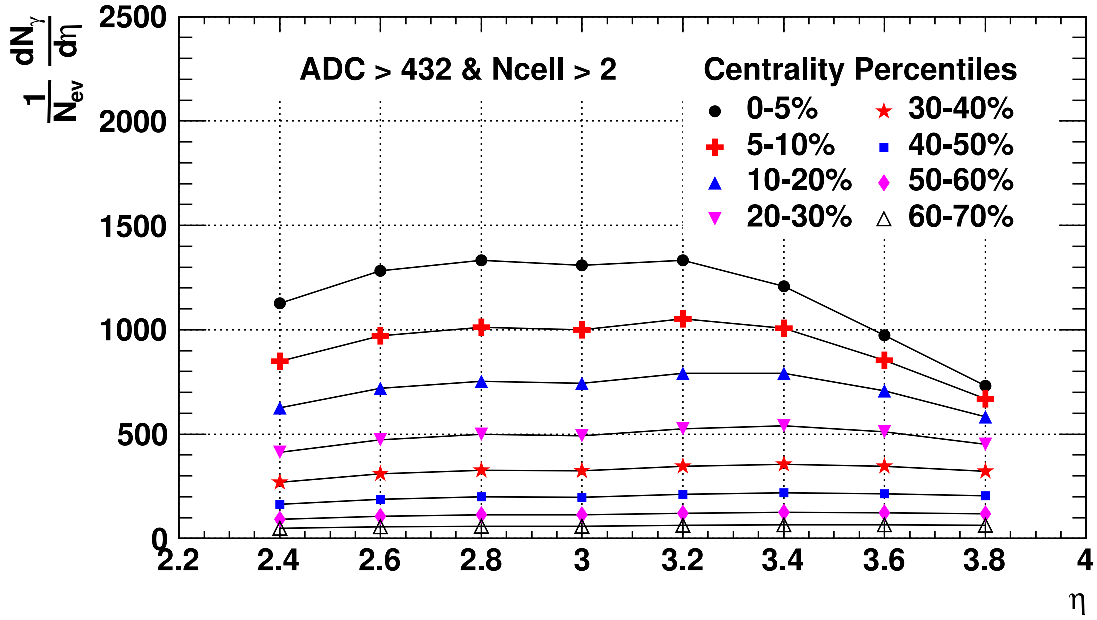

(a)

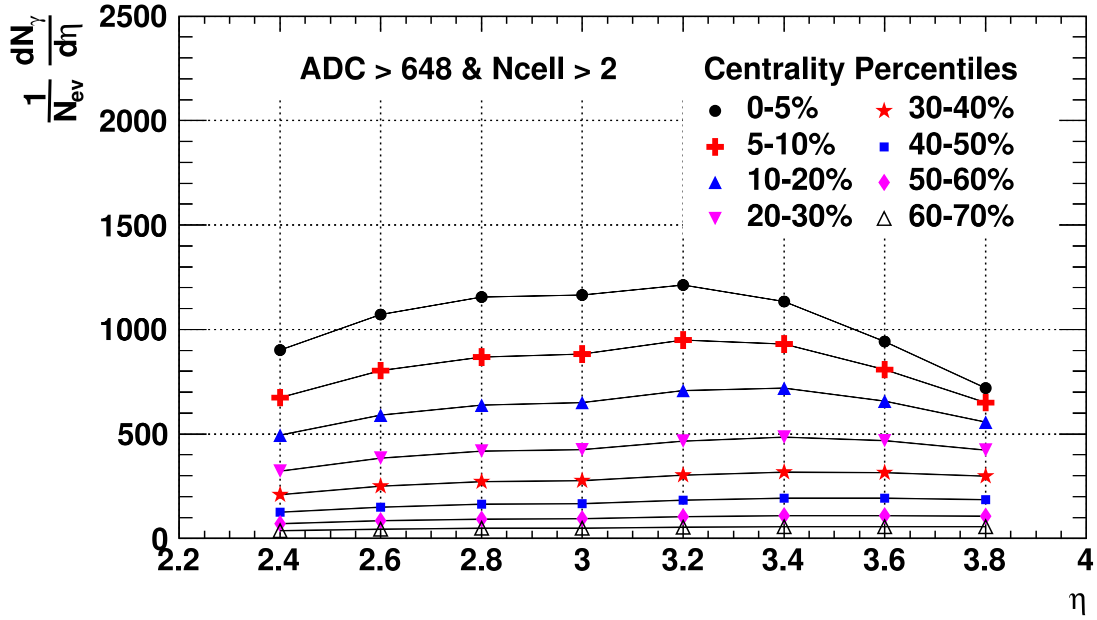

(b)

Figure 3.23. Uncorrected pseudorapidity distributions of photons for two different thresholds: (a) ADC > 432 and Ncell > 2. (b) ADC > 648 and Ncell > 2.

that $dN_\gamma/d\eta$ shows an increase from peripheral to central collisions. The HIJING model predictions for the most central collisions is also shown for comparison with the data.

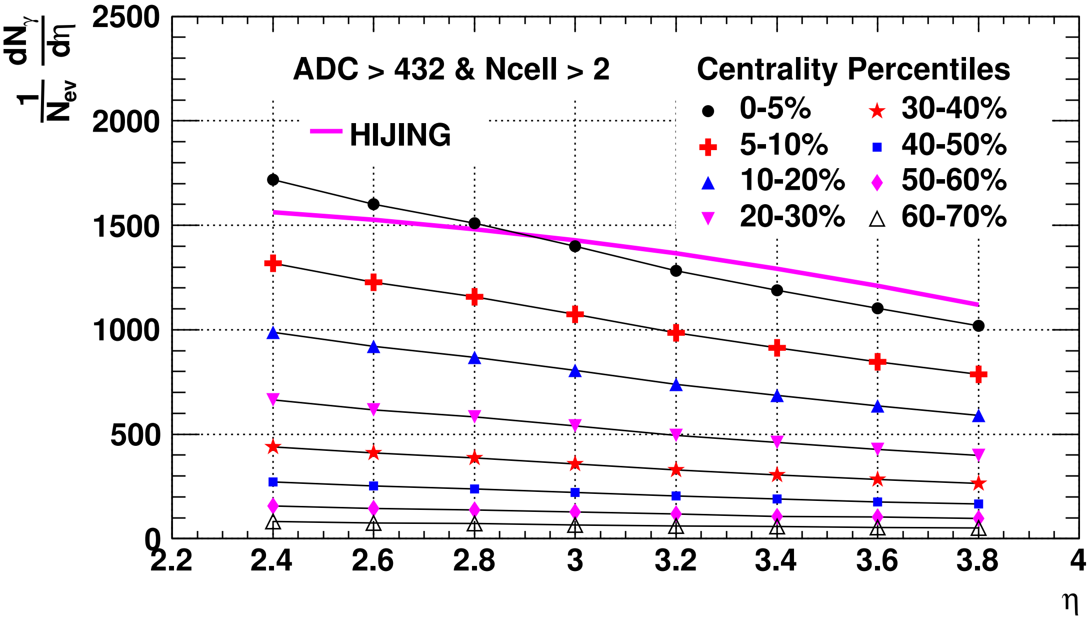

(a)

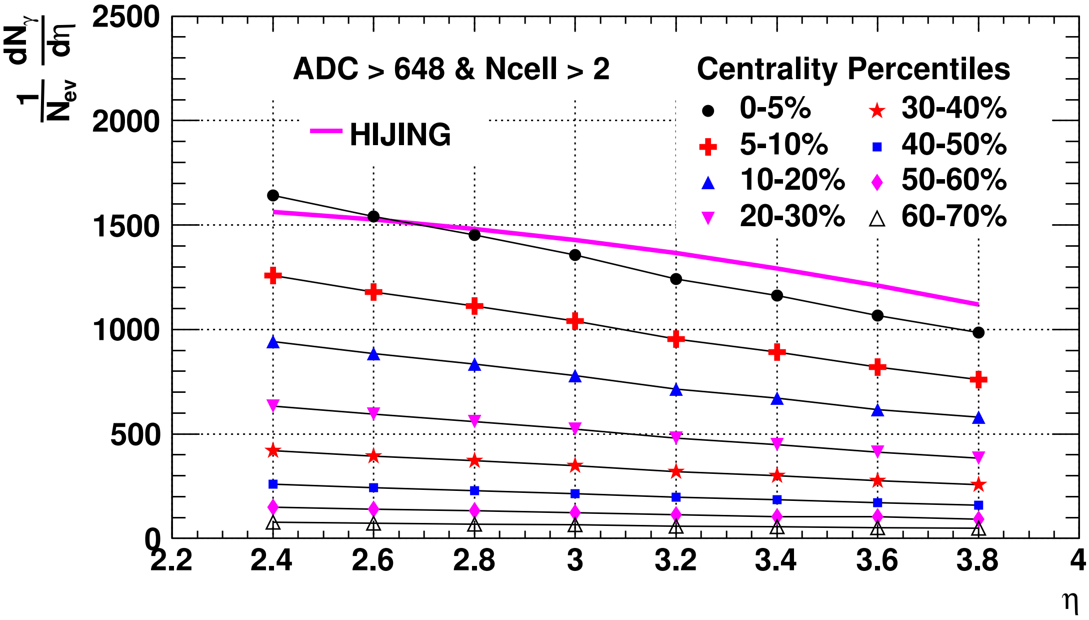

(b)

Figure 3.24. Efficiency-purity corrected pseudorapidity distributions of photons for two different thresholds: (a) ADC > 432 and Ncell > 2. (b) ADC > 648 and Ncell > 2.

3.5.1 Limiting Fragmentation Behavior of Photons

The particle production process in the higher rapidity region is subject of interest in terms of hypothesis of Limiting Fragmentation [105]. According to this hypothesis, in the frame of the target, the projectile hadron looks like a Lorentz contracted disk. When this Lorentz contracted projectile passes through the target, it may break up into fragments. If one assumes that the total hadronic cross sections become constant at large c.m. energy, then the excitation and break-up of a hadron would be independent of the c.m. energy and the observed pseudorapidity density of particle as a function of $\eta' = \eta - y_{\text{beam}}$ would approach a limiting value in the fragmentation region even if the colliding energy is increased. Here $y_{\text{beam}} = \ln(\sqrt{s_{\text{NN}}}/m_p)$ is a beam rapidity. Since total hadronic cross-sections are not constant at high energies, therefore, it is expected that limiting fragmentation should fail at higher collision energies. However, limiting fragmentation has been observed in a wider rapidity region, even extending nearly to midrapidity, and it is referred to as extended longitudinal scaling [106].

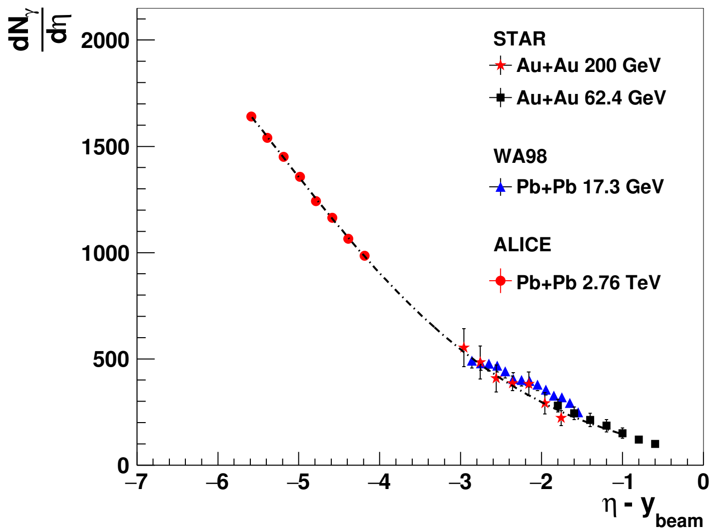

Figure 3.25. Photon multiplicity density per participant pair for different energies and collision systems are shown in the projectile rest frame. Line is the extrapolation for better visualization.

The normalized $dN_{\text{ch}}/d\eta$ per participant pair as a function of $\eta' = \eta - y_{\text{beam}}$ for different collision systems and different energies has been studied and found that charged particle follow limiting fragmentation scaling upto LHC energies. We study limiting fragmentation behavior of photons. In Fig. 3.25 we study $dN_\gamma/d\eta$ as a function of η' for Au+Au collisions at $\sqrt{s_{\text{NN}}} = 62.4, 200 GeV$ and Pb+Pb collisions at beam energy 158AGeV and

$\sqrt{s_{\rm NN}}$ = 2.76 TeV. $dN_\gamma/d\eta$ in Pb+Pb collisions at $\sqrt{s_{\rm NN}}$ = 2.76 seems to follow the limiting fragmentation behavior. The $dN_\gamma/d\eta$ data are available for a very small pseudorapidity coverage. Still, the nature of the $dN_\gamma/d\eta$ shows the longitudinal scaling behavior as consequences of limiting fragmentation.

3.6 Results on Photon Multiplicity in Pb+Pb Collisions at $\sqrt{s_{\rm NN}} = 2.76$ TeV

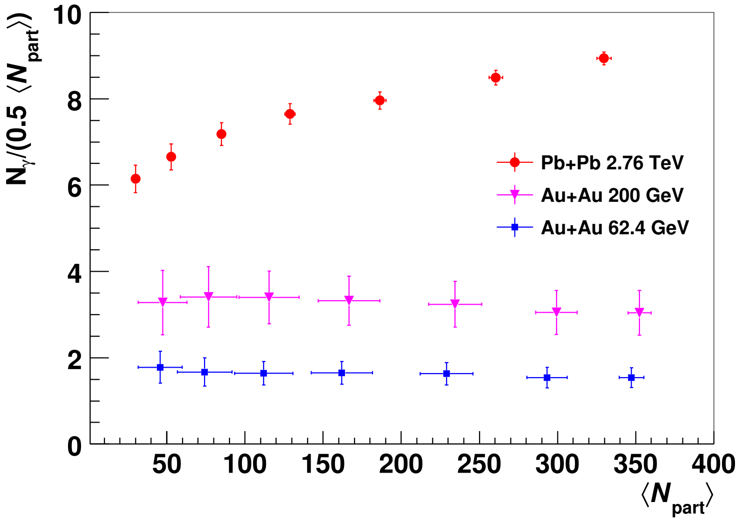

Figure 3.26. N_γ per participant pair as a function of $N_{\rm part}$

In Fig. 3.26, we show photon multiplicity per participant pair ($N_\gamma/(N_{\rm part}/2)$) as a function of collision centrality. One can see that $N_\gamma/(N_{\rm part}/2)$ in Pb+Pb collisions at $\sqrt{s_{\rm NN}}$ = 2.76 TeV shows a centrality dependent behavior in contrast to the centrality independent behavior of $N_\gamma/(N_{\rm part}/2)$ measured in Au+Au at 62.4 and 200 GeV in STAR experiment at RHIC. Here N_γ is the value of the total number of photon counted by the PMD in the pseudorapity coverage of $2.3 < \eta < 3.9$. This behaviour of N_γ is similar to what observed for charged particle measurements, and discussed and explained in chapter 5. For all the results shown in this chapter, systematic studies are not yet performed.

3.7 Summary

In summary, we have presented the results of inclusive photon production in Pb+Pb at $\sqrt{s_{\mathrm{NN}}}$ = 2.76 TeV using the Photon Multiplicity Detector at forward rapidity in ALICE. We have corrected the multiplicity density using efficiency-purity correction method to overcome the detector effects. The results are compared with HIJING model predictions, which give a reasonable description of experimental data. The energy dependence of the longitudinal scaling of inclusive photons has been studied, where photon measurement in Pb+Pb collisions at $\sqrt{s_{\mathrm{NN}}} = 2.76$ TeV using PMD ($2.3 < \eta < 3.9$) shown to follow limiting fragmentation behaviour. But due to the limited acceptance of the detector no firm conclusion can be made regarding the limiting fragmentation behavior of photons. The study of centrality dependance of N_γ is presented. $N_\gamma/(N_{\mathrm{part}}/2)$ measured by PMD in ALICE shows a centrality dependent behavior whereas measurements in STAR experiment show centrality independent behavior. This opens up new problems in understanding the RHIC vs. LHC photon production mechanism through the inclusion of new processes in the model study.

Chapter 4

Transverse Energy and Charged Particle Production in Heavy-Ion Collisions: From RHIC to LHC

The transverse energy and charged particle multiplicity are one of the key observables in characterizing the bulk properties of the matter created in heavy-ion collisions. Nuclei being extended objects, their collisions occur at various impact parameters and are characterized by collision centrality. The dependence of charged multiplicity and transverse energy on the collision geometry, *i.e.* on centrality and collision energy is of paramount importance to understand the particle production mechanism. The charge particle multiplicity provides important information on the initial entropy and its subsequent evolution in the hot and dense matter. This may give an insight to the partonic phase that might be created in heavy-ion collisions.

In this chapter, first we show the estimation of the number of nucleon and quark participants in a nuclear overlap model in a way done previously to study the global properties of matter created in heavy-ion collisions [42, 107], like transverse energy and charged particle multiplicity and the enhancement of multi-strange baryons in heavy-ion collisions [108]. We study the centrality and collision energy dependence of charged particle and transverse energy production at midrapidity. After finding out a universality in particle production, we give the prediction for the pseudorapidity density of charged particle multiplicity ($\frac{dN_{\rm ch}}{d\eta}$) and transverse energy ($\frac{dE_{\rm T}}{d\eta}$), and the barometric observable, $\frac{dE_{\rm T}/d\eta}{dN_{\rm ch}/d\eta}(\equiv \frac{E_{\rm T}}{N_{\rm ch}})$ at midrapidity, for Pb+Pb collisions at $\sqrt{s_{\rm NN}} = 5.5$ TeV. Possible physical reasons for the enhancement in $\frac{E_{\rm T}}{N_{\rm ch}}$ at LHC is discussed in the light of the proposed universality and gluon saturation picture.

4.1 Calculation of the Number of Participants

Here, nucleons are considered as superposition of constituent or "dressed" quarks (partons or valons). There are three constituent quarks per nucleon. Baryons are composed of three and mesons are of two such quarks. The concept of constituent quarks is well known [109–111] and was considered in the realm of the discovery of constituent quark scaling of identified particle elliptic flow at RHIC [112]. The constituent quark approach is successful in explaining many features of hadronic and nuclear collisions [113]. These include global properties like the charged particle and transverse energy density per participant pair [42, 107]. QCD calculations support the presence of three objects of size 0.1-0.3 *fm* inside a nucleon [114]. Furthermore it has been seen that nucleus-nucleus collisions and p+p collisions have similar initial states if the results are scaled by the number of constituent quark participants [52, 115, 116]. These observations also indicate that the particle production is essentially controlled by number of constituent quark pairs participating in the collision. In a constituent quark picture, nucleon-nucleon (NN) collision looks like a collision of two light nuclei with essentially one quark-quark (qq) pair interacting in the collision, leaving other quarks as spectators. These quark spectators form hadrons in the nucleon fragmentation region with a part of the entire nucleon energy being used for the particle production ($\sqrt{s_{\rm qq}} \sim \sqrt{s_{\rm NN}}/3$). Contrary, in AA collisions, due to large nucleus size and the higher probability of quark-quark interaction from same projectile and different target nucleons, more than one quark per nucleon take part in the interaction.

The calculations of the mean number of nucleon/quark participants are done using a Monte Carlo based implementation [117] of the nuclear overlap model [118]. In the nuclear overlap model, the mean number of nucleon participants, $N_{\mathrm{N-part}}$, in the collisions of a nucleus A and a nucleus B with impact parameter b is given by

$$\begin{aligned} N_{N-part,AB} = &\int d^2s\ T_A(\vec{s})\{1-[1-\frac{\sigma_{NN}T_B(\vec{s}-\vec{b})}{B}]^B\} \\ &+\int d^2s\ T_B(\vec{s})\{1-[1-\frac{\sigma_{NN}T_A(\vec{s}-\vec{b})}{A}]^A\}, \end{aligned} \tag{4.1}$$

where $T(\mathrm{b}) = \int_{-\infty}^{\infty} \mathrm{dz\ n_A}(\sqrt{\mathrm{b^2+z^2}})$ is the thickness function, defined as the probability of having a NN collision within the transverse area element db. $[1-\sigma_{\mathrm{NN}}T_{\mathrm{A}}(\mathrm{b})/\mathrm{A}]^{\mathrm{A}}$ is the probability for a nucleon to pass through the nucleus without any collision. A and B are the mass numbers of two nuclei participating in the collision process. We use the Woods-Saxon nuclear density profile,

$$n_A(r) = \frac{n_0}{1+exp[(r-R)/d]}, \tag{4.2}$$

with parameters, the normal nuclear density $n_0 = 0.17\ \mathrm{fm^{-3}}$, the nuclear radius $\mathrm{R} = (1.12\mathrm{A}^{1/3} - 0.86^{-1/3})$ fm and the skin depth d = 0.54 fm. The inelastic nucleon-nucleon cross section, *i.e.* σ_{NN}, are 42 ± 3 mb at $\sqrt{s_{\mathrm{NN}}} = 200$ GeV and 64 ± 5 mb at $\sqrt{s_{\mathrm{NN}}} = 2.76$ TeV [119]. In order to calculate the number of quark participants, $N_{\mathrm{q-part}}$, in nucleus-nucleus collisions, the density for quarks inside the nucleus is changed to three times that of the nucleon density ($n_0^q = 3n_0 = 0.51\ \mathrm{fm^{-3}}$). Instead of nucleon-nucleon cross section, quark-quark cross section is used which is 4.67 mb and 7.1 mb at $\sqrt{s_{\mathrm{NN}}} = 200$ GeV and 2.76 TeV, respectively [42, 107, 108, 120]. For making predictions for Pb+Pb collisions at $\sqrt{s_{\mathrm{NN}}} = 5.5$ TeV, we have used $\sigma_{\mathrm{NN}} = 72$ mb [121] and $\sigma_{\mathrm{NN}}/9 = 8$ mb for

$N_{\mathrm{N-part}}$ and $N_{\mathrm{q-part}}$ calculations, respectively.
At lower center of mass energies, it has been found that the particle production scales with the number of participating nucleons, contrary to the case of high energies where hard processes dominate. Hard processes have much smaller cross section than the soft processes. However, the number of binary collisions increase with increase in collision centrality faster than the number of participants, as a result the particle production per participant nucleon increases with increase in centrality. By using constituent quark approach, we are going to show how the particle production at higher energies depends on the participating quarks. It should be mentioned here that at energies higher to top RHIC energy, gluons play a vital role in particle production. For these studies, we have taken the centrality dependence of pseudorapidity density of charge particles and transverse energy from top RHIC energy to LHC $\sqrt{s_{\mathrm{NN}}} = 2.76$ TeV. To study the constituent quarks dependence of charged particle and transverse energy production, we need to estimate the number of participant quarks, which has been done in the framework of nuclear overlap model as discussed above.

Since the quark participants are calculated in the framework of nuclear overlap model, it is essential to check how good is our estimation of number of participating nucleons in the collision. In order to do that, the mean number of participating nucleons, calculated in overlap model, are compared with the number estimated by the ALICE experiment [36]. ALICE uses the Glauber MC technique for the estimation of the number of nucleon participants. We have found a reasonably good agreement with ALICE calculations excepting extreme peripheral collisions. This is shown in Fig. 4.1. Solid circles represent the ALICE values and the solid squares represent the overlap model calculations. The lower panel of Fig. 4.1, represents the ratio of ALICE values and the overlap model values.

We have then estimated the number of quark participants within the discussed prescription. The ratio of quark participants and nucleon participants is shown in Fig. 4.2 as a function of nucleon participants,

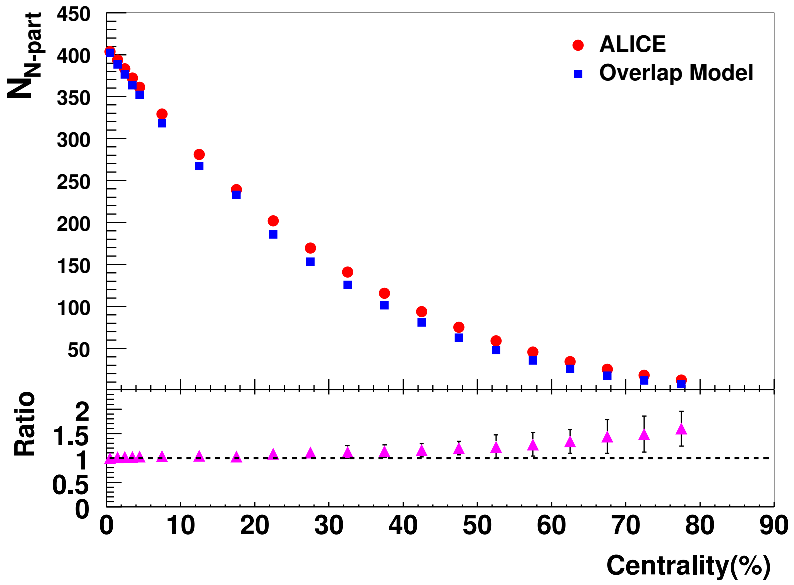

Figure 4.1. The number of nucleon participants, $N_{\mathrm{N-part}}$, as a function of collision centrality for Pb+Pb collisions at $\sqrt{s_{\mathrm{NN}}} = 2.76$ TeV from the estimations by overlap model and by the ALICE collaboration. [36]. The lower panel shows the ratio of both indicating the agreement of both the estimations. Figure is published in Ref. [122].

which is a measure of collision centrality. The ratio shows a sharp increase for $N_{\mathrm{N-part}} \leq 100$ and then shows a type of linear monotonic rise going from peripheral to central collisions.

4.2 Centrality Dependence of $\frac{dN_{\mathrm{ch}}}{d\eta}$

Figure 4.3 (a) shows the 0.5 $N_{\mathrm{N-part}}$-normalized pseudorapidity density of charge particles at midrapidity for Pb+Pb collisions at $\sqrt{s_{\mathrm{NN}}} = 2.76$ TeV for LHC and for Au+Au collisions at $\sqrt{s_{\mathrm{NN}}} = 200$ GeV for RHIC, as a function of collision centrality [122]. Henceforth, in this chapter we would avoid mentioning "midrapidity" explicitly, unless otherwise required, as the data in general, are at midrapidity. A scaling factor of 2.15 has been multiplied with the RHIC data to make a direct comparison with that of LHC data. Going from peripheral to central collisions the production of

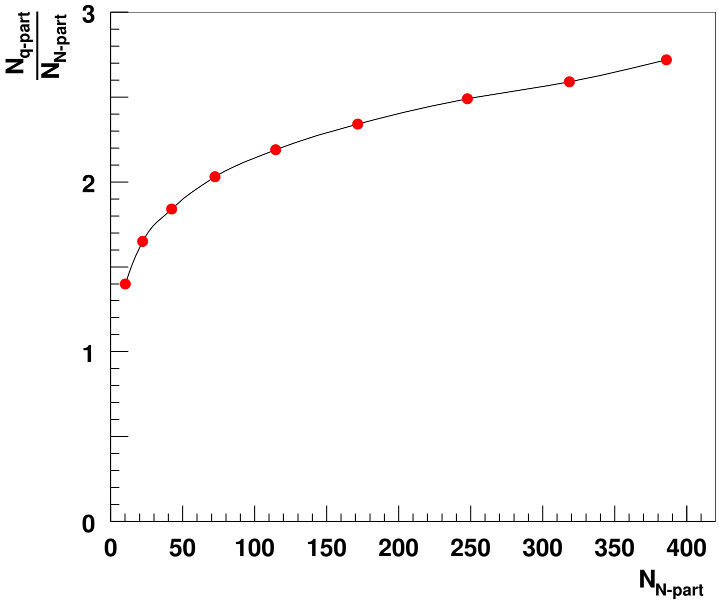

Figure 4.2. The ratio of $N_{\mathrm{q-part}}/N_{\mathrm{N-part}}$ as a function of centrality for Pb+Pb collisions at $\sqrt{s_{\mathrm{NN}}} = 2.76$ TeV from the overlap model calculations.

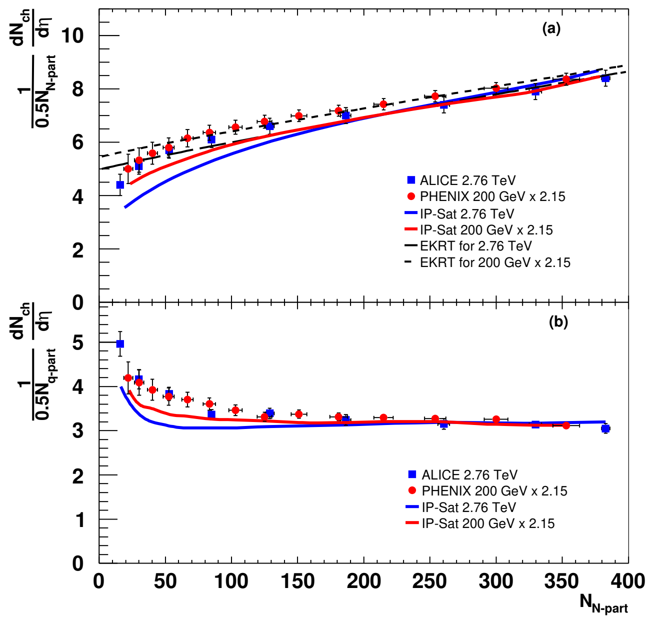

Figure 4.3. (a) $0.5\ N_{\mathrm{N-part}}$-normalized and (b) $0.5\ N_{\mathrm{q-part}}$-normalized $\frac{dN_{\mathrm{ch}}}{d\eta}$ for Pb+Pb collisions at $\sqrt{s_{\mathrm{NN}}} = 2.76$ TeV for LHC and for Au+Au collisions at $\sqrt{s_{\mathrm{NN}}} = 200$ GeV for RHIC as a function of collision centrality. Figure is published in Ref. [122].

charged particles show a rise, when normalized with number of participant pairs. This rise in both the data sets are fitted with a function of the type:

$$\frac{1}{0.5N_{N-part}}\frac{dN_{ch}}{d\eta} = AN^{n}_{N-part}, \tag{4.3}$$

where, A and n are fitting parameters, the values of which are enlisted in Table 4.1, both for nucleon and quark participant sectors. The expectations from IP-saturation model [123] and the EKRT model [124], which are based on initial state gluon saturation, are also shown for a direct comparison with data. In EKRT model the centrality dependence of charged particle multiplicity density in pseudorapidity is described by the function:

$$\frac{dN_{ch}}{d\eta}|_{b=0} = C\ \frac{2}{3}\ 1.16(\frac{N_{N-part}}{2})^{0.92}(\sqrt{s})^{0.40} \tag{4.4}$$

Fig. 4.3 (b) shows the 0.5 $N_{\rm q-part}$-normalized $\frac{dN_{\rm ch}}{d\eta}$ for Pb+Pb collisions at $\sqrt{s_{\rm NN}}$ = 2.76 TeV for LHC and for Au+Au collisions at $\sqrt{s_{\rm NN}}$ = 200 GeV for RHIC as a function of collision centrality. A scaling factor of 2.15 has been multiplied with the RHIC data set to make a direct comparison with the corresponding LHC data. A similar function as is given by Eq. 4.3 has been fitted to both the data sets. With top peripheral collisions as exceptions, where the calculation of nucleon and quark participants are not good, the 0.5 $N_{\rm q-part}$-normalized $\frac{dN_{\rm ch}}{d\eta}$ both for RHIC and LHC data, show an almost centrality independent number of constituent quarks scaling behaviour. The comparison of both the above figures reveals that the particle production is better described in terms of constituent quarks towards more central collisions. This may be understood in line with the observation of very high initial energy densities being produced in central high-energy nuclear collisions [125]. Hence, it seems more suitable to consider quarks as the sources of particle production than nucleons.

4.3 Centrality Dependence of $\frac{dE_{\rm T}}{d\eta}$

The total transverse energy, which is measured on event-by-event basis, carries significant information regarding the explosiveness of the reaction

Table 4.1. power-law fitting parameters for Fig. 4.3 and Fig. 4.4.

	$\sqrt{s_{\rm NN}}$ (TeV)	$N_{\text{N-part}}$-normalization $A(B)$	n	$N_{\text{q-part}}$-normalization $A(B)$	n
Fig. 4.3	0.2	2.74 ± 0.24	0.183 ± 0.017	5.38 ± 0.40	-0.091 ± 0.014
	2.76	2.63 ± 0.25	0.190 ± 0.018	6.20 ± 0.50	-0.122 ± 0.011
Fig. 4.4	0.2	2.9 ± 0.20	0.202 ± 0.014	5.96 ± 0.34	-0.08 ± 0.01
	2.76	2.5 ± 0.40	0.234 ± 0.027	6.01 ± 0.14	-0.074 ± 0.007

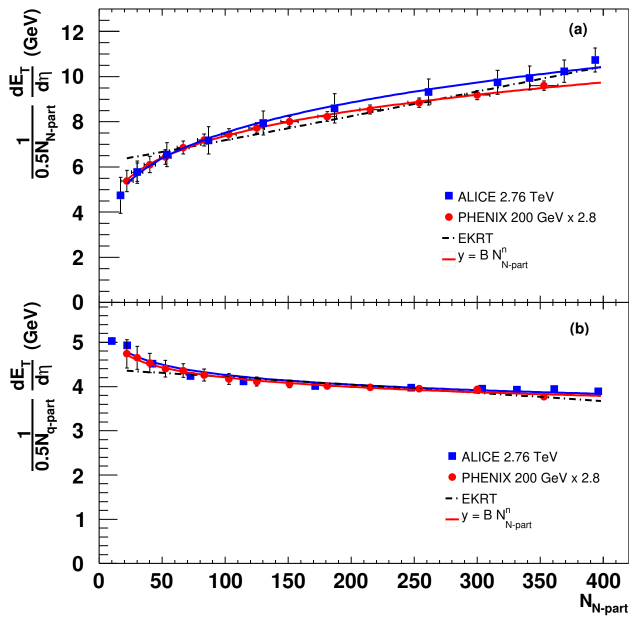

Figure 4.4. (a) 0.5 $N_{\rm N-part}$-normalized and (b) 0.5 $N_{\rm q-part}$-normalized $\frac{dE_{\rm T}}{d\eta}$ for Pb+Pb collisions at $\sqrt{s_{\rm NN}} = 2.76$ TeV for LHC and for Au+Au collisions at $\sqrt{s_{\rm NN}} = 200$ GeV for RHIC as a function of collision centrality. Figure is published in Ref. [122].

and on characterizing the global properties of the produced system. The estimation of transverse energy provides model based calculation of the initial energy density produced in the collision. This in turn gives information regarding a possible formation of a partonic phase, when compared with that of lattice QCD prediction of critical energy density for the deconfinement transition [126]. In nucleus-nucleus collisions, transverse energy is generated by the initial scattering of the partonic constituents of the incoming nuclei and by the rescattering of the produced partons and hadrons [127, 128]. The transverse energy depends on the initial state of the collision and the viscosity of the partonic matter as it comes to the final state through interactions and expansion process [129]. Additionally it also depends on the entropy and temperature of the system [130]. In Fig. 4.4 (a), 0.5 $N_{\rm N-part}$-normalized $\frac{dE_{\rm T}}{d\eta}$ for Pb+Pb collisions at $\sqrt{s_{\rm NN}}$ = 2.76 TeV for LHC and for Au+Au collisions at $\sqrt{s_{\rm NN}}$ = 200 GeV for RHIC are shown as a function of collision centrality. A scaling factor of 2.8 has been multiplied with both the $N_{\rm N-part}$ and $N_{\rm q-part}$-normalized RHIC data to make a direct comparison with the corresponding LHC data. Both the data sets show a functional trend which is governed by an equation,

$$\frac{1}{0.5N_{N-part}}\frac{dE_T}{d\eta} = BN^n_{N-part}, \tag{4.5}$$

where, B and n are fitting parameters. Here B has the dimension of energy. The values of the fitting parameters are given in Table 4.1, both for nucleon and quark participant sectors. Fig. 4.4 (b) shows the 0.5 $N_{\rm q-part}$-normalized $\frac{dE_{\rm T}}{d\eta}$ for Pb+Pb collisions at $\sqrt{s_{\rm NN}}$ = 2.76 TeV for LHC and for Au+Au collisions at $\sqrt{s_{\rm NN}}$ = 200 GeV for RHIC as a function of collision centrality. A similar function as is given by Eq. 4.5 has been fitted to both the data sets. With top peripheral collisions as exceptions, the 0.5 $N_{\rm q-part}$-normalized $\frac{dE_T}{d\eta}$ both for RHIC and LHC data within errors, show a nearly centrality independent number-of-constituent-quarks scaling behaviour. Similar observations have been made recently at RHIC energies [131]. The value of the power, n in the power-law gets smaller (becomes negative) while going from $N_{\rm N-part}$ to $N_{\rm q-part}$-normalization, thereby making the spectra in $N_{\rm q-part}$ flatter compared to $N_{\rm N-part}$-normalization. The shapes of the centrality dependent $N_{\rm N-part}$ or $N_{\rm q-part}$-normalized $\frac{dN_{\rm ch}}{d\eta}$ and $\frac{dE_T}{d\eta}$ show similar features for top RHIC and LHC energies. The relative enhancement of $N_{\rm N-part}$-normalized $\frac{dN_{\rm ch}}{d\eta}$ in A+A collisions with respect to that in $p+p$ collisions is the same at RHIC and LHC energies. This was seen in the framework of models based on multiple scattering and mutual boosting of saturation scales and shadowing [132].

4.4 Collision Energy Dependence of $\frac{dN_{\rm ch}}{d\eta}$

In order to understand the collision energy dependence of charged particle and transverse energy production, we use the following fitting functions:

$$\frac{1}{0.5N_{part}}\frac{dX}{d\eta} = D + E\ \ln\sqrt{s_{NN}} \tag{4.6}$$

$$\frac{1}{0.5N_{part}}\frac{dX}{d\eta} = F(s_{NN})^n \tag{4.7}$$

$$\frac{1}{0.5N_{part}}\frac{dX}{d\eta} = P + Q\ \ln\sqrt{s_{NN}} + R(\sqrt{s_{NN}})^n \tag{4.8}$$

Here $X = N_{\rm ch}$ or $E_{\rm T}$ and $N_{\rm part}$ is either $N_{\rm N-part}$ or $N_{\rm q-part}$ depending on the case under discussion. The logarithmic and power-law functions given by Eqs. 4.6 and 4.7, respectively, are motivated by the trend of the experimental data. However, the form of the hybrid function given by Eq. 4.8 is motivated by the energy dependent behaviour of charged particle production and in addition, by the following results from the non-equilibrium statistical relativistic diffusion model (RDM) [133]. It is explicitly shown by the works of G. Wolschin *et al.* [134–136] that the RHIC and LHC multiplicity could be explained by the combination of a midrapidity gluonic source and a fragmentation source. midrapidity gluonic sources predict a power-law type behaviour of charged particle multiplicity, whereas the fragmentation sources predict a logarithmic behaviour. Energies lower to that of RHIC, where particle multiplicity seems to obey a logarithmic behaviour, could be explained by fragmentation sources. The power-law seems to take over after the top RHIC energy in describing the energy dependence of charged particle multiplicity and the transverse energy production. Additionally, it should be noted here that the trapezoidal approximation for the pseudorapidity distribution of charged particles [137–139], which follows from the logarithmic behaviour with collision energy, seems to fail at LHC energies [140].

In Fig. 4.5, $\frac{dN_{\rm ch}}{d\eta}$ normalized to both $N_{\rm N-part}$ and $N_{\rm q-part}$ is shown as a function of collision energy. Up to top RHIC energy $N_{\rm N-part}$-normalized

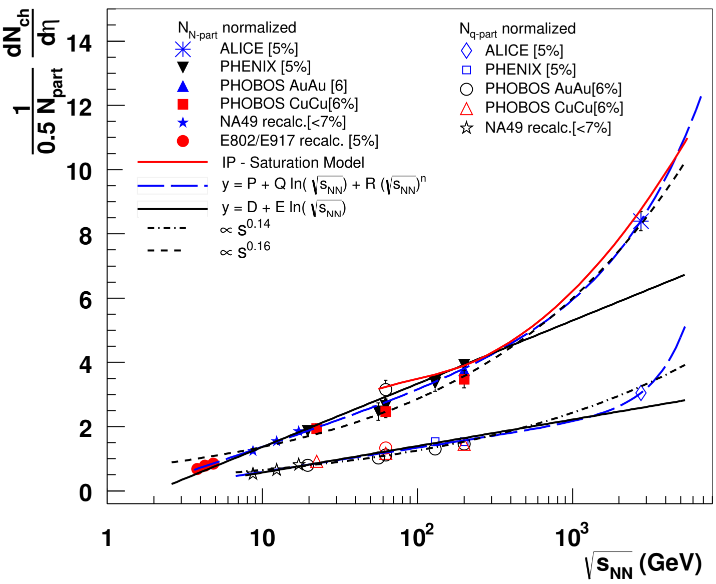

Figure 4.5. $N_{\mathrm{N-part}}$ and $N_{\mathrm{q-part}}$ normalized $\frac{dN_{\mathrm{ch}}}{d\eta}$ as a function of collision energy from lower AGS, SPS and RHIC to LHC energy. Figure is published in Ref. [122]

$\frac{dN_{\mathrm{ch}}}{d\eta}$ is well described by logarithmic function given by Eq. 4.6 [137–139]. However, this function fails to describe the ALICE data for 2.76 TeV. The estimation based on logarithmic function for the $N_{\mathrm{N-part}}$-normalized $\frac{dN_{\mathrm{ch}}}{d\eta}$ is 1180 ± 22 for $\sqrt{s_{\mathrm{NN}}} = 2.76$ TeV, which underestimates the data by 26%. A power-law function (dash-dotted line) given by Eq. 4.7, discribes both RHIC and LHC heavy-ion data but overestimates lower-energy measurements. Contrary, the collision energy dependence of $\frac{dN_{\mathrm{ch}}}{d\eta}$ normalized by $N_{\mathrm{q-part}}$ is very well described by logarithmic function for the whole range of energies under discussion with little deviation towards LHC energies. In this case, the power-law gives a better description of data at the level of quark participants.

The power in the power-law function decreases from $N_{\mathrm{N-part}}$ to $N_{\mathrm{q-part}}$ normalization, thereby going towards a flatter behaviour as a function of collision energy. The predicted value of $\frac{dN_{\mathrm{ch}}}{d\eta}$ for Pb+Pb collisions at $\sqrt{s_{\mathrm{NN}}} = 5.5$ TeV based on the extrapolation of power-law function fitted to $N_{\mathrm{q-part}}$ and $N_{\mathrm{N-part}}$-normalization is around 2116 ± 52 and 2005 ± 28, respectively. On the other hand, the predicted value based on a logarithmic extrapolation of $N_{\rm N-part}$-normalization data is 1310 ± 22. Looking at the low-energy and high-energy behaviours of charge particle production being well described by a logarithmic function and power-law functions, respectively, we have tried to fit a hybrid function (a combination of both) given by Eq. 4.8. Both $N_{\rm N-part}$ to $N_{\rm q-part}$-normalized $\frac{dN_{\rm ch}}{d\eta}$ for the whole range of energies are very well described by this hybrid function, as is seen from Fig. 4.5. At the level of $N_{\rm q-part}$ and $N_{\rm N-part}$-normalization, the $\frac{dN_{\rm ch}}{d\eta}$ estimated by the hybrid function for Pb+Pb collisions at $\sqrt{s_{\rm NN}}$ = 2.76 TeV deviates from the experimental data by 0.06% and 0.44%, showing a reasonably good agreement with the data. The predicted values of $\frac{dN_{\rm ch}}{d\eta}$ for Pb+Pb collisions at $\sqrt{s_{\rm NN}}$ = 5.5 TeV based on the extrapolation of the hybrid function fitted to $N_{\rm q-part}$ and $N_{\rm N-part}$-normalizations are around 2836 ± 85 and 2168 ± 73, respectively. The predictions from IP-saturation model for the top RHIC energy and higher, are also shown for a comparison with the corresponding experimental data.

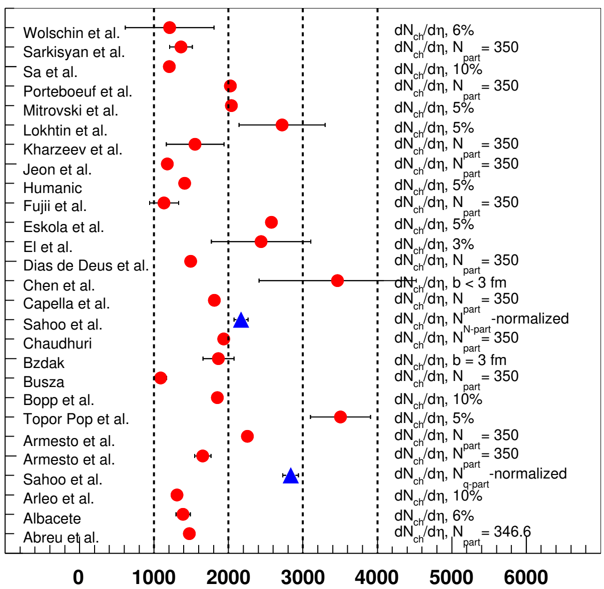

Figure 4.6. Predictions for midrapidity $\frac{dN_{\rm ch}}{d\eta}$ for central Pb+Pb collisions at $\sqrt{s_{\rm NN}} = 5.5$ TeV at the LHC. Figure is published in Ref. [122].

In Fig. 4.6, the predictions for midrapidity $\frac{dN_{\rm ch}}{d\eta}$ for central Pb+Pb collisions at $\sqrt{s_{\rm NN}} = 5.5$ TeV at the LHC, are shown and compared with our predictions from the hybrid function at nucleon and quark participant level. Other data are taken from Ref. [141]. For central heavy-ion collisions at midrapidity, the charged particle multiplicity as a function of collision energy could be parametrized in the framework of the hybrid function, as

$$\frac{dN_{ch}}{d\eta} = 0.5N_{N-part}[P + Q \ \ln \sqrt{s_{NN}} + R(\sqrt{s_{NN}})^n] \qquad (4.9)$$

where $P = -0.255 \pm 0.100, Q = 0.691 \pm 0.141, R = 0.0061 \pm 0.0020 \ GeV^{-1}$ and $n = 0.789 \pm 0.470$.

Table 4.2. Hybrid function fitting parameters for Fig. 4.5 and Fig. 4.7.

	$N_{\text{N-part}}$-normalization			
	P	Q	R	n
Fig. 4.5	-0.255 ± 0.100	0.691 ± 0.141	$6.1 \times 10^{-3} \pm 0.002$	0.789 ± 0.470
Fig. 4.7	-0.416 ± 0.121	0.600 ± 0.090	$8.9 \times 10^{-3} \pm 0.006$	0.832 ± 0.211
	$N_{\text{q-part}}$-normalized			
Fig. 4.5	-0.163 ± 0.046	0.327 ± 0.005	$3.4 \times 10^{-7} \pm 0.002$	2.108 ± 0.285
Fig. 4.7	-0.113 ± 0.346	0.218 ± 0.217	$6.8 \times 10^{-3} \pm 0.045$	0.733 ± 0.777

Table 4.3. Logarithmic function fitting parameters for Fig. 4.5 and Fig. 4.7.

	$N_{\text{N-part}}$-normalization		$N_{\text{q-part}}$-normalization	
	D	E	D	E
Fig. 4.5	-0.60 ± 0.07	0.85 ± 0.02	-0.26 ± 0.04	0.36 ± 0.01
Fig. 4.7	-0.76 ± 0.07	0.81 ± 0.02	-0.43 ± 0.05	0.35 ± 0.02

4.5 Collision Energy Dependence of $\frac{dE_{\rm T}}{d\eta}$

A similar analysis is done for $\frac{dE_T}{d\eta}$-normalized to $N_{\rm N-part}$ and $N_{\rm q-part}$ and is plotted as a function of collision energy in Fig. 4.7. Up to top RHIC

Table 4.4. Power-law fitting parameters for Fig. 4.5 and Fig. 4.7.

	$N_{\text{N-part}}$-normalization		$N_{\text{q-part}}$-normalization	
	F	n	F	n
Fig. 4.5	0.65 ± 0.02	0.33 ± 0.01	0.34 ± 0.01	0.286 ± 0.011
Fig. 4.7	0.34 ± 0.02	0.441 ± 0.010	0.18 ± 0.01	0.386 ± 0.007

energy $N_{\mathrm{N-part}}$-normalized $\frac{dE_{\mathrm{T}}}{d\eta}$ is well described by logarithmic function given by Eq. 4.6. However, this fails to describe the ALICE data for 2.76 TeV. The estimation of $\frac{dE_{\mathrm{T}}}{d\eta}$ based on logarithmic function for the $N_{\mathrm{N-part}}$-normalized $\frac{dE_{\mathrm{T}}}{d\eta}$ is 1114 ± 24 GeV, which underestimates the data by 47% for $\sqrt{s_{\mathrm{NN}}} = 2.76$ TeV. A power-law function (dash-dotted line) given by Eq. 4.7, discribes both RHIC and LHC heavy-ion data but underestimates lower-energy measurements. Contrary, the collision energy dependence of $\frac{dE_{\mathrm{T}}}{d\eta}$ normalized by $N_{\mathrm{q-part}}$ is very well described by logarithmic function up to top RHIC energy and shows considerable deviation at energies higher to top RHIC energy. The power-law function given by Eq. 4.7 describes the $N_{\mathrm{q-part}}$-normalized $\frac{dE_T}{d\eta}$ data quite well.

Like $\frac{dN_{\mathrm{ch}}}{d\eta}$, the power in the power-law function, decreases from $N_{\mathrm{N-part}}$ to $N_{\mathrm{q-part}}$ normalization, thereby going towards a flatter behaviour as a function of collision energy. The most interesting observation is that the power-law motivated function better describes the transverse energy production with collision energy compared to the logarithmic function. The predicted value of $\frac{dE_{\mathrm{T}}}{d\eta}$ for Pb+Pb collisions at $\sqrt{s_{\mathrm{NN}}} = 5.5$ TeV based on the extrapolation of power-law function fitted to $N_{\mathrm{q-part}}$ and $N_{\mathrm{N-part}}$-normalized $\frac{dE_T}{d\eta}$ are around 2683 ± 62 GeV and 2760 ± 50 GeV, respectively. Like the case of charge particle production, looking at the low-energy and high-energy behaviours of the transverse energy production being well described by a logarithmic function and power-law functions, respectively, we have tried to fit the same hybrid function given by Eq. 4.8. The $N_{\mathrm{N-part}}$-normalized $\frac{dE_{\mathrm{T}}}{d\eta}$ for the whole range of energies is very well described by this function, as is seen from Fig. 4.7. The $N_{\mathrm{q-part}}$-normalized $\frac{dE_{\mathrm{T}}}{d\eta}$ is also very

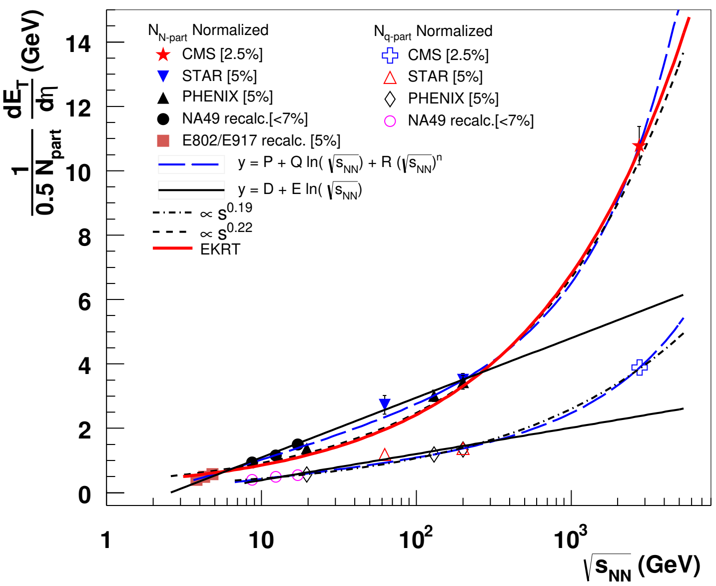

Figure 4.7. $N_{\rm N-part}$ and $N_{\rm q-part}$ normalized $\frac{dE_{\rm T}}{d\eta}$ as a function of collision energy from lower AGS, SPS and RHIC to LHC energy. Figure is published in Ref. [122].

well described by the hybrid function. Irrespective of nucleons or quarks are the sources of particle production, this hybrid function describes the charged particle and transverse energy production for all range of energies starting from lower AGS, SPS, RHIC to LHC. The estimations of $\frac{dE_{\rm T}}{d\eta}$ from the hybrid function fitting to the $N_{\rm q-part}$ and $N_{\rm N-part}$-normalized data for Pb+Pb collisions at $\sqrt{s_{\rm NN}} = 2.76$ TeV deviate from the CMS collaboration experimental data [130] by 0.05% and 1.18%, respectively. The predicted value of $\frac{dE_{\rm T}}{d\eta}$ for Pb+Pb collisions at $\sqrt{s_{\rm NN}} = 5.5$ TeV based on the extrapolation of the hybrid function fitted to $N_{\rm q-part}$ and $N_{\rm N-part}$-normalizations are around 3056 ± 44 GeV and 3222 ± 42 GeV, respectively. Like charged particle multiplicity, for central heavy-ion collisions at midrapidity, the $\frac{dE_{\rm T}}{d\eta}$ as a function of collisions energy could be parametrized in the framework of the hybrid function, as

$$\frac{dE_T}{d\eta} = 0.5 N_{N-part}[P + Q \;\ln\sqrt{s_{NN}} + R(\sqrt{s_{NN}})^n] \tag{4.10}$$

where $P = -0.416 \pm 0.121$ GeV, $Q = 0.60 \pm 0.09$ GeV, $R = 0.0089 \pm 0.0060$

and $n = 0.832 \pm 0.211$. The transverse energy production as a function of energy in the framework of EKRT model, which is based on initial state gluon saturation [124], is given by,

$$\frac{dE_T}{d\eta} = 0.46\ A^{0.92}(\sqrt{s})^{0.40}[1 - 0.012\ \ln A + 0.061\ \ln\sqrt{s}], \tag{4.11}$$

where A is the mass number of the colliding nuclei for a symmetric collision species. This takes into account a reduced initial number of scattering centers in the nuclear parton distribution functions. Here we have compared the EKRT model estimations for transverse energy for all collision energies under discussion. It is observed that the transverse energy production at higher energies is very well described by EKRT model. However, EKRT model fails to describe the low energy data. This is an indication of gluon saturation effect at higher collision energies, which is absent at lower energies. To understand the deviation from logarithmic behaviour in a more qualitative way, one considers a purely thermodynamic system in equilibrium. The entropy is proportional to the energy of the system, when the volume is assumed to be constant for non-expanding and homogeneous fireballs. This could be written as a Taylor expansion in $e^{\nu \ln \mathrm{E}}$, where ν is a constant and E is the total energy of the system. Here $\frac{dN_{\rm ch}}{d\eta}/(0.5N_{\rm part})$ represents a scaled-entropy [142] and at the freeze-out surface, where the volume of the fireball is fixed and we define a constant temperature of the system, this could be expressed as a function of collision energy up to second order in approximation, as:

$$\begin{aligned} \frac{dN_{ch}}{d\eta}/(0.5N_{part}) &= e^{\nu \ln(\sqrt{s_{NN}})} \\ &\simeq \alpha + \beta\ \ln\sqrt{s_{NN}} + \gamma\ (\ln\sqrt{s_{NN}})^2 \end{aligned} \tag{4.12}$$

We have observed that both collision energy dependence of $\frac{dN_{\rm ch}}{d\eta}/(0.5N_{\rm part})$ and $\frac{dE_{\rm T}}{d\eta}/(0.5N_{\rm part})$ data up to top RHIC energy are explained by the above function. This may indicate that the produced system is thermalized and one uses equilibrium statistical mechanics to describe the system. However, LHC data are very much underestimated by this function. The charged particle multiplicity at LHC has two components- thermalized soft component and a non-thermal hard component coming from jet fragmentation, which is almost more than 50%. The contribution of this non-thermal component to the final state entropy becomes significant at LHC, which may be the cause of this observed discrepancy. This may also lead to a jump in $E_{\rm T}/N_{\rm ch}$ while going from top RHIC energy to LHC, where the statistical thermal model fails to explain the LHC data. This is discussed in the following section.

4.6 Transverse Energy per Charged Particle and Freeze-out

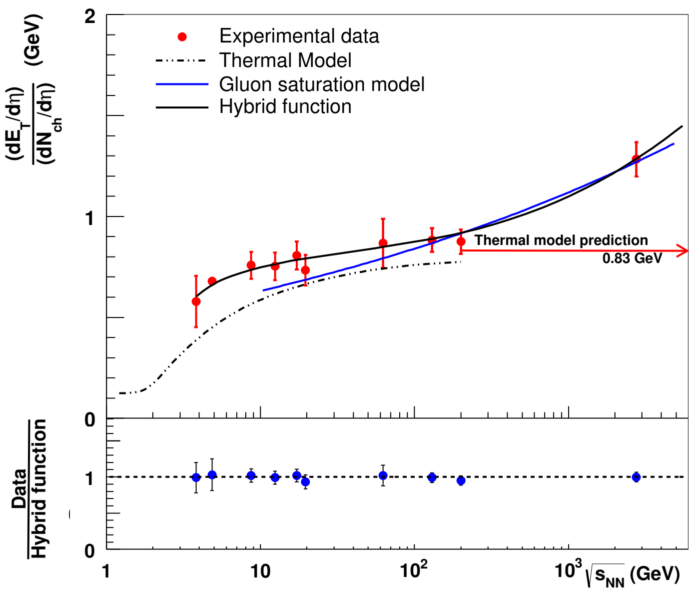

Figure 4.8. The ratio of $\frac{dE_{\rm T}}{d\eta}$ and $\frac{dN_{\rm ch}}{d\eta}$ as a function of center of mass energy. Experimental data are compared to the predictions from thermal model [144–146], gluon saturation model [123] and the estimations obtained in the framework of the hybrid model fitting to transverse energy and charged particle data. Figure is published in Ref. [122].

The ratio of pseudorapidity densities of transverse energy and number of charged particles at midrapidity, *i.e.* $E_{\rm T}/N_{\rm ch}$ has been studied both experimentally [125, 130, 143] and phenomenologically [144–147] to understand the underlying particle production mechanism. This observable is known as global barometric measure of the internal pressure in the ultra-dense matter produced in heavy-ion collisions. This quantity depends on the initial state of the collision and the viscosity of the matter as it expands to its final state, when it is observed by the detectors. This observable when studied as a function of collision energy (as shown in Fig. 4.8), shows two regions of interest. The first one from the lower SIS energies to SPS energies shows a steep increase of $E_{\mathrm{T}}/N_{\mathrm{ch}}$ values, thereby indicating that the mean energy of the system increases. In the second region, from SPS to top RHIC energy, $E_{\mathrm{T}}/N_{\mathrm{ch}}$ shows a very weak collision energy dependence, *i.e.* like a saturation behaviour. In this region the mean energy doesn't increase, whereas the collision energy increases. This may indicate that the increase in collision energy results in new particle production in this energy domain. This behaviour has been well described in the context of a statistical hadron gas model (SHGM) [144–146]. In the framework of SHGM, it has been predicted that $E_{\mathrm{T}}/N_{\mathrm{ch}}$ would saturate at energies higher to that of top RHIC energy with a limiting value of 0.83 GeV [144–146]. This goes in-line with Hagedorn's conjecture of a limiting temperature ($T_{\mathrm{H}} = 165$ MeV) for elementary and nuclear collisions at higher collision energies [148, 149] and the subsequent observation of a saturation behaviour in the freeze-out temperature (T_{fo}) in heavy-ion collisions [150]. The SHGM prediction of $E_{\mathrm{T}}/N_{\mathrm{ch}}$ at LHC collision energy of 2.76 TeV has been found to be inconsistent with the experimental observation of its value, which is 1.25 ± 0.08 GeV [130]. This could be because of more high-p_{T} particle and jet production at LHC, which makes LHC measurements quite different from that of RHIC. The estimated values of $E_{\mathrm{T}}/N_{\mathrm{ch}}$ from the hybrid equation fitting to the corresponding $N_{\mathrm{q-part}}$-normalized data, for Pb+Pb collisions at 2.76 and 5.5 TeV collisions energies are 1.33 ± 0.05 and 1.49 ± 0.05 GeV, respectively. Here we have taken the $N_{\mathrm{q-part}}$-normalized data and the corresponding fitting of the hybrid function, as it describes energy dependence of both charged particle and transverse energy production. This shows that the $E_{\mathrm{T}}/N_{\mathrm{ch}}$ shows a very strong dependence on collision energy beyond the top RHIC energy, thereby creating a third region in the $E_{\rm T}/N_{\rm ch}$ versus collision energy diagram. If the freeze-out occurs on a fixed isotherm for all energies, it is expected that the energy per particle will be the same. A comparison of $T_{\rm fo}$ and $E_{\rm T}/N_{\rm ch}$ versus collision energy indicates that from SPS to top RHIC energies the $T_{\rm fo}$ and the value of $E_{\rm T}/N_{\rm ch}$ are almost independent of collision energy. Beyond top RHIC energy, the value of $E_{\rm T}/N_{\rm ch}$ gets a jump, which indicates that the $T_{\rm fo}$ at LHC should be different than that is at RHIC. We have estimated the $T_{\rm fo}$ for the LHC energies from the SHGM parametrized equations used in Ref. [150], which are given by

$$T(\mu_B) = a - b\mu_B^2 - c\mu_B^4, \tag{4.13}$$

where $a = 0.166 \pm 0.002$ GeV, $b = 0.139 \pm 0.016$ GeV^{-1}, and $c = 0.053 \pm 0.021$ GeV^{-3} and

$$\mu_B(\sqrt{s}) = \frac{d}{1 + e\sqrt{s}} \tag{4.14}$$

where $d = 1.308 \pm 0.028$ GeV and $e = 0.273 \pm 0.008$ GeV^{-1}. The value of the freeze-out temperature, $T_{\rm fo}$, for RHIC 200 GeV, LHC 2.76 TeV and 5.5 TeV are around 166 ± 2 MeV. The $T_{\rm fo}$ obtained from the SHGM estimation of fitting to experimentally obtained particle ratios at RHIC and LHC is $T_{\rm fo} = 164$ MeV, with $\mu_{\rm B}$ is 24 MeV and 1 MeV, respectively [151, 152]. The SHGM predictions for $T_{\rm fo}$ is consistent with its measurements at LHC. However, it should be mentioned here that the $\bar{p}/\pi^-$ ratio is sensitive to the determination of chemical freeze-out temperature. $T_{\rm fo} \equiv T_{\rm chem} = 164$ MeV, over predicts the value of $\bar{p}/\pi^-$ in hydrodynamical calculations [153], for the measurements at LHC energy [152, 154], which is known as "proton puzzle" [155]. Inclusion of baryon anti-baryon $\rm B - \bar{B}$ channels in phenomenological models [156] reduces the final state proton, anti-proton multiplicity and thus explains the proton puzzle of LHC. On the other hand, the SHGM predicted value of $E_{\rm T}/N_{\rm ch}$, which is 0.83 GeV is inconsistent with the corresponding measurements at LHC. The observation that $T_{\rm fo}$ doesn't change while going from RHIC to LHC energies, when $E_{\rm T}/N_{\rm ch}$ gets a jump, needs to be understood from thermodynamics view point. $T_{\rm fo}$ being independent of collision species and energy is a consequence of the fact that the system produced in heavy-ion collisions irrespective of the initial conditions comes to the same final state. $E_{\rm T}/N_{\rm ch}$, the mean energy per particle, getting enhanced beyond top RHIC energy, could be a consequence of LHC being dominated by high-$p_{\rm T}$ jets and as a barometric parameter, its increase implies, higher initial pressure being created in LHC collisions compared to that of RHIC. This also is reflected from the values of radial flow parameters measured at RHIC [157] and LHC [152]. Radial flow for central collisions at LHC is 10% higher than the corresponding value at RHIC in the same $p_{\rm T}$ range [152]. At midrapidity, mean transverse mass ($< m_{\rm T} >$) is essentially the average energy of the particle ($E = m_{\rm T}$coshy) and is proportional to the temperature of the system in a thermodynamic picture. From RHIC [157, 158] to LHC [152] around 25% increase in $< m_{\rm T} >$ is observed, which could explain the observation of the jump in $E_{\rm T}/N_{\rm ch}$ from RHIC to LHC [130]. However, there are other factors which may affect $< m_{\rm T} >$ and thus need to be considered for a proper interpretation of data [142].

In addition, this rise in $E_{\rm T}/N_{\rm ch}$ is expected in gluon saturation model due to the increase of the number of participating gluons with the increase of collision energy. At very high-energy, the gluon creation and annihilation balance out leading to a saturation in gluon number. As gluon density does not have a linear collision energy dependence, the saturation scale depends non-linearly on the center of mass energy, *i.e.* $E_{\rm T}/N_{\rm ch} = k(\sqrt{s})^{\lambda}$, where k and λ are constants [159]. This function when fitted to the top RHIC and LHC data, gives a good description of the energy dependent behaviour of $E_{\rm T}/N_{\rm ch}$ and the value of λ obtained from this fitting is found to be 0.12, which lies between $\lambda = 0.15$ (IP-sat model prediction) and $\lambda = 0.11$ (b-CGC model estimation) [159, 160]. Hence, gluon saturation picture at LHC energies may also explain the observed jump in $E_{\rm T}/N_{\rm ch}$ [129].

4.7 Summary

In this chapter, we study the charged particle and transverse energy production as a function of collision centrality and collision energy, in the framework of nucleon and quark participants estimated using a Monte Carlo based implementation of nuclear overlap model. The ratio of number of quark participants and number of nucleon participants shows a non-linear increase with collision centrality for a particular collision energy. The centrality dependence of $N_{\rm N-part}$-normalized $\frac{dN_{\rm ch}}{d\eta}$ both for Au+Au collisions at $\sqrt{s_{\rm NN}} = 200$ GeV and Pb+Pb collisions at $\sqrt{s_{\rm NN}} = 2.76$ TeV, which show a increase with centrality, seems to show a nearly centrality independent scaling behaviour when normalized to $N_{\rm q-part}$. This gives the indication of partonic activities at RHIC and LHC energies. Similar is the observation for $\frac{dE_{\rm T}}{d\eta}$ both for the RHIC and LHC data.

The charged particle production as a function of collision energy has been studied both in the nucleon and quark participant frameworks. In contrast to the nucleon participants where the logarithmic function fails to describe the measurements up to the LHC energies, in the quark participant sector, the logarithmic function describes the data well up to 2.76 TeV. A power-law function however, describes the high-energy data for midrapidity $\frac{dN_{\rm ch}}{d\eta}$ with a nice agreement with LHC 2.76 TeV measurement. On the other hand, it underestimates the low energy data. A hybrid function, which is a combination of logarithmic and power-law in collision energy, describes the data for 0.5 $N_{\rm part}$-normalized $\frac{dN_{\rm ch}}{d\eta}$ and $\frac{dE_{\rm T}}{d\eta}$ at all available energies both for the nucleon and quark participants, indicating a universality in multi-particle production. We give the predictions for $\frac{dN_{\rm ch}}{d\eta}$ for Pb+Pb collisions at $\sqrt{s_{\rm NN}} = 5.5$ TeV from this universal hybrid function. On the other hand, the EKRT model based on a initial state gluon saturation and the power-law function better describes the high-energy behaviour of transverse energy production. This points to gluon saturation effects at energies higher to RHIC. We have estimated the value of $\frac{dE_{\rm T}}{d\eta}$ for Pb+Pb collisions at $\sqrt{s_{\rm NN}} = 2.76$ TeV by using this hybrid model which agrees with the corresponding LHC measurements. Based on this, we give a prediction of $\frac{dE_{\rm T}}{d\eta}$ for the Pb+Pb collisions at $\sqrt{s_{\rm NN}} = 5.5$ TeV. The value of $E_{\rm T}/N_{\rm ch}$ for Pb+Pb collisions at $\sqrt{s_{\rm NN}} = 2.76$ TeV estimated by the hybrid function agrees with the corresponding measurement by CMS collaboration at LHC and reproduces the jump from RHIC to LHC, in its energy dependence behaviour. This may indicate a higher initial pressure of the ultra-dense matter at LHC compared to that is formed at RHIC energies. In this framework, we give the prediction for this barometric observable for the future LHC Pb+Pb collisions at $\sqrt{s_{\rm NN}} = 5.5$ TeV. In conclusion, the charged particle and the transverse energy measurements are well described by the hybrid function for all available energies and collision species in heavy-ion collisions indicating a universality in particle production.

Chapter 5

Participant Effective energy & Multiparticle production

Multiparticle production is one of the most intriguing topics in high-energy particle and nuclear collision studies. Bulk observables such as multiplicity and transverse energy bring important information on the underlying dynamics of strong interaction. However, the multiparticle production dynamics in high-energy collisions is a matter of intense research in view of the available higher collision energies. It is already more than half a century as the multiplicity of the produced particles are considered to be derived by the collision energy [161–163]. In this picture, the energy pumped into the collision zone in the very first stage of the collision defines the volume of the interaction lump of participant patterns. Later on, the approach of "wounded" nucleons, or nucleon participants, has been proposed to describe the multiplicity and particle distributions [164]. In this approach, the multiplicity is expected to be proportional to the number of participants. However, it was observed at RHIC and similarly at LHC energies, that the concept of wounded nucleons does not describe the measurements, where the data found to demonstrate an increase with the number of nucleon participants. The problem has been addressed in the nuclear overlap model using Monte Carlo simulation in the constituent quark framework, and the scaling has been shown to be restored [122, 165–169]. In addition, it was observed that the multiplicity and midrapidity-density distributions are similar in e^+e^- and in the most central (head-on) nuclear collisions [50] at the same center-of-mass (c.m.) energy pointing to the universality of multihadron production. However, the expectation to observe this type of universality in hadronic and nuclear collisions at similar c.m. energy per nucleon has not been shown by the data, where the measurements in hadron-hadron collisions show significantly lower values compared to those in central heavy-ion collisions [27, 170]. A solution has been proposed by introducing a dissipative energy approach [115]. In this approach, effective energy factor 1/3 is proposed to be used in nucleon-nucleon collisions to relate to central A+A collisions.

The proposed factor 1/3 allows to relate c.m. energy dependence of both the observables, multiplicity and midrapidity, in e^+e^- and $p + p(\bar{p})$ interactions. This solves the problem of the factor 1/2, introduced in [171] to account for the half of the energy lost attributed to the leading protons. If the factor 1/2 is found to lead to some similarity in the multiplicity data ($N_{\rm ch}$), it can not encompass the comparison of the midrapidity density ($dN_{\rm ch}/d\eta$). Interestingly, the 3NLO perturbative QCD [172] fit to e^+e^- data has been shown [28] to describe the multiplicity measurements in $p + p(\bar{p})$ interactions up to TeV energies provided the inelasticity is set to ≈ 0.35, *i.e.* the effective 1/3 energy in hadronic interactions. Earlier, the factor 1/3 has been already shown to provide an agreement in e^+e^- and $p+p(\bar{p})$ mean multiplicity data [51]. Such a universality is found to correctly predict [115] the value of the midrapidity density in $p+p$ interactions at the TeV LHC energies [173].

In this chapter, in the framework of the approach of the dissipating effective energy of constituent quark participants, or, for brevity, the Participant Dissipating Energy (PDE) approach, we study $\sqrt{s_{\rm NN}}$ and number of nucleon participants ($N_{\rm part}$), or centrality dependencies of charged particle pseudorapidity density at midrapidity ($dN_{\rm ch}/d\eta$), measured in nucleus-nucleus collisions. Based on this energy dissipation picture, we apply effective energy consideration to the pseudorapidity density of the transverse energy at midrapidity ($dE_{\rm T}/d\eta$), measured in heavy-ion collisions in the RHIC and LHC experiments. We also extend the previous studies of the charged particle mean multiplicity $N_{\rm ch}$, [115] to LHC energies. We show that $\sqrt{s_{\rm NN}}$ dependence of $N_{\rm ch}$ in most central collisions is well described within the proposed approach. In addition, here we study the centrality dependence of the $N_{\rm ch}$ at RHIC and LHC energies. We introduce a new scaling, referred to as the "energy balanced limiting fragmentation scaling", which allows us to describe the pseudorapidity density spectra independently of the collision centrality. Using this scaling, a complementarity between the multiplicities measured in head-on nuclear collisions and obtained from the centrality data (corresponding to different impact parameters) is found. The study clarifies some differences of the centrality dependence of multiplicities measured at RHIC and LHC. Finally, predictions are made for the investigated dependencies for the forthcoming higher energy measurements in $p + p(\bar{p})$ and heavy-ion collisions at the LHC.

5.1 The Participant Dissipating Energy Approach

In this section, we briefly describe the PDE approach, as it is proposed in [115]. This approach quantifies the process of particle production in terms of the amount of energy deposited by interacting constituent quark participants inside the small Lorentz-contracted volume formed at the early stage of a collision. The whole process of a collision is then represented as the expansion of an initial state and the subsequent break-up into secondary particles. This approach resembles the Landau phenomenological hydrodynamic approach of multiparticle production in relativistic particle interactions [163], which was found to be in a good agreement with the multiplicity data in particle and nuclear collisions in a wide energy range [174]. In the picture considered here, the Landau hydrodynamics is employed in the framework of constituent (or dressed) quarks, in accordance with the additive quark model [175–179]. This makes the secondary particle production to be basically driven by the amount of the initial effective energy deposited by constituent quarks into the Lorentz-contracted region. In $p+p(\bar{p})$ collisions, a single constituent quark from each nucleon is considered to take part in a collision and the remaining quarks are treated as spectators. The spectator quarks do not participate in the secondary particle production, but they result into formation of leading particles and carry away a significant part of the collision energy. Thus, the effective energy for the production of secondary particles is the energy of interaction of a single quark pair, *i.e.*, 1/3 of the entire nucleon energy. On the contrary, in the head-on heavy-ion collisions, the participating nucleons are considered colliding with all three constituent quarks from each nucleon. This makes the whole energy of the colliding nucleons (participants) available for the secondary particle production. Within this picture, one expects the results for bulk observables from head-on heavy-ion collisions at $\sqrt{s_{\rm NN}}$ to be similar to those from the $p+p(\bar{p})$ collisions but corresponding to a three times larger c.m. energy, *i.e.*, at $\sqrt{s_{pp}} \simeq 3\sqrt{s_{\rm NN}}$ (for a better clarity instead of using $\sqrt{s}$ for $p+p(\bar{p})$ c.m. energy, we use $\sqrt{s_{pp}}$). Such an universality is found to correctly predict [115] the value of the midrapidity density in $p+p(\bar{p})$ interactions measured at the TeV LHC energies [173]. In addition, the multiplicity measurements in $p+p(\bar{p})$ interactions up to TeV energies are shown to be well reproduced by e^+e^- data as soon as the inelasticity is set to ≈ 0.35 [28], *i.e.* effectively 1/3 of the hadronic interaction energy. This is in agreement with the dissipation energy picture where the structureless colliding leptons are considered to deposit their total energy into the collision volume, similar to nucleons in head-on nuclear collisions [115].

Landau hydrodynamical model predicts that the pseudorapidity spectra of the produced particles to follow a Gaussian distribution [163]. However, later Carruthers and Duong-van used rapidity variable (y) to characterize the particle production using Landau hydrodynamics [30]. Therefore, while dealing with Landau hydrodynamical model we use pseudorapidity variable. The pseudorapidity density of charged particles in Landau hydrodynmic model is given by

$$\frac{dN_{ch}}{d\eta} = \frac{N_{ch}}{\sqrt{2\pi L}}\ exp\left(-\frac{\eta^2}{2L}\right) \tag{5.1}$$

where $L = \ln\gamma = \frac{1}{2}\ln(s_{\rm NN}/4m_p^2)$ gives a measure of the thickness of the Lorentz-contracted disks of colliding species, γ is the Lorentz contraction factor, m_p proton mass and $\sqrt{s_{\rm NN}}$ is c.m. energy per nucleon. At midrapidity ($\eta = 0$), Eq. 5.1 is simplified as

$$\frac{dN_{ch}}{d\eta} = \frac{N_{ch}}{\sqrt{2\pi L}} \tag{5.2}$$

Now for heavy-ion collisions, one uses $N_{\rm part}$ normalized variables,

$$\frac{2}{N_{part}}\frac{dN_{ch}}{d\eta} = \frac{2N_{ch}}{N_{part}}\frac{1}{\sqrt{2\pi L}} \equiv \rho(0) \tag{5.3}$$

and for $p + p(\bar{p})$ collisions:

$$\frac{dN_{ch}}{d\eta} = \frac{N_{ch}^{pp}}{\sqrt{2\pi L}} \equiv \rho_{pp}(0). \tag{5.4}$$

Hence

$$\frac{\rho(0)}{\rho_{pp}(0)} = \frac{2N_{ch}}{N_{part}\ N_{ch}^{pp}}\sqrt{\frac{L_{PP}}{L_{NN}}} \tag{5.5}$$

According to the approach considered, m_p is the proton mass in nucleus-nucleus collisions and the constituent quark mass in $p + p(\bar{p})$ collisions set to $\frac{1}{3}m_p$. $N_{\rm ch}$ and $N_{\rm ch}^{pp}$ are the mean multiplicities in nucleus-nucleus and nucleon-nucleon collisions, respectively, and $N_{\rm part}$ is the number of participants.

$L_{\rm pp}$ and $L_{\rm NN}$ can be given by the following formulae:

$$\begin{aligned} L_{pp} = \ln\left(\frac{\sqrt{s_{pp}}}{2m_q}\right) &= \frac{1}{2}\ln\left(\frac{s_{pp}}{4m_q^2}\right) \\ L_{NN} = \ln\left(\frac{\sqrt{s_{NN}}}{2m_p}\right) &= \frac{1}{2}\ln\left(\frac{s_{NN}}{4m_p^2}\right) \end{aligned} \tag{5.6}$$

Now,

$$\frac{L_{pp}}{L_{NN}} = \frac{\frac{1}{2}\ln\left(\frac{s_{pp}}{4m_q^2}\right)}{\frac{1}{2}\ln\left(\frac{s_{NN}}{4m_p^2}\right)}. \tag{5.7}$$

Within the PDE approach, in nucleon - nucleon and head-on nucleus - nucleus collisions, we consider $\sqrt{s_{\rm NN}} = \sqrt{s_{pp}}/3$ and $m_q = m_p/3$. Then, one evolves Eq. (5.5) for the rapidity density $\rho(0)$ and the multiplicity, $N_{\rm ch}$ at $\sqrt{s_{\rm NN}}$; and the rapidity density $\rho_{pp}(0)$ and the multiplicity $N_{\rm ch}^{pp}$ at $3\sqrt{s_{\rm NN}}$:

$$\begin{aligned} \rho(0) &= \rho_{pp}(0)\,\frac{2N_{ch}}{N_{part}\,N_{ch}^{pp}}\sqrt{1-\frac{4\ln 3}{\ln(4m_p^2/s_{NN})}}\,, \\ &\sqrt{s_{NN}} = \sqrt{s_{pp}}/3\,. \end{aligned} \tag{5.8}$$

It was found [115] that Eq. (5.8) very well reproduces the c.m. energy dependence of of the midrapidity density, measured in the most central heavy-ion collisions up to the top RHIC energy. Moreover, it was also shown that similarly, the total multiplicities in these types of collisions follow the energy-dependence universality. Further development, as outlined below, treats this dependence in terms of centrality [41]. The centrality is regarded as the degree of the overlap of the volumes of the two colliding nuclei, characterized by the impact parameter. The centrality is closely related to the number of nucleon participants determined using Monte Carlo Glauber calculations: number of nucleon participant increases while going from peripheral to most central collisions. Thus, the centrality is related to the amount of energy released in the collisions, *i.e.*, to the effective energy, $\varepsilon_{\rm NN}$. The effective energy, in the framework of the proposed approach, can be defined as a fraction of the c.m. energy available in a collision according to the centrality, α:

$$\varepsilon_{NN} = \sqrt{s_{NN}}(1-\alpha). \tag{5.9}$$

Conventionally, the data are divided into centrality intervals, so that α is the mid point of the centrality interval expressed in fractional form, *e.g.* $\alpha = 0.25$ for the centrality interval of 20–30% centrality class.

Then, for the effective c.m. energy $\varepsilon_{\rm NN}$, Eq. (5.8) reads:

$$\begin{aligned} \rho(0) &= \rho_{pp}(0)\, \frac{2N_{\rm ch}}{N_{\rm part}\, N_{\rm ch}^{pp}} \sqrt{1 - \frac{2\ln 3}{\ln(2m_p/\varepsilon_{NN})}}\,, \\ \varepsilon_{NN} &= \sqrt{s_{pp}}/3\,, \end{aligned} \tag{5.10}$$

where $N_{\rm ch}$ is the mean multiplicity in central nucleus-nucleus collisions measured at $\sqrt{s_{\rm NN}} = \varepsilon_{\rm NN}$. The rapidity density $\rho_{pp}(0)$ and the multiplicity $N_{\rm ch}^{pp}$ are taken from the existing data or, where not available, calculated using the corresponding experimental c.m. energy fits at $\sqrt{s_{pp}} = 3\,\varepsilon_{\rm NN}$. The $N_{\rm ch}$ values are as well taken from the measurements in central heavy-ion collisions wherever available, while for the non-existing data the "hybrid" fit [122] is used. This hybrid fit is inspired by the measurements as well as by theoretical considerations. It is observed that $\sqrt{s_{\rm NN}}$ dependence of multiplicity is well described by linear logarithmic fit up to the top RHIC energy [115, 180]. However, the data clearly show a preference for the power-law behaviour as the collision energy increases above 1−2 TeV at the LHC [180–182]. From the theoretical description point of view, such a c.m. energy dependence is expected [183] as soon as the logarithmic dependence is considered to characterize the fragmentation source(s), while the power-law behaviour is believed to come from the gluon-gluon interactions [184–187].

In fact, each of the scalings described by Eqs.(5.8) and (5.9) regulates a particular physics ingredient used in the modelling of the PDE approach. The scaling introduced by Eq.(5.8) embeds the constituent quark model, which leads to establishing a similarity between hadronic and nuclear collisions. The scaling driven by Eq.(5.9) is appealed to define the energy budget effectively retained for multiparticle production in the most central collisions to determine the variables obtained from centrality data.

5.2 Charged Particle Pseudo-rapidity Density

5.2.1 Centrality Dependence

In Fig. 5.1, $(dN_{\rm ch}/d\eta)/(N_{\rm part}/2)$ at midrapidity as a function of $N_{\rm part}$ is shown as measured by PHOBOS experiment in Au+Au collisions at RHIC at c.m. energy of $\sqrt{s_{\rm NN}} = 19.6$ to 200 GeV [139] and by CMS experiment in Pb+Pb collisions at LHC at $\sqrt{s_{\rm NN}} = 2.76$ TeV [181], respectively. The PHOBOS data at $\sqrt{s_{\rm NN}} = 200$ GeV multiplied by 2.12 are also shown to allow comparison with the LHC data and the model calculations. As it is noted above, this dependence cannot be reproduced by the wounded nucleon model where a number-of-nucleon-participant scaling is expected.

In the framework of the model of constituent quarks combined with Landau hydrodynamics, we calculate the centrality dependence of the charged particle midrapidity density using Eq. (5.10) to reproduce the centrality data shown in Fig. 5.1. The calculations are shown by solid triangles. One can see that within this model, where the collisions are derived by the centrality-defined effective c.m. energy $\varepsilon_{\rm NN}$, the model calculations are in very good overall agreement with the measurements irrespective of the collision energies discussed here. Similar results are obtained for the data taken by the of the PHENIX [188], STAR [189], or CuCu PHOBOS [139] measurements from RHIC and ALICE [190] or ATLAS [180] from LHC (not shown). However, some slightly lower values are seen in the model predictions compared to the data for some low-$N_{\rm part}$, *i.e.* for the most peripheral collisions, at $\sqrt{s_{\rm NN}} = 19.6$ GeV, and for a couple of central data points obtained at the highest $\sqrt{s_{\rm NN}}$. The deviation observed in the peripheral collisions at $\sqrt{s_{\rm NN}} = 19.6$ GeV looks to be due to the experimental limita-

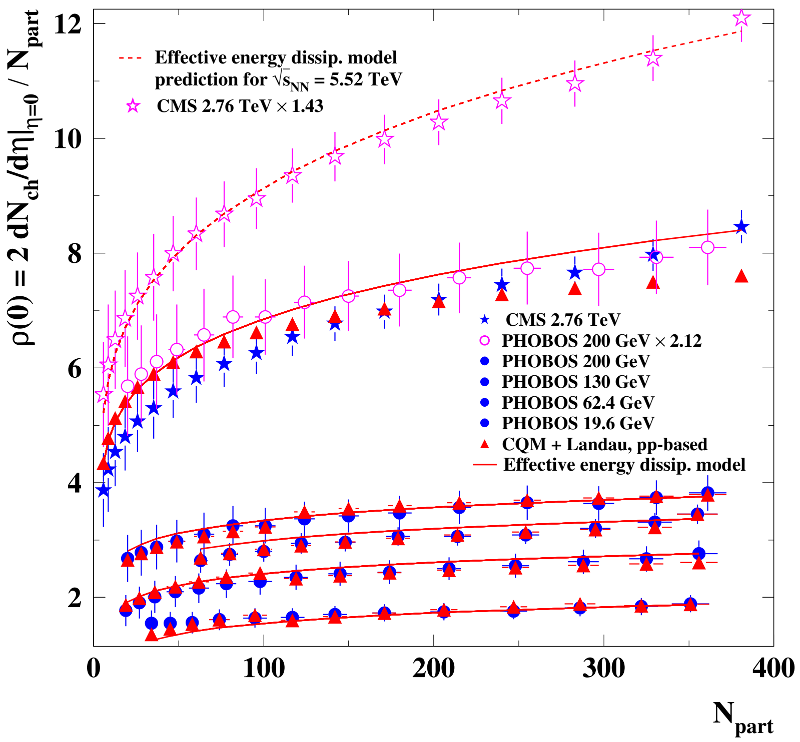

Figure 5.1. The charged particle pseudorapidity density at midrapidity per participant pair as a function of the number of participants, $N_{\rm part}$ [41].

tions and the extrapolation used in the reconstruction for the measurements in this region of very low multiplicity [139]. This may also explain the $N_{\rm part}$-scaling of the data at $\sqrt{s_{\rm NN}} = 19.6$ GeV in the most peripheral region, so the data of these centrality intervals do not follow the common trend of decreasing as it is observed in higher-energy measurements. The low values obtained in the model for a few most central collisions at the LHC energy can be explained by no data on $N_{\rm ch}^{pp}$ being available at $\sqrt{s_{pp}} > 1.8$ TeV. Moreover, for $\sqrt{s_{pp}} > 53$ GeV, the second-order logarithmic polynomial fit to the $\sqrt{s_{pp}}$ dependence of $N_{\rm ch}^{pp}$ is indistinguishable from the exponential function fit [28]. The latter regularity is used here for the $\sqrt{s_{pp}}$ dependence to calculate $N_{\rm ch}^{pp}$ above the Tevatron energy.

Given the obtained agreement between data and the model, and considering the similarity put forward for $\varepsilon_{\rm NN}$ and $\sqrt{s_{\rm NN}}$, one would expect the measured centrality data at $\varepsilon_{\rm NN}$ to follow the $\sqrt{s_{\rm NN}}$ dependence of the midrapidity density in the most central nuclear collisions. In Fig. 5.2, the measurements of the charged particle pseudorapidity density at midrapidity in head-on nuclear collisions are plotted against the $\sqrt{s_{\rm NN}}$ from a few GeV at GSI to a few TeV at the LHC along with the centrality data, shown as a function of $\varepsilon_{\rm NN}$, from low-energy RHIC data by STAR at 9.2 GeV [191], and the measurements, shown in Fig. 5.1, by PHOBOS [139] and CMS [181] experiments as a function of $\varepsilon_{\rm NN}$.

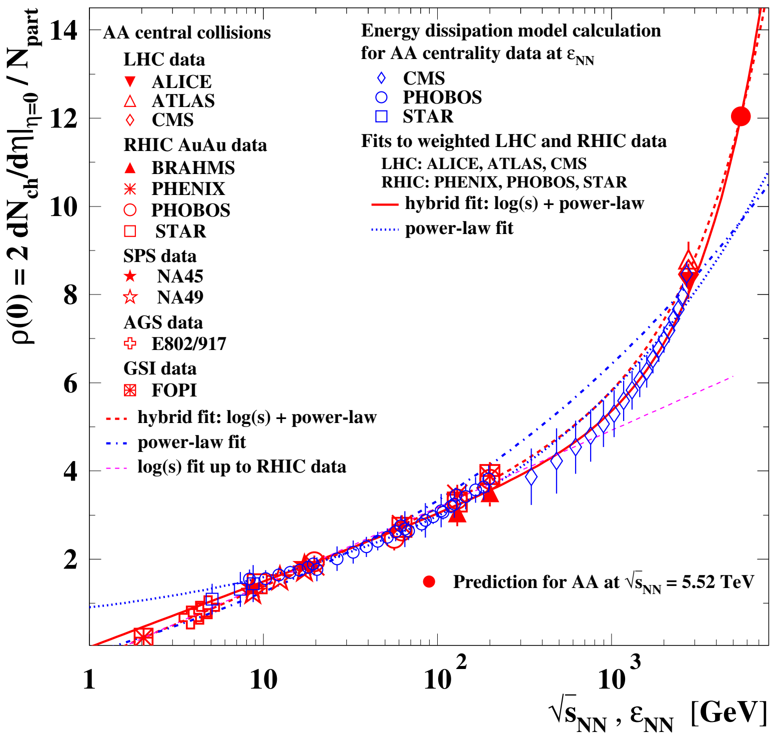

Figure 5.2. The charged particle pseudorapidity density per participant pair at midrapidity as a function of c.m. energy per nucleon, $\sqrt{s_{\rm NN}}$, in central nucleus-nucleus (AA) collisions (shown by large symbols), and as a function of effective c.m. energy, $\varepsilon_{\rm NN}$ (Eq. (5.9)), for AA collisions at different centralities (small symbols) [41].

5.2.2 Centre of Mass Energy Dependence

Figure 5.2 shows that $\varepsilon_{\rm NN}$ dependence of centrality data follow the trend of $\sqrt{s_{\rm NN}}$ dependence of most central collision data. We fit the weighted average of the midrapidity density from the head-on collisions (when data at same $\sqrt{s_{\rm NN}}$ are taken by different experiments) by following hybrid fit function,

$$\rho(0) = (-0.306 \pm 0.027) + (0.364 \pm 0.009)\,\ln(s_{NN}/s_0) \\ +(0.0011 \pm 0.0011)\,(s_{NN}/s_0)^{(0.50 \pm 0.06)}. \quad (5.11)$$

Here, $s_0 = 1$ GeV^2. In subsequent discussions, the factor s_0 is taken the same in all fit functions and omitted for brevity. The hybrid function is, as it is noticed above, inspired by the measurements and supported by theoretical considerations. The fit combines the linear-log dependence on $\sqrt{s_{\rm NN}}$ observed up to the top RHIC energy [139, 188] and the power-law dependence obtained with the LHC data [180–182]. This fit is shown in Fig. 5.2 by the dashed line. One can see that the fit is as well close to the centrality data. To clarify, the weighted average of the centrality data, as discussed above, are also fitted by the hybrid function,

$$\rho(0) = (0.002 \pm 0.080) + (0.646 \pm 0.022)\,\ln(\varepsilon_{NN}/\varepsilon_0) \\ +(0.0003 \pm 0.0001)\,(\varepsilon_{NN}/\varepsilon_0)^{(1.158 \pm 0.034)}, \quad (5.12)$$

here, $\varepsilon_0 = 1$ GeV^2. In subsequent discussions, the factor ε_0 is taken the same in all fit functions and omitted for brevity. In addition to the low-energy STAR data and the measurements, shown in Fig. 5.1, by the PHENIX and CMS experiments, the midrapidity density data on the centrality dependence from ALICE [190], ATLAS [180], PHOBOS [139] and STAR [189] are included (not shown). The fit is shown by the solid line and is very close to the fit made to the centrality data. From this one can conclude that the model well reproduces the data under the assumption of the effective energy deriving the multiparticle production process pointing to the similarity in all the data from peripheral to the most central measurements to follow the same energy behaviour. From the fit, we estimate the midrapidity density value to be of about 12.0 in the most central collisions at $\sqrt{s_{\rm NN}} = 5.52$ TeV, which is shown by the solid circle in Fig. 5.2.

In addition to the hybrid fits, in Fig. 5.2 we show the linear-log fit [115] up to the top RHIC energy (thin dashed line) and the power law fit for the entire energy range (dashed-dotted line) to the most central collision data along with the power law fit to the centrality data (dotted line). All the fits are made by using the weighted average data as above. One can see that the power-law fit describes well the head-on collision measurements [170] within the error bars, which does not differ from the linear-log or the hybrid functions up to the RHIC energies. However, it deviates from the most central collision hybrid fit as soon as the LHC measurements are included. The power-law fit to the centrality data are much closer to the hybrid fits, and it is almost indistinguishable from the hybrid fit to the central data up to the head-on collision LHC points. Both the power-law fits, to the head-on collision data and to the centrality data, give predictions close to each other but lower than the hybrid fits. Interestingly, using the PDE approach, one can clearly see the transition to a possibly new regime in the multihadron production in heavy-ion collisions demonstrated by the data as $\sqrt{s_{\rm NN}}$ increases up to about 600–700 GeV. The centrality data still follow the central collision data and the log fit up to these energies while then the energy behaviour changes to the power-law one. The change in the $\sqrt{s_{\rm NN}}$-dependence from the logarithmic to the power-law one seems to be a reason of lower-value predictions by theoretical models [182]. The change also restrains predictions for heavy-ions within the universality picture [115], which however gives the correct predictions for $p + p(\bar{p})$ [173], where both the logarithmic [192] and the power-law [181] functions provide equally good fits to the data up to $\sqrt{s_{pp}} = 7$ TeV.

Now, using the effective c.m. energy approach, we apply the obtained hybrid function fit of the midrapidity density measured in head-on collision data, Eq. (5.11), to the centrality data, shown in Fig. 5.1 as a function of $N_{\rm part}$. The calculations are shown by the solid lines. One can see that the model well describes the measurements and actually follows the predictions by Eq. (5.10), except the LHC data, where it is better than the calculations of Eq. (5.10), though slightly overshoots the measurements. Similar to the model combining constituent quarks and Landau hydrodynamics, the calculations using the effective energy $\varepsilon_{\rm NN}$ show lower values for the very peripheral points at the lowest c.m. energy, $\sqrt{s_{\rm NN}} = 19.6$ GeV. The difference, as mentioned above, seems to be due to the difficulties in the measurements because of the very low multiplicity in these data. A slight overestimation of the LHC data is due to the fact that the fit (Eq. 5.11) uses the highest centrality (0-2%) ATLAS data of the head-on collisions.

Similar to the above calculations for the existing data on the $N_{\rm part}$-dependence of the midrapidity density, we made the predictions for the forthcoming heavy-ion collisions at $\sqrt{s_{\rm NN}} = 5.52$ TeV. The predictions are shown by the dashed line in Fig. 5.1, where the centrality and $N_{\rm part}$ values are taken as in the 2.76 TeV data. The expectations show increase of the $\rho(0)$ with $N_{\rm part}$ (decrease with centrality) from about 5 to 12. The increase looks to be faster than at $\sqrt{s_{\rm NN}} = 2.76$ TeV, especially in the peripheral region. Similar kind of change in behaviour has been seen as one moves from the RHIC 200 GeV to the LHC 2.76 TeV measurements, shown in Fig. 5.2. We find that the predictions made here are well reproduced when the LHC data are scaled by a factor 1.43, similar to the multiplication factor (of 2.12 shown here) found [180, 181, 190] to reproduce the 2.76 TeV LHC data by the 200 GeV RHIC ones.

Recently, ALICE has recorded data at $\sqrt{s_{\rm NN}} = 5.02$ TeV for Pb+Pb collisions [40] and the results have been reported on charged particle pseudorapidity as shown in Fig. 5.3. According to the consideration, Eq. 5.10, the calculations are made at $\sqrt{s_{pp}} = 3\varepsilon_{\rm NN}$. The midrapidity density $\rho_{pp}(0)$ and the multiplicity $N_{\rm ch}^{pp}$ are taken from the existing $p+p(\bar{p})$ data [28, 193], and the $N_{\rm ch}$ values are taken from the heavy-ion collision data [194, 195] where available, while otherwise the corresponding experimental c.m. energy fits are applied. The calculations use the power-law fits for $N_{\rm ch}^{pp}$ [28] and for ρ_{pp} at $\sqrt{s_{pp}} > 53$ GeV [181], the linear-log fit [28] for ρ_{pp} at $\sqrt{s_{pp}} \leq$ 53 GeV, and the "hybrid" $\sqrt{s_{\rm NN}}$ fit [41] for $N_{\rm ch}$. From Fig. 5.3 one can see that within PDE approach calculations show a very good overall agreement with the recent ALICE measurements at 5.02 TeV.

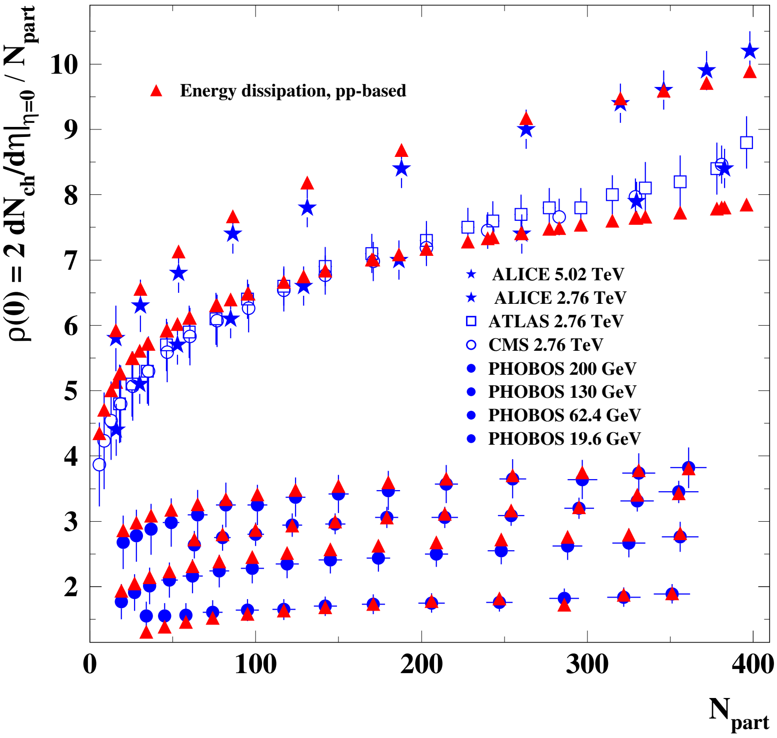

Figure 5.3. The charged particle pseudorapidity density at midrapidity per participant pair as a function of the number of participants, N_{part}. The calculations within PDE approach (solid triangles) show a good agreement with recent data (upper most solid stars) taken by ALICE at 5.02 TeV [194].

5.3 Transverse Energy Pseudorapidity Density

5.3.1 Centre of Mass Energy Dependence

The effective c.m. energy approach is also applied to another important global observable, such as the pseudorapidity density of the transverse energy, $\rho_{\text{T}}(\eta) = (2/N_{\text{part}})\, dE_{\text{T}}/d\eta$, at midrapidity, $\eta \approx 0$. The charged particle density and the transverse energy density are closely related and have been studied together to provide important characteristics of the underlying dynamics of the multihadron production. The transverse energy measurements, as well as the pseudorapidity data, have been shown to be reasonably well modelled by the constituent quark picture [122, 125, 166].

In Fig. 5.4, the $\sqrt{s_{\text{NN}}}$ dependence of the $(dE_{\text{T}}/d\eta)(N_{\text{part}}/2)$ at midra-

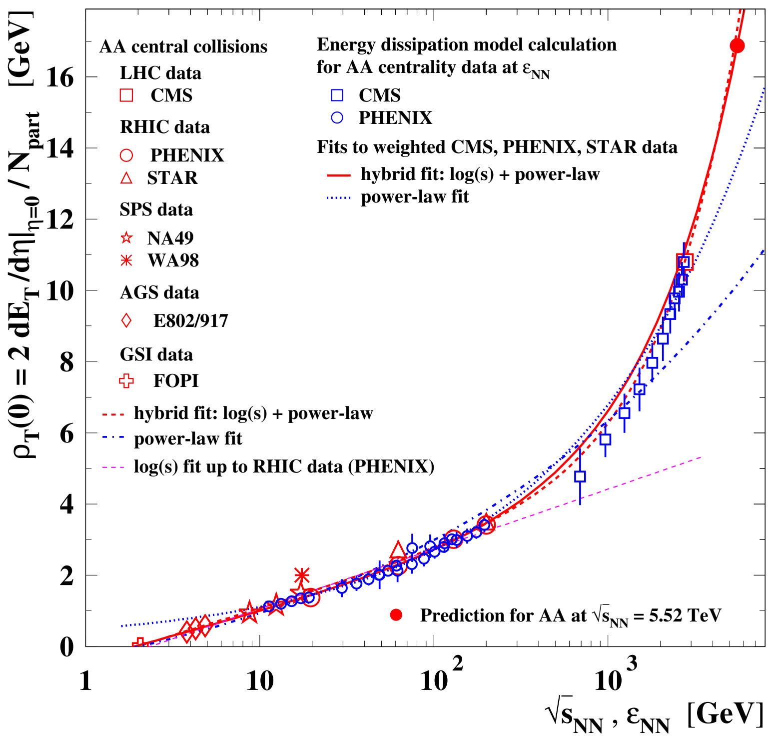

Figure 5.4. The charged particle transverse energy pseudorapidity density per participant pair at midrapidity as a function of c.m. energy per nucleon, $\sqrt{s_{\rm NN}}$, in central nucleus-nucleus (AA) collisions (shown by large red symbols), and as a function of effective energy, $\varepsilon_{\rm NN}$ (Eq. (5.9)), for AA collisions at different centrality (small blue symbols) [41].

pidity is displayed as measured in head-on collisions at the experiments from a few GeV at GSI to a few TeV at the LHC, shown by the big symbols. On top of these data, the centrality data from the PHENIX experiment at RHIC [125] and the CMS experiment at LHC [196] are added as a function of the effective c.m. energy, $\varepsilon_{\rm NN}$, which are shown by small symbols. One can see that centrality data follow well the head-on collision data, similar to the case of the charged particle density at midrapidity.

To better trace the similarity in the energy dependence of the central collision and the centrality-dependent data, we fit the data by the hybrid function, as is done in Fig. 5.2 for pseudorapidity densities of the particles. For the central collisions one gets:

$$\rho_T(0) = (-0.447 \pm 0.014) + (0.327 \pm 0.011)\,\ln(s_{NN}) + (0.002 \pm 0.003)\, s_{NN}^{0.50\pm0.08}, \quad (5.13)$$

and similar fit to the centrality data reads:

$$\rho_T(0) = (-0.387 \pm 0.090) + (0.574 \pm 0.032)\,\ln(\varepsilon_{NN}) + (0.011 \pm 0.005)\, \varepsilon_{NN}^{0.818\pm0.064}\,. \quad (5.14)$$

The fits of Eqs. 5.13 and 5.14 are shown in Fig. 5.4 by the dashed and solid lines, respectively. The data from different experiments at the same c.m. energy are weighted. One can see that the two fits are amazingly close to each other for the entire energy range. This allows to conclude that the effective energy approach provides a good description of the E_{T} production in heavy-ion collisions. We estimate the value of $\rho_{\mathrm{T}}(0)$ to be about 16.9 GeV for most central collisions at $\sqrt{s_{\mathrm{NN}}} = 5.52$ TeV shown by the solid circle in Fig. 5.4. One can see that the LHC data demonstrate a clear departure from the linear-log regularity in the region of $\sqrt{s_{\mathrm{NN}}} \simeq 500 - 700$ GeV; the log fit to the data up to the top RHIC energy is shown by the thin dashed line and is taken from Ref. [188]. This observation supports a possible transition to a new regime in heavy-ion collisions at $\sqrt{s_{\mathrm{NN}}}$ above a few hundred GeV as indicated by the midrapidity density in Fig. 5.2. In Fig. 5.4, we also show the power-law fits to the central collision measurements by the dashed-dotted line and to the centrality data by the dotted line. As above, in the fits, the data from different experiments at the same c.m. energy are weighted. One can see that the power-law fit to the central collision data underestimates the LHC measurement at 2.76 TeV data and deviates from the data at $\sqrt{s_{\mathrm{NN}}} \sim 1$ TeV. However, the power-law fit to the centrality data describes well the data in the full available c.m.-energy region, though lies slightly lower than the hybrid fit, Eq. (5.14). The fit overestimates the data below $\sqrt{s_{\mathrm{NN}}} \approx 10$ GeV, similar to the case of the centrality data of multiplicity density (Fig. 5.2). Interestingly, the shown power-law fit curve to the centrality data is similar to that reported by CMS experiment [196]. Here CMS has made the power-law fit for $\sqrt{s_{\rm NN}} \geq 8.7$ GeV including its 2.76 TeV measurements at LHC. This again demonstrates the multihadron production in heavy-ion collisions to be well described by the effective c.m. energy dissipation model.

5.3.2 Centrality Dependence

To further exploit the effective energy approach with the centrality data, in Fig. 5.5, we show the $N_{\rm part}$ dependence of the centrality data along with the central collision data fit, Eq. (5.13), but as a function of the centrality-dependent c.m. effective energy, $\varepsilon_{\rm NN}$.

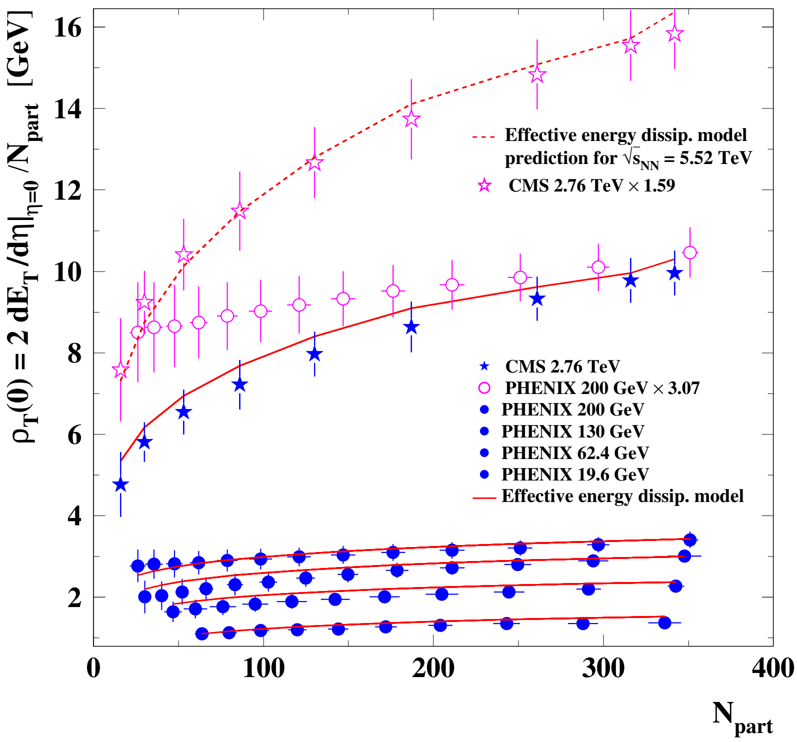

Figure 5.5. The charged particle transverse energy pseudorapidity density at midrapidity per participant pair as a function of the number of participants, $N_{\rm part}$ [41].

One can see that the fit well describes the data. In this case, the agreement is even better than for the midrapidity density, as one concludes from the comparison with the LHC centrality data. The PHENIX data at $\sqrt{s_{\rm NN}}$ = 200 GeV scaled by 3.07, are shown to allow comparison with the LHC data. Interestingly, the PHENIX data demonstrate much less decrease as the centrality increases (more peripheral data), than that observed for the LHC data. This is different from the $(dN_{\rm ch}/d\eta)(N_{\rm part}/2)$ measurements at midrapidity, which is shown in Fig. 5.1. In contrast to the scaled PHENIX data, the effective energy approach (continuous red line) follows well the LHC measurements.

Similar to the above comparison to the existing data on the $N_{\rm part}$-dependence of the midrapidity transverse energy density, we make the predictions for the future heavy-ion collisions at $\sqrt{s_{\rm NN}}$ = 5.52 TeV within the PDE approach. The predictions are shown by the dashed line in Fig. 5.4. The predictions show more rapid increase of the $\rho_{\rm T}(0)$ with $N_{\rm part}$ (decrease with centrality) than at $\sqrt{s_{\rm NN}}$ = 2.76 TeV, especially for the peripheral region. The similar change in behaviour has been seen as one moves from the RHIC to the LHC measurements. The charged particle pseudorapidity density also shows a similar kind of behaviour (Fig. 5.2). We find that the predictions made are well reproduced as the LHC data are scaled by a numerical factor 1.59, as shown by open stars in Fig. 5.5.

5.4 Charged Particle Mean Multiplicity

Solving Eq. (5.5) for the charged particle multiplicity $N_{\rm ch}$ at a given rapidity density $\rho(0)$ at $\sqrt{s_{\rm NN}}$ for A+A collisions, and for the rapidity density $\rho_{pp}(0)$ and the multiplicity $N_{\rm ch}^{pp}$ at $3\sqrt{s_{\rm NN}}$ for $p+p(\bar{p})$, one gets,

$$\frac{2N_{ch}}{N_{part}} = N_{ch}^{pp} \frac{\rho(0)}{\rho_{pp}(0)} \sqrt{\frac{L_{NN}}{L_{pp}}}\,, \tag{5.15}$$

here

$$\frac{L_{NN}}{L_{pp}} = 1 - \frac{2\ln 3}{\ln(4.5\sqrt{s_{NN}}/m_p)}, \tag{5.16}$$

combining Eq. 5.16 and Eq.5.15 we get,

$$\frac{2N_{ch}}{N_{part}} = N_{ch}^{pp} \frac{\rho(0)}{\rho_{pp}(0)} \sqrt{1 - \frac{2\ln 3}{\ln(4.5\sqrt{s_{NN}}/m_p)}}\,,$$
$$\sqrt{s_{NN}} = \sqrt{s_{pp}}/3\,. \tag{5.17}$$

In the form of effective centre of mass energy $\varepsilon_{\rm NN}$, Eq. (5.17) reads:

$$\frac{2\,N_{ch}}{N_{part}} = N_{ch}^{pp} \frac{\rho(0)}{\rho_{pp}(0)} \sqrt{1 - \frac{2\ln 3}{\ln(4.5\,\varepsilon_{NN}/m_p)}}\,,$$
$$\varepsilon_{NN} = \sqrt{s_{pp}}/3\,, \tag{5.18}$$

where $\rho(0)$ is the midrapidity density in central nucleus-nucleus collisions measured at $\sqrt{s_{\rm NN}} = \varepsilon_{\rm NN}$.

5.4.1 Centre of Mass Energy Dependence

Figure 5.6 shows the c.m. energy dependence of the multiplicity measured in head-on nucleus-nucleus collisions (solid symbols) in the energy range of $\sqrt{s_{\rm NN}}$ = 2 GeV to 2.76 TeV. Given the fact that the measurements support the 2nd-order logarithmic dependence on $\sqrt{s_{\rm NN}}$ up to the top RHIC energy [115, 139], while the power-law dependence is obtained for the LHC data [195], we fit the head-on data by the "hybrid" fit function,

$$\begin{aligned}\frac{2\,N_{ch}}{N_{part}} = (-0.577 \pm 0.177) + (0.394 \pm 0.094)\,\ln(s_{NN})\\ +(0.213 \pm 0.014)\,\ln^2(s_{NN})\\ +(0.005 \pm 0.009)\,s_{NN}^{(0.55\pm0.11)}.\end{aligned} \tag{5.19}$$

This fit is shown in Fig. 5.6 by the solid line. Note that from the theoretical description point of view, the logarithmic dependence is considered to characterize the fragmentation source(s) while the power-law behaviour is believed to come from the gluon-gluon interactions [183]; for a review, see Ref. [29].

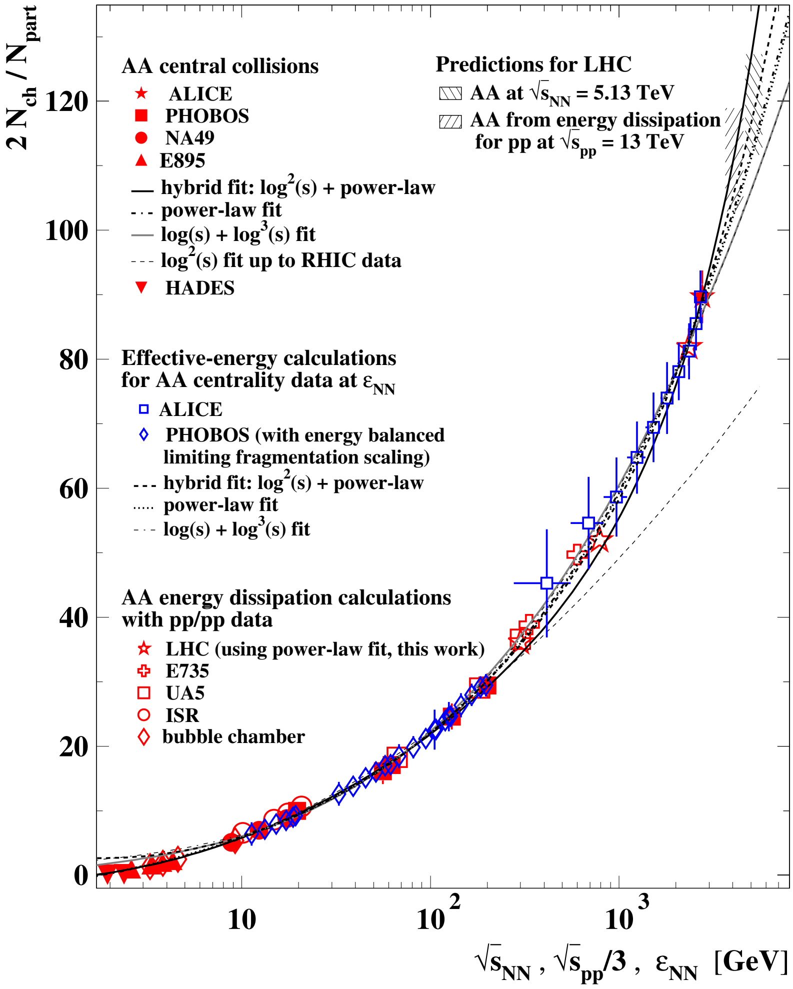

Figure 5.6. The energy dependence of the charged particle mean multiplicity per participant pair. [201]

We also fit the head-on collision multiplicities with the power-law function. The power-law dependence of the multiplicity is expected in different theoretical approaches [197–199] and the data from nuclear and $p + p(\bar{p})$ collisions seem to follow this type of behaviour at higher energies [28, 195]. The power-law fit gives:

$$\frac{2\,N_{ch}}{N_{part}} = (-6.72 \pm 1.44) + (5.42 \pm 1.11)\, s_{NN}^{(0.18 \pm 0.02)}, \tag{5.20}$$

and is shown by the dashed-dotted line in Fig. 5.6.

Recently, it was shown [200] that the multiplicity of the gluon-gluon interactions are better described within a non-equilibrium statistical relativistic diffusion model using $\log^3(s_{\rm NN})$ dependence. Using this behaviour we fit the c.m. energy dependence by the corresponding fit function,

$$\frac{2\,N_{ch}}{N_{part}} = (0.72 \pm 1.85) + (0.75 \pm 0.39)\ \ln(s_{NN}) \\ +(0.019 \pm 0.002)\ \ln^3(s_{NN}). \qquad (5.21)$$

Here, the linear-log term reflects the multiplicity from the fragmentation sources, as noticed above. The fit is shown by the pink solid line in Fig. 5.6. One can see that the fit seems to be indistinguishable from the power-law function for the entire fit range, and is slightly below the power-law behaviour above the current LHC data. Some enhancement in the low-energy range is expected due to no gluonic source considered to be present at these energies.

In addition to these fits, we show the $\log^2(s_{\rm NN})$-fit [115] up to the top RHIC energy (thin dashed line). One can see that the power-law fit well describes the data and is almost indistinguishable from the hybrid fit up to the LHC data. Some minor deviation between the two fits can be seen in the range from the top RHIC energy to the LHC energy. Meantime, the 2nd-order log-polynomial lies below the data for $\sqrt{s_{\rm NN}} > 200$ GeV. This observation supports a possible transition to a new regime in heavy-ion collisions at $\sqrt{s_{\rm NN}}$ of about 1 TeV, as indicated earlier in the studies of charged particle pseudorapidity density and transverse energy density at midrapidity [41].

Addressing now Eq. (5.17), we calculate the mean multiplicity $N_{\rm ch}/(N_{\rm part}/2)$ for nucleus-nucleus interactions using the $p + p(\bar{p})$ measurements. The calculated values are shown in Fig. 5.6 by large open symbols. The rapidity density $\rho_{pp}(0)$ and the multiplicity $N_{\rm ch}^{pp}$ are taken from the existing data [193] or, where not available, calculated using the corresponding experimental $\sqrt{s_{pp}}$ fits at $\sqrt{s_{pp}} = 3\,\sqrt{s_{\rm NN}}$, in accordance with the approach considered here. The $\rho(0)$ values are taken from the measurements in central heavy-ion collisions wherever available, while for the non-existing data the experimental fit is used.

One can see that the calculated $N_{\rm ch}/(N_{\rm part}/2)$ values follow the measurements from nucleus-nucleus collisions at $\sqrt{s_{\rm NN}}$ from a few GeV up to the TeV LHC energy. The observed agreement between the heavy-ion measurements of $N_{\rm ch}/(N_{\rm part}/2)$ and the values obtained from the $p+p(\bar{p})$-based calculations points to the universality of the multiparticle production process in different types of collisions [201].

Solving Eq. (5.17) for the mean multiplicity $N_{\rm ch}^{pp}$ in $p+p(\bar{p})$ collisions, we estimate its values for $\sqrt{s_{pp}} >$ 2 TeV to be about 47 at $\sqrt{s_{pp}} = 2.36$ TeV, 67 at 7 TeV, and 79 at 13 TeV with 5% uncertainties. Here for the calculations, one uses the fit to the heavy-ion midrapidity density data $\rho(0)$, as described above, and the fit by ALICE to the head-on heavy-ion data on the mean multiplicity [195] (similar to the results of the fits of Eqs. (5.19) and (5.20)), along with the LHC measurements [192, 202–204] of the pseudorapidity density $\rho_{pp}(0)$. The calculated values of $N_{\rm ch}^{pp}$ are shown as a function of $\sqrt{s_{pp}}$ by open stars in Fig. 5.7, along with the existing multiplicity measurements from $p+p(\bar{p})$ collisions.

The measured $N_{\rm ch}^{pp}$ dependence on $\sqrt{s_{pp}}$ in the energy range spanning the interval between a few GeV to 1.8 TeV are fitted with the power-law, 2nd-order log-polynomial and the hybrid functions. The hybrid and the power-law fits read,

$$N_{ch}^{pp} = (1.60 \pm 0.23) + (-0.03 \pm 0.10)\, \ln(s_{pp})$$
$$+(0.18 \pm 0.01)\, \ln^2(s_{pp}) + (0.03 \pm 0.02)\, s_{pp}^{(0.29 \pm 0.06)}, \qquad (5.22)$$

and

$$N_{ch}^{pp} = (-7.36 \pm 0.16) + (6.97 \pm 0.12)\, s_{pp}^{(0.133 \pm 0.001)}, \qquad (5.23)$$

respectively.

From Fig. 5.7 one can conclude that the available data do not give any

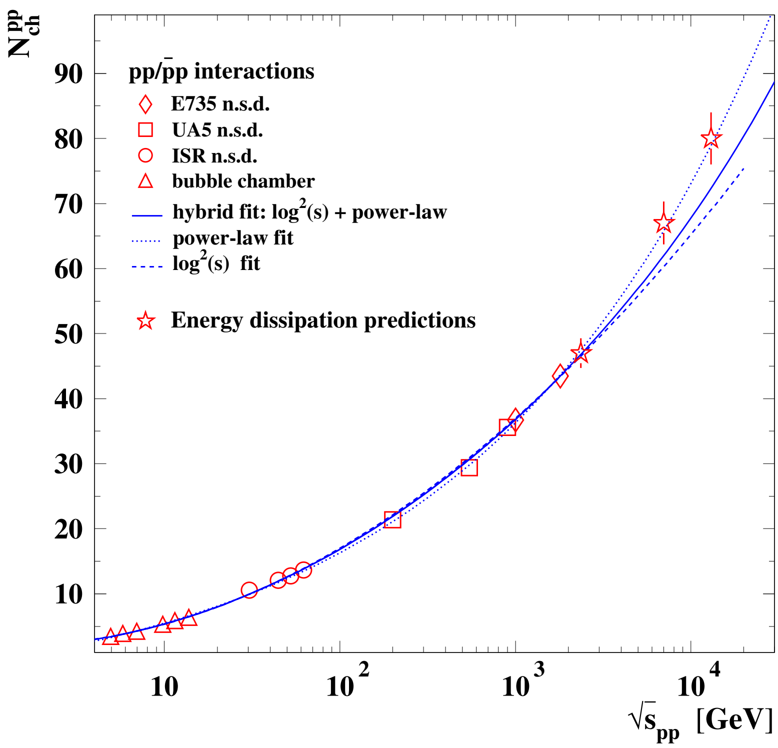

Figure 5.7. The c.m. energy dependence of the charged particle mean multiplicity in $p + p(\bar{p})$ collisions [201].

preference to one or another fit function. This is similar to the pre-LHC observations where the power-law fit were found to be indistinguishable from the log^2-polynomial fit at $\sqrt{s_{pp}} > 53$ GeV [28]. Interestingly, these two functions are also found to fit equally well the non-single diffractive midrapidity density, as obtained by CMS experiment and are reported in Ref. [181, 192]. The fit functions start to deviate from each other at the c.m. energy above a few TeV but still not far from each other even at $\sqrt{s_{pp}} \sim 10$ TeV. This may point to apparently no change in the multihadron production in $p+p(\bar{p})$ interactions up to the highest LHC energy, in contrast to a new regime possibly emerging at $\sqrt{s_{\rm NN}} \approx 1$ TeV in heavy-ion collisions.

It is remarkable how well the PDE predictions on $N_{\rm ch}^{pp}$ at $\sqrt{s_{pp}} >$ 2 TeV follow the power-law fit made to the measurements for $\sqrt{s_{pp}} \leq 1.8$ TeV. This and the above-indicated no-change in the hadroproduction in $p + p(\bar{p})$ collisions as soon as one moves to TeV energies, both are in an agreement with the prediction [115], which seems to be the only successful one for the midrapidity density in $p+p(\bar{p})$ collisions at $\sqrt{s_{pp}} = 7$ TeV [173].

5.4.2 Centrality Dependence

In this section, we address the point whether the centrality dependence of the mean multiplicity from heavy-ion experiments is described by Eq. (5.18), similar to the midrapidity pseudorapidity density in Fig. 5.1 [41]. In Fig. 5.8, we show the N_{part}-dependence of $N_{\text{ch}}/(N_{\text{part}}/2)$. The data are taken from the measurements by the PHOBOS experiment at RHIC [139] and by the ALICE experiment at LHC [205]. The solid triangles show the estimations using Eq. (5.18). As above, in the case of the $\sqrt{s_{\text{NN}}}$-dependence, the rapidity densities $\rho_{pp}(0)$ and $\rho(0)$, and the multiplicity N_{ch}^{pp} are taken from the existing data [193] or, where not available, are calculated from the fits described above. According to the consideration developed here, $\rho(0)$ is taken at $\sqrt{s_{\text{NN}}} = \varepsilon_{\text{NN}}$, and $\rho_{pp}(0)$ and N_{ch}^{pp} are taken at $\sqrt{s_{pp}} = 3\,\varepsilon_{\text{NN}}$.

One can see that the calculations, which are driven by the centrality-defined effective c.m. energy, ε_{NN}, well reproduce the LHC data except slightly underestimating a couple of the most peripheral measurements. For the RHIC data, however, the difference between the calculations and the measurements is visible already for medium centralities, *i.e.*, for more central collisions. These observations are also interrelated with the difference observed in the measurements at RHIC *vs.* those from LHC. Indeed, at RHIC, the $N_{\text{ch}}/(N_{\text{part}}/2)$ is found to be independent of centrality, while a monotonic increase with N_{part} is observed at the LHC. This becomes even clearer when the 200 GeV PHOBOS data are multiplied by a factor of 2.87 (open circles in Fig. 5.8), which allows matching the ALICE data from the highly central collisions.

In Fig. 5.8, the above-obtained c.m. energy fit, Eq. (5.19), made to the head-on collision data, is applied to the centrality measurements at $\sqrt{s_{\text{NN}}} = \varepsilon_{\text{NN}}$ and the results are shown by the dashed lines. The observations made for the calculations are valid here as well. This points

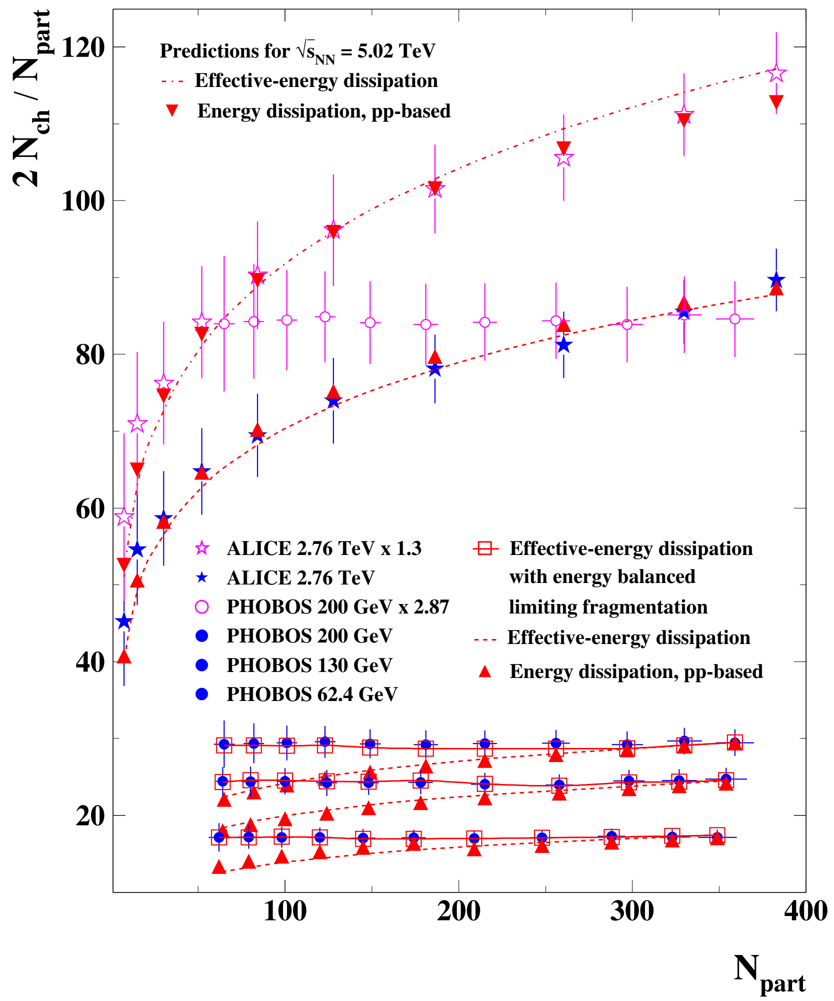

Figure 5.8. The charged particle mean multiplicity per participant pair as a function of the number of participants, N_{part} [201].

to the complementarity of central collisions and centrality data once the calculations are made in terms of the c.m. effective-energy, ε_{NN}.

To clarify the observed differences, in the following sections the distributions of the pseudorapidity density are investigated in the context of the PDE picture considered here.

5.5 Pseudorapidity Density Distribution in Heavy-ion Collisions: Central *vs.* Non-central Collisions

Figure 5.9 shows the distributions of $(dN_{\rm ch}/d\eta)/(N_{\rm part}/2)$ measured in head-on and more central heavy-ion collisions and in $p+p(\bar{p})$ interactions. The heavy-ion data represent the PHOBOS measurements made in Au+Au collisions at the RHIC at $\sqrt{s_{\rm NN}}$ = 19.6, 62.4 and 200 GeV [139] and the ALICE measurements from Pb+Pb collisions at the LHC at $\sqrt{s_{\rm NN}} = 2.76$ TeV [195]. The distributions from $p+p(\bar{p})$ interactions are taken as measured by the UA5 experiment [206] at $\sqrt{s_{pp}}$ = 53 GeV at the ISR, at $\sqrt{s_{pp}}$ = 200 GeV by the P238 experiment at the SPS [207] and by the CDF experiment at the Tevatron at $\sqrt{s_{pp}}$ = 630 GeV [208]. We also use measurements at $\sqrt{s_{pp}}$ = 7 TeV by the CMS [192], LHCb [209] and TOTEM [210] experiments at the LHC. The data shown are taken at the c.m. energies $\sqrt{s_{pp}} \approx 3\sqrt{s_{\rm NN}}$ or $3\,\varepsilon_{\rm NN}$. Except for the CMS measurements, the negative-η data points from $p+p(\bar{p})$ interactions are the reflections of the measurements taken in the positive-η region.

Within the considered approach of constituent quarks and the Gaussian form of the pseudorapidity distribution in Landau hydrodynamics, the relationship between the pseudorapidity density distributions $\rho(\eta)$ and $\rho_{pp}(\eta)$ reads

$$\frac{\rho(\eta)}{\rho_{pp}(\eta)} = \frac{2N_{ch}}{N_{part}\,N_{ch}^{pp}}\sqrt{1+\frac{2\ln 3}{L_{NN}}}\,\exp\left[\frac{-\eta^2}{L_{NN}\,(2+L_{NN}/\ln 3)}\right]. \tag{5.24}$$

Here, all variables are defined the same way as in Eq. (5.5), *i.e.*, taking into account the constituent quark scaling of the c.m. energy as soon as one relates $p+p(\bar{p})$ interactions to central heavy-ion collisions.

Using Eq. (5.24), the heavy-ion distributions are calculated based on the $\rho_{pp}(\eta)$ spectra shown in Fig. 5.9. The calculated distributions are shown

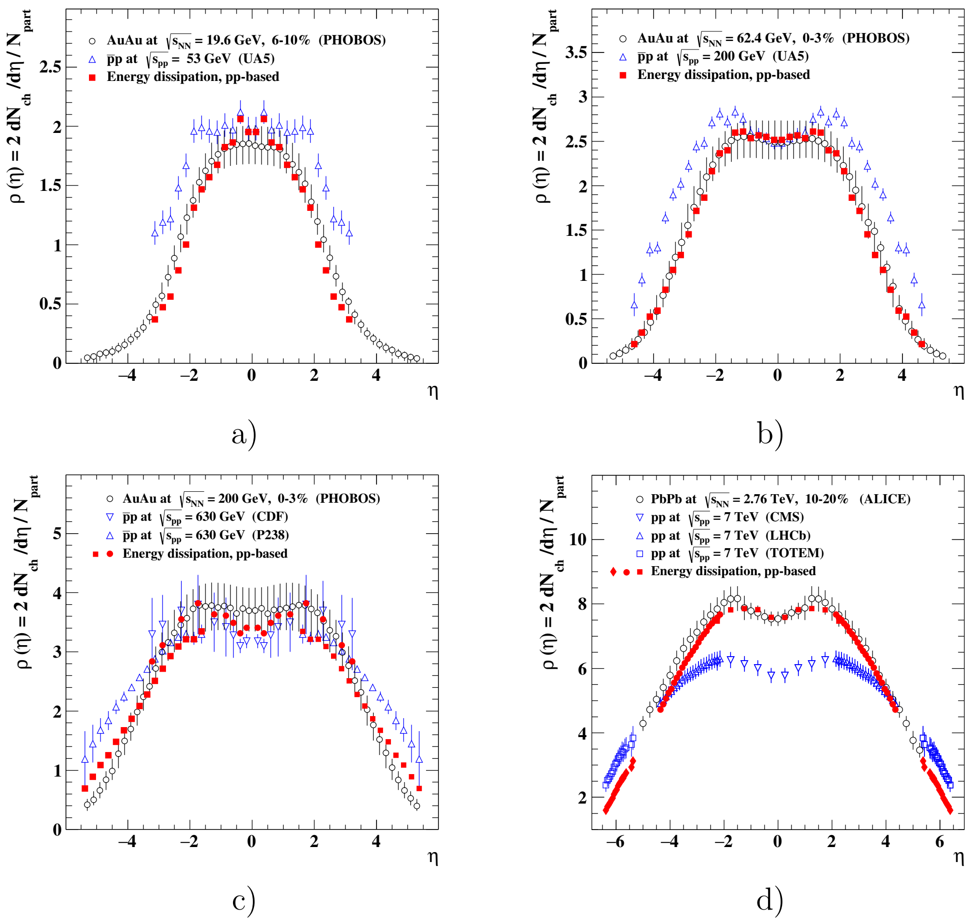

Figure 5.9. The pseudorapidity distributions of charged particle pseudorapidity density per participant pair [201].

by solid symbols in Fig. 5.9.

One can see that the calculations are in very good agreement with the measurements. Minor deviations are due to some mismatch between $\sqrt{s_{pp}}$ and $3\sqrt{s_{\rm NN}}$ (or $3\,\varepsilon_{\rm NN}$) and, as expected, due to a slight non-centrality. This is especially visible at $\sqrt{s_{\rm NN}} = 19.6$ GeV, where the energy mismatch is of a largest fraction. It is noticeable how well the PDE picture allows one to reproduce the pseudorapidity density distributions from heavy-ion interactions in the full-η range, from central-η to forward-η regions, in the $\sqrt{s_{\rm NN}}$ range spanning over more than two orders of magnitude. Remarkably, the pseudorapidity density distributions, measured in $p + p(\bar{p})$ collisions, despite being above those measured in heavy-ion collisions at 19.6 GeV or, on the contrary, lying far below the heavy-ion data from the LHC almost in the full-η range, equally well reproduce the heavy-ion data as soon as being recalculated within the PDE approach. Interestingly, the calculations at the LHC energies, well reproduce the heavy-ion pseudorapidity spectra data despite the fact that the $p + p(\bar{p})$ measurements are from three different experiments and are combined to have the distribution over full pseudorapidity. A slight deviation in the negative-η region is due to some asymmetry in the ALICE data.

Let us now address peripheral collisions to clarify the deviation in centrality dependence between the data and the calculations as it is observed in Fig 5.8. In Fig. 5.10(a) the distribution $\rho(\eta)$ measured [139] in Au+Au collisions by the PHOBOS experiment at $\sqrt{s_{\rm NN}} = 130$ GeV at 45-50% centrality, $\alpha = 0.475$, is shown along with the $\rho_{pp}(0)$ distribution measured in $p + \bar{p}$ collisions by the UA5 experiment at $\sqrt{s_{pp}} = 200$ GeV [206], *i.e.*, at $\sqrt{s_{pp}} \approx 3\,\varepsilon_{\rm NN}$ according to our approach.

Applying Eq. (5.24), we calculate the $\rho(\eta)$ spectrum, which is shown in Fig. 5.10(a) by solid squares. The calculations agree well with the measurements in the central-η region while fall below the data outside this region. This finding shows that in non-central collisions, the calculations within the PDE approach reproduces well the pseudorapidity density around the midrapidity while underestimate the mean multiplicity.

Let us clarify the obtained features through the following discussions.

In the PDE picture proposed here, the global observables are defined by the energy of the participating constituent quarks pumped into the overlapped zone of the colliding nuclei. Hence, the bulk production is driven by the initial energy deposited at zero time at rapidity $\eta = 0$, similar to the Landau hydrodynamics. Then, as it is expected and commented just above, the pseudorapidity density at midrapidity is well reproduced for all types of nuclear collisions, from the most central to peripheral ones. Similarly, the centrality dependence of the transverse energy density at midrapidity is well reproduced by the calculations and complements the c.m. energy dependence of the head-on data. Note that this similarity in the $dN_{\rm ch}/d\eta$ and the $dE_{\rm T}/d\eta$ is in accordance with the same functional form of the (pseudo)rapidity density distribution obtained either in the longitudinally expanding system considered in the original Landau model or when the development in the transverse direction is included [211–213].

From Fig. 5.10(a), one can see that the calculated distribution $\rho(\eta)$ is narrower than that of the data. The narrowness of the calculated distribution with respect to the measured one is explained by a smaller value of $\varepsilon_{\rm NN}$ compared to the value of the actual collision energy, $\sqrt{s_{\rm NN}}$. However, the calculations in Eq. (5.24) are made with the multiplicity, $N_{\rm ch}$, taken from the most central nucleus-nucleus collisions at the c.m. energy equal to $\varepsilon_{\rm NN}$ for the midrapidity density $\rho(0)$. In other words, in the approach applied here, similar to the Landau hydrodynamics, the collisions of nuclei are treated head-on-like.

5.6 Energy Balanced Limiting Fragmentation

It is established that at high enough energies, in different types of interactions the pseudorapidity density spectra, measured at different c.m. energies become similar in the fragmentation region. It means that they are independent of a projectile frame (which is the beam or target rest frame) for the same type of colliding objects, *i.e.* being considered as a function of $\eta' = \eta - y_{\rm beam}$, where $y_{\rm beam} = \ln(\sqrt{s_{\rm NN}}/m_p)$ is the beam rapidity [27, 174]. This observation obeys the hypothesis of the limiting fragmentation scaling [214].

Considering the limiting fragmentation hypothesis within the effective-energy approach, one expects the limiting fragmentation scaling of the distribution $\rho(\eta)$, which is measured at $\sqrt{s_{\rm NN}}$, to be similar to that of the calculated distribution but taken at the effective energy, $\varepsilon_{\rm NN}$. Note that the limiting fragmentation phenomenon, though being expected as an universal phenomenon for the Gaussian form of $\rho(\eta)$ [174, 215, 216],

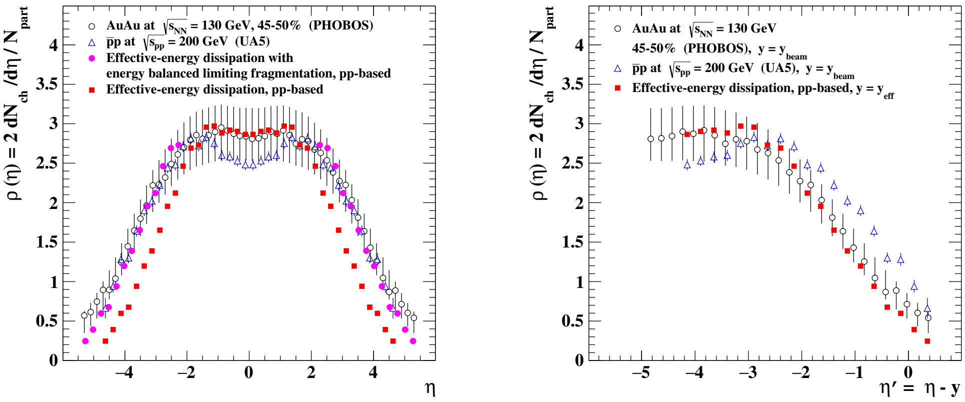

a) b)

Figure 5.10. (a) The charged particle pseudorapidity density per participant pair as a function of pseudorapidity. (b) Same as (a) but the measured distributions of Au+Au and $p + p(\bar{p})$ collisions are shifted by the beam rapidity, $\eta' = \eta - y_{\text{beam}}$, with $y_{\text{beam}} = \ln(X/m_p)$, where X is, correspondingly, $\sqrt{s_{\text{NN}}}$ or $\sqrt{s_{pp}}$, and the calculated distribution is shifted to $\eta' = \eta - y_{\text{eff}}$ with $y_{\text{eff}} = \ln(\varepsilon_{\text{NN}}/m_p)$. The distribution measured in Au+Au collisions and the calculated distribution coincide in the fragmentation region, when being shifted by y_{beam} for Au+Au data and by y_{eff} for the calculations, that represent the energy balanced limiting fragmentation scaling [201].

naturally arises in Landau hydrodynamics [163].

In Fig. 5.10(b), the limiting fragmentation hypothesis is applied to both the measured and the calculated pseudorapidity density distributions $\rho(\eta)$ from Fig. 5.10(a) using the c.m. energy and the effective energy, respectively. Therefore the measured distribution $\rho(\eta)$ is shifted by the beam rapidity, y_{beam}, while the calculated distribution from Eq. (5.24) is shifted by $y_{\text{eff}} = \ln(\varepsilon_{\text{NN}}/m_p)$ and becomes a function of $\eta' = \eta - y_{\text{eff}}$, as expected. One can see that the calculated $\rho(\eta')$ distribution of non-central heavy-ion collisions agrees well with the measured distribution $\rho(\eta')$. This finding points to a new energy scaling as soon as the effective-energy approach is applied. In analogy with the limiting fragmentation scaling, we call the observed scaling " the energy balanced limiting fragmentation scaling". Due to this scaling, the calculated pseudorapidity density is getting corrected outside the central-η region accordingly.

To this end, in Fig. 5.10(a), the calculated distribution $\rho(\eta)$ is shifted by the difference $(y_{\text{eff}} - y_{\text{beam}})$ in this region: $\eta \to \eta - \ln(\varepsilon_{\text{NN}}/\sqrt{s_{\text{NN}}})$, or, using the effective energy definition, Eq. (5.9), $\eta \to \eta - \ln(1-\alpha)$. The calculated distribution $\rho(\eta)$, where the shift is applied, is shown by the solid circles in Fig. 5.10(a). The shift *balances* the energy and this brings the calculations to the measured pseudorapidity density distribution in the full-η range in non-central heavy-ion collision. It is clear that in head-on or very central collisions, α approaches zero which makes the shift negligible.

This finding allows to obtain N_{ch} within the PDE approach. Namely, the difference between the two N_{ch} values, one obtains by integrating the calculated pseudorapidity density distribution from Eq. (5.24), and another one of the same distribution but being shifted to the left by $\ln(1-\alpha)$, is added to the N_{ch} value obtained from Eq. (5.18). Where no pseudorapidity density distributions are available in $p + p(\bar{p})$ measurements at $\sqrt{s_{pp}} = 3\,\varepsilon_{\text{NN}}$, the energy balanced limiting fragmentation scaling is applied to reproduce the calculated $\rho(\eta)$: the measured distribution from a non-central heavy-ion collision is shifted by $(y_{\text{beam}} - y_{\text{eff}})$, *i.e.* $\eta \to \eta + \ln(1-\alpha)$. Then N_{ch} is calculated as above, by adding to the calculation of Eq. (5.18) the difference between the integral from the obtained shifted distribution and the measured multiplicity in this non-central heavy-ion collision.

Using this ansatz, the values of N_{ch} are calculated for each centrality for the RHIC measurements. The calculations are shown by open squares in Fig. 5.8. One can see that now the calculations well reproduce the measurements from RHIC, with no deficit in non-central collisions.

The energy balanced limiting fragmentation scaling provides an explanation of the "puzzle" between the centrality independence of the N_{part}-normalized mean multiplicity and the monotonic decrease of the normalized midrapidity pseudorapidity density with the centrality, as observed at RHIC. As shown above, the pseudorapidity density at midrapidity is determined by the effective energy of centrally colliding nucleon participants. Hence, the value of this observable increases towards head-on collisions as soon as the effective energy increases with increasing number of participants. However, the multiplicity is measured in the full η-region, so it gets additional contribution from beyond the midrapidity. In the context of the PDE picture, this contribution is due to the balance between the collision c.m. energy shared by all nucleons of colliding nuclei and the centrality-defined effective energy of the interacting participants. The more peripheral is the collision, the larger the additional contribution is. This contribution can be directly estimated by the energy balanced limiting fragmentation scaling introduced here, which leads to the scaling between the measured pseudorapidity distribution and the distribution calculated within the PDE approach.

From Fig. 5.8 one can conclude that, in contrast to the RHIC measurements, almost no additional contribution is needed for the PDE calculations of Eq. (5.18) in order to describe the LHC mean multiplicity data. As the calculations imply, they are made by considering the nucleus-nucleus collisions as head-on collisions at the c.m. energy of the value of $\varepsilon_{\mathrm{NN}}$. However, as shown above, the additional contribution to the mean multiplicity increases with increasing collision centrality, *i.e.* while going towards more peripheral collisions. For head-on collisions, however, this contribution tends to zero. It is observed that the multiplicity measurements at the LHC are well reproduced without the energy balanced additional contribution. Therefore, one concludes that in heavy-ion collisions at the LHC energies the multihadron production obeys a head-on collision regime, for all the measured centrality intervals. This points to apparently different regimes of hadroproduction occurring in heavy-ion collisions with $\sqrt{s_{\mathrm{NN}}}$ between a few hundred GeV and TeV energies. This observation supports a similar conclusion made above, which is suggested from the observation of a change of the functional type of the fit needed to describe the energy behaviour as soon as the LHC data are included (Fig. 5.6).

The discussed difference between the mean multiplicity, and hence the full pseudorapidity density distributions, measured in heavy-ion collisions at RHIC and at LHC have been earlier addressed in Ref. [183, 200], where the model of three sources, the gluon-gluon midrapidity and two quark-gluon fragmentation sources, are applied to understand the observations from experimental data. In the context of the PDE approach given here, the difference in the nature of collisions at effective c.m. energy explains different centrality dependence of the data from the two colliders. Similar to calculations in Ref. [183, 200], additional contribution from the fragmentation regions are shown to be needed at RHIC. However, no such contribution is needed at the LHC energy. Meantime, the midrapidity pseudorapidity densities measured at RHIC and at LHC do not show different behaviour with centrality and are found to be well reproduced by the PDE calculations where no preference is given to midrapidity or fragmentation sources.

There are other approaches, which also consider the three effective regions in pseudorapidity density distributions of charged particles produced in $p + p(\bar{p})$ and in heavy-ion collisions. In the string percolation model [199, 217], the fragmentation region is populated by strings of valence quarks and the midrapidity region by additional short strings between quarks and antiquarks. In other approaches, one introduces a leading particle activity within the hydrodynamic [218–221] or thermal [222] pictures of the multiparticle production processes. Like in the PDE consideration, a similarity of the mechanism of particle production in $p+p(\bar{p})$ and heavy-ion collisions is also assumed in these approaches. Whereas, within the PDE approach the leading particles resulting from the spectators are considered to be produced in nucleon-nucleon collisions, where a single quark pair interaction is assumed and no leading particle effect is implied for central nucleus-nucleus collisions, where the entire energy of the participants is considered to be available for bulk hadron production. As already noticed above, also no difference in the particle production sources in different pseudorapidity regions is assumed in the PDE approach. Then, the c.m. energy scaling due to the key picture of the constituent quarks, applied to the Landau hydrodynamics, allows revealing the universality of the multihadron dynamics in hadronic and nuclear interactions.

5.7 Effective Energy Dependence of Multiplicity in Central and Non-central collisions

Given the obtained agreement between the data and the calculations, and considering the similarity put forward for $\varepsilon_{\rm NN}$ and $\sqrt{s_{\rm NN}}$, one would expect the measured centrality data at $\varepsilon_{\rm NN}$ to follow the $\sqrt{s_{\rm NN}}$ dependence of the mean multiplicity in the most central nuclear collisions. In Fig. 5.6, the centrality measurements of $N_{\rm ch}$ by the PHOBOS [139] and the ALICE [205] experiments are added to the head-on nuclear collision data. The centrality data are plotted as a function of $\varepsilon_{\rm NN}$. Due to the above finding of the energy balanced limiting fragmentation scaling, explaining the lack of centrality dependence of the mean multiplicity at RHIC energies, these data are plotted by subtracting the energy balanced contribution. From Fig. 5.6, one concludes that effective-energy dependence of the centrality data complements the c.m. energy behaviour of the head-on collision data.

To better trace the similarity between the head-on collision and centrality data, we fit the $\varepsilon_{\rm NN}$-dependence of the centrality data by the hybrid and the power-law functions, similar to the head-on collisions. For the hybrid fit one gets

$$\frac{2\,N_{ch}}{N_{part}} = (3.04 \pm 0.60) - (1.40 \pm 0.24)\ln(\varepsilon_{NN})$$
$$+(1.12 \pm 0.04)\ln^2(\varepsilon_{NN}) + (0.032 \pm 0.028)\varepsilon_{NN}^{(0.848 \pm 0.106)}. \qquad (5.25)$$

This fit is shown by the dashed line in Fig. 5.6. This fit agrees well with the same type of the fit to the head-on collision data in the entire available energy range except $\sqrt{s_{\rm NN}} \lesssim 10$ GeV. For the $\log^3(\varepsilon_{\rm NN})$ fit function of the three-sources approach, similar to Eq. (5.21), one finds:

$$\frac{2\,N_{ch}}{N_{part}} = (1.70 \pm 1.49) + (1.18 \pm 0.54)\,\ln(\varepsilon_{NN}) \\ +(0.152 \pm 0.008)\,\ln^3(\varepsilon_{NN}). \qquad (5.26)$$

The fit is shown by the thin dashed-dotted line in Fig. 5.6, and lies on top of the analogous fit, Eq. (5.21) to the head-on data, except a slight enhancement for $\sqrt{s_{\rm NN}} \lesssim 10$ GeV, similar to the hybrid fit. The power-law $\varepsilon_{\rm NN}$-fit for the centrality data is shown by the dotted line in Fig. 5.6. It is found to be similar to the power-law $\sqrt{s_{\rm NN}}$-fit, Eq. (5.20), to the head-on collision data shown by the dashed-dotted line.

From this, one concludes that within the picture proposed here, the data are well reproduced under the assumption of the effective energy which governs the multiparticle production. This points to the the same energy behaviour in multihadron production for all types of heavy-ion collisions, from peripheral to the most central collisions.

Here, let us stress an important corollary of the PDE approach. As soon as the effective energy in nucleus-nucleus collisions determines the pseudorapidity density at midrapidity, then the midrapidity pseudorapidity densities at the same effective energy but at different c.m. energy get the same value. In other words, the densities are defined by the effective energy independent of the energy of the collision. The observation made here for the $\varepsilon_{\rm NN}$ dependence of $N_{\rm ch}$ confirms the observation made earlier for the midrapidity densities [41]. In addition, it adds another important ingredient which takes into account the additional energy balanced contribution to the mean multiplicity in non-central nucleus-nucleus collisions.

From the hybrid fits obtained, we estimate the multiplicity for the future LHC heavy-ion run. Since the hybrid fit for the head-on collision data and the fit to the centrality data show slightly different increase with c.m. energy, the predictions of the two fits are averaged. Hence, $N_{\rm ch}/(N_{\rm part}/2)$ value is predicted to be about 119 with 5% uncertainty in the most central heavy-ion collisions at $\sqrt{s_{\rm NN}} = 5.13$ TeV. The prediction is shown by the right-inclined hatched area in Fig. 5.6. In addition, the fit-averaged prediction based on $p + p(\bar{p})$ collisions at $\sqrt{s_{pp}} = 13$ TeV, recalculated within the PDE approach, is shown in Fig. 5.6 as the left-inclined hatched area.

The predictions are made as well for the centrality dependence and are given in Fig. 5.8. We give the predictions for $\sqrt{s_{\rm NN}} = 5.02$ TeV, considering the recent measurements reported by ALICE for the rapidity density [40] and expecting the mean multiplicity measurements at this energy. The two types of predictions are shown.

First, similar to the above predictions made to the head-on collisions we use the fit functions. Within the effective-energy approach we treat non-central collisions as central collisions at energy $\varepsilon_{\rm NN}$ and use the head-on collision multiplicity fits to predict the centrality dependence. This is similar to that made for the existing data as shown in Fig. 5.8 by the dashed lines. However, for the predictions, we use the average values of the hybrid and the power-law fits, Eqs. (5.19) and (5.20), as soon as those deviate for $\sqrt{s_{\rm NN}}$ above 2.76 TeV. The prediction for $\sqrt{s_{\rm NN}} = 5.02$ TeV centrality dependence is shown by the dashed-dotted line. The centrality and $N_{\rm part}$ values are alike in the shown 2.76 TeV data. The expectations show an increase of the mean multiplicity with $N_{\rm part}$ from about 52 to about 118. The increase looks to be slightly faster than at $\sqrt{s_{\rm NN}} = 2.76$ TeV, especially for the peripheral region.

Second, the PDE set of prediction is made using the calculations based on Eq. (5.18) combining the constituent quark model and the Landau hydrodynamics. This prediction for the centrality dependence is shown by the solid inverted triangles in Fig. 5.8. One can see that the predictions are close to ones obtained from the head-on collision data fits.

The predictions are compared with the LHC data at $\sqrt{s_{\rm NN}} =$ 2.76 TeV. To better match the predictions for highly central collisions, the 2.76 TeV data points are multiplied by 1.3. One can see that the predictions are well reproduced by the scaled data. This indicates no change of the hadroproduction mechanism expected with increase of the c.m. energy at LHC, in contrast to what is seen when one compares the scaled 200 GeV RHIC data with the 2.76 TeV measurements.

An interesting issue to be addressed in the framework of the PDE picture is to consider asymmetric collisions, such as nucleon-nucleus (p/d-nucleus) ones. In these interactions the multiplicity is also expected to have no centrality dependence. This is due to the many nucleon-nucleon interactions of the incident proton with the nucleons of the interacting nucleus while the secondary particles produced in the reaction are assumed to be created out of the c.m. energy deposited to the interaction zone. The proton and nucleus are considered to interact via a single pair of constituent quarks, one from the proton and another one from a nucleon in the interacting nucleus. Then, no centrality dependence of the multiplicity is expected in p-nucleus collisions with the multiplicity values to be similar to that from $p + p(\bar{p})$ interactions at the c.m. energy $\sqrt{s_{pp}} \simeq \sqrt{s_{\rm NN}}$. As a consequence, this, at a given centrality, results to $N_{\rm part}/2$ for the ratio $N_{\rm ch}/N_{\rm ch}^{pp}$. These features have been indeed obtained in d-Au interactions at RHIC [223]. Moreover, the effect of the $N_{\rm part}$-dependence of the multiplicity ratio obtained at RHIC has been also observed in hadron-nucleus collisions at lower $\sqrt{s_{\rm NN}} \approx$ 10–20 GeV [137, 223]. These observations seem to be also obtained at LHC, where the $\sqrt{s_{\rm NN}}$ dependence of the $dN_{\rm ch}/d\eta$ measured in p-Pb collisions at $\sqrt{s_{\rm NN}} = 5.02$ TeV is observed [224] to be consistent with a power-law $\sqrt{s_{pp}}$-fit to $p + p(\bar{p})$ data and its centrality dependence is shown [225, 226] to demonstrate the importance of nucleon-nucleon interactions for p-Pb results.

5.8 Summary

In summary, the multihadron production process in nucleus-nucleus collisions and its universality in nuclear and hadronic interactions are studied. We analyzed the midrapidity pseudorapidity density of charged particles and of the transverse energy measured in nucleus-nucleus collisions in the whole available range of the collision c.m. energy per nucleon, $\sqrt{s_{\rm NN}}$, from a few GeV at GSI up to a few TeV at the LHC. The dependencies of these key observables on $\sqrt{s_{\rm NN}}$ and on the number of participants (or centrality) have been revealed within the participant dissipating energy (PDE) approach. In this approach, the participants are considered to form the initial zone of a collision and to determine the production of hadrons at the very early stage of the collision. In this consideration, one combines the constituent quark picture with Landau hydrodynamics and interrelates the multihadron production in different types of collisions by a proper scaling of the c.m. energy of collisions. In particular, an energy-scaling factor of 1/3 in $p+p(\bar{p})$ measurements is shown to reveal the universality of the multiplicity dependencies in nucleon-nucleon and nucleus-nucleus interactions.

Within this model, we find that the dependence of the pseudorpaidity density at midrapidity from the RHIC to LHC data is well reproduced as soon as the effective c.m. energy variable is introduced as the centrality-defined fraction of the collision c.m. energy. Based on this finding, it is shown that the most central collision data and the centrality-dependent data follow a similar $\sqrt{s_{\rm NN}}$ dependence obtained for the central collision data as soon as the centrality data is rescaled to the effective energy. Within the effective energy approach, the hybrid fit to the central collision data is found to well reproduce the centrality dependence of the midrapidity densities. Similar observations are made for the transverse energy midrapidity density measurements: as soon as the centrality data is recalculated for the c.m. effective energy, these measurements are found to well complement to the $\sqrt{s_{\rm NN}}$ dependence central collision data. The hybrid fit made to the central collision data is shown to reproduce well the midrapidity transverse energy dependence on the number of participants. For both the variables studied, a clear departure of the data as a function of the effective c.m. energy from the linear-log dependence to the power-law one is observed at $\sqrt{s_{\rm NN}} \simeq 500 - 700$ GeV indicating a possible transition to a new regime in heavy-ion collisions. The data at $\sqrt{s_{\rm NN}} \sim 1$ TeV would be extremely useful to clarify the observations made here. Based on the hybrid fits in the framework of the discussed model, the predictions for the energy and the number of participant dependencies for the measurements in the forthcoming heavy-ion runs at LHC at $\sqrt{s_{\rm NN}} = 5.52$ TeV are made.

In the entire available $\sqrt{s_{\rm NN}}$ range of about a few TeV, the energy dependence of the multiplicity in head-on collisions is also found to be well described by the calculations performed within the effective-energy approach based on $p+p(\bar{p})$ data. Meanwhile, depending on the data sample, the calculations are found either to describe the measured centrality dependence or to show some deviation between the calculations and the data. For the RHIC data, the deficit in the predictions is observed for non-central collisions so that the predictions do not follow a constancy with the centrality as it is observed at RHIC. However, the centrality dependence mean multiplicity at LHC is found to be well described by the calculations including the increase from peripheral to the most central collisions.

To clarify the observations, approach of the effective-energy of the quark participants is applied to the pseudorapidity density distribution measured in heavy-ion collisions. The energy balanced limiting fragmentation scaling is introduced based on assumption of the similarity of the fragmentation region of the measured distribution in the beam rest frame and that determined from the calculations by using the effective energy. The revealed scaling allows us to reproduce the pseudorapidity density distributions independent of the centrality of collisions and then to correctly describe the centrality independence of the mean multiplicity measured at RHIC. Moreover, this finding provides a solution to the RHIC "puzzle" of the difference between the centrality independence of the mean multiplicity *vs.* the monotonic decrease of the midrapidity pseudorapidity density with the increase of centrality. The mean multiplicity is shown to get a fraction of additional contribution to account for the balance between the collision c.m. energy shared by all nucleons and the effective energy of the participants. However,the midrapidity pseudorapidity density is fully defined by the effective energy of colliding participants.

The agreement between the calculations made in the context of the proposed PDE approach and the LHC measurements at TeV energies suggest that no energy-balanced additional contribution is required even at relatively small number of participants at TeV energies.

Based on the above findings, the complementarity of the head-on collisions and the centrality data is shown resulting in the similar energy behaviour of the mean multiplicity measurements as soon as the data are considered in terms of the effective energy. A departure of the c.m. energy dependence of the data from the 2nd-order logarithmic behaviour to the power-law or higher-order logarithmic polynomial function at $\sqrt{s_{\rm NN}} \sim 1$ TeV suggests a transition to a new regime in nucleus-nucleus collisions at TeV energies. Interestingly, these findings made for a full collision rapidity range are similar to those drawn from the studies [41] of the pseudorapidity density and the transverse energy density at midrapidity. This is also in accordance with the centrality dependence behaviour of mean multiplicity which also indicates a possible change of the regime of multihadron production as one moves from the RHIC to LHC energies.

The hybrid and the power-law fits are found to describe well the existing data on the charged particle multiplicity from $p+p(\bar{p})$ interactions in the entire c.m. energy range up to the top Tevatron energy of 1.8 TeV. However, in this case, no clear change from the power-law behaviour to the quadratic log-polynomial is observed. Moreover, the predictions made here for the mean multiplicity for $\sqrt{s_{pp}}$ in the LHC energy range of 2.36 TeV to 13 TeV within the PDE approach demonstrate a closeness between the predicted values and the lower-energy $\sqrt{s_{pp}}$ fit. One concludes that, in contrast to heavy-ions, no change in multihadron production in $p + p(\bar{p})$ collisions is expected up to the foreseen LHC energy.

Based on the results of the hybrid fits, the predictions for the charged particle mean multiplicity in head-on heavy-ion collisions at $\sqrt{s_{\rm NN}} = 5.02$ TeV at the LHC are given. Within the obtained complementarity of head-on collisions and centrality data, the predictions are made for the centrality dependence mean multiplicity to be measured.

The soon-to-come measurements at the LHC are of crucial importance for further understanding of the multihadron dynamics. This will shed light on the universality of the multihadron production process in different types of collisions and clarify the PDE approach and the obtained energy-balanced limiting fragmentation, which has been shown to successfully describe the features of global key observables by relating hadronic and nuclear collisions.

Chapter 6

Summary and Outlook

In this thesis, we have studied the inclusive photon production at forward rapidity ($2.3 < \eta < 3.9$) in Pb+Pb collisions at $\sqrt{s_{\rm NN}} = 2.76$ TeV using the data from the Photon Multiplicity Detector (PMD) in ALICE. The data analysis starts with identifying good runs and following the method outlined in the thesis. We do the gain calibration for each honeycomb proportional counter to make gain uniform throughout preshower plane of the PMD. Measured number of photons in each η bin is corrected using "efficiency-purity correction method" to get rid of the detector effects. The pseudorapidity distributions are compared with the available model predictions and it is found that none of the models could explain all aspects of the data at $\sqrt{s_{\rm NN}} = 2.76$ TeV. The findings at LHC, thus, opens up new issues which need proper training of the event generators through the inclusion of new physics processes /mechanisms.

The longitudinal scaling of inclusive photons has been studied for Au+Au collisions at $\sqrt{s_{\rm NN}} = 62.4$, 200 GeV and Pb+Pb collisions at beam energy 158AGeV and $\sqrt{s_{\rm NN}} = 2.76$ TeV. The data seem to follow the limiting fragmentation behaviour. But due to limited acceptance of the PMD, it is difficult to make any conclusion regarding the longitudinal scaling of photons in forward rapidity region. Since the HIJING could not explain the data in forward rapidity region in Pb+Pb collisions at $\sqrt{s_{\rm NN}} = 2.76$ TeV, it would be very interesting to introduce new models (or new physics ingredients) to understand the underlying physics. We have presented the results for study of collision centrality dependance of charged particle multiplicity per participant pair ($N_\gamma/0.5N_{part}$). It is observed that $N_\gamma/0.5N_{part}$

increases monotonically with centrality, which is contrary to the centrality independent behavior of $N_\gamma/0.5N_{part}$ measured in Au+Au at 62.4 and 200 GeV in STAR experiment at RHIC. The results of centrality dependance of $N_\gamma/0.5N_{part}$ at forward rapidity have been found consistent with the charged particle multiplicity measurements at midrapidity in Pb+Pb collisions at $\sqrt{s_{\rm NN}}$ =2.76 TeV at LHC. These measurements at RHIC and LHC energies need to be understood with model comparison.

We have presented the result for the study of charged particle and transverse energy production as a function of collision centrality and collision energy, in the framework of nucleon and quark participants. These participants are estimated using a Monte Carlo-based implementation of nuclear overlap model. The centrality dependence of N_{part}-normalized $dN_{ch}/d\eta$ both for Au+Au collisions at $\sqrt{s_{\rm NN}}$ = 200 GeV and Pb+Pb collisions at $\sqrt{s_{\rm NN}}$ = 2.76 TeV show a monotonic increase with centrality. Whereas a nearly centrality independent scaling behavior is observed for N_{q-part}-normalized data. This gives the indication of partonic activities at RHIC and LHC energies. Similar observation is found for $dE_T/d\eta$.

The charged particle production as a function of c.m. collision energy has been studied both in the nucleon and quark participant frameworks. In contrast to the nucleon participants, where the logarithmic function fails to describe the measurements up to the LHC energies, in the quark participant sector, the logarithmic function describes the data well-up to 2.76 TeV. A power-law function, however, describes the high-energy measurements at LHC energy but underestimates the low energy measurements. We have introduced a "hybrid function", which is a combination of logarithmic and power-law in collision energy, describes the data for $dN_{ch}/d\eta$ and $dE_T/d\eta$ at all available energies both for the nucleon and quark participants, indicating a universality in multi-particle production. The physics motivation behind the hybrid function is that the multiplicity could be explained by the combination of a mid rapidity gluonic sources and fragmentation sources. mid rapidity gluonic sources predict a power-law type behavior of charged particle multiplicity, whereas the fragmentation sources predict a logarithmic behavior. On the other hand, the EKRT model based on a initial state gluon saturation and the power-law function better describes the high-energy behavior of transverse energy production. The value of E_T/N_{ch} for Pb+Pb collisions at $\sqrt{s_{\rm NN}} = 2.76$ TeV estimated by the hybrid function agrees with the corresponding measurement by CMS Collaboration at LHC and reproduces the jump from RHIC to LHC, in its energy dependence behavior. This may indicate a higher initial pressure of the ultra-dense matter at LHC compared to that is formed in RHIC energies. We give the predictions for $dN_{ch}/d\eta$, $dE_T/d\eta$ and E_T/N_{ch} for Pb + Pb collisions at $\sqrt{s_{\rm NN}} = 5.5$ TeV from this universal hybrid function. In conclusion, the charged particle and the transverse energy measurements are well-described by the hybrid function for all available energies and collision species in heavy-ion collisions indicating a universality in particle production mechanism.

In addition, we have analyzed $dN_{ch}/d\eta$ and $dE_t/d\eta$ at midrapidity within the Participant Dissipating Energy (PDE) approach, which combines constituent quarks with Landau hydrodynamics. Within this approach, we found that from RHIC to LHC energies, the $dN_{ch}/d\eta$ is well reproduced as soon as the effective c.m. energy variable (ϵ_{NN}) is introduced as the centrality-defined fraction of the collision c.m. energy. Based on this finding, it is shown that the most central collision data and the centrality dependent data follow a similar $\sqrt{s_{\rm NN}}$ dependence as soon as the centrality data is rescaled to the effective energy. The hybrid fit is found to well reproduce the N_{part} dependence of $dN_{ch}/d\eta$ within the effective-energy approach. Similar observations have been found for the $dE_T/d\eta$ measurements. For both the variables studied, a clear departure of the data as a function of the effective c.m. energy from the linear-log dependence to the power-law one is observed at $\sqrt{s_{\rm NN}} \sim$ 500-700 GeV indicating a possible transition to a new regime in heavy-ion collisions. The data at $\sqrt{s_{\rm NN}}$ $\sim$1 TeV would be extremely useful to clarify the observations made here. Based on the hybrid fits the predictions for the energy and the number-of-participant dependencies for the measurements in the heavy-ion runs at LHC at $\sqrt{s_{\rm NN}} = 5.52$ TeV are made.

We have also studied collision energy and centrality dependance of N_{ch} within the PDE approach. In the entire available range of $\sqrt{s_{\rm NN}}$, the collision energy dependence of the N_{ch} in head-on collisions is found to be well described by the calculations performed within the effective-energy approach based on $p + p(\bar{p})$ data. The centrality dependance mean multiplicity at LHC is found to be well described by the calculations including the monotonic increase from peripheral to the most central collisions. However, for the RHIC data, the deficit in the predictions is observed for non-central collisions. To clarify these observations, approach of the effective energy of the quark participants is applied to the pseudorapidity density distribution measured in heavy-ion collisions. The "energy-balanced limiting fragmentation scaling" is introduced based on assumption of the similarity of the fragmentation region of the measured distribution in the beam rest frame and that determined from the calculations by using the effective energy. The revealed scaling allows us to reproduce the pseudorapidity density distributions independently of the centrality of collisions and then to correctly describe the centrality independence of the mean multiplicity measured at RHIC. Moreover, this finding provides a solution to the "puzzle" at RHIC of the difference between the centrality independence of the mean multiplicity vs. the monotonic decrease of the midrapidity pseudorapidity density with the increase of centrality. Based on the above findings, the complementarity of the head-on collisions and the centrality data is shown, resulting in the similar energy behavior of the mean multiplicity measurements as soon as the data are considered in terms of the effective energy. A departure of the c.m. energy dependence of the data from the second-order logarithmic behavior to the power-law or higher-order logarithmic polynomial function one observes at the region of 1 TeV suggests a transition to a new regime in nucleus-nucleus collisions at TeV energies. Interestingly, these findings for a full collision rapidity range are similar to the midrapidity pseudorapidity measurements.

The hybrid and the power-law fits are found to describe well the existing data on the charged particle multiplicity from $p + p(\bar{p})$ interactions in the entire c.m. energy $\sqrt{s_{pp}}$ range up to the top Tevatron energy of 1.8 TeV. Based on the results of the hybrid fits, the predictions for the charged particle mean multiplicity in head-on heavy-ion collisions at $\sqrt{s_{\rm NN}} = 5.13$ TeV at the LHC are given. Within the obtained complementarity of head-on collisions and centrality data, the predictions are made for the mean multiplicity centrality dependence to be measured at upcoming energies.

Bibliography

[1] R. K. Ellis *et al.*, W. J. Stirling, and B. R. Webber, "QCD and Collider Physics", Cambridge University Press (2003).

[2] F. Wilczek, "A crack in the Standard Model?" Nature **380**, 19 (1996).

[3] F. Englert and R. Brout, Phys. Rev. Lett. **13**, 321 (1964).

[4] P. W. Higgs, Phys. Lett. **12**, 132 (1964); P. W. Higgs, Phys. Rev. Lett. **13**, 508 (1964).

[5] G. Aad *et al.* Physics Letters B **716**, 1 (2012).

[6] S. Chatrchyan *et al.* (CMS Collaboration), Physics Letters B **716**, 30 (2012).

[7] Roel Aaij et al. L(HCb Collaboration) Phys. Rev. Lett. **115**, 072001 (2015).

[8] D. J. Gross and F. Wilczek, Phys. Rev. Lett. **30**, 1343 (1973).

[9] S. Bethke, Nucl. Phys. Proc. Suppl. **121**, 7481 (2003).

[10] F. Karsch, Lech. Notes Phys. **583**, 209 (2002).

[11] F. Karsch, Nucl.Phys. A **698**, 199 (2002).

[12] M. M. Aggarwal *et al.*, (STAR Collaboration), arXiv:nucl-ex/10072613. (2010).

[13] Models and Data Analysis Initiative (MADAI) https://madai-public.cs.unc.edu.

[14] STAR Collaboration, Nucl. Phys. A **757**, 102 (2005); Phys. Rev. Lett. **108**, 072301 (2012).

[15] K. Adcox, *et al.* (PHENIX Collaboration), Nucl. Phys. A **757**, 184 (2005).

[16] G. Aad *et al.* (ATLAS Collaboration), Phys. Rev. Lett. **105**, 252303 (2010).

[17] B. Abelev *et al.* (ALICE Collaboration), Phys. Rev. Lett. **110**, 082302 (2013).

[18] B. Abelev *et al.* (ALICE Collaboration), Phys. Rev. Lett. **109**, 072301 (2012),

[19] A. Adare *et al.* (PHENIX Collaboration), Phys. Rev. Lett. **98**, 232301 (2007).

[20] J. Alam, D. K. Srivastava, B. Sinha and D. N. Basu, Phys. Rev. D **48** , 1117 (1993).

[21] A. Dumitru, U. Katscher, J. A. Maruhn, H. Stocker, W. Greiner and D. H. Rischke, Phys. Rev. C **51**, 2166 (1995).

[22] J. J. Neumann, D. Seibert and G. Fai, Phys. Rev. C **51**, 1460 (1995).

[23] S. Jeon, V. Koch, Phys. Rev. Lett. **85**, 2076 (2000).

[24] Masayuki Asakawa, Ulrich Heinz, and Berndt Muller, Phys. Rev. Lett. **85**, 2072 (2000).

[25] M. Bleicher, S. Jeon, and V. Koch Phys. Rev. C **62**, 061902 (2002).

[26] Sangyong Jeon and Volker Koch, In Quark-Gluon-Plasma 3, Ed. R.C. Hwa and X.N. Wang, 430 (2004); arXiv:hep-ph/0304012v1.

[27] W. Kittel, E.A. DeWolf, Soft Multihadron Dynamics (World Scientific, Singapore, 2005), p. 652

[28] J. F. Grosse-Oetringhaus, PhD thesis, University of Munster, 2009.

[29] R. Sahoo, A. N. Mishra, N. K. Behera, B. K. Nandi, Adv. High Energy Phys. **2015**, 612390 (2015).

[30] P. Carruthers and M. Duong-van, Phys. Rev. D **8**, 859 (1973).

[31] F.-H. Liu, Y.-H. Chen, Y.-Q. Gao, and E.-Q.Wang, Adv. High Energy Phys. **2013**, 710534 (2013).

[32] C. Y. Wong, Introduction to high-energy Heavy-Ion Collisions, World Scientific, River Edge, NJ, USA, 1994.

[33] L. D. Landau, Izvestiya Akademii Nauk SSR, Seriya Fizicheskaya, vol. **17**, 51 (1953).

[34] C. Alt, T. Anticic, B. Baatar *et al.*, Phys. Rev. C **77**, 024903 (2008).

[35] E. Abbas, B. Abelev, J. Adam *et al.*, Phys. Lett. B **726**, 610(2013).

[36] K. Aamodt *et al.*, (ALICE Collaboration), Phys. Rev. Lett. **106** 032301 (2011).

[37] A. Bialas, M. Bleszynski, and W. Czyz, Nucl. Phys. B **111**, 461 (1976).

[38] X. -N. Wang and M. Gyulassy, Phys. Rev. Lett. **86**, 3496 (2001).

[39] D. Kharzeev and M. Nardi, Phys. Lett. B **507**, 121 (2001).

[40] J. Adam *et al.* (ALICE Collaboration) arXiv:1512.06104.

[41] A. N. Mishra, R. Sahoo, E. K. G. Sarkisyan, A. S. Sakharov, Eur. Phys. J. C **74**, 3147 (2014).

[42] S. Eremin and S. Voloshin, Phys. Rev. C **67**, 064905 (2003).

[43] P. K. Netrakanti and B. Mohanty, Phys. Rev. C **70**, 027901 (2004).

[44] B. De and S. Bhattacharyya, Phys. Rev. C **71**, 024903 (2005).

[45] R. Nouicer, AIP Conference Proceedings, vol. **828**, 11 (2006).

[46] R. Nouicer (PHOBOS Collaboration), AIP Conference Proceedings, **842**, 86 (2006).

[47] R. Nouicer, Eur. Phys. J. C **49**, 281 (2007).

[48] G. Wolschin, J. Phys. G **40** ,045104 (2013).

[49] G. Wolschin, Eur. Phys. J. C **5**, 85 (1999).

[50] B.B. Back *et al.*, (PHOBOS Collaboration), Phys. Rev. C **74**, 021902 (2006).

[51] P. V. Chliapnikov, V.A. Uvarov, Phys. Lett. B **251**, 192 (1990).

[52] E. K. G. Sarkisyan and A. S. Sakharov, AIP Conf. Proc. **828**, 35 (2005) and [hep-ph/0510191].

[53] J.F. Grosse-Oetringhaus, K. Reygers, J. Phys. G **37**, 083001 (2010).

[54] Lyndon Evans and Philip Bryant, LHC Machine, JINST, **3**, S08001 (2008).

[55] J. P. Blewett, 200GeV intersecting storage accelerators,Proceeding of the 8th international Conference on High-Energy Accelerators, CERN, Geneva Switzerland (1971).

[56] PYTHIA 6.4, Physics and Manual, hep-ph/0603175, FERMILAB-PUB-06-052-CD-T, March (2006).

[57] ALICE Collaboration, Technical Design Report of Inner Tracking System (ITS): CERN-LHCC-99-012, http://edms.cern.ch/file/398932/1.

[58] ALICE Technical Design Report of Time Projection Chamber: https://edms.cern.ch/file/398930/1/ALICE-DOC-2003-011.pdf.

[59] F. Carminati *et al.*, (ALICE Collaboration), Physics Performance Report, Volume 1, J. Phys. G 30 (2004) 1517.

[60] P. Christiansen, (ALICE Collaboration), Nuclear Physics **A 00**, 1 (2012).

[61] W. R. Leo, Techniques for Nuclear and Particle Physics Experiments, page 23-28, Narosa Publishing House.

[62] J. Alme, Y. Andres, H. Appelshauser, S. Bablok, N. Bialas, *et al.*, Nucl. Instrum. Meth., **A622**, 316, 2010.

[63] ALICE Collaboration, Technical Design Report of Transition-Radiation Detector: CERN-LHCC-2001-021, http://cdsweb.cern.ch/record/519145.

[64] ALICE Collaboration, Technical Design Report of Time-Of-Flight system: CERN-LHCC-2000-012, http://cdsweb.cern.ch/record/430132;

[65] ALICE Collaboration, addendum to the Technical Design Report of Time-Of-Flight system: CERN-LHCC-2002-016, http://cdsweb.cern.ch/record/545834.

[66] B. Alessandro *et al.*, (ALICE Collaboration), ALICE: Physics Performance Report, volume II, J. Phys. G 32 (2006) 1295.

[67] A. Akindinov *et al.*, Eur. Phys. J. C **32**, s165 (2004).

[68] Nuclear Instruments and Methods in Physics Research **A 602**, 658 (2009).

[69] ALICE Collaboration, Technical design report of the High Momentum Particle IDentification, CERN-LHCC-98-019, http://cdsweb.cern.ch/record/381431.

[70] F. Q. Wang and N. Xu, Phys. Rev. C **61** (2000) 021904.

[71] ALICE Collaboration, Technical design report of the PHOton Spectrometer: CERN-LHCC-99-004, http://cdsweb.cern.ch/record/381432.

[72] ALICE Collaboration, Technical design report of the Electro Magnetic Calorimeter: CERN-LHCC-2006-014, http://cdsweb.cern.ch/record/932676.

[73] U. Abeysekara *et al.*, (ALICE Collaboration), ALICE EMCal Physics Performance Report: arXiv:1008.0413

[74] The Alice Collaboration, Alice Technical Design Report, JINST, vol-3 (2008), p.S08002, http://iopscience.iop.org/1748-0221/3/08/S08002.

[75] ALICE Collaboration, Technical design report of the ALICE forward detectors: FMD, T0 and V0: CERN-LHCC-2004-025, http://cdsweb.cern.ch/record/781854.

[76] ALICE Collaboration, Technical design report of Zero-Degree Calorimeter (ZDC): CERN-LHCC-99-005, http://cdsweb.cern.ch/record/381433.

[77] ALICE Collaboration, Technical Design Report, of Photon Multiplicity Detector (PMD): CERN-LHCC-99-032; http://cdsweb.cern.ch/record/451099.

[78] ALICE Collaboration, Addendum to the TDR of the Photon Multiplicity Detector (PMD): CERN-LHCC-2003-038, http://cdsweb.cern.ch/record/642177.

[79] ALICE Collaboration, Technical design report of the MUON Spectrometer: CERN/LHCC 99-22 (1999), http://cdsweb.cern.ch/record/401974

[80] ALICE Collaboration, ALICE Technical Proposal: CERN/LHCC 95-71 (1995).

[81] ALICE Collaboration, MUON Spectrometer Technical Proposal: CERN/LHCC 96-32 (1996), http://cdsweb.cern.ch/record/314011

[82] ALICE Collaboration, Addendum to the TDR of the muon Spectrometer: CERN-LHCC 2000-046 (2000).

[83] ALICE Collaboration, ALICE Technical Design Report of the Trigger, Data Acquisition, High Level Trigger and Control System: CERN-LHCC-2003-062, (2003), https://edms.cern.ch/document/456354/2.

[84] F. Bergsma *et al.*, CERN ALICE DAQ Group, ALICE DAQ and ECS users guide, ALICE Internal Note ALICE-INT-2005-015, http://cdsweb.cern.ch/record/960457.

[85] The ALICE experiment offine project, http://www.cern.ch/ALICE/Projects/offine/aliroot/Welcome.html

[86] J. Durand, O. Barring, S. Ponce and B. Couturier, CASTOR: Operational issues and new developments, in Interlaken, Computing in high-energy physics and nuclear physics, 1221-1226 (2004).

[87] S. Bagnasco *et al.*, AliEn: ALICE environment on the GRID, J. Phys.: Conf. Ser. 119 Volume 119 (2008) 062012.

[88] R. Brun and F. Rademakers, ROOT: An object oriented data analysis framework, Nucl. Instrum. Meth. A **389**, 81 (1997).

[89] PYTHIA 6.4, Physics and Manual, hep-ph/0603175, FERMILAB-PUB-06-052-CD-T, March 2006.

[90] T. Sjostrand, Comput. Phys. Commun. 82, **74** (1994).

[91] R. Engel, Z. Phys. C **66**, 203 (1995).

[92] R. Engel, J. Ranft, S. Roesler, Phys. Rev. D **52**, 1459 (1995).

[93] M. Gyulassy, X. -N. Wang, Phys. Rev. C **80**, 024906 (2009).

[94] Stefan Roesler *et al.*, arXiv:hep-ph/0012252v1.

[95] Z. W. Lin, C. M. Co, B. A. Li, B. Zhang and S. Pal, Phys. Rev. C **72**, 064901(2005).

[96] S. Agostinelli *et al.*, Geant4, a simulation toolkit, Nucl. Instrum. Meth. A **506**, 250 (2003), CERN-IT-2002-003, http://cdsweb.cern.ch/record/602040; http://wwwinfo.cern.ch/asd/geant4/geant4.html.

[97] A. Fasso et al., FLUKA: present status and future developments, Proceedings of the IV International Conference on Calorimeters and their Applications, World Scientific, Singapore (1994).

[98] M. M. Aggarwal *et al.*, (WA93 Collaboration), CERN/SPSC/90-14, SPSC/P-252, 1990.

[99] H. H. Gutbrod *et al.*, Proposal for a large acceptance hadron and photon spectrometer, CERN-SPSLC-91-17, CERN-P260, 1991, 87p.

[100] K. H. Ackermann *et al.*, Nucl. Instr. Meth. A **499**, 624 (2003).

[101] M. M. Aggarwal *et al.*, hep-ex/980726, Nucl. Instr. Meth. in Phys. Res. **A421** (1999) 558.

[102] ALICE Collaboration, ALICE Photon Multiplicity Detector (PMD): Technical De- sign Report, CERNLHCC-99-032; http://cdsweb.cern.ch/record/451099.

[103] S. C. Phatak, Clustering Algorithm For PMD Data, http://www.iopb.res.in/phatak/cluster/clusters.html.

[104] M. M. Mondal, Ph.D. Thesis, Calcutta University, 2010.

[105] J. Benecke, T. T. Chou, C. N. Yang, and E. Yen, Physical Review, **188**, 2159 (1969).

[106] B. B. Back *et al.*, (PHOBOS Collaboration), Nucl. Phys. **A 757**, 28 (2005).

[107] P. K. Netrakanti and B. Mohanty, Phys. Rev. C **70**, 027901 (2004).

[108] N. K. Behera, R. Sahoo and B. K. Nandi, Adv. in High Eng. Phys. **2013**, 273248 (2013).

[109] R. C. Hwa and C. S. Lam, Phys. Rev. D **26**, 2338 (1982).

[110] V. V. Anisovich, Phys. Letts. B **57**, 87 (1975).

[111] V. V. Anisovich, Y. M. Shabelsky and V. M. Shekhter, Nucl. Phys. B **133**, 477 (1978).

[112] J. Adams *et al.*, (STAR Collaboration), Phys. Rev. Lett. **95**, 122301 (2005).

[113] V. V. Anisovich, M. N. Kobrinsky, J. Nyiri and Y. M. Shabelsky, *Quark Model and High Energy Collisions* (World Scientific, Singapore, 2004).

[114] E. Shuryak, Phys. Letts. B **486**, 378 (2000).

[115] E. K. G. Sarkisyan and A. S. Sakharov, Eur. Phys. J. C **70**, 533 (2010).

[116] Rachid Nouicer, AIP Conf. Proc. **828**, 11 (2006). and Preprint nucl-ex/0512044.

[117] D. Miskowiec, http://www. gsi. de/ misko/overlap/.

[118] K. J. Eskola, K. Kajantie, and J. Lindfors, Nucl. Phys. B **323**, 37 (1989).

[119] Particle Data Group Collaboration, Review of Particle Physics, J. Phys. G **37**, 075021 (2010).

[120] Bhaskar De and S. Bhattacharyya, Phys. Rev. C **71**, 024903 (2005).

[121] T. Csörgö *et al.*, (TOTEM Collaboration), Prog. Theor. Phys. Suppl. **193**, 180 (2012).

[122] R. Sahoo, A. N. Mishra, Int. J. Mod. Phys. E **23**, 1450024 (2014).

[123] P. Tribedy and R. Venugopalan, Phys. Letts. B **710**, 125 (2012).

[124] K. J. Eskola, K. Kajantie, P. V. Ruuskanen, and K. Tuominen, Nucl. Phys. B **570**, 379 (2000).

[125] S. S. Adler *et al.*, (PHENIX Collaboration), Phys. Rev. C **71**, 034908 (2005) and references therein.

[126] F. Karsch, Nucl. Phys. A **698**, 199c (2002).

[127] M. Jacob and P. V. Landshoff, Mod. Phys. Lett. A **1**, 657 (1986).

[128] X. N. Wang, Phys. Rep. **280**, 287 (1997).

[129] P. Petreczky, Physics **5**, 112 (2012).

[130] S. Chatrchyan *et al.*, (CMS Collaboration), Phys. Rev. Lett. **109**, 152303 (2012).

[131] S. S. Adler *et al.*, (PHENIX Collaboration), Phys. Rev. C **89**, 044905 (2014).

[132] H. J. Pirner, K. Reygers and B. Z. Kopeliovich, Phys. Rev. C**87**, 054906 (2013).

[133] G. Wolschin, Eur. Phys. J. A **5**, 85 (1999).

[134] G. Wolschin, M. Biyajima and N. Suzuki, Phys. Letts. B **633** (2006) 38.

[135] D. Röhrscheid and G. Wolschin, Phys. Rev. C **86**, 024902 (2012).

[136] G. Wolschin, Europhys. Letts. **95**, 61001 (2011).

[137] W. Busza, Acta Physica Pol. B **35**, 2873 (2004).

[138] W. Busza, Nucl. Phys. A **830**, 35c (2009).

[139] B. Alver *et al.*, Phys. Rev. C **83**, 024913 (2011).

[140] E. Abbas *et al.*, (ALICE Collaboration), Phys. Lett. **B 726**, 610 (2013).

[141] N. Armesto, arXiv: 0903. 1330 and references therein.

[142] B. Mohanty *et al.*, Phys. Rev. C **68**, 021901 (2003).

[143] J. Adams *et al.*, (STAR Collaboration), Phys. Rev. C**70**, 054907 (2004).

[144] J. Cleymans, R. Sahoo, D. P. Mahapatra, D. K. Srivastava and S. Wheaton, Phys. Letts. B **660**, 172 (2008).

[145] J. Cleymans, R. Sahoo, D. P. Mahapatra, D. K. Srivastava and S. Wheaton, J. Phys. G **35**, 104147 (2008).

[146] J. Cleymans, R. Sahoo, D. K. Srivastava and S. Wheaton, Eur. Phys. J. ST **155**, 13 (2008).

[147] D. Prorok, Nucl. Phys. A **749**, 194c (2005).

[148] R. Hagedorn, Prog. Sci. Culture **1**, 395 (1976).

[149] R. Hagedorn, Suppl. Nuovo Cimento **3**, 147 (1965).

[150] J. Cleymans, H. Oeschler, K. Redlich and S. Wheaton, Phys. Rev. C**73**, 034905 (2006).

[151] A. Adronic, P. Braun-Munzinger, J. Stachel and H. Stocker, Phys. Letts. B **697**, 203 (2011).

[152] B. Abelev *et al.*, (ALICE Collaboration), Phys. Rev. Lett. **109**, 252301 (2012).

[153] C. Shen, U. Heinz, P. Huovinen and H. Song, Phys. Rev. C **84**, 044903 (2011).

[154] M. Floris, J. Phys. G **38**, 124025 (2011).

[155] H. Song, Nucl. Phys. A **904-905**, 114c (2013).

[156] H. Song, S. Bass and U. Heinz, Phys. Rev. C **83**, 024912 (2011).

[157] B. Abelev *et al.*, (STAR Collaboration), Phys. Rev. C **79**, 034909 (2009).

[158] B. Abelev *et al.*, (STAR Collaboration), Phys. Rev. C **81**, 024911 (2010).

[159] T. Lappi, Eur. Phys. J. C **71**, 1699 (2011).

[160] G. Watt and H. Kowalski, Phys. Rev. D **78**, 014016 (2008).

[161] W. Heisenberg, *Zs. Phis.* **126** (1949) 569.

[162] E. Fermi, *Prog. Theor. Phys.* **5** (1950) 570.

[163] L. D. Landau, Izv. Akad. Nauk: Ser. Fiz. **17**, 51 (1953). English translation: *Collected Papers of L. D. Landau*, ed. by D. Ter-Haarp (Pergamon, Oxford, 1965), p. 569. Reprinted in: *Quark-Gluon Plasma: Theoretical Foundations*, ed. by J. Kapusta, B. Müller, J. Rafelski (Elsevier, Amsterdam, 2003), p. 283.

[164] A. Białas, B. Bleszyński, W. Czyż, Nucl. Phys. B **111** (1976) 461; for review, see: A. Białas, J. Phys. G **35**, 044053 (2008).

[165] S. Eremin, S. Voloshin, Phys. Rev. C **67**, 064905 (2003).

[166] P. K. Netrakanti, B. Mohanty, Phys. Rev. C **70**, 027901 (2004).

[167] B. De, S. Bhattacharyya, Phys. Rev. C **71**, 024903 (2005).

[168] R. Nouicer, *AIP Conf. Proc.* **828** (2005) 11, **842** (2006) 86, Eur. Phys. J. C **49**, 281 (2007).

[169] Nirbhay K. Behera, Raghunath Sahoo and Basanta K. Nandi, Adv. in High Eng. Phys. **2013**, 273248 (2013).

[170] R. Singh, L. Kumar, P.K. Netrakanti, B. Mohanty, Adv. High Energy Phys. **2013**, 761474 (2013).

[171] PHOBOS Collab., B.B. Back *et al.*, Nucl. Phys. A **757**, 28 (2005).

[172] I. M. Dremin, J.W. Gary, Phys. Lett. B **459**, 341 (1999).

[173] R. Rougny (for the CMS Collaboration), *Nucl. Phys. B (Proc. Suppl.)* **207-208**, 29 (2010).

[174] See *e.g.* P. Steinberg, JPCS **9**, 280 (2005).

[175] E. M. Levin, L.L. Frankfurt, JETP Lett. **2**, 65 (1965).

[176] H. J. Lipkin, F. Scheck, Phys. Rev. Lett. **16**, 71 (1966).

[177] J. J. J. Kokkedee, L. Van Hove, Nuovo Cim. **42**, 711 (1966).

[178] For review and a collection of reprints on original papers on quarks and composite models, including [175–177], see: J.J.J. Kokkedee, *The Quark Model* (W.A. Benjamin, Inc., New York, 1969).

[179] For review, see: V.V. Anisovich, N.M. Kobrinsky, J. Nyiri, Yu.M. Shabelsky, *Quark Model and High Energy Collisions* (World Scientific, Singapore, 2004).

[180] G. Aad *et al.*, (ATLAS Collaboration), Phys. Lett. B **710**, 363 (2012).

[181] S. Chatrchyan *et al.*, (CMS Collaboration), J. High Energy Phys. **08**, 141 (2011).

[182] K. Aamodt *et al.*, (ALICE Collaboration), Phys. Rev. Lett. **105**, 252301 (2010).

[183] G. Wolschin, J. Phys. G **40**, 045104 (202013).

[184] G. Wolschin, Eur. Phys. J. A **5**, 85 (1999).

[185] G. Wolschin, M. Biyajima and N. Suzuki, Phys. Lett. B **633**, 38 (2006).

[186] D. Rohrscheid and G. Wolschin, Phys. Rev. C **86**, 024902 (2012).

[187] G. Wolschin, Europhys. Lett. **95**, 61001 (2011).

[188] S. S. Adler *et al.*, (PHENIX Collaboration), Phys. Rev. C **74**, 049901 (2005).

[189] B. I. Abelev *et al.*, (STAR Collaboration), Phys. Rev. C **79**, 034909 (2009).

[190] K. Aamodt *et al.*, (ALICE Collaboration), Phys. Rev. Lett. **106**, 032301 (2011).

[191] B. I. Abelev *et al.*, (STAR Collaboration), Phys. Rev. C **81**, 024911 (2010).

[192] V. Khachatryan *et al.*, (CMS Collaboration), Phys. Rev. Lett. **105**, 022002 (2010).

[193] The Review of Particle Physics, K.A. Olive *et al.* (Particle Data Group), Chin. Phys. C **38**, 090001 (2014).

[194] E. K. G. Sarkisyan, A.N. Mishra, R. Sahoo, A. S. Sakharov, arXiv:1603.09040, Phys. Rev. D Rapid Comms. (In Press).

[195] E. Abbas *et al.*, (ALICE Collaboration), Phys. Lett. B **726**, 610 (2013).

[196] S. Chatrchyan *et al.*, (CMS Collaboration), Phys. Rev. Lett. **109**, 152303 (2012).

[197] E. Levin, A.H. Rezaeian, Phys. Rev. D **83**, 11401 (2011).

[198] A. Capella, E.G. Ferreiro, Eur. Phys. J. C **72**, 1936 (2012).

[199] I. Bautista, J. G. Milhano, C. Pajares, and J. Dias. de Deus, Phys. Lett. B **715**, 230 (2012).

[200] G. Wolschin, Phys. Rev. C **91**, 014905 (2015).

[201] E. K. G. Sarkisyan, A. N. Mishra, R. Sahoo, A. S. Sakharov, Phys. Rev. D93 (2016) no. 7, 079904.

[202] V. Khachatryan *et al.*, (CMS Collaboration), J. High Energy Phys. **02**, 041 (2010).

[203] K. Aamodt *et al.*, (ALICE Collaboration), Eur. Phys. J. C **68**, 89 (2010).

[204] G. Aad *et al.*, (ATLAS Collaboration), New J. Phys. **13**, 053033 (2011).

[205] J. Adam *et al.*, (ALICE Collaboration), Phys. Lett. B **754**, 373 (2016).

[206] G. J. Alner *et al.*, (UA5 Collaboration), Z. Phys. C **33**, 1 (1986).

[207] R. Haar *et al.*, (P238 Collaboration), Phys. Lett. B **401**, 176 (1997).

[208] F. Abe *et al.*, (CDF Collaboration), Phys. Rev. D **41**, 2330 (1990).

[209] R. Aaij *et al.*, (LHCb Collaboration), Eur. Phys. J. C **72**, 1947 (2012).

[210] G. Antchev *et al.*, (TOTEM Collaboration), Europhys. Lett. **98**, 31002 (2012).

[211] G. A. Milekhin, Sov. Phys. JETP **8**, 829 (1959).

[212] E. V. Shuryak, Sov. J. Nucl. Phys. **20**, 295 (1974).

[213] E. L. Feinberg, in *Relativistic Heavy-Ion Physics* (ed. by L. P. Csernai, D. D. Strottman): Int. Rev. Nucl. Phys., vol. 6 (World Scientific, Singapore, 1991), p 341.

[214] J. Benecke, T.T. Chou, C.N. Yang, E. Yen, Phys. Rev. **188**, 2159 (1969).

[215] C. -Y. Wong, Phys. Rev. C **78**, 054902 (2008).

[216] A. Sen, J. Gerhard, G. Torrieri, K. Read, C.-Y. Wong, Phys. Rev. C **91**, 024901 (2015).

[217] I. Bautista, C. Pajares, J. G. Milhano, and J. Dias de Deus Phys. Rev. C **86**, 034909 (2012).

[218] Z. J. Jiang, H. L. Zhang, Mod. Phys. Lett. A **29**, 1450130 (2014).

[219] Z. J. Jiang, H. L. Zhang, J. Wang, K. Ma, Adv. High Energy Phys. **2014**, 248360 (2014).

[220] Jiang, Y. Zhang, H. L. Zhang, H.P. Deng, Nucl. Phys. A **941**, 188 (2015).

[221] L. -N. Gao, F.-H. Liu, Adv. High Energy Phys. **2015**, 184713 (2015).

[222] B. -C. Li, Y. -Z. Wang, F. -H. Liu, X. -J. Wen, Y. -E. Dong, Phys. Rev. D **89**, 054014 (2014).

[223] B. Back *et al.*, Phys. Rev. C **72**, 031901(R) (2005).

[224] B. Abelev *et al.*, (ALICE Collaboration), Phys. Rev. Lett. **110**, 032301 (2013).

[225] J. Adam *et al.*, (ALICE Collaboration), Phys. Rev. C **91**, 064905 (2015).

[226] G. Aad *et al.*, (ATLAS Collaboration), arXiv:1508.00848.